

SPECIFIC AND NON-SPECIFIC INTERACTIONS ON CARBON MATERIAL SURFACES

Aurik Yann Andreu



A thesis submitted to
The Robert Gordon University
in partial fulfilment of the requirements for
the award of the degree of Doctor of Philosophy

October 2010, Aberdeen

To my parents
and
to my wife and daughter,
Ling-Ying (玲瑩) and Lya (俐婭),
for their love, patience and support.

Abstract

The interactions which occur between both polar and non-polar fluid phases and surfaces of various carbon materials: porous Activated Carbon (AC), non-porous Carbon Black (CB) and Multiwall Carbon Nanotubes (MWCNTs) with different surface chemistry have been studied. These are currently of great interest as they govern the interfacial behaviour of carbons in a wide range of applications; separation and composite technologies being two prime examples. Consequently, techniques for chemical modification of carbon surfaces are also of interest.

Surface oxygen functional groups have been introduced, or modified, using the following oxidation techniques: liquid-phase oxidation (both AC and CB), Fenton and Birch reduction treatment (MWCNTs) and in a more controlled manner using gas-phase ozone treatment (CB). The chemistry of all the resulting carbon surfaces were characterised using X-ray Photoelectron Spectroscopy (XPS), which gives a quick and direct quantitative measure of the external surface composition. This technique, which has not yet been extensively employed in detailed adsorption studies, is a promising alternative to Temperature Programmed Desorption (TPD) and Boehm titration method in the determination of oxygen and other surface groups. Physical effects of the various surface modifications have been studied using a variety of techniques appropriate for the material in question. Scanning Electron Microscopy (SEM) images show some deteriorating effects of the liquid-phase oxidations on the structure of both activated carbon and carbon black materials. Conversely, surface areas from nitrogen adsorption at 77°K, coupled with immersion calorimetry data for toluene, show that the physical structure of the carbon blacks is not modified by ozone treatment. This has allowed a detailed study of the effects of surface oxygen level (i.e. polarity) on vapour adsorption. Regarding the MWCNT materials, detailed High-Resolution Transmission Electron Microscopy (HRTEM) photographs show that the multi-wall structure of the nanotubes

is not significantly disrupted during the introduction of active functional groups by the Fenton or Birch treatment and therefore keeping intact their mechanical properties which augurs well for their use as reinforcement in composite structures whilst also improving their dispersion properties in polar fluids.

A systematic shift to higher adsorption values, due to the increasing specific interactions between the alcohol –OH groups and the surface oxygen groups, is observed in all the isotherms of alcohols from the CB series as the total surface oxygen concentration ($[O]_T$) increases. Moreover, this effect was observed to be most significant for methanol confirming that the mechanism of adsorption is dominated by hydrogen bonding and therefore dependant on the surface concentration of oxygen sites; whereas it becomes less marked in the case of ethanol and isopropanol respectively due to the increasing non-specific, dispersion, interactions of the alkyl chain with the non-polar carbon surface. Overall correlations were observed between the surface oxygen concentration $[O]_T$, the resulting enthalpy of immersion $-\Delta H_i$ values and the characteristic energy E of the Dubinin–Radushkevich–Kaganer (DRK) equation obtained for toluene and these alcohols and the influence of the carbon surface chemistry on the character of the adsorption isotherms is also discussed.

This behaviour is also observed and much more pronounced in the case of water adsorption on other oxidised carbon materials (AC, CB and MWCNT) due to the higher polarity of water molecules. The water adsorption data were analysed using in particular the Dubinin–Serpinsky (DS) equation and also some of its recent variations such as Barton and D’Arcy & Watt equations. The DS2 and various Barton equations were found to fit best the AC and CB materials modified by liquid-phase oxidations and also for the CB O₃ series with increasing level of oxidation while both D’Arcy & Watt equations gave the best fittings for the MWCNTs materials. It was also shown that the resulting parameters a_0 (for the DS equation) describing the surface concentration of primary polar adsorption sites and as the limiting water adsorption value were both linked to the surface oxygen level $[O]_T$. Regarding interfacial bonding, the oxidised CB and MWCNT

materials are expected to show an improved physicochemical wetting of their surfaces by various resin compounds.

KEYWORDS: Carbon black (CB), Activated carbon (AC), Multiwall carbon nanotubes (MWCNTs), Adsorption, Immersion calorimetry, X-ray photoelectron spectroscopy (XPS), Ozone modification, Surface chemistry, Dispersion and polar interactions.

Résumé

Les travaux présentés dans cette thèse décrivent les interactions entre vapeurs polaires et non-polaires et divers adsorbants carbonés tels que Noirs de Carbone (CB), Charbon Actif (AC) et Nanotubes de Carbone Multi-feuillets (MWCNT) ayant différentes chimies de surface.

Les groupes fonctionnels contenant des atomes d'oxygène ont été introduits par les techniques d'oxydation suivantes: oxydation acide en phase liquide (pour les noirs de carbone et charbons actifs), oxydation Fenton et réduction Birch (pour les MWCNTs) et d'une manière mieux contrôlée grâce au traitement à l'ozone en phase gazeuse (pour les CBs). Les surfaces carbonées résultantes ont été analysées par Spectrométrie Photoélectronique X (XPS), qui fournit une mesure quantitative rapide et directe de la composition chimique de la surface. Les images produites par Microscopie Electronique à Balayage (MEB/SEM) ont quant à elles été utilisées pour nous donner des informations sur la nature des dommages structuraux des noirs de carbone et charbon actifs induits par les différentes méthodes d'oxydation, en particulier les traitements à l'acide. Inversement, les surfaces spécifiques à partir de l'adsorption d'azote à 77°K ainsi que les données d'enthalpies d'immersion dans le toluène indiquent que la structure physique des noirs de carbone n'a subi aucune modification majeure par l'oxydation à l'ozone. Cela nous a permis de mener une étude détaillée des effets de la concentration d'oxygène de surface (i.e. polarité de surface) sur l'adsorption de diverses vapeurs. En ce qui concerne les MWCNTs, les photographies détaillées obtenues par Microscopie Electronique en Transmission Haute Résolution (HRTEM) montrent que la structure multi-feuillet des nanotubes n'a pas été vraiment perturbé durant l'introduction des groupes fonctionnels par les deux traitements Fenton et Birch, ce qui permet de déduire qu'ils ont gardé intact leurs propriétés mécaniques nécessaires à la majorité de leurs applications.

Pour la série des noirs de carbone oxydés à l'ozone, un décalage systématique vers des valeurs d'adsorption plus élevées est observé dans toutes les isothermes d'alcools lorsque la concentration d'oxygène $[O]_T$ en surface augmente causant ainsi une multiplication des interactions spécifiques entre le groupe alcool $-OH$ et les sites actifs de surface contenant les atomes d'oxygène. Cet effet est beaucoup plus significatif dans le cas du méthanol ce qui confirme que le mécanisme d'adsorption pour cette molécule est dominé par les liaisons hydrogène de type dipôle/dipôle et donc fortement sensible au niveau d'oxydation de la surface. Cette tendance est en revanche respectivement moins prononcée pour l'éthanol et l'isopropanol en raison de l'augmentation des interactions non-spécifiques, appelées aussi interactions de dispersion, entre la chaîne alkyle et la surface carbonée non-polaire. Des corrélations globales existantes entre la concentration d'oxygène de surface $[O]_T$, les enthalpies d'immersion et l'énergie caractéristique E de l'équation Dubinin–Radushkevich–Kaganer (DRK) obtenue pour le toluène et ces trois alcools ont d'ailleurs été mises en évidence. Nous nous sommes aussi intéressés à l'influence de la chimie de surface de ces matériaux carbonés sur le caractère des isothermes d'adsorption pour ces vapeurs.

Un comportement identique est observé dans le cas de l'adsorption d'eau sur ces trois types de matériaux oxydés (AC, CB et MWCNTs) mais tout en étant beaucoup plus prononcé en raison de la plus grande polarité des molécules d'eau. Les isothermes d'adsorption d'eau ont été analysées en particulier à l'aide de l'équation de Dubinin–Serpinsky (DS) mais nous avons aussi utilisé quelques unes de ses récentes variations telles que les équations de Barton et d'Arcy & Watt. Pour tous ces matériaux, les résultats obtenus par modélisation des équations précédentes montrent que le paramètre a_0 décrivant le nombre de sites primaire d'adsorption mais aussi a_s représentant la quantité d'eau adsorbée limite sont dépendant du niveau d'oxydation de surface $[O]_T$. En ce qui concerne les liaisons au niveau des interfaces, nous nous attendons à ce que les surfaces des noirs de carbone et MWCNTs oxydés présentent une amélioration

considérable de leur mouillage physico-chimique dans une gamme variée de résine, ceci dans le but d'améliorer les propriétés et performance du matériau composite ainsi formé.

MOTS-CLÉS: Noir de charbon, Charbon actif, Nanotubes de carbone multi-feuillets, Adsorption, Calorimétrie d'immersion, Spectrométrie photo-électronique X (XPS), Oxydation de surface à l'ozone, Chimie de surface, Interactions de types : dispersion et polaires.

Acknowledgements

I would like to express my sincere gratitude to my director of studies Prof. Bob Bradley for all his guidance, help and encouragements throughout the course of my studies within the Advanced Materials & Biomaterials Research Centre.

I would also like to thank my secondary supervisor, Dr. Marcus Davidson, for the support and advice he gave me during the first stage of my PhD, especially his experimental advice and guidance on the XPS.

My sincere gratitude goes also to Prof. Fritz Stoeckli and Dr. Deirdre Hugi-Cleary who welcomed me in their research group in the University of Neuchatel (Switzerland) for a short time. I am indebted to them for the benefit of their experience in the area of Carbon Science and also for the very helpful technical discussions we had regarding the experimentation methods.

I am deeply grateful to Dr. R. Andrews and Prof. M. Meier from The University of Kentucky – Center for Applied Energy Research (UKY – CAER, US) who kindly provided the MWCNT materials and also carried out the oxidation treatments on these samples. I would also like to express my thanks to Prof W. Zhou from the Electron Microscopy Group at University of St Andrews who performed the HRTEM observations on the MWCNT samples.

My special thank is given to my colleague and dear friend, Mr Maurizio Falco, for his encouragement, patience toward me and particularly his willing assistance at all times.

I would like to thank the Robert Gordon University (with SFC RDG/EPSRC DTG) for this PhD studentship and many staff in the School of Engineering who have help me over the years: Mr Bill Walker, Mr John Dickson, Mr Allan MacPherson, Mr Steven Pirie, Mr Martin Johnstone, Mr Graeme Budge and Mr Steve Allardyce for their technical support, Mr Iain Tough who allowed me to use the SEM microscope, Mr Les

Maclaren for his technical assistance when I was using the blowtorch apparatus and Prof. Edward Gobina who let me use some of his equipments.

I also say thank you to my former and current colleagues from the Robert Gordon University, particularly, Stephen Mitchell, Susan Osbeck, Chee Chong Chen, Ali Temimi, Barry McKenzie, Gennady Lubarsky and Maurizio Falco.

I would like to thank all of my family who have supported me unconditionally throughout the years, especially, my parents Jean-Pierre and Marie-José, my granny Mamie Jeanine, my sister Alix and finally, my wife Ling-Ying and daughter Lya for their continuing encouragement, patience, enthusiasm and love.

Declaration

The research work presented in this thesis has resulted in the following publications and conference presentations:

- ✓ A. Andreu, H. F. Stoeckli and R. H. Bradley, “*Influence of activated carbon surface chemistry and porosity on vapour adsorption*”, poster presented at the British Carbon Group Workshop - Carbon Materials: Science and Art, Brighton, UK (2005).
- ✓ A. Andreu, R. H. Bradley and H. F. Stoeckli, “*Specific and non-specific interactions on non-porous carbon surfaces*”, presented at the International Conference on Carbon, Aberdeen, Scotland (2006).
- ✓ A. Andreu and R. H. Bradley, “*Adsorption interactions on carbon surfaces*”, presented at the SCI Scotland (Society of Chemical Industry Scotland section) meeting on Nanotechnology, Aberdeen, Scotland (2006).
- ✓ R. H. Bradley, A. Andreu, H. F. Stoeckli, keynote lecture: “*Correlation of water adsorption isotherms with oxygen groups on carbon black surfaces*”, presented at the International Conference on Carbon, Seattle, USA (2007).
- ✓ A. Andreu, H. F. Stoeckli and R. H. Bradley, “*Specific and non-specific interactions on non-porous carbon black surfaces*”, *Carbon* 45 (2007) 1854–1864.
- ✓ R. H. Bradley and A. Andreu, Keynote Lecture: “*Interactions of polar molecules with carbon surfaces*”, presented at the International Conference on Carbon, Biarritz, France (2009).
- ✓ R. H. Bradley, A. Andreu, R. Andrews and M. Meier, “*Surface functionalisation of multi-wall carbon nanotubes*”, poster presented at the International Conference on Carbon, Biarritz, France (2009).

Table of content

ABSTRACT	I
RÉSUMÉ	IV
ACKNOWLEDGEMENTS	VII
DECLARATION	IX
TABLE OF CONTENT	X
LIST OF FIGURES	XIII
LIST OF TABLES	XIX
ABBREVIATIONS AND ACRONYMS	XX
SYMBOLS	XXII
CHAPTER 1 INTRODUCTION	<u>1</u>
CHAPTER 2 THEORY AND LITERATURE REVIEW	<u>6</u>
2.1 GAS/SOLID INTERACTIONS	6
2.2 ADSORPTION BY POROUS AND NON-POROUS SOLIDS	14
2.3 CASE OF WATER ADSORPTION	24
2.4 IMMERSION CALORIMETRY	30
2.5 MEASURE OF THE EXTERNAL SURFACE AREA	32
2.6 NON-POROUS AND POROUS CARBON ADSORBENTS	33
2.7 OXYGEN ON CARBON SURFACES	46
CHAPTER 3 EXPERIMENTAL	<u>64</u>
3.1 ADSORPTION MEASUREMENT	64

3.2 IMMERSION CALORIMETRY	66
3.3 X-RAY PHOTOELECTRON SPECTROSCOPY (XPS)	69
3.4 THERMOGRAVIMETRY ANALYSIS (TGA)	79
3.5 MICROSCOPY TECHNIQUES	80
3.6 OXIDATION AND REDUCTION OF CARBON MATERIALS	86
<u>CHAPTER 4 INITIAL INVESTIGATIONS AND CHARACTERISATION OF GRAPHITE, CARBON BLACK AND ACTIVATED CARBON</u>	<u>96</u>
<hr/>	
4.1 INTRODUCTION	96
4.2 AFM OBSERVATIONS ON BASE AND OXIDISED GRAPHITE MATERIALS	97
4.3 TEM OBSERVATIONS OF THE UNTREATED CARBON BLACK N330	101
4.4 SEM OBSERVATIONS OF THE EFFECTS OF THE OXIDATION TREATMENTS ON VARIOUS CARBON SURFACES	103
4.5 THERMOGRAVIMETRIC ANALYSIS (TGA) AND DIFFERENTIAL THERMAL GRAVIMETRY (DTG) ON OXIDISED CARBON MATERIALS	111
4.6 THERMAL REDUCTION ON ACTIVATED CARBON BPL	115
<u>CHAPTER 5 SPECIFIC AND NON-SPECIFIC INTERACTIONS (DURING THE ADSORPTION OF ALCOHOLS) ON NON-POROUS CARBON BLACK SURFACES</u>	<u>124</u>
<hr/>	
5.1 INTRODUCTION AND THEORETICAL	125
5.2 EXPERIMENTAL	129
5.3 RESULTS AND DISCUSSION	131
5.4 CONCLUSIONS	155
<u>CHAPTER 6 CORRELATION OF WATER ADSORPTION ISOTHERMS WITH OXYGEN GROUPS ON CARBON SURFACES</u>	<u>162</u>
<hr/>	
6.1 INTRODUCTION AND THEORETICAL	163
6.2 EXPERIMENTAL	165

6.3 RESULTS AND DISCUSSION	166
6.4 CONCLUSIONS	195
<u>CHAPTER 7 SURFACE STUDIES OF FUNCTIONALISED MULTI-WALL CARBON NANOTUBES</u>	<u>200</u>
7.1 INTRODUCTION	201
7.2 EXPERIMENTAL: MATERIALS AND METHODS	202
7.3 RESULTS AND DISCUSSION	209
7.4 CONCLUSIONS	229
<u>CHAPTER 8 CONCLUSIONS</u>	<u>234</u>
APPENDIX A GLASS AMPOULE FABRICATION	239

List of figures

FIGURE 2.1: POTENTIAL ENERGY DIAGRAM OF TWO ATOMS OF ARGON.	8
FIGURE 2.2: CLASSIFICATION OF THE FIVE TYPES OF ADSORPTION ISOTHERM (BDDT), TOGETHER WITH TYPE VI, THE STEPPED ISOTHERM.	10
FIGURE 2.3: SCHEMATIC DRAWING OF THE DIFFERENT TYPES OF PORES IN AN ACTIVATED CARBON PARTICLE.	12
FIGURE 2.4: WATER ADSORPTION ISOTHERMS GENERATED FROM THE DIFFERENT MODELS AT 303°K. THE FOLLOWING PARAMETERS HAVE BEEN USED FOR THE CALCULATIONS: $c = 2$, $A_0 = 0.1$ MMOL/G, $A_s = 0.9$ MMOL/G; FOR B2, $A_c = 4$ MMOL/G; FOR GB, $N = 6$ DESCRIBING STRICTLY MICROPOROUS CARBONS WITH MORE VISIBLE UPWARD RISE AND PLATEAU. FOR THE D'ARCY & WATT MODEL, $C_{DS} = 0.88$, $A_{0,DS} = 0.11$ MMOL/G, $A_{ML} = 0.07$ MMOL/G, $K_L = 0.4$ MBAR ⁻¹ AND $P_s = 42.42$ MBAR. ADDITIONALLY EXPERIMENTAL DATA ON CARBON BLACK N330 IS ALSO REPRESENTED.	29
FIGURE 2.5: SIMPLIFIED ILLUSTRATION OF THE OIL FURNACE REACTOR. THE OIL FEED STOCK IS INJECTED INTO A VERY HIGH TEMPERATURE GAS FLAME AND THE CARBON BLACK FORMATION IS CONTROLLED VIA A QUENCH WATER SYSTEM.	34
FIGURE 2.6: SEQUENCE OF THE STRUCTURE DEVELOPMENT OF CARBON BLACK FROM THE PRIMARY PARTICLE TO AGGLOMERATE (WHICH IS A PACKING OF AGGREGATES THROUGH WEAK ELECTRONIC FORCES). AGGREGATES ARE THE BASE STRUCTURE OF CARBON BLACK, THEY ARE INDIVISIBLE.	35
FIGURE 2.7: SCHEMATIC REPRESENTATION OF THE STRUCTURE OF ACTIVATED CARBON (ADAPTED FROM STOECKLI [1][34]).	39
FIGURE 2.8: CRYSTAL STRUCTURE OF HEXAGONAL GRAPHITE. EACH CARBON ATOM IN THE HONEYCOMB NETWORK IS BONDED THROUGH SP ² BONDS TO THE THREE NEAREST NEIGHBOURS WITHIN THE BASAL PLANE. THE LAYERS ARE STACKED IN ABAB SEQUENCE DUE TO WEAK INTERPLANAR INTERACTIONS (DELOCALIZED π BONDS). THE RESULTING IN-PLANE INTERATOMIC DISTANCE A_{c-c} IS EQUAL TO 1.421 Å WHEREAS THE INTERPLANAR DISTANCE $c/2$ IS EQUAL TO 3.354 Å (WITH $c = 6.708$ Å).	40
FIGURE 2.9: SCHEMATIC DIAGRAM SHOWING THE CHIRAL VECTOR Ch AND THE CHIRAL ANGLE θ_{Ch} . THE CHIRAL VECTOR IS DEFINED BY THE VECTOR $n \cdot a1 + m \cdot a2$, $a1$ AND $a2$ BEING THE UNIT VECTORS OF THE TWO DIMENSIONAL GRAPHENE SHEET. THE CHIRAL ANGLE IS DEFINED AS THE ANGLE BETWEEN THE CHIRAL VECTOR Ch AND THE ZIGZAG AXIS $a1$	42
FIGURE 2.10: SWCNTs WITH DIFFERENT CHIRALITIES. (A) (5,5) ARMCHAIR NANOTUBE, (B) (9,0) ZIGZAG NANOTUBE AND (C) (10,5) CHIRAL NANOTUBE.	44
FIGURE 2.11: STONE-WALES TRANSFORMATION OCCURRING IN AN ARMCHAIR NANOTUBE UNDER AXIAL TENSION.	45
FIGURE 2.12: HRTEM PHOTOGRAPH OF AS-PRODUCED MWCNT. THE MULTIWALL STRUCTURE FORMED BY CONCENTRIC GRAPHENE SHEET IS CLEARLY VISIBLE ON EACH SIDE.	46
FIGURE 2.13: CLOSE VIEW ON THE HEXAGONAL STRUCTURE OF GRAPHITE SHEET, IN PARTICULAR THE FOOTPRINT AREA OF THE CENTRAL CARBON ATOM REPRESENTED BY THE COLOURED TRIANGLE.	48
FIGURE 3.1: SCHEMATIC DIAGRAM OF THE IGA (INTELLIGENT GRAVIMETRIC ANALYSER).	65

FIGURE 3.2: SCHEMATIC REPRESENTATION OF: A) THE C80 II TIAN-CALVET TYPE CALORIMETER AND B) THE IMMERSION CELL CONTAINING THE AMPOULE USED TO DETERMINE ENTHALPIES OF IMMERSION.....	67
FIGURE 3.3: CHARACTERISTIC THERMOGRAM OF A MEASURE OF ENTHALPY OF IMMERSION. (SAMPLE: CB N330 O ₃ 30MIN IN ISOPROPANOL).....	68
FIGURE 3.4: PHOTOGRAPHS OF A) COMMERCIAL AMPOULE AND B) LAB-MADE GLASS AMPOULE WITH THIN CAPILLARY.....	69
FIGURE 3.5: A) ATOMIC MODEL FOR THE XPS EMISSION PROCESS. AN INCOMING PHOTON CAUSES THE EJECTION OF THE PHOTOELECTRON. B) ATOMIC MODEL FOR THE RELAXATION PROCESS RESULTING IN THE EMISSION OF A 2P AUGER ELECTRON. THE INSTANTANEOUS REARRANGEMENT OF ATOMIC LEVELS RESULTS IN A FINAL STATE WITH TWO ELECTRONS VACANCIES ON THE L _{2,3} OR 2P LEVEL.....	71
FIGURE 3.6: TYPICAL X-RAY PHOTOELECTRON SURVEY SPECTRUM OF MULTI WALLED CARBON NANOTUBES AS-PRODUCED EXCITED BY AL KA (1486.6 eV). ARE ALSO REPRESENTED THE NARROW SCANS FOR OXYGEN AND CARBON ELEMENT, O1S AND C1S PEAKS RESPECTIVELY.....	74
FIGURE 3.7: PHOTOGRAPH OF THE XPS APPARATUS USED IN THIS WORK.....	75
FIGURE 3.8: SCHEMATIC DIAGRAM OF THE KRATOS HSI AXIS SPECTROMETER.....	76
FIGURE 3.9: STANDARD STUB WITH ADDITIONAL METAL RETAINING CLIP.....	78
FIGURE 3.10: NEW DESIGNED STUB FOR GRANULAR AND POWDERED SAMPLES.....	79
FIGURE 3.11: AFM IMAGE AND DEPTH PROFILE OF A) CD SAMPLE USED FOR PRELIMINARY CHECK-UP AND B) COMPARISON WITH DVD DATA FILM SAMPLE.....	86
FIGURE 3.12: FLUIDISED BED-TYPE REACTOR USED FOR OZONE TREATMENT.....	88
FIGURE 3.13: A) INFLUENCE OF THE FEED GAS FLOW RATE ON THE OZONE CONCENTRATION FOR THE THREE DIFFERENT FEED GAS: OXYGEN, DRY AIR AND AMBIENT AIR. B) INFLUENCE OF THE VOLTAGE/FREQUENCY AND ALSO FLOW RATE ON THE OZONE CONCENTRATION IN THE CASE OF OXYGEN CHOSEN AS FEED GAS.....	89
FIGURE 4.1: AFM IMAGE OF THE UNTREATED GRAPHITE SURFACE AT LOW MAGNIFICATION.....	97
FIGURE 4.2: AFM IMAGES OF THE SURFACE OF: A) THE OZONE OXIDISED GRAPHITE AND B) H ₂ O ₂ TREATED GRAPHITE AT LOW MAGNIFICATION.....	99
FIGURE 4.3: A) AFM 3D TOPOGRAPHY OF THE SURFACE OF THE OZONE OXIDISED GRAPHITE AND B) DEPTH PROFILE PERPENDICULARLY TO THE GRAPHENE SHEET AT HIGH MAGNIFICATION.....	100
FIGURE 4.4: TEM HIGH RESOLUTION PHASE CONTRAST IMAGES OF THE BASE MATERIAL N330 CARBON BLACK AT DIFFERENT MAGNIFICATIONS.....	102
FIGURE 4.5: SEM MICROGRAPHS (AT X50) OF BASE AND SELECTED MODIFIED N330 CARBON BLACK SAMPLES: A) BASE MATERIAL, B) AFTER AMMONIUM PERSULFATE MODIFICATION, C) AFTER NITRIC ACID MODIFICATION AND D) AFTER OZONE TREATMENT.....	104
FIGURE 4.6: SEM MICROGRAPHS AT HIGHER MAGNIFICATION (X1000) OF BASE AND SELECTED MODIFIED N330 CARBON BLACK SAMPLES: A) BASE MATERIAL, B) AFTER AMMONIUM PERSULFATE MODIFICATION, C) AFTER NITRIC ACID MODIFICATION AND D) AFTER OZONE TREATMENT.....	105
FIGURE 4.7: SEM MICROGRAPHS OF BASE N234 CARBON BLACK SAMPLES: A) X100, B) X1K, C) X5K AND D) X10K.....	106

FIGURE 4.8: SEM MICROGRAPHS (AT X50) OF BASE AND SELECTED MODIFIED BPL ACTIVATED CARBON SAMPLES: A) BASE MATERIAL, B) AFTER AMMONIUM PERSULFATE MODIFICATION, C) AFTER NITRIC ACID MODIFICATION, D) AFTER OZONE TREATMENT AND E) AFTER HYDROGEN PEROXIDE TREATMENT.....	108
FIGURE 4.9: SEM MICROGRAPHS AT HIGHER MAGNIFICATION (AT X1000) OF BASE AND SELECTED MODIFIED BPL ACTIVATED CARBON SAMPLES: A) BASE MATERIAL, B) AFTER AMMONIUM PERSULFATE MODIFICATION, C) AFTER NITRIC ACID MODIFICATION, D) AFTER OZONE TREATMENT AND E) AFTER HYDROGEN PEROXIDE TREATMENT.....	110
FIGURE 4.10: WEIGHT LOSS AND TEMPERATURE PROFILE DURING THE TGA EXPERIMENT FOR A) THE BASE N330 CARBON BLACK AND B) THE N330 OXIDISED WITH OZONE.	112
FIGURE 4.11: DTG AND TEMPERATURE PROFILES ON THE BASE AND MODIFIED CARBON BLACK MATERIALS.....	113
FIGURE 4.12: WEIGHT LOSS AND TEMPERATURE PROFILE DURING THE TGA EXPERIMENT FOR A) THE BASE BPL ACTIVATED CARBON AND B) THE BPL TREATED WITH NITRIC ACID.	114
FIGURE 4.13: DTG AND TEMPERATURE PROFILES ON THE BASE AND MODIFIED ACTIVATED CARBON MATERIALS.	115
FIGURE 4.14: EFFECTS OF HEAT-TREATMENT ON XPS MEASURED SURFACE OXYGEN LEVELS FOR BPL CARBON. LINEAR FITTING WITHIN THE TEMPERATURE RANGE OF 400 TO 1100°C IS ALSO INCLUDED.....	116
FIGURE 4.15: SURVEY SCANS OBTAINED FOR ACTIVATED CARBON BPL. A) BASE MATERIAL AND B) CARBON HEAT TREATED AT 1100°C UNDER N_2	118
FIGURE 4.16: O1S NARROW SCAN SPECTRA FOR THE HEAT TREATED ACTIVATED CARBON SERIES. A) BPL BASE, B) BPL 500°C N_2 , C) BPL 900°C N_2 AND D) BPL 1100°C N_2	120
FIGURE 4.17: A) TOLUENE ADSORPTION ISOTHERMS ON THE HEAT TREATED BPL CARBONS AT 303°K AND B) CORRESPONDING DR PLOTS.....	121
FIGURE 5.1: SURVEY SCANS OBTAINED FOR BOTH A) UNTREATED AND B) OZONE OXIDIZED (60MIN) CARBON BLACK.	132
FIGURE 5.2: C1S NARROW SCAN SPECTRA FOR A) UNTREATED AND B) OZONE OXIDIZED (60MIN) CARBON BLACK.....	133
FIGURE 5.3: O1S NARROW SCAN SPECTRA FOR THE OXIDIZED CARBON BLACK SERIES. A) UNTREATED, B) N330 O_3 5MIN, C) N330 O_3 10MIN, D) N330 O_3 30MIN, E) N330 O_3 60MIN AND F) N330 O_3 2H.	135
FIGURE 5.4: OXYGEN LEVEL $[O]_T$ (AT.%) MEASURED BY XPS FOR OZONE-TREATED CARBON BLACK N330 AS A FUNCTION OF OXIDATION TIME.	137
FIGURE 5.5: A) NITROGEN ADSORPTION ISOTHERMS AT 77°K FOR CARBON BLACKS AND B) EXPANDED LOW PRESSURE DOMAINS ($p/p_0 < 0.1$).	138
FIGURE 5.6: NITROGEN ADSORPTION DATA ANALYSIS WITH A) A_5 METHOD AND B) DRK METHOD.	139
FIGURE 5.7: A) $-\Delta H_i$ (DISPLAYED AS $-H_i$ ON THE GRAPHS) VALUES AS A FUNCTION OF SURFACE OXYGEN LEVELS FOR WATER AND TOLUENE AND B) FOR METHANOL, ETHANOL AND ISOPROPANOL.	141
FIGURE 5.8: A), B) AND C) ADSORPTION ISOTHERMS FOR METHANOL, ETHANOL AND ISOPROPANOL INCLUDING IN D), E) AND F) THE EXPANDED LOW PRESSURE DOMAINS ($p/p_0 < 0.6$) SHOWING DISPLACEMENT DUE TO INCREASING SPECIFIC INTERACTIONS IN SUB-MONOLAYER REGION AND ISOTHERM CONVERGENCE NEAR MONOLAYER CAPACITY.	144

FIGURE 5.9: DRK PLOTS FOR THE ADSORPTION OF: A) NITROGEN AT 77°K, B) METHANOL, C) ETHANOL AND D) ISOPROPNOL AT 303°K.....	148
FIGURE 5.10: SCHEMATIC REPRESENTATION OF THE GROWTH MODE OCCURRING DURING THE ADSORPTION OF NON-POLAR MOLECULES AT DIFFERENT COVERAGE REGIMES. THIS MODE IS ALSO KNOWN AS LAYER-BY-LAYER GROWTH OR FRANK - VAN DER MERVE MODE. THE SURFACE ACTIVE SITES ARE REPRESENTED AS RED SPHERES WHEREAS THE NON-POLAR MOLECULES (SUCH AS TOLUENE OR IN LONG-CHAIN ALCOHOLS) ARE REPRESENTED BY THE GREEN SPHERES.....	150
FIGURE 5.11: ALCOHOL ISOTHERMS PLOTTED ON: A) THE BASE N330, B) N330 O ₃ 10MIN (8.1 AT.% OXYGEN) AND C) N330 O ₃ 60MIN (11.2 AT.% OXYGEN) SHOWING EFFECTS OF ADSORBATE CHEMISTRY. ZOOMS ON THE LOW PRESSURE REGION ARE ALSO INCLUDED IN D), E) AND F) RESPECTIVELY.	153
FIGURE 5.12: ALCOHOLS ADSORBED ON GRAPHITIZED CARBON BLACK N234G SHOWING TYPE III/V CHARACTER OF INITIAL REGIONS OF ISOTHERMS. A) FULL ADSORPTION ISOTHERM AND B) ZOOM IN THE VERY LOW PRESSURE REGION.	153
FIGURE 5.13: VALUES OF B_{DRK} (ALCOHOLS) (WITH N_2 AS REFERENCE) AS A FUNCTION OF TOTAL SURFACE OXYGEN $[O]_T$ (AT.%).	155
FIGURE 6.1: $-\Delta H_i$ VALUES AS A FUNCTION OF SURFACE OXYGEN LEVELS FOR WATER, TOLUENE AND METHANOL.....	168
FIGURE 6.2: WATER ADSORPTION ISOTHERMS AT 303°K FOR A) N330 AND N330 OXIDISED CARBON BLACKS AND B) N330, N234 AND N234G (GRAPHITIZED) AND CARBON BLACKS.	170
FIGURE 6.3: SCHEMATIC REPRESENTATION OF THE GROWTH MODE OCCURRING DURING THE ADSORPTION OF WATER AT DIFFERENT COVERAGE REGIMES. THIS MODE IS ALSO KNOWN AS ISLAND GROWTH OR VOLLMER-WEBER (VW) MODE. THE SURFACE ACTIVE SITES ARE REPRESENTED AS RED SPHERES WHEREAS THE WATER (OR POLAR ADSORPTIVE) MOLECULES ARE REPRESENTED BY THE BLUE SPHERES.	171
FIGURE 6.4: FITS OF EXPERIMENTAL DATA POINTS TO DS2 EQUATION REPRESENTED BY SOLID LINES FOR N330 BASE MATERIAL (1.7 AT.% OXYGEN) AND N330 60 MIN. (11.2 AT.% OXYGEN).	172
FIGURE 6.5: A) RELATIONSHIP BETWEEN $[O]_T$, THE CARBON BLACK SURFACE OXYGEN LEVEL IN AT.%, AND THE PRIMARY ADSORPTION SITE PARAMETER, A_0 , OF THE DS2 EQUATION (CORRELATION COEFFICIENT = 0.87) AND B) THE EFFECT OF A_0 ON THE MEASURED LIMITING WATER ADSORPTION PARAMETER A_s	174
FIGURE 6.6: SURVEY SCAN OBTAINED FOR N330 CARBON BLACK OXIDIZED WITH AMMONIUM PERSULFATE.	175
FIGURE 6.7: C1S NARROW SCAN SPECTRA FOR THE CARBON BLACKS SUBJECTED TO LIQUID-PHASE OXIDATION. A) BASE N330, B) N330 HNO ₃ , C) N330 AMM PER AND D) N330 H ₂ O ₂	177
FIGURE 6.8: O1S NARROW SCAN SPECTRA FOR THE CARBON BLACKS SUBJECTED TO LIQUID-PHASE OXIDATION. A) BASE N330, B) N330 HNO ₃ , C) N330 AMM PER AND D) N330 H ₂ O ₂	179
FIGURE 6.9: WATER ADSORPTION ISOTHERMS AT 303°K FOR N330 CARBON BLACKS SUBJECTED TO LIQUID-PHASE OXIDATION. A) WHOLE ISOTHERMS WITH ADSORPTION AND DESORPTION BRANCHES AND B) EXPANDED LOW PRESSURE DOMAINS ($P/P_0 < 0.16$).	181
FIGURE 6.10: WATER ADSORPTION ISOTHERM FITS USING THE EQUATIONS OF DUBININ-SERPINSKY, BARTON AND D'ARCY & WATT FOR THE FOLLOWING MATERIALS: A) N330 BASE, B) N330 AMM PER, C) N330 HNO ₃ AND D) N330 H ₂ O ₂	182

FIGURE 6.11: RELATIONSHIP BETWEEN $[O]_T$, THE CARBON BLACK SURFACE OXYGEN LEVEL (IN AT.%), AND THE PRIMARY ADSORPTION SITE PARAMETER, A_0 , OBTAINED USING THE VARIOUS WATER EQUATIONS (EXCEPT D'ARCY & WATT EQUATIONS).....	183
FIGURE 6.12: RELATIONSHIP BETWEEN THE PRIMARY ADSORPTION SITE PARAMETER, A_0 , AND THE MEASURED LIMITING WATER ADSORPTION PARAMETER, A_s	185
FIGURE 6.13: SURVEY SCAN OBTAINED FOR BPL ACTIVATED CARBON OXIDIZED WITH NITRIC ACID.....	186
FIGURE 6.14: C1S NARROW SCAN SPECTRA FOR THE ACTIVATED CARBONS SUBJECTED TO LIQUID-PHASE OXIDATION. A) BASE BPL, B) BPL HNO ₃ AND C) BPL H ₂ O ₂	188
FIGURE 6.15: O1S NARROW SCAN SPECTRA FOR THE ACTIVATED CARBONS SUBJECTED TO LIQUID-PHASE OXIDATION. A) BASE BPL, B) BPL HNO ₃ AND C) BPL H ₂ O ₂	190
FIGURE 6.16: N1S NARROW SCAN SPECTRA FOR THE ACTIVATED CARBONS TREATED WITH NITRIC ACID (HNO ₃).	191
FIGURE 6.17: WATER ADSORPTION ISOTHERMS AT 303°K FOR BPL ACTIVATED CARBONS SUBJECTED TO LIQUID-PHASE OXIDATION. A) WHOLE ISOTHERMS WITH ADSORPTION AND DESORPTION BRANCHES AND B) EXPANDED LOW PRESSURE DOMAINS ($p/p_0 < 0.16$).	192
FIGURE 6.18: WATER ADSORPTION ISOTHERM FITS USING THE EQUATIONS OF DUBININ-SERPINSKY, BARTON AND D'ARCY & WATT FOR THE FOLLOWING MATERIALS: A) BPL BASE, B) BPL HNO ₃ AND C) BPL H ₂ O ₂	193
FIGURE 6.19: RELATIONSHIP BETWEEN $[O]_T$, THE ACTIVATED CARBON SURFACE OXYGEN LEVEL (IN AT.%), AND THE PRIMARY ADSORPTION SITE PARAMETER, A_0 , OBTAINED USING THE VARIOUS WATER EQUATIONS (EXCEPT D'ARCY & WATT EQUATIONS). SOLID LINE: REGRESSION ANALYSIS OF THE DS2 DATA POINTS.	195
FIGURE 7.1: A) CVD DEPOSITED MWCNTS AND B) EXAMPLE OF HRTEM IMAGE SHOWING MULTI-WALL STRUCTURE OF ONE OF THE MWCNT STUDIED IN THIS WORK.....	204
FIGURE 7.2: EXAMPLES OF CHEMO-SPECIFIC PATHWAYS TO HYDROXYLATED AND ESTERIFIED MWCNT SURFACES.....	206
FIGURE 7.3: POSSIBLE CROSS-LINKING REACTION OF RESIN EPOXIDE RING WITH CARBON FIBRE SURFACE CARBOXYLIC ACID ACCORDING TO FITZER ET AL. [].	208
FIGURE 7.4: SEM MICROGRAPHS OF BASE MWCNT SAMPLES: A) x59, B) x10K, C) x20K AND D) x50K.	210
FIGURE 7.5: HRTEM IMAGES OF THE BASE MWCNT. A) GLOBAL VIEW, B) AND C) HIGHER MAGNIFICATION IMAGES.	211
FIGURE 7.6: HRTEM IMAGES OF THE FENTON SONICATED MWCNT: A) GLOBAL VIEW AND B) HIGHER MAGNIFICATION IMAGE.....	213
FIGURE 7.7: HRTEM IMAGES OF THE HIGHLY GRAPHITIZED BASE MWCNT. A) GLOBAL VIEW, B) HIGHER MAGNIFICATION IMAGE SHOWING THE HIGHLY GRAPHITIC MULTILAYER STRUCTURE AND C) INTERESTING VIEW OF THE TERMINATION OF ONE MWCNT.	214
FIGURE 7.8: HRTEM IMAGES OF THE GRAPHITIZED FENTON MWCNT (A) AND (B) CORRESPONDING TO LOWER AND HIGHER MAGNIFICATION IMAGES RESPECTIVELY.	215
FIGURE 7.9: HRTEM IMAGES OF THE GRAPHITIZED HNO ₃ TREATED MWCNT. A) GLOBAL VIEW OF ONE TUBE AND B) HIGHER MAGNIFICATION IMAGE SHOWING THE CHANGE OF DIRECTION OF THE GRAPHENE LAYERS.	217
FIGURE 7.10: A) C1S AND B) O1S PEAK ENVELOPES FROM UNTREATED MWCNTS.....	219

FIGURE 7.11: A) C1S AND B) O1S PEAK ENVELOPES FROM MWCNTS TREATED USING THE FENTON REACTION.	221
FIGURE 7.12: A) C1S AND B) O1S PEAK ENVELOPES FROM BIRCH REDUCED MWCNTS.	222
FIGURE 7.13: FE2P PEAK ENVELOPES A) FOR THE UNTREATED MWCNTS AND B) FOR THE SONICATED FENTON MWCNTS.	224
FIGURE 7.14: TOLUENE ADSORPTION ISOTHERMS MEASURED AT 303°K FOR AS PRODUCED AND MODIFIED MWCNTS. A) VIEW OF THE FULL ISOTHERMS AND B) EXPANSION OF THE VERY LOW PRESSURE REGIONS.	225
FIGURE 7.15: WATER ADSORPTION ISOTHERMS MEASURED AT 303°K FOR UNTREATED AND OXIDIZED MWCNTS. A) VIEW OF THE FULL ISOTHERMS AND B) EXPANSION OF THE LOW PRESSURE REGIONS WHERE NUCLEATION AT PRIMARY (OXYGEN) SITES TAKES PLACE.	227
FIGURE 7.16: EXPERIMENTAL WATER ADSORPTION DATA FITTED WITH THE FOLLOWING EQUATIONS: A) DUBININ AND SERPINSKY, B) GENERALIZED BARTON AND C) D'ARCY & WATT.	228

List of tables

TABLE 2.1: TYPICAL SURFACE FUNCTIONAL GROUPS PRESENT ON OXIDISED CARBON SURFACE.....	50
TABLE 2.2: OXYGEN SURFACE GROUPS AND THEIR PYROLYTIC ELIMINATION TEMPERATURES.....	52
TABLE 2.3: O1S BINDING ENERGY AND C1S CHEMICAL SHIFTS RELATED TO PRIMARY C1S PEAK AT 284.6eV AND FOR DIFFERENT CHEMICAL GROUPS.....	53
TABLE 5.1: C1S DECOMPOSITION RESULTS FOR BASE AND 60-MIN OZONATED CARBON BLACK.	134
TABLE 5.2: O1S DECOMPOSITION RESULTS FOR BASE AND OXIDISED CARBON BLACKS.	136
TABLE 5.3: PHYSICOCHEMICAL CHARACTERISTICS OF CARBON BLACKS.....	140
TABLE 5.4: SURFACE AREA (S_{BET} AND S_{DRK}), CHARACTERISTIC ENERGY E_{DRK} , C_{BET} CONSTANT VALUES AND ENTHALPY PARAMETERS FROM ALCOHOL DATA.	145
TABLE 6.1: SURFACE COMPOSITION OF N330 CARBON BLACKS SUBJECTED TO LIQUID-PHASE OXIDATION.	176
TABLE 6.2: C1S DECOMPOSITION RESULTS FOR CARBON BLACKS SUBJECTED TO LIQUID-PHASE OXIDATION.	178
TABLE 6.3: O1S DECOMPOSITION RESULTS FOR CARBON BLACKS SUBJECTED TO LIQUID-PHASE OXIDATION.....	179
TABLE 6.4: SURFACE COMPOSITION OF BPL ACTIVATED CARBONS SUBJECTED TO LIQUID-PHASE OXIDATION.....	187
TABLE 6.5: C1S DECOMPOSITION RESULTS FOR ACTIVATED CARBONS SUBJECTED TO LIQUID-PHASE OXIDATION.....	189
TABLE 6.6: O1S DECOMPOSITION RESULTS FOR ACTIVATED CARBONS SUBJECTED TO LIQUID-PHASE OXIDATION.	191
TABLE 7.1: MECHANICAL PROPERTIES OF SWCNT AND MWCNT COMPARED TO CARBON FIBRES AND STAINLESS STEEL [] [] [] [].	203
TABLE 7.2: SURFACE COMPOSITION DATA (IN AT.%) FROM XPS.....	218

Abbreviations and acronyms

<i>AC</i>	<i>Activated Carbon</i>
<i>AFM</i>	<i>Atomic Force microscopy</i>
<i>Amm Per</i>	<i>Ammonium persulfate</i>
<i>BDDT Classification</i>	<i>Brunauer, Deming, Deming, and Teller classification</i>
<i>BET</i>	<i>Method Brunauer, Emmett and Teller method</i>
<i>CAER</i>	<i>Center for Applied Energy Research</i>
<i>CB</i>	<i>Carbon black</i>
<i>CF</i>	<i>Carbon fibre</i>
<i>CNT</i>	<i>Carbon nanotube</i>
<i>CVD</i>	<i>Chemical vapour deposition</i>
<i>DA equation</i>	<i>Dubinin-Astakhov equation</i>
<i>DFT</i>	<i>Density Functional Theory</i>
<i>DR equation</i>	<i>Dubinin-Radushkevich equation</i>
<i>DRK equation</i>	<i>Dubinin-Radushkevich-Kaganer equation</i>
<i>DS equation</i>	<i>Dubinin-Serpinsky equation</i>
<i>DW equation</i>	<i>D'Arcy & Watt equation</i>
<i>FAT</i>	<i>Fixed analyser transmission</i>
<i>FRR</i>	<i>Fixed retarding ratio</i>
<i>FWHM</i>	<i>Full width at half maximum</i>
<i>GC/MS</i>	<i>Gas Chromatograph/Mass Spectrometer</i>
<i>GB equation</i>	<i>Generalised Barton equation</i>
<i>GDW equation</i>	<i>Generalised D'Arcy & Watt equation</i>
<i>HRTEM</i>	<i>High resolution transmission electron microscopy</i>
<i>HTT</i>	<i>Heat treatment temperature</i>
<i>IGA</i>	<i>Intelligent Gravimetric Analyser</i>
<i>IUPAC</i>	<i>International Union of Pure and Applied Chemistry</i>
<i>L-J potential</i>	<i>Lennard-Jones potential</i>

<i>MWCNT</i>	<i>Multi-wall carbon nanotube</i>
<i>PU</i>	<i>Polyurethane</i>
<i>PZC</i>	<i>Point of zero charge</i>
<i>RGU</i>	<i>The Robert Gordon University</i>
<i>SEM</i>	<i>Scanning electron microscopy</i>
<i>STM</i>	<i>Scanning tunnelling microscopy</i>
<i>SWCNT</i>	<i>Single-wall carbon nanotube</i>
<i>TEM</i>	<i>Transmission electron microscopy</i>
<i>TGA</i>	<i>Thermogravimetry Analysis</i>
<i>TPD</i>	<i>Temperature programmed desorption</i>
<i>TVFM</i>	<i>Theory of volume filling of micropores</i>
<i>UKY</i>	<i>University of Kentucky</i>
<i>UV</i>	<i>Ultra-violet</i>
<i>vdW</i>	<i>Van der Waals</i>
<i>XPS</i>	<i>X-ray photoelectron spectroscopy</i>

Symbols

$A = -\Delta G$	<i>Polanyi adsorption potential</i>
a	<i>amount adsorbed at the relative pressure h</i>
a	<i>length of the unit lattice vector (nanotubes)</i>
a_0	<i>surface concentration of primary adsorption centres</i>
a_0	<i>lattice constant (graphite structure)</i>
a_1 and a_2	<i>lattice vectors of the graphene sheet (nanotubes)</i>
a_{c-c}	<i>in-plane interatomic distance between carbon atoms (graphite structure)</i>
$a_{m,L}$	<i>total concentration of all Langmuir sites</i>
a_s	<i>maximum adsorbed amount (water molecules)</i>
$b = k_a/k_d$	<i>ratio of the adsorption and desorption rate constants</i>
$c = k_a/k_d$	
C	<i>dispersion constant of the dipole-dipole interaction</i>
c	<i>circumference of the nanotube (nanotubes)</i>
$c/2$	<i>interplanar distance (graphite structure)</i>
C_{BET}	<i>BET constant</i>
C_h	<i>chiral vector (nanotubes)</i>
C_x	<i>atomic fraction of the element x</i>
d_0	<i>pore width for slit type pores or pore diameter for cylindrical pores</i>
E	<i>characteristic energy of a given solid</i>
E	<i>peak area (calorimetry)</i>
E_0	<i>characteristic adsorption energy of the solid (for the reference vapour)</i>
E_B	<i>binding energy to the atomic orbital where the emitted electron comes from</i>
E_K	<i>kinetic energy of the emitted electron</i>
$h = p/p_s$	<i>relative pressure</i>

h	<i>Planck constant ($6.62 \times 10^{-34} \text{ J s}$)</i>
$h\nu$	<i>energy of the incident photon</i>
$-h_i$	<i>specific enthalpy of wetting</i>
I_i	<i>intensity of the peak associated to the element i</i>
J_0	<i>flux of X-rays per unit area</i>
k	<i>constant in Barton equation</i>
k_a	<i>rate constants for adsorption</i>
k_d	<i>rate constants for desorption</i>
k_L	<i>Langmuir constant</i>
L	<i>accessible slit-shaped micropore width</i>
L_{mean}	<i>nanotube mean length</i>
m	<i>mass of the solid</i>
n	<i>exponent of the DA equation</i>
N	<i>total number of adsorption sites</i>
N_A	<i>Avogadro's number</i>
N_a	<i>amount of adsorbed molecules at relative pressure p/p_0</i>
N_{a0}	<i>limiting amount adsorbed</i>
N_{am}	<i>amount of gas corresponding to the monolayer capacity</i>
$N_{am}(DRK)$	<i>monolayer capacity</i>
N_i	<i>number of atoms of element i per volume</i>
$[O]_T$	<i>total oxygen concentration</i>
P or p	<i>pressure</i>
P	<i>power (calorimetry)</i>
p_0	<i>saturation pressure</i>
p_s	<i>saturated vapour pressure of water</i>
q	<i>integer (nanotubes)</i>
q_1	<i>heat of adsorption for the first layer</i>
q_L	<i>heat of liquefaction of the adsorbate</i>
q^{net}	<i>net heat of adsorption</i>
q^{st}	<i>isosteric heat of adsorption</i>

r	<i>interatomic separation distance</i>
R	<i>ideal gas law constant</i>
R	<i>correlation coefficient</i>
r_0	<i>distance at the minimum of the potential</i>
r_c	<i>rate of condensation</i>
r_e	<i>rate of evaporation</i>
S_{BET}	<i>BET surface area of the solid</i>
S_{DRK}	<i>DRK surface area of the solid</i>
S_{ext}	<i>external surface area of the solid</i>
S_i	<i>sensitivity factor of element i</i>
S_{mic}	<i>surface area of the slit-shaped micropores</i>
T	<i>temperature</i>
t -plot	<i>plotting method developed by Lippens and de Boer</i>
T_i	<i>analyser transmission (for element i)</i>
V_m	<i>molar volume of the liquid adsorbate</i>
W	<i>volume of micropore system accessible to the adsorbate at p</i>
W_0	<i>total volume of micropore system accessible to the adsorbate</i>
α_L	<i>thermal expansion coefficient</i>
α	<i>molar polarisability</i>
α_S plot	<i>plotting method developed by Sing</i>
β and β_{DRK}	<i>affinity coefficient or similarity constant</i>
γ	<i>surface tension</i>
ΔG	<i>Gibbs free energy</i>
$-\Delta H_i$	<i>enthalpy of immersion of a microporous solid</i>
ε	<i>potential well depth</i>

$\varepsilon(r)$	<i>potential energy</i>
θ_{emi}	<i>angle of emission from the surface normal</i>
θ_{chi}	<i>chiral angle (nanotubes)</i>
θ	<i>surface coverage</i>
λ_i	<i>inelastic mean free path of electron extracted from element i</i>
σ_{hs}	<i>hard sphere diameter</i>
σ	<i>footprint area of an adsorbate molecule</i>
$\sigma_i(h\nu)$	<i>photoelectron cross-section (from the relevant inner shell per atom of i by a photon energy $h\nu$ for emission of a photoelectron)</i>
ν	<i>frequency of the radiation</i>
\emptyset	<i>nanotube diameter</i>
Φ_S	<i>extraction work of the electrons of the sample</i>
$\Phi(z)$	<i>total potential energy</i>
Ω	<i>parachor</i>

1

Chapter 1 Introduction

The properties and applications of activated carbons strongly depend on their porosity but the chemical nature of the surface plays an important role as well. This is also true for other type of carbon materials such as carbon black which are usually non-porous, carbon nanotubes or carbon fibres. Both hydrophobic graphene sheets and hydrophilic surface functional groups are contained in these materials. Non-specific interactions between a molecule/atom in the fluid phase and the atoms composing the solid result from the London forces and are highly dependent upon the physical structure of the carbon i.e. specific surface area/porosity. Thus, the graphene layers will be responsible for the adsorption of non-polar species. As for the specific interactions, they occur at the individual chemical groups, usually oxygen (but some others can contain phosphorus, sulphur, etc...) by polar interactions. These groups will act preferentially as primary adsorption centres for polar interactions (with water or methanol for example). Both of these adsorption mechanisms will be discussed more in details within this thesis. In the course of this work, the effects of surface chemical modification on various carbon materials have been studied with specific reference to their interactions with vapour molecules. Where possible, the initial structure of the carbon material has been considered as well as any changes caused by the chemical treatments.

Typically, in a porous solid, the physical structure including the porous network strongly depends on the choice of material precursor used then it can be controlled and

modified using different carbonisation and activation conditions (atmosphere, temperature, duration of treatment, etc...). On the other hand, the surface chemistry can be modified via post-processing chemical treatment. Chemical functional groups are intrinsically present on the carbon surface depending of the different chemical composition of the precursor chosen for the production. To suit a practical application, more of these groups can be introduced or existing groups removed, using one or combination of the following methods: acidic treatment, ammonia treatment (to introduce nitrogen-containing functional groups), heat treatment in oxidant/inert/reducing atmosphere, microwave treatment, ozone treatment, plasma modification, etc... The oxygen surface groups, which are bound to the carbon structure, are responsible for wettability [1], adsorption behaviour [2][3] and as well catalytic [4][5] and electrical properties [6]. So modification of surface chemistry of these carbon materials is becoming a very attractive cost effective and viable pathway in order to design suitable materials for novel applications. Examples of these applications are: structural and chemical modification of activated carbon for its application in electrochemical capacitors [7], preparation of carbon black for new printing ink formulation, removal of metal cations from aqueous solution using oxidised activated carbon clothes [8] or multiwall carbon nanotubes [9] and bonding and stress transfer in carbon composites [10], etc...

Nowadays, researchers are not only focused on how to modify the surface chemistry but also on the characterisation. They also try to get a better understanding of the chemical groups present of the carbon surface in order to optimize existing applications and broaden to other practical applications. A variety of experimental techniques to assess and determine the type and concentration of surface functional groups exist. Common examples are: the Boehm Titration method, Temperature Programmed Desorption (TPD), (Fourier Transform) Infra-Red Spectroscopy (FTIR) and X-ray Photoelectron Spectroscopy (XPS) which was the main technique used in this work to characterise our carbon materials.

In the first part of this work, the effects of liquid-phase oxidation on the structure of several carbon materials: graphite, carbon black and activated carbon were investigated and compared using microscopy techniques SEM and AFM. Thermal treatment on the surface chemistry using XPS and thermal gravimetric analysis (TGA) was also studied. Following this initial investigation, the prime aim of this work was to study the effects of oxygen-containing functional groups present on the carbon black surface on the adsorption characteristics of polar and non-polar vapours. The carbon black was oxidised using ozone in order to minimize the alteration/damage of the carbon structure resulting from the treatment. Additionally, the reactivity of the surface oxygen groups was also probed using water adsorption for activated carbons and carbon blacks oxidised with various acids. Finally, the last part of this work was carried out on functionalised multiwall carbon nanotubes (MWCNTs). The different nanotubes materials were characterised using microscopy techniques (mainly Transmission Electron Microscopy (TEM)) and XPS whereas the reactivity of the active groups was probed with water adsorption.

Structure of the thesis

The first part of this thesis consists in the theoretical background relative to this work. The conceptual notions to gas/solid interactions and to the different types of porosity will be presented. This part also includes a description of the porous and non-porous carbon materials used in this work and the different theories describing the adsorption of vapours/gases on these solids will also be discussed including the special case of water. Finally, an overview of the oxidation of carbon surfaces will also be presented at the end of this chapter.

The second part of the thesis provides details of the different procedures used to modify the surface chemistry of the carbon materials as well as a brief description of the experimental techniques adopted for their characterisation.

The third part which presents the results and discussions is composed of four sections. The initial observations of the effect of oxidation and heat treatment on the different carbon materials are presented in the first section. The second section covers the adsorption of increasing chain-length alcohols on carbon black surfaces modified using ozone oxidation. The third section deals with adsorption of water on ozonated carbon black and on carbon black and activated carbon modified by liquid-phase oxidations. Finally the fourth section is focused on the characterisation of functionalised multiwall carbon nanotubes and the influence of the surface chemistry on water adsorption for this material.

The thesis ends with a summary and the possible outlook perspectives for further research.

References

- ¹ F. Rodriguez-Reinoso, M. Molina-Sabio and M. T. Gonzalez. Effect of oxygen surface groups on the immersion enthalpy of activated carbons in liquids of different polarity. *Langmuir* **13** (1997) 2354-2358.
- ² F. Rodriguez-Reinoso, M. Molina-Sabio and M. A. Munecas. Effect of Microporosity and Oxygen Surface Groups of Activated Carbon in the Adsorption of Molecules of Different Polarity. *J. Phys. Chem.* **96** (1992) 2707-2713.
- ³ A. M. Siasli, M. Jorge, F. Stoeckli and N. A. Seaton. Modelling of water adsorption by activated carbons: effects of microporous structure and oxygen content. *Carbon* **42** (2004) 1947-1952.
- ⁴ S. Dong Jin, P. Tae-Jin and I. Son-Ki. Effect of surface oxygen groups of carbon supports on the characteristics of Pd/C catalysts. *Carbon* **31** (1993) 427-435.
- ⁵ C. Prado-Burguete, A. Linares-Solano, F. Rodriguez-Reinoso and C. S.-M. de Lecea. The effect of oxygen surface groups of the support on platinum dispersion in Pt/carbon catalysts. *Journal of Catalysis* **115** (1989) 98-106.
- ⁶ B. R. Puri. *Chemistry and physics of carbon* (P. J. Walker, Jr., Marcel Dekker, New York, 1970).
- ⁷ G. Lota, T. Centeno, E. Frackowiak and F. Stoeckli. Improvement of the structural and chemical properties of a commercial activated carbon for its application in electrochemical capacitors. *Electrochimica Acta* **53** (2008) 2210-2216.
- ⁸ C. Moreno-Castilla, M. Alvarez-Merino, L. Pastrana-Martínez and M. López-Ramón. Adsorption mechanisms of metal cations from water on an oxidized carbon surface. *Journal of Colloid and Interface Science* **345** (2010) 461-466.
- ⁹ J. Hu, C. L. Chen, X. X. Zhu and X. K. Wang. Removal of chromium from aqueous solution by using oxidized multiwalled carbon nanotubes. *J. Hazard. Mater.* **162** (2009) 1542-1550.
- ¹⁰ R. Andrews and M. C. Weisenberger. Carbon nanotube polymer composites. *Current Opinion in Solid State and Materials Science* **8** (2004) 31-37.

2

Chapter 2 Theory and Literature review

2.1 Gas/solid interactions

2.1.1 Adsorption forces

The adsorption of a gas by a solid is the result of attraction between adsorptive molecules (individual molecules of the gas) and the atoms or ions composing the solid surface (adsorbent). Once adsorbed in an extremely thin surface layer of the solid, the gas molecules are denoted “*adsorbate*”. For indication, the IUPAC (International Union of Pure and Applied Chemistry) definition [1] of adsorption is the following: “*an increase in the concentration of a dissolved substance at the interface of a condensed and a liquid phase due to the operation of surface forces. Adsorption can also occur at the interface of a condensed and a gaseous phase*”.

These forces include dispersion forces which are attractive and short range repulsive forces. Also electrostatic (Coulombic) forces arise if the solid and/or the gas are polar. Dispersion forces, also called London forces, were first characterised by London in 1930 [2][3]. The rapid fluctuation in electron density within each atom induces an electrical dipole moment in neighbouring atoms, leading to an attraction between the atoms. If one considers now the case of two atoms, by using the perturbation theory from quantum mechanics, one obtains [4]:

$$\varepsilon_D(r) = -C \cdot r^{-6} \quad \text{Eq. 2.1}$$

where r is the interatomic separation distance and C the dispersion constant of the dipole-dipole interaction.

In this equation, dipole-quadrupole and quadrupole-quadrupole interactions have been neglected due to the relatively small contributions. On the other hand, the repulsion forces (resulting of overlapping electron orbitals) can be expressed as [4]:

$$\varepsilon_R(r) = B \cdot r^{-12} \quad \text{Eq. 2.2}$$

where B is an empirical constant.

By summation of the pairwise attractive and repulsive interaction, one obtains the total potential energy between the two atoms as represented in Figure 2.1:

$$\varepsilon(r) = -C \cdot r^{-6} + B \cdot r^{-12} \quad \text{Eq. 2.3}$$

This relation is also referred to as the Lennard-Jones (L-J) potential [5][6] or the 6-12 potential who first proposed it in 1931. The other form of the L-J potential is:

$$\varepsilon(r) = 4\varepsilon \cdot \left[\left(\frac{\sigma_{hs}}{r} \right)^{12} - \left(\frac{\sigma_{hs}}{r} \right)^6 \right] \quad \text{Eq. 2.4}$$

where ε is the well depth and σ_{hs} is the hard sphere diameter.

The relation is often written as:

$$\varepsilon(r) = \varepsilon \cdot \left[\left(\frac{r_0}{r} \right)^{12} - 2 \left(\frac{r_0}{r} \right)^6 \right] \quad \text{Eq. 2.5}$$

where $r_0 = 2^{1/6} \cdot \sigma_{hs}$ is the distance at the minimum of the potential.

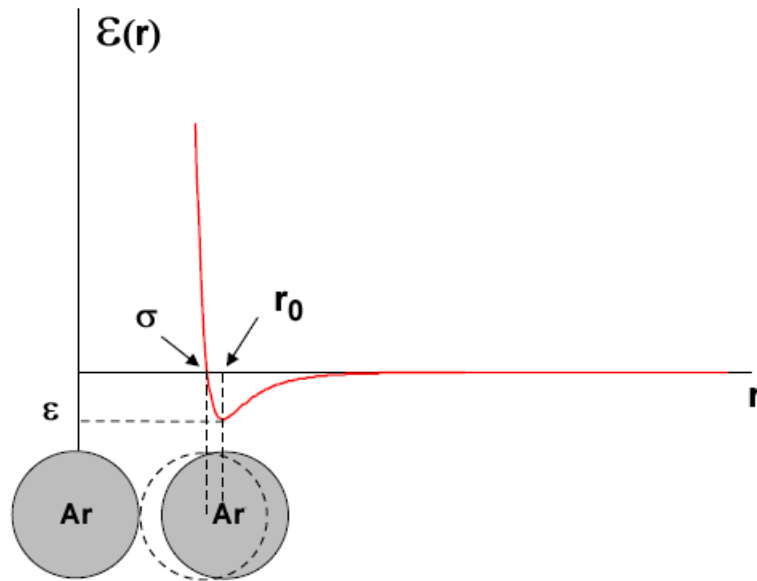


Figure 2.1: Potential energy diagram of two atoms of argon.

In the case of the adsorption of a gas on a solid, the total energy will be the summation of the individual interactions of each atom within the gas phase with each atom of the adsorbent:

$$\Phi(z) = \sum_{i,j} \varepsilon_{ij}(r_{ij}) \quad \text{Eq. 2.6}$$

2.1.2 Adsorption isotherms

When a solid is exposed to a gas or vapour then the concentration of the gas/vapour at the solid surface and into its pores if it has porosity, becomes greater than in the gas/vapour phase [7]. This phenomenon which brings this enrichment of material is called “adsorption” as defined earlier. It must not be mistaken with “absorption” in which molecules enter the bulk phase of solid material and are taken up by the volume not by the surface.

In a closed system, adsorption of gas onto the solid can be measured by monitoring the fall in pressure of the adsorptive within a known volume (volumetric system) or the mass gain of the solid due to adsorbing gas molecules in the case of a gravimetric system. In the latter system, a spring balance is commonly used.

The amount of gas Na taken up by a given material is a function of the mass m of the solid, the temperature T , the pressure p of the gas and the physical and chemical characteristics of both solid and gas/vapour.

$$Na = f(T, p, \text{solid}, \text{gas/vapour}) \quad \text{Eq. 2.7}$$

For a given system at a constant temperature, the adsorption isotherm can be expressed in the convenient form:

$$Na = f\left(\frac{p}{p_0}\bigg|_T, \text{solid}, \text{gas/vapour}\right) \quad \text{Eq. 2.8}$$

where p_0 is the saturation pressure of the gas/vapour at the temperature T .

Many different types of isotherms have been reported in the literature [8][9]. These isotherms can have various shapes depending on the type and nature of the adsorbent and adsorbate and particularly the intermolecular interaction between the gas/vapour and the surface.

The first classification to interpret adsorption isotherms was originally proposed by Brunauer, Deming, Deming and Teller (BDDT)ⁱ [10] in 1940 and comported five types. The BDDT classification has become the core of the modern IUPAC classification [11] with an additional one (type VI) introduced much later by Sing [7]. These six isotherm classes are presented in Figure 2.2.

ⁱ Also sometimes referred to as the Brunauer classification.

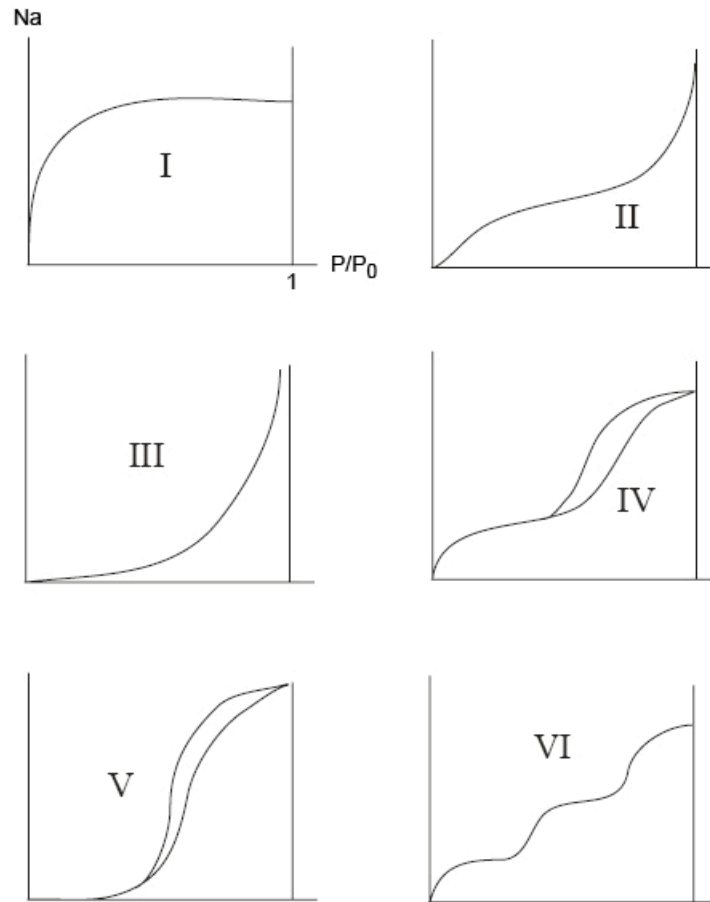


Figure 2.2: Classification of the five types of adsorption isotherm (BDDT), together with type VI, the stepped isotherm.

Type I isotherms are typically observed by adsorption on microporous solids. Micropore filling occurs at low relative pressure ($< 0.1 p/p_0$). This isotherm is characteristic of the adsorption on activated carbons and zeolites.

Type II isotherms result from the physical adsorption of gases by nonporous solids as carbon blacks. This isotherm describes multilayer adsorption on an open surface. But it can be also a combination of a type I (micropores) with a pure type II (open surface).

Type III and type V isotherms reveal weak gas-solid interactions [12] whereas the adsorbate-adsorbate interactions are relatively strong. It is the case of water adsorption on hydrophobic surfaces (for example graphite or activated carbon with low oxygen content). In addition, type V possesses a hysteresis loop characteristics of the presence of mesopores where capillary condensation occurs.

Type IV isotherms are from the adsorption on mesoporous solids. They have also a hysteresis loop.

Finally, type VI isotherm is an isotherm with steps reflecting the formation of successive monolayer on very homogeneous and non porous surface. This case is relatively rare but it is interesting theoretically. The adsorption of krypton on graphitised carbon black at 90°K is an example of type VI isotherm [13].

New classification of adsorption isotherm [14], taking into account adsorption for subcritical and supercritical conditions (temperature above critical temperature) is arising. Murata and Kaneko [15] have proposed a new equation to describe the phenomena of supercritical gas adsorption which correlated well with both experimental data and DFT (Density Functional Theory) results.

2.1.3 Notions of porosity

The origin of the word pore is from the Greek word '*poros*' which means passage. So the role of a pore is to act as a passage between the external and the internal surfaces of a solid and allowing gas or vapour molecules to enter, go through or out of the solid. For catalysis or purification/separation applications, most of the adsorbents possess porosity which in the same time enhances their internal surface area. The number of pores, their size and shape can vary greatly for different adsorbents and even within the same solid. This will determine, for example, the adsorption capacity and also the dynamic

adsorption rate of an activated carbon. According to IUPAC [16], three groups of pores are distinguished:

Macropores: $d_0 > 50nm$

Mesopores: $2nm \leq d_0 \leq 50nm$

Micropores: $d_0 < 2nm$

where d_0 is the pore width for slit type pores or pore diameter for cylindrical pores. But in the literature, these porosity classes may often overlap in terms of size and definitions.

The different kinds of pores inside an activated carbon granule are represented in the Figure 2.3. Moreover “closed” pores (isolated void within the solid) and “blinded” pores (pores which do not lead to any other pore or surface) may also be present inside the solid.

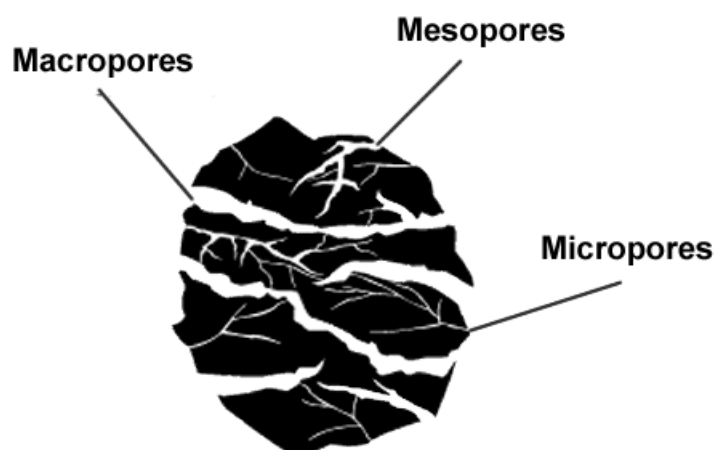


Figure 2.3: Schematic drawing of the different types of pores in an activated carbon particle.

A series of interconnecting tubes or slits is a common misconception to describe the porosity in carbon. A more realistic view would be that the carbon atoms are regrouped together in imperfect aromatic sheets and form a three dimensional covalently bonded network. The spaces or interstices between these sheets or lamellae represent the porosity

of carbon and is resulting from the carbonisation and activation process during the fabrication of the material.

The basis for pore classification is that each size range corresponds to different adsorption effects (or mechanism), as observed in adsorption isotherm.

2.1.3.1 Macroporosity

Macropores act as transport highway to the interior of the carbon particle and only have interest for kinetic considerations. Major cracks, fissures and other structural defects will lead to the formation of this kind of porosity which is considered as an external surface. Their contribution to the surface area of the solid is relatively low ($< 5 \text{ m}^2/\text{g}$). Adsorption process follows the layer by layer mechanism typical of non-porous solids. The adsorptive molecules travel through the macropores and mesopores, from where they finally enter the micropores.

2.1.3.2 Mesoporosity

Mesopores are also providing a transport system for the molecules to allow them to enter the microporosity. This is the place where capillary condensation occurs, resulting in a hysteresis loop in the adsorption isotherm (at high relative pressure) characteristic of the differences between the pore filling and emptying processes. The mesopores filling occurs at the final stage of the isotherm via multilayer formation to the point where the cylindrical meniscus reaches its critical radius. It is also assumed that at this stage all the micropores are completely filled up.

2.1.3.3 Microporosity

Micropores generally contribute to the major part of internal surface area and also to pore volume of the activated carbon. These pores, filled at very low relative pressure, are representative of type I isotherms. They are considered to be of similar size of the adsorbate molecules. Most of the adsorption takes place within these micropores, where the interaction energy is much greater than in larger pores due to the closeness of pore

walls, resulting in a relatively deep and sharp potential well and enhanced adsorption for very low relative pressure. This is part of the theory developed by Dubinin and will be explained more comprehensively in the paragraph 2.2.3.

The filling process inside the micropores can be divided into two steps:

- i. monolayer formation
- ii. micropore filling by cooperative effects [¹⁷].

The adsorption process within the micropores is completely reversible due to their narrow widths which inhibit the phenomenon of capillary condensation.

2.2 Adsorption by porous and non-porous solids

To all the isotherms seen previously correspond different mathematical models but usually these models ignore some structural features of the adsorbent and the influence of adsorbate-adsorbent interactions. This section reviews the most common models. Most have been used in this work.

2.2.1 Langmuir equation

Langmuir [¹⁸][¹⁹] was first to produce a relationship between the amount of gas adsorbed and equilibrium pressure. According to Langmuir, adsorption equilibrium is governed by a dynamic process between the molecules arriving on the surface and those leaving the surface. One can write separately the rate of condensation r_c (Eq. 2.9) and the rate of evaporation r_e (Eq. 2.10).

$$r_c = k_a \cdot p \cdot (1 - \theta) \qquad \text{Eq. 2.9}$$

$$r_e = k_d \cdot \theta \quad \text{Eq. 2.10}$$

where $\theta = Na/N$ is the fraction of surface covered, with N , total number of adsorption sites, Na , amount of adsorbed molecules. k_a and k_d represent the rate constants for adsorption and desorption respectively.

Langmuir assumes the surface of the adsorbent is homogeneous, there is no adsorbate-adsorbate interaction and only monolayer adsorption can occur. At equilibrium, the two rates are equal, i.e. $r_c = r_e$, one obtains the Langmuir equation:

$$\theta = \frac{b \cdot p}{1 + b \cdot p} \quad \text{Eq. 2.11}$$

where p is the pressure of the gas (mbar for example) and $b = k_a/k_d = b_0 \cdot e^{Q/(R \cdot T)}$ with b_0 a parameter being reciprocal of pressure (mbar^{-1}) and Q representing the energy of adsorption.

2.2.2 The Brunauer, Emmett and Teller (BET) model

To generalise the Langmuir theory to multilayer adsorption, Brunauer, Emmett and Teller [20] developed a model, known as the BET model. The physical adsorption on non-porous solid leads generally to a type II isotherm, starting with the creation of a statistical monolayer on the solid surface. The basic assumptions are that in all the layers, except the first one, the heat of adsorption q is equal to q_L the heat of condensation (or liquefaction) of the liquid adsorbate. Also a molecule can condense or evaporate only on or from exposed surfaces. The BET equation in a convenient form is expressed as:

$$\frac{p/p_0}{Na \cdot (1 - p/p_0)} = \frac{1}{Nam \cdot C} + \frac{C - 1}{Nam \cdot C} \cdot p/p_0 \quad \text{Eq. 2.12}$$

where p_0 is the saturation vapour pressure, N_a is the amount of gas adsorbed at the relative pressure p/p_0 , N_{am} is the amount of gas corresponding to the monolayer capacity and C_{BET} is the BET constant given in practice by:

$$C_{BET} = \exp\left(\frac{q_1 - q_L}{R \cdot T}\right) \quad \text{Eq. 2.13}$$

where q_1 is the heat of adsorption for the first layer, q_L is the heat of liquefaction of the adsorbate and R the ideal gas law constant.

So $q_1 - q_L$ is the net heat of adsorption [7].

Mathematically, the BET equation is linearisable over the range $0.05 < p/p_0 < 0.35$ by plotting the left member $\frac{p/p_0}{(1-p/p_0)}$ versus p/p_0 . So, the monolayer capacity N_{am} and the C_{BET} constant can be determined from this graphical representation. Then, the surface area of the adsorbent can be calculated using the simple relation:

$$S_{BET} = N_{am} \cdot \sigma \cdot N_A \quad \text{Eq. 2.14}$$

where S_{BET} is the surface area of the solid (in m^2/g), N_{am} is the monolayer capacity (in mol/g), σ is the footprint area of an adsorbate molecule (in $\text{m}^2/\text{molecule}$) and N_A is the Avogadro's number (molecules/mol).

A criticism of BET model is the assumption that all the adsorption sites on the solid surface are energetically identical. That's why this equation is not linear at the very low pressure. In reality, most of surfaces are energetically heterogeneous. Another disadvantage is that the model neglects adsorbate-adsorbate interactions. And this type of interactions becomes more and more preponderant when the layer is approaching completion. Moreover, the capillary condensation phenomenon is also a source of deviations in the graph. These can explain the non-linearity of the BET representation for high relative pressure ($> 0.5 p/p_0$) [7].

The applicability of this model may be questioned for microporous solid as it fails to describe adequately the adsorption and filling in the micropores [21]. It could result in an unrealistic large monolayer capacity, hence high surface area, resulting from the enhanced adsorption inside the micropores (capillarity condensation) before the final completion of the monolayer.

2.2.3 Theory of Dubinin

The Theory of Volume Filling of Micropores (TVFM) developed by Dubinin in late 1940s and reviewed several times since then [22][21][23] is one of the most widely used to describe physical adsorption of gas and vapours on microporous solids. This theory and all equations which originate from it find their fundamental basis in Polanyi's potential theory of adsorption [24][25]. Polanyi defines the thermodynamic potential A as the differential molar work needed to transfer one mole of the gas phase to a given place on the surface. The potential A is expressed as:

$$A = R \cdot T \cdot \ln(P^0/p) = -\Delta G \quad \text{Eq. 2.15}$$

where $-\Delta G$ is the Gibbs free energy and R is the ideal gas law constant.

For a planar and homogeneous surface, all the points being at the same distance of this surface draw an equipotential surface and this potential decreases with the distance and at the end becomes null. The space between each set of equipotential surfaces and the solid surface corresponds to a definite volume W in which adsorption occurs. The main proposition of the Polanyi theory is that the adsorption potential A at constant volume filling W is temperature independent:

$$\left(\frac{\partial A}{\partial T}\right)_W = 0 \quad \text{Eq. 2.16}$$

This proposition has been confirmed by voluminous experimental data. Dubinin conceived adsorption as a volume filling of the micropores (adsorption space) rather than the typical physical image, successive adsorbed layers onto the pore walls.

Dubinin postulated that the volume of vapour adsorbed W by activated carbon at the relative pressure P/p_0 is a function of the thermodynamic potential A .

2.2.3.1 Dubinin-Radushkevich (DR) equation

The Dubinin-Radushkevich (DR) equation was devised to describe the adsorption of various vapours onto many microporous carbons. After the analysis of experimental data on the adsorption of different vapours onto active carbons with different pore structure [26][27], Dubinin and Radushkevich [28][29] arrived to the following relationship:

$$W = W_0 \cdot \exp \left[- \left(\frac{A}{\beta \cdot E_0} \right)^2 \right] \quad \text{Eq. 2.17}$$

where W_0 is the total volume of micropore system accessible to the adsorbate, E_0 is the characteristic adsorption energy of the solid (for the reference vapour) and the parameter β is the affinity coefficient or similarity constant and is equal to the ratio of adsorption potentials of the adsorptive to a reference vapour.

By convention, benzene is usually used as reference compound and is by definition given the value $\beta_{benz} = 1$. This coefficient is specific to the nature of the adsorptive and will be discussed more in details later. They assumed that the pore size distribution is a Gaussian function so the value of the exponent n was chosen equal to 2.

The characteristic energy of a given solid/adsorptive system is related to the parameters E_0 and β by the following relation:

$$E = \beta \cdot E_0 \quad \text{Eq. 2.18}$$

2.2.3.2 Dubinin-Astakhov (DA) equation

At a later stage, Dubinin and Astakhov [30] proposed the following expression known as the Dubinin-Astakhov (DA) equation:

$$W = W_0 \cdot \exp \left[- \left(\frac{A}{\beta \cdot E_0} \right)^n \right] \quad \text{Eq. 2.19}$$

where n reflects the heterogeneity of the solid and is usually smaller than 4~6. n increases with the homogeneity of the solid.

Obviously, the DR and DA equation are identical if $n = 2$.

2.2.3.3 Determination of L and S_{mic}

These equations can be written in term of amount adsorbed (not in volume) with the following expression:

$$Na = Na_0 \cdot \exp \left[- \left(\frac{A}{\beta \cdot E_0} \right)^2 \right] \quad \text{Eq. 2.20}$$

or

$$Na = Na_0 \cdot \exp \left[- \left(\frac{A}{\beta \cdot E_0} \right)^n \right] \quad \text{Eq. 2.21}$$

where Na is the amount adsorbed at the relative pressure p/p_0 and Na_0 is the limiting amount adsorbed.

One has the relation:

$$W_0 = Na_0 \cdot V_m \quad \text{Eq. 2.22}$$

where W_0 is in cm^3/g , Na_0 in mol/g and V_m , the molar volume of the liquid adsorbate in cm^3/mol .

The molar volume in the adsorbed phase can be different from the one of the liquid. But in first approximation, it is convenient to say that the adsorbate state is not different from the liquid state [31]. So, as a working hypothesis, the molar volume of liquid adsorbate is usually used.

For activated carbons, Stoeckli et al. [32] showed that the characteristic energy E_0 can be linked to the accessible slit-shaped micropore width L by the following empirical expression:

$$L \text{ (nm)} = \frac{10.8 \text{ (nm.kJ.mol}^{-1}\text{)}}{E_0 \text{ (kJ.mol}^{-1}\text{)} - 11.4 \text{ (kJ.mol}^{-1}\text{)}} \quad \text{Eq. 2.23}$$

This relationship found her roots in the work of Dubinin et al. [33] who used small-angle X-ray scattering to investigate different active carbons, and later on a systematic study based on adsorption and immersion calorimetry techniques with molecules of various size [34][35].

Then the surface area of the slit-shaped micropores can be estimated by the following geometrical relation:

$$S_{mic} = \frac{2 \cdot 10^3 \cdot W_0}{L} \quad \text{Eq. 2.24}$$

where L is in nm, W_0 in cm^3/g and S_{mic} in m^2/g .

2.2.3.4 Determination of n

The parameter n of the DA equation reflects the heterogeneity of the adsorbent and can be used as a measure of the sharpness of the micropore size distribution. This parameter usually lies in the range 1~3 for carbonaceous materials. From the literature, adsorbents with a relatively narrow micropore size distribution associated with small size possess an n value approaching three. On the contrary, if the solid has a wide pore size distribution, the n value will be smaller and tend to ~ 1 as the heterogeneity increases. A good

example of this was the study made by Burevski [36] on the micropore structure and the energetic heterogeneities of two active carbons.

In the case of a new type of adsorbent, the optimum n value should be determined. A simple mathematical transformation of the DA equation leads to:

$$\ln \left[\ln \left(\frac{W_0}{W} \right) \right] = n \cdot \ln(A) - n \cdot \ln(\beta \cdot E_0) \quad \text{Eq. 2.25}$$

with $W_0 = Na_0 \cdot V_m$ and Na_0 is the limiting amount adsorbed (“plateau” in the case of type I isotherm).

A representation of the left member $\ln \left[\ln \left(\frac{W_0}{W} \right) \right]$ versus $\ln(A)$ gives n and then E_0 .

2.2.3.5 The affinity coefficient β

For different vapours, the attractive forces between the molecules and the surface of the adsorbent are not the same. It leads to the idea that plots of adsorption capacity versus adsorption potential ε for different vapours produce different curves [37]. They can superimpose or coalesce into one “correlation curve” by applying an appropriate coefficient. These coefficients are scaling factors called “affinity coefficients” or “similarity coefficients” and designated by the letter β . By convention, benzene is taken as reference compound and $\beta_{benz} = 1$ is assumed.

In a case of non-polar adsorbent, β is only related to the properties of the adsorptive. But in the opposite case, the polarity of the adsorbent can have a major influence on the β values. As an example, later discussed in the Chapter 5 of this work, the functional oxygen groups present on the carbon black surface have been shown to have a significant influence on $\beta_{alcohol}$ values.

It has been suggested that affinity coefficients can be calculated from molecular and physical properties of the adsorptive (or adsorbate). The relations the most commonly used to approximate β are the ratios of:

✓ Molar polarisabilities α [38]:

$$\beta = \frac{\alpha}{\alpha_{REF}} \quad \text{Eq. 2.26}$$

✓ Molar volumes V_m of the adsorbate in the liquid-state [39]:

$$\beta = \frac{V_m}{V_{m,REF}} \quad \text{Eq. 2.27}$$

✓ Parachors Ω [40]:

$$\beta = \frac{\Omega}{\Omega_{REF}} = \frac{V_m \cdot \gamma^{1/4}}{V_{m,REF} \cdot \gamma_{REF}^{1/4}} \quad \text{Eq. 2.28}$$

where γ is the surface tension.

The parachor concept started on completely empirical grounds with Macleod [41] who proposed in 1923 a remarkably simple equation to estimate the surface tension of a liquid as everyone expected to see the surface tension of a liquid changing inversely of its density with temperature. As stated now (Sugden's form [42]), the parachor is considered to be an additive quantity and has been used to solve several structural problems [43]. Balasubrahmanyam published an excellent historical review [44] on the parachor concept and its relation to Einstein and the molecular volume.

These three relations have been compared in several previous works and recently by Wood [45] who concluded that these three different ways give good predictability but that the use of power functions with exponents less than unity provided slightly better fits of predictions to experimental values.

The topic of affinity coefficients including prediction models and criteria for selecting reference compound is not trivial and is still nowadays under discussion. Reucroft et al. [46] obtained better agreement when the reference compound used was of

similar polarity of vapours under considerations, also did Noll et al. [47], while Golovoy and Braslaw [48] and Wood [49] found a single reference compound would be sufficient.

Recently, Wu et al. [50] developed a model based on only three parameters: volume, molecular weight (related to the size of the adsorbate) and energy of interactions (between the compound and a graphite model surface). These parameters are calculated from the physicochemical structure of the adsorbate. The interaction energy parameter describes directly specific interactions (including hydrogen bonding) between the adsorbate molecules and the surface of the adsorbent. It was found that this model predicted better than the usual method based on parachor, molar polarisability or molar volume. But it is more difficult to make use of it due to many calculations.

2.2.3.6 Dubinin-Radushkevich-Kaganer (DRK) equation

In the case of the adsorption of vapours on non-porous surfaces such as carbon black [51] and manganese dioxide (α -MnO₂), Dubinin's theory can be extended and Kaganer [52] suggested a variant to the DR equation. The so-called Dubinin-Radushkevich-Kaganer (DRK) equation takes the form:

$$Na = Nam(DRK) \cdot \exp \left[- \left(\frac{A}{\beta \cdot E_0} \right)^2 \right] \quad \text{Eq. 2.29}$$

where $Nam(DRK)$ represents the monolayer capacity.

The adsorption data are usually examined for relative pressure $p/p_0 < 0.1$. Obviously, the DRK equation does not take into account multilayer adsorption as the BET model does. For most of the systems, the plot of $\ln(Na)$ versus A^2 reveals a linear section before multilayer adsorption takes place. This will lead to an extrapolated value of the monolayer capacity $Nam(DRK)$. An important information about the DRK equation is the influence of the surface chemistry on the first layer adsorbed $p/p_0 < 0.1$ which is less the case with the BET equation. This is an advantage for the study of the

adsorption of polar adsorbate molecules on polar surface before multilayer adsorption set in.

2.3 Case of water adsorption

The adsorption mechanism of water, which is a small polar particle, on carbon surfaces is very different from the one of other adsorptive such as nitrogen, carbon dioxide, toluene or other organic vapours. From a qualitative point of view, water adsorption differs because of two main reasons:

- ✓ Interaction between water molecules is much stronger than interaction between water and carbon atoms on the surface designed as weak gas-solid interactions. The dispersion interaction of water with pure carbon surface is equal to ~ -35 kJ/mol. This phenomenon is reversed in the case of organic molecules.
- ✓ Adsorption process is dominated by polar interactions on the surface i.e. mostly controlled by formation of hydrogen bonding between water molecules and hydrophilic centres, called also surface primary sites.

It is well known that a clean carbon surface is essentially hydrophobic due to weak dispersion energy. Type III and V isotherms are characteristic of water adsorption on this kind of surface, with type V being given by mesoporous solid where capillary condensation occurs. The weakness of adsorbent-adsorbate interactions will induce the water uptake at low relative pressure ($< 0.3 \sim 0.4 \frac{p}{p_s}$) to be very small. While at the same relative pressure, the organic vapour has already completely filled up the micropores. At a relative pressure of $0.4 \sim 0.6 \frac{p}{p_s}$, a fast increase of the amount adsorbed is observed. This can be explained by the fact that once a molecule has become adsorbed on a primary site, this molecule will act as a secondary centre. Then, because the adsorbate-adsorbate forces are strong, the adsorption of further molecules will be

promoted – a cooperative chain reaction process – and will cause the formation of water molecule aggregates (or cluster) connecting to each other and the micropores will be filled up [⁵³].

Therefore, the properties and characteristics of the surface of carbon materials may be modified with the introduction or elimination of oxygen functional groups [⁵⁴]. These groups essentially of type carboxyl, hydroxyl, quinone and lactone will condition (influence) the amount of water adsorbed at low and intermediate relative pressure. For an increasing concentration of oxygen groups, the isotherm will move to larger adsorbed amount at identical relative pressure. At the same time, the isotherm changes shape progressively from a type III to a type II isotherm, increasing the competitiveness of water in relation to organic vapours. To understand the water adsorption mechanism, it is therefore necessary to understand the relative influence of the porous structure and the surface chemistry.

In the last two decades, the description of water adsorption mechanism on carbonaceous materials was more studied but only few of the published articles describe this mechanism due to its complexity. In the mid 1950s, Dubinin et al. [⁵⁵] postulated that oxygen complexes (energy privileged sites) act as primary active centre on which water adsorption occurs through hydrogen bonding and forms isolated clusters. In the literature, these clusters are often called secondary adsorption centres. As the adsorption process continues, these clusters then increase in volume. Finally when the relative pressure is higher, adsorption process leads to continuous layers of water molecules for non-porous solids and links the pore walls in the case of microporous carbons. Originally, the authors proposed the following relations (also denoted as DS1 equation) to describe quantitatively the water adsorption phenomenon:

$$a = c \cdot (a_0 + a) \cdot h \qquad \text{Eq. 2.30}$$

or

$$a = \frac{a_0 \cdot c \cdot h}{1 - c \cdot h} \quad \text{Eq. 2.31}$$

where a is the amount adsorbed at the relative pressure h ($= p/p_s$ or p/p_0 where p and p_s (or p_0) are equilibrium and saturated vapour pressure of water, respectively), a_0 is the surface concentration of primary adsorption centres, c is the ratio of the adsorption and desorption rate constants ($= k_{ads}/k_{des}$).

This relation gives a very good description of the water adsorption on non-porous adsorbents mainly (only hydrogen bonding interactions) but less for porous carbons. On the other hand, it gives very useful information about the number of primary sites on the surface. Therefore, there is a serious inconvenient to this model which is the assumption of unlimited adsorption space i.e. the amount adsorbed tends to infinity when the relative pressure approaches the value $1/c$.

Thus, it was modified to take into account limited adsorption space (pore volume) keeping the initial stage (in low pressure region) of water adsorption mechanism described previously. The following equation (DS2 equation) proposed by Dubinin and Serpinsky [⁵⁶] applies to describe the water adsorption on microporous carbon.

$$a = c \cdot (a_0 + a) \cdot (1 - k \cdot a) \cdot h \quad \text{Eq. 2.32}$$

or in the other form:

$$h = \frac{a}{c \cdot (a_0 + a) \cdot (1 - k \cdot a)} \quad \text{Eq. 2.33}$$

Moreover, many alternatives to the original DS2 equation exist. Barton and co-workers proposed two main relations [⁵⁷] and the first one (denoted as B1 equation) is written as:

$$a = c \cdot (a_0 + a) \cdot (1 - k \cdot a^2) \cdot h \quad \text{Eq. 2.34}$$

The other one (denoted as B2 equation) was proposed few years later and is supposed to describe better the final part of the isotherm [58].

$$a = c \cdot (a_0 + a) \cdot (1 - \exp[-k^2 \cdot (a - a_c)^2]) \cdot h \quad \text{Eq. 2.35}$$

In this equation, the authors stated that a_c does not have a proper physical meaning. In the last three equations, k is a constant fixed by the condition that for $h = p/p_s = 1$, the total amount adsorbed is a_s (where a_s is the maximum adsorption) [56]. For Barton et al. [57] the parameter k is controlling the decline in adsorptive power (when adsorption increases).

Also Furmaniak et al. [59] proposed to generalize the equation of Dubinin and Serpinsky as well as Barton et al. [57]. This improvement leads to the following adsorption isotherm equation (GB equation):

$$a = c \cdot (a_0 + a) \cdot (1 - k \cdot a^n) \cdot h \quad \text{Eq. 2.36}$$

The value of the exponent has a major influence on the isotherm shape. The plateau region becomes more and more visible when the exponent n increases. It is also important to notice that the previous generalised equation can be reduced to these expressions:

DS1 if $k=0$

DS2 if $n=1$

Or B1 if $n=2$

This equation has been designed to describe with more accuracy the middle and final pressure ranges of water isotherms for microporous carbons. These two pressure ranges correspond to upward rise in adsorption and to the plateau region respectively.

The adsorption of water on highly oxidised activated carbon can be studied by two other models. The first one is the D'Arcy & Watt equation [60] (DW equation) and is composed of one Langmuir isotherm describing the adsorption on primary sites (hydrophilic groups) and of one DS1 isotherm describing the adsorption of water molecules on secondary sites.

$$a = a_{prim} + a_{sec} = \frac{a_{m,L} \cdot k_L \cdot h}{1/p_s + k_L \cdot h} + \frac{c_{DS} \cdot a_{0,DS} \cdot h}{1 - c_{DS} \cdot h} \quad Eq. 2.37$$

where $a_{m,L}$ is the total concentration of all Langmuir sites and k_L is the Langmuir constant.

It should be pointed out that the D'Arcy & Watt approach contains some inconsistencies as mentioned by Barton et al. [61]. The chemisorbed water molecules (primary sites) cannot act as secondary centres.

It has also been shown by Furmaniak et al. [59] that the DW equation could be generalised taking into account the primary and secondary sites during water adsorption. The generalised D'Arcy & Watt equation (GDW equation) is written as:

$$a = \frac{a_{m,L} \cdot k_L \cdot h}{1/p_s + k_L \cdot h} + \frac{w \cdot a_{m,L} \cdot k_L \cdot h}{1/p_s + k_L \cdot h} \cdot \frac{c_{DS1} \cdot h}{1 - c_{DS1} \cdot h} \quad Eq. 2.38$$

where w determines the amount of primary centres involved in the formation of the secondary sites.

Another solution to describe the adsorption of water on oxidised carbons is to decomposed the original type IV isotherm into two contributions, both following the DA equation [62][63]. The first contribution is a type I isotherm for the low pressure region and is associated with adsorption by acidic centres. The second contribution is a type V which can also be described with the Dubinin-Serpinsky approach.

Water adsorption isotherms at 303°K generated from the various models are represented in Figure 2.4 together with experimental data points obtained on carbon black N330. Furmaniak et al. published recently another review [64] on most popular analytical approaches for water adsorption on carbons which contains adsorption isotherms generated from a multitude of theoretical and semi-empirical models.

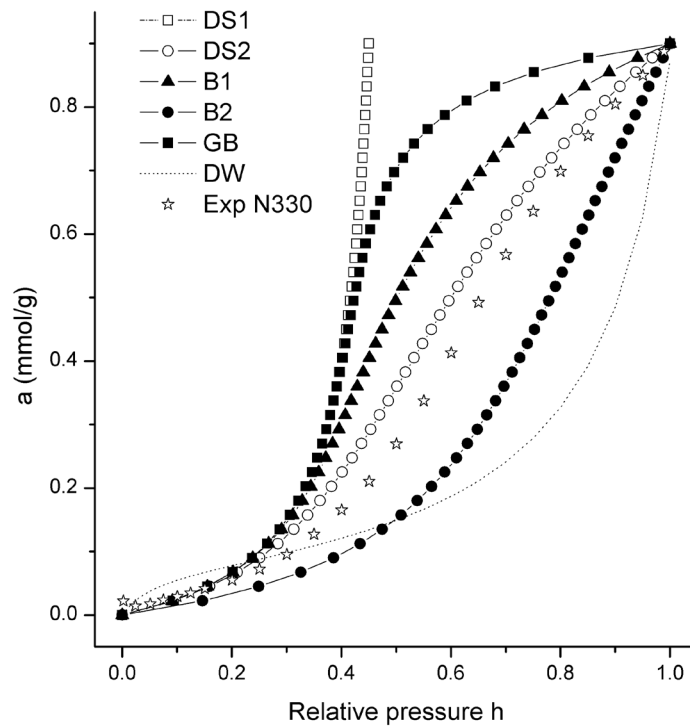


Figure 2.4: Water adsorption isotherms generated from the different models at 303°K. The following parameters have been used for the calculations: $c = 2$, $a_0 = 0.1$ mmol/g, $a_s = 0.9$ mmol/g; for B2, $a_c = 4$ mmol/g; for GB, $n = 6$ describing strictly microporous carbons with more visible upward rise and plateau. For the D'Arcy & Watt model, $c_{DS} = 0.88$, $a_{0,DS} = 0.11$ mmol/g, $a_{mL} = 0.07$ mmol/g, $K_L = 0.4$ mbar⁻¹ and $p_s = 42.42$ mbar. Additionally experimental data on carbon black N330 is also represented.

2.4 Immersion calorimetry

Immersion calorimetry is a complementary technique to gas/vapours adsorption methods in the characterisation of carbon surfaces. In both techniques, information collected regarding a surface are specific to the adsorbate used. The enthalpy of immersion $-ΔH_i$ (J/g or J/m²) is related to the heat release during the immersion, in the desired liquid, of an outgassed carbon powder. The enthalpy of immersion is known to be directly proportional to the surface for solids which have only an open surface such as graphite, non porous carbon fibre, graphitized carbon black and also some non graphitized carbon black. Thus, the heat of immersion is a good way to determine in first approximation the surface of a solid provided that an appropriate calibration is available. However, regarding activated carbons or more generally microporous solids, several factors influence the release of the heat. These factors (surface chemical composition, pore structure and volume) make impossible the use of a single calibration value obtained from calorimetric measurement which is equally applicable to all carbons. Therefore, surface area estimation from immersion calorimetry is subjective in nature.

The procedure to use calorimeters to determine enthalpy of immersion has been widely reported in the literature whether it be a static type calorimeter [65] or a flow microcalorimeter as designed by Groszek [66]. In this work, the calorimeter used was of Calvet type which belongs to the first category of calorimeter and will be described more in details in the experimental section.

It has been shown that heats of immersion using organic liquids or water could be related to either the characteristic energy $β·E_0$ of the Dubinin-Radushkevich equation or the Dubinin-Serpinsky equation.

In the case of organic liquids, from the definition of the net heat of adsorption q^{net} and the established link between the enthalpy of immersion of a microporous solid and the isosteric heat of adsorption q^{st} , a fundamental relation for the enthalpy of immersion has been devised:

$$-\Delta H_i = \frac{\beta \cdot E_0 \cdot W_0 \cdot \sqrt{\pi} \cdot (1 + \alpha_L \cdot T)}{2 \cdot V_m} + h_i \cdot S_{ext} \quad \text{Eq. 2.39}$$

Where β , E_0 and W_0 are the parameters of Dubinin's theory as mentioned earlier, V_m is the molar volume, α_L is the thermal expansion coefficient, S_{ext} is the external surface area of the solid and h_i (or $-h_i$) is the specific enthalpy of wetting usually obtained using non-porous carbon blacks.

In the case of immersion into water, it has been shown by Kraehenbuehl et al. [67] that the enthalpy of immersion was related to the number of primary adsorption sites a_0 present on the carbon surface.

$$-\Delta H_i = -25.0 \cdot a_0 - 0.6 \cdot (a_s - a_0) \quad \text{Eq. 2.40}$$

where $-\Delta H_i$ is in J/g, a_s (maximum adsorbed amount) and a_0 are expressed in mmol/g and the coefficients are expressed in J/mmol (H₂O).

Knowing a_0 from adsorption experiment or from direct measurement by XPS, it is possible to compare the calculated value of $-\Delta H_i$ to the experimental enthalpy of immersion [68].

As described in Chapter 6, when a carbon sample is immersed in water or water is adsorbed on its surface, heat is released due to the interactions of water molecules and carbon surface. This release of energy originates from two distinct processes [69]:

- i. Creation of water cluster by hydrogen-bonds on the primary adsorption sites (a_0)
- ii. Dispersion of the water molecules on the oxygen-free carbon surface

These two processes have significantly different energetic contributions because their natures are not the same. This explains the difference between the two coefficients of the previous equation: -25.0 J/mmol (H₂O) for i) and -0.6 J/mmol (H₂O) for ii).

2.5 Measure of the external surface area

2.5.1 The Gregg-Lanford's or pre-adsorption method

This method is surely the most direct technique to evaluate the external surface area of a porous solid. It consists to fill up the micropores whilst leaving the mesopores, macropores and external surface free. Gregg and Lanford [70] proposed the use of n-nonane as pre-adsorbate, because n-alkane with long chain are very slow to leave the pores by pumping at room temperature. Then, nitrogen adsorption at 77°K should be done permitting to calculate the external surface area from BET or α_S method. An important decrease of the C_{BET} constant in comparison to the global isotherm is a direct consequence of micropore volume disappearance.

2.5.2 α_S plot and t-plot

The t-plot from Lippens and de Boer [71] was originally devised to detect deviations of experimental isotherm from a standard isotherm. But one problem met in this method is the necessity to know the thickness of the adsorbed layer on the walls of the pores. But since the object is to compare the shape of the experimental isotherm with the one of the standard isotherm, it is not necessary to know the number of molecular layer n/n_m .

This is, accurately, the basis of the method developed by Sing [72] where the isotherm is normalised by the factor n_s or $n_{0.4}$. The plot $n/n_{0.4}$ ($= \alpha_S$) versus the relative pressure p/p_0 represents the normalised adsorption of a reference solid.

This α -curve should be used to build an α_S plot from the isotherm of a test solid by plotting the amount adsorbed of the experimental sample against the α_S value of the reference for each corresponding relative pressure. The important advantages of this method are that its applicability is not restricted to nitrogen and it can be used for both type II and type III isotherms.

Nitrogen adsorption at 77°K is generally regarded as the most suitable method for the determination of surface area and porosity. In the particular case of carbon materials, a number of authors have published reliable standard data [73][74] to use for the characterization of microporous and non-porous carbon materials. But other adsorptives with different size, shape and polarity are available to characterize more effectively carbon materials. Standard adsorption data have been produced for a small range of adsorptive (benzene [75], methanol [76], CO₂ [77], etc...) using graphitized and ungraphitized carbon black. In this work, the reference data from Carrot et al. [76] for the adsorption of methanol have been used. It should be pointed out that due to the polarity of the methanol molecules, the isotherm shape is expected to be fairly sensitive to surface oxygen concentration, which of course changes from one carbon black to another.

Regarding nitrogen adsorption, reference data using graphitized carbon black N234G has been produced and give good agreement with Sing et al. data [73].

2.6 Non-porous and porous carbon adsorbents

2.6.1 Carbon black

Carbon black is another form of elemental carbon, consisting of spherical-like particles and has been used the most in this work. The majority of carbon black is produced by the oil furnace process i.e. the incomplete combustion of heavy aromatic feedstock in a hot flame of (preheated) air and natural gas [78]. Carbon black can also be manufactured from the thermal decomposition in inert atmosphere (absence of oxygen).

A schematic picture of the reactor used in the oil furnace process is shown in the Figure 2.5.

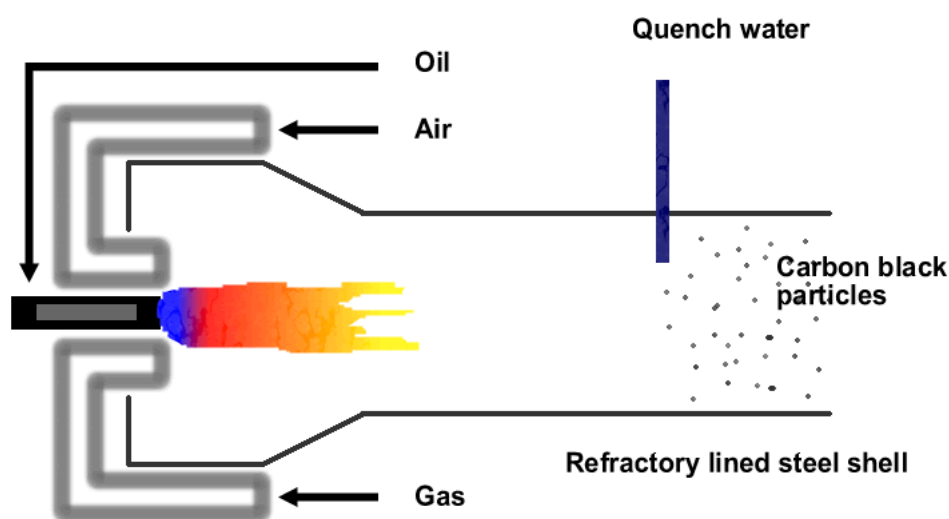


Figure 2.5: Simplified illustration of the oil furnace reactor. The oil feed stock is injected into a very high temperature gas flame and the carbon black formation is controlled via a quench water system.

Carbon blacks are used as reinforcing fillers to optimize the physical properties of tires. It represents 85% of the carbon black manufactured worldwide. The other 15% are used mainly in the paint industry [79].

The mechanism of carbon black formation is quite complex but three main steps, independently of the different production process, can be drawn off:

- i. Nucleation which lead to the transformation of a molecular system in particles system (10 to 150 nm diameter for these primary particles). The average size of the primary particles is the most important factor to determine colour strength.
- ii. Aggregation of the primary units of carbon black by the collision and fusion of these particles inside the combustion zone of the reactor. The size (extent) and complexity of the spherical-like “cluster” are controlled in the reactor and are link to the structure grade of the final product.

- iii. Finally, those aggregates may be held together by weak forces to form agglomerates like chain (up to 1 mm length). But these agglomerates can break down easily during mixing or other process.

The structure development of the carbon black material is displayed in the Figure 2.6. The parallel lines on the primary particle represent the graphene sheets. More details will be given in the paragraph 4.3 where the structure of the carbon black used in this study was observed using HRTEM.

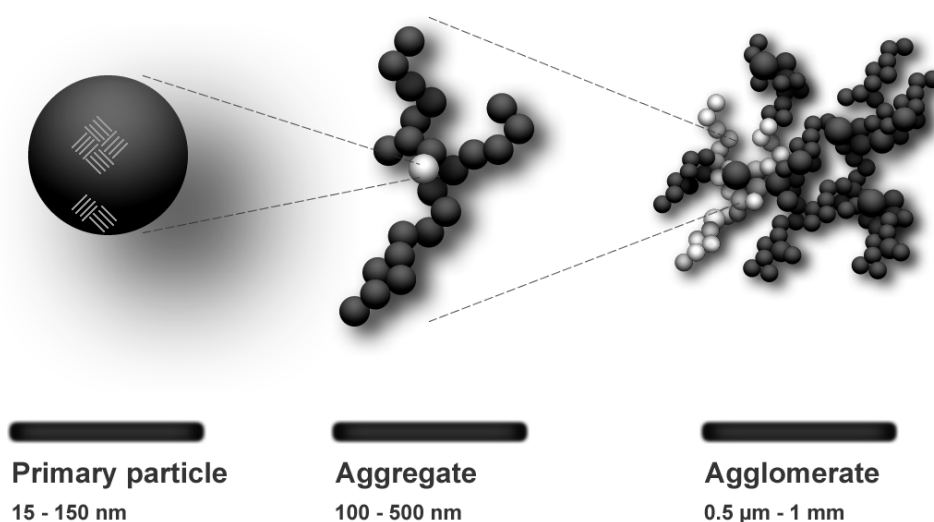


Figure 2.6: Sequence of the structure development of carbon black from the primary particle to agglomerate (which is a packing of aggregates through weak electronic forces). Aggregates are the base structure of carbon black, they are indivisible.

2.6.1.1 Surface oxidation of carbon black

Like written previously, different grades of carbon black can be produced by controlling the reactor geometry, the flows of air, gas and liquid feedstock and the position of the water quench. Carbon black may contain small quantities of chemisorbed heteroatoms on

its surface (mainly oxygen up to 8 at.% and less than 1 at.% hydrogen, sulphur and nitrogen). Some carbon blacks are post treated in an oxidative process to increase the oxygen amount on the surface. This surface oxidation has an effect on the performances of carbon black for some applications. For example, in coating application and printing ink field, the rate of dispersion and the stability of the product improve with high oxygen amount. But on the other hand, an oxidised carbon black will lose its electrical conductivity.

2.6.2 Activated carbon

Activated carbon, also called active or microporous carbon is a non-graphitic form of carbon, characterised by a large internal surface area ranging from 500 to ~ 2000 m²/g and a high internal porosity, making it suitable for a wide range of applications.

Activated carbons can be manufactured from a wide variety of materials such as peat, coal, wood and coconut shell. In general, any carbonaceous source can be converted into activated carbon via several methods [31][80]. Therefore, expensive synthetic resins or polymeric materials can also be used as precursor to improve reproducibility and/or to meet specifications for special applications. In fact, the most desirable method to control the end-product properties is to adjust processing conditions.

The manufacturing process is divided into two steps: carbonisation and activation. The pyrolysis or carbonisation is the thermal decomposition of an organic material under vacuum or inert atmosphere over a temperature range from 400 to 1000°C. Most of the non-carbon elements (i.e. heteroatoms such as oxygen, hydrogen, nitrogen and sulphur) are removed from the original source material as volatiles. This changes the properties of the porosity and opens up closed porosity. The carbon atoms will regroup together in aromatic sheets. The spaces between these sheets or lamellar create a preliminary porosity (interstices) of the product.

This is followed by the activation process which results in a large internal surface area and development of the porous structure via an activation agent which reacts with carbon. Two routes are available to activate the material: *chemical activation* or *physical activation*.

The chemical activation involves the treatment (impregnation) of the raw material with $ZnCl_2$ (zinc chloride) or H_3PO_4 (phosphoric acid) prior to carbonisation. During carbonisation, primarily, the chemical agent attacks on the cellulosic structures in the precursor. The pore size distribution is dependent on the ratio of chemical compound to precursor. The main inconvenient of this method is that the resulting activated carbon is not of high purity due to the presence of heteroatoms (Cl, P, N, etc...) on the surface. Also, the activation agents are considered hazardous chemicals and not friendly for environment.

The physical activation refers to the gasification of carbon by oxidising gases such as carbon dioxide, steam and air in the temperature range of 700~1100°C. It is the most commonly used method to produce activated carbon. Thus the extent of development of porosity and these characteristics depend on [³¹]:

- ✓ initial structure of the carbon
- ✓ the oxidising gas
- ✓ the temperature and duration of gasification
- ✓ the pressure of the gas
- ✓ the particle size of the carbon
- ✓ the presence of impurities in the carbon

The gas molecule must penetrate into the interior of the particle to remove a carbon atom from its initial position. So, generally, the slower the reaction the more extensive is the development of the porosity inside the particle. The reactions of carbon with steam and carbon dioxide are the following:



The reaction of CO₂ with solid carbon is known as the Boudouard reaction. Steam is often preferred to CO₂ because the water molecule is smaller than CO₂ one so the access into the micropores is easier.

The activation process and the mechanisms involved are extremely complicated in theory but it is easy to acknowledge how different activation conditions influence the range of porosities created. So in practice, the desired pore structure of an activated carbon end-product is attained by combining the correct raw material and activation conditions.

Activated carbon is a widely used adsorbent because it adsorbs a large variety of organic compounds, it is cheap and it can be reused if the adsorbed substances are removed. This regeneration or re-activation is usually achieved by heating under vacuum. Related to the type of application, various forms of activated carbons can be used including powders, cylindrical extrudates, spherical beads, granules and fibres (or cloth).

According to Stoeckli, the microstructure of activated carbon can be represented with a slit-shaped model as seen in the Figure 2.7.



Figure 2.7: Schematic representation of the structure of activated carbon (adapted from Stoeckli [⁸¹][³⁴]).

The most important properties of activated carbon, which will determine its usage, are the pore structure and the surface chemistry. These are described in detail in paragraphs 2.1.3 and 2.7.

2.6.3 Graphite

Graphite is one of the two crystallographic forms of elemental carbon with diamond. The crystal lattice of graphite consists of a lamellar structure in which carbon atoms within each lamellae (basal plane) form hexagonal ring system. Each atom of carbon is bonded through sp^2 hybridised orbitals to three nearest neighbours within the plane (strong σ covalent bonds stronger than the bonds of diamond). The fourth electron unhybridised $2p_z$ orbital leads to the formation of π bonds with neighbouring atoms.

Two forms of graphite exist depending of the stacking order of basal planes: the most common is the hexagonal structure, represented in Figure 2.8, where the layers are stacked in an ABAB sequence. The resulting in-plane interatomic distance is $a_{c-c} =$

1.421 Å and the lattice constant is $a_0 = 2.461$ Å. The interplanar distance is $c/2 = 3.35$ Å [82].

The other form of well-crystallised graphite has a rhombohedral structure and is less stable than the hexagonal form. The graphene sheets are arranged relative to each other in an ABC stacking sequence.

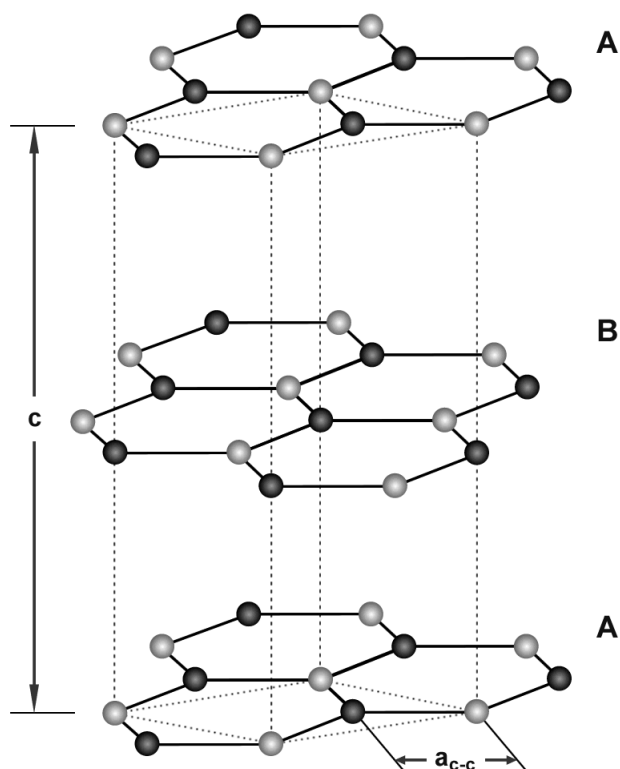


Figure 2.8: Crystal structure of hexagonal graphite. Each carbon atom in the honeycomb network is bonded through sp^2 bonds to the three nearest neighbours within the basal plane. The layers are stacked in ABAB sequence due to weak interplanar interactions (delocalized π bonds). The resulting in-plane interatomic distance a_{c-c} is equal to 1.421 Å whereas the interplanar distance $c/2$ is equal to 3.354 Å (with $c = 6.708$ Å).

The weak interactions between layers originate from the small overlap of the $2p_z$ orbitals. These interactions between basal planes are predominantly dominated by long-

range Van der Waals forces. These two kinds of interactions i.e. covalent and *VdW* along different crystal directions make graphite a very highly anisotropic material [⁸³][³¹].

2.6.4 Carbon nanotubes

Carbon nanotubes (CNTs) are often believed to be first discovered by Ijima [⁸⁴] in 1991 but in reality they have been observed before that as for example, Oberlin, Endo and Koyama [⁸⁵] who published a TEM image of what could be the first SWCNT ever observed. Regarding the MWCNTs, from the editorial of Monthieux and Kuznetsov [⁸⁶] published in 2006 in the journal Carbon, it appears that Radushkevich and Lukyanovich [⁸⁷] published a report in the early 1950s, showing hollow carbon fibres (that is to say multi-walled carbon nanotubes) for the first time. Since the undoubted tremendous impact paper from Ijima in 1991, date of the “*re-discovery*” of the CNTs, the nanotubes have been the focus of considerable research in the fields of physics, chemistry and material science. Numerous investigators all over the world have since reported remarkable properties for this novel form of carbon material. From unique electronic properties to mechanical properties (and also chemical stability) exceeding any current materials, carbon nanotubes offer tremendous opportunities in the rapidly growing field of nanotechnology. Most theoretical studies on CNTs focus on the understanding of the relationship between nearly one-dimensional structure and diverse properties. Carbon nanotubes can be described as graphene sheets that have been rolled up into a tube (and closed at each end with half of a fullerene). As stated before, nanotubes are considered as nearly one-dimensional structures because they generally have a very high length to diameter ratio (about 1000). Nanotubes can exist as either two main structures: single walled carbon nanotubes (SWCNTs) are considered as tubes with only one wrapped sheet of graphite and multi-walled carbon nanotubes (MWCNTs) are composed of a collection of concentric SWCNTs with different diameters. The length and diameter of

these two structures differ a lot and as consequence, their properties are also very different.

As represented in the Figure 2.9, a single walled nanotube is usually characterised by a single vector \vec{C}_h called chiral vector. Two atoms from the graphene are chosen. One will be used as the origin. The graphene sheet is then rolled up in the direction of the chiral vector until the two atoms coincide. The vector pointing from the origin toward the other atom is defined as the chiral vector. And the direction of the nanotube axis is orthogonal to this chiral vector.

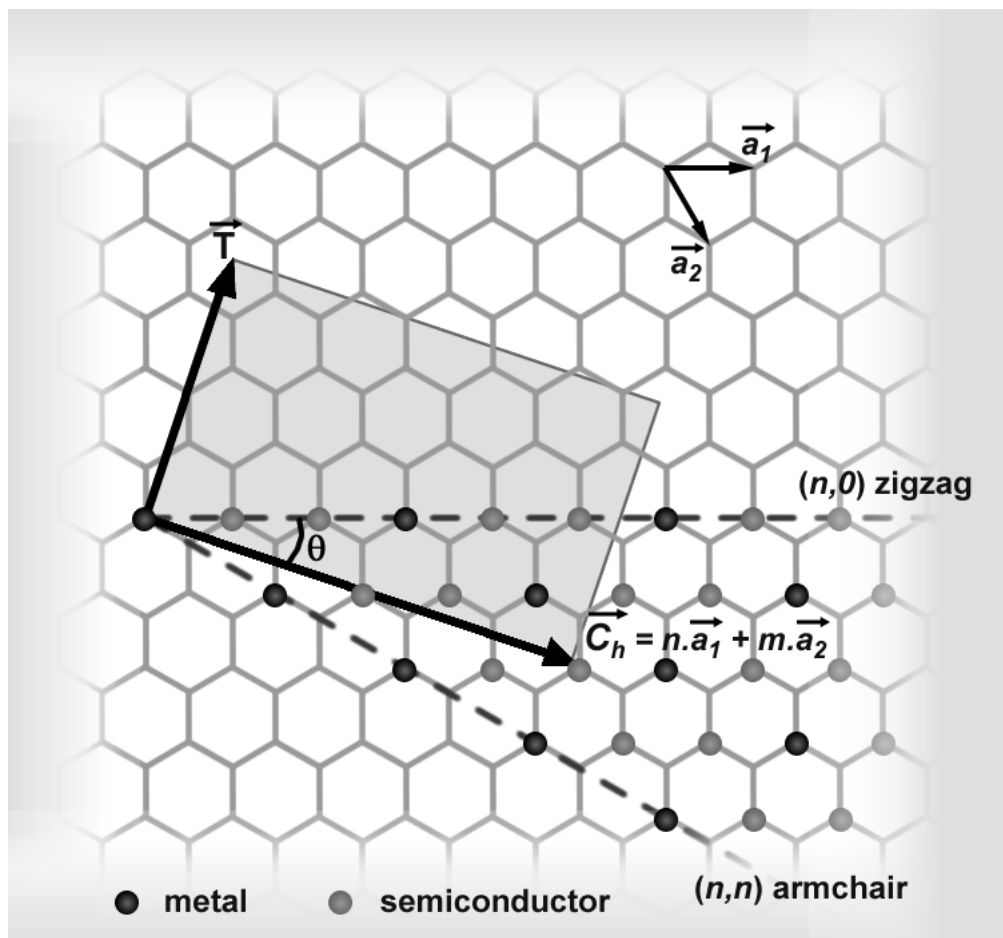


Figure 2.9: Schematic diagram showing the chiral vector \vec{C}_h and the chiral angle θ_{chi} . The chiral vector is defined by the vector $n \cdot \vec{a}_1 + m \cdot \vec{a}_2$, \vec{a}_1 and \vec{a}_2 being the unit vectors of the two dimensional graphene sheet. The chiral angle is defined as the angle between the chiral vector \vec{C}_h and the zigzag axis \vec{a}_1 .

The chiral vector is defined with the following relation:

$$\vec{C}_h = n \cdot \vec{a}_1 + m \cdot \vec{a}_2 \equiv (n, m) \quad \text{Eq. 2.43}$$

where n and m are two integers, a_1 and a_2 are the lattice vectors of the graphene sheet.

The chiral angle θ_{chi} ($0 \leq \theta_{chi} \leq 30^\circ$) is the angle between the chiral vector \vec{C}_h and the a_1 direction $(n, 0)$. Two special cases of nanotubes exist: the “zigzag” $(n, 0)$ and “armchair” (n, n) nanotubes with respective chiral angle of 0 and 30° . All the other ones are called chiral nanotubes (n, m) with $n \neq m$. The Figure 2.10 gives a visual idea of the structure of armchair, zigzag and chiral SWCNTs.

The circumference of the nanotube corresponds to the length of the chiral vector \vec{C}_h .

$$c = \|\vec{C}_h\| = a \cdot \sqrt{n^2 + m^2 + n \cdot m} \quad \text{Eq. 2.44}$$

where a is the length of the unit lattice vector (\vec{a}_1 or \vec{a}_2) and equals:

$$a = \|\vec{a}_1\| = \|\vec{a}_2\| = a_{c-c} \sqrt{3} \quad \text{Eq. 2.45}$$

It is well known that for graphite, the in-plane carbon-carbon bond length is $a_{c-c} = 1.421 \text{ \AA}$ and in a first approximation, the same value can be used for carbon nanotubes. But in reason of the curvature of the carbon nanotube, a larger value such as 1.44 \AA is more realistic [⁸⁸][⁸⁹].

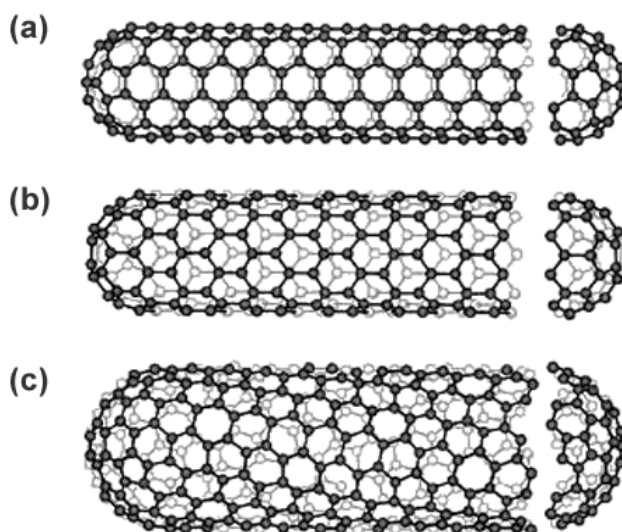


Figure 2.10: SWCNTs with different chiralities. (a) (5,5) armchair nanotube, (b) (9,0) zigzag nanotube and (c) (10,5) chiral nanotube.

The chirality of the carbon nanotube plays a significant role on the properties of the material, in particular on its electronic properties. It has been discovered that the nanotubes can be either metallic if $|n - m| = 3 \cdot q$ or semiconducting if $|n - m| = 3 \cdot q \pm 1$ (q is an integer) [90].

Usually, carbon nanotubes are closed with a fullerene cap at the end of the tube, called termination cap. These caps are formed from pentagons and hexagons and are derived from the well known C_{60} hemisphere fullerene.

Regarding the morphology of the nanotube, defects can be introduced in the tube structure via the Stone-Wales transformation. The Stone-Wales transformation (see Figure 2.11) is achieved by a reversible diatomic interchange and the resulting structure is formed of two pentagons and two heptagons in pairs. These heptagons permit concave areas within the tube and allow many equilibrium shapes to be obtained.

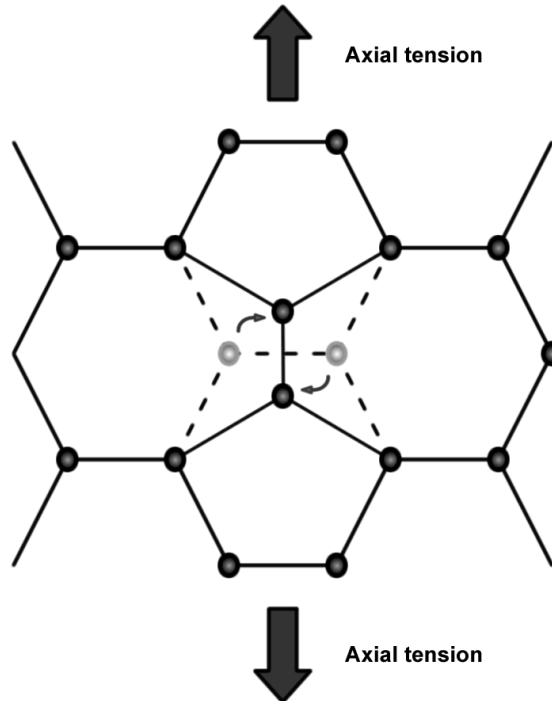


Figure 2.11: Stone-Wales transformation occurring in an armchair nanotube under axial tension.

As stated before, multi-walled carbon nanotubes are concentric graphene cylinders nested in each other. These concentric nanotubes are held together by weak Van der Waals forces and also have different chirality. The Figure 2.12 represents a high resolution transmission electron microscope (HRTEM) micrograph showing the nanostructure of an as-produced MWCNT used in this work. According to theoretical calculations or based on TEM images, the intershell spacing between two successive graphene tubes is in a range from 3.4 to 3.6 Å [⁹¹][⁹²], slightly larger than in graphite.

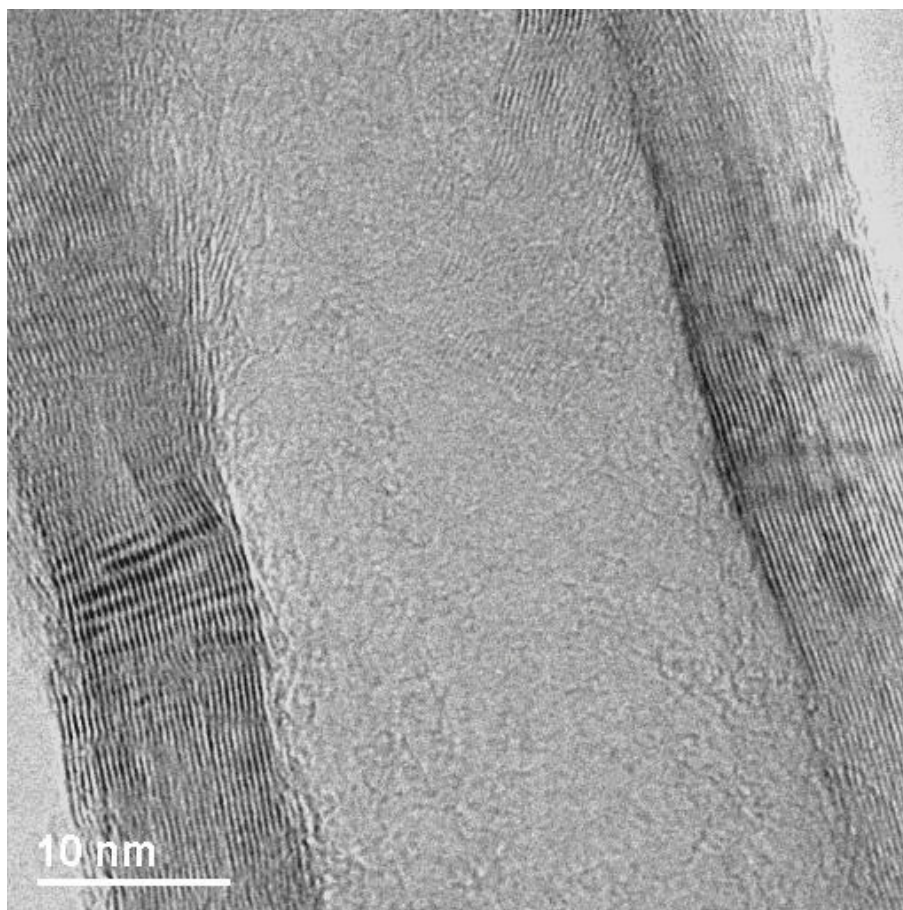


Figure 2.12: HRTEM photograph of as-produced MWCNT. The multiwall structure formed by concentric graphene sheet is clearly visible on each side.

2.7 Oxygen on carbon surfaces

2.7.1 Overview

In the older literature and still nowadays, the chemical nature of the adsorbent surface has often been overshadowed by the role played by porosity and physical morphology regarding the properties and applications of carbon materials.

However, functional groups on carbon surfaces (oxygen, nitrogen, sulphur, etc...) play a decisive role in diverse fields and applications such as adsorption selectivity and behaviour, catalysis, wettability and moisture content. And it is interesting to note that these heteroatoms, especially oxygen are always present (in small concentration) on the

surface of carbonaceous materials [93]. The preparation process of these materials will influence which functional groups can be formed or removed.

Reaction between oxygen and carbon surfaces is one of the most common reaction involving elemental carbon and also one of the oldest known. In 1863, Smith discovered that charcoal could bind oxygen chemically if it was exposed to high temperature [94][95]. This was confirmed few decades later by Rhead and Wheeler [96]. Then, in the second part of the XXth century, numerous studies appeared focusing on chemical properties of oxidised carbons and identification of surface functional groups [97][98][99][100][101].

But why are the effects of oxygen so pronounced? A realistic explanation to answer the previous question could lie in this simple calculation.

Stoekli [34] has postulated that an ideal graphene sheet should have an approximate surface area of $S_{graphene} = 2000 \text{ m}^2/\text{g}$. This value includes both sides so one obtains $S_{1/2 \text{ graphene}} = 1000 \text{ m}^2/\text{g}$ for one side only. The number of atoms of carbon present on one square metre surface area can be calculated (Eq. 2.46) using the Avogadro number, the carbon molar weight and the surface area of one side.

$$N_{carbon \ atoms}/\text{m}^2 = \frac{N_A}{S_{1/2 \text{ graphene}} \cdot M_w[C]} = 5.018 \cdot 10^{19} \quad \text{Eq. 2.46}$$

where $N_A = 6.022 \cdot 10^{23} \text{ at/mol}$ and $M_w[C] = 12.011 \text{ g/mol}$.

But a more accurate value can be obtained using the calculated footprint area of one carbon atom from the crystal structure of hexagonal graphene sheet (see Figure 2.8 and Figure 2.13).

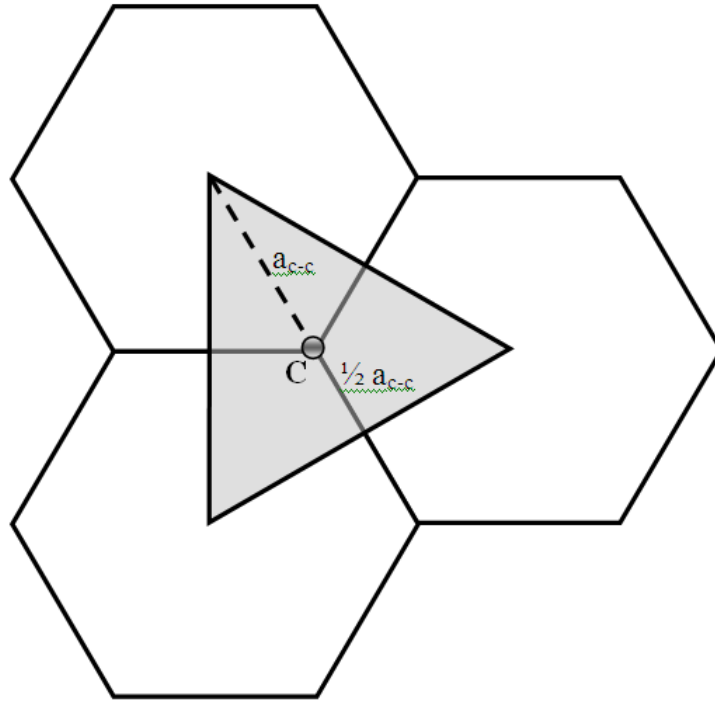


Figure 2.13: Close view on the hexagonal structure of graphite sheet, in particular the footprint area of the central Carbon atom represented by the coloured triangle.

From simple geometry considerations, one can calculate the theoretical footprint area for one carbon atom within the hexagonal graphite structure using Eq. 2.47. This area is represented by the grey triangle around the carbon atom and is equal to half the area of the hexagon composed by six carbon atom.

$$\begin{aligned}
 A_{\text{Footprint carbon atom}} &= \frac{A_{\text{hexagon}}}{2} = \frac{3\sqrt{3}}{4} a_{c-c}^2 \\
 &= 2.623 \times 10^{-20} \text{m}^2
 \end{aligned}
 \tag{Eq. 2.47}$$

With this equation, a value of $2.623 \times 10^{-20} \text{m}^2$ per atom of carbon is obtained. This gives a value of $1316.3 \text{m}^2/\text{g}$ as the theoretical surface area for graphene layer which is slightly higher than the value proposed by Stoeckli.

Coming back now to the surface oxidation of the carbon, if one considers a carbon surface with 1 at.% oxygen, it means that $4\sim 5 \times 10^{17}$ oxygen atoms are exposed on the surface and can potentially act as active centre for adsorption.

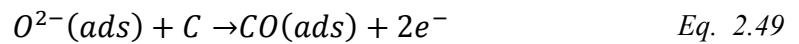
For comparison with TPD or titration, the oxygen level $[O]_{T(TPD \text{ or } Titration)}$ measured with these techniques is expressed in mmol/g. So if one converts, for example, 1 mmol/g in number of oxygen atoms per square meter (considering an ideal carbon surface as described by Stoeckli), one obtains, via the equation below, a value ($6 \times 10^{17} \text{ O}_{\text{atoms}}/\text{m}^2$) which is really close to the value obtained for 1 at.% oxygen ($5 \times 10^{17} \text{ O}_{\text{atoms}}/\text{m}^2$).

$$N_{\text{oxygen atoms}}/\text{m}^2 = \frac{N_A \cdot [O]_{T(TPD \text{ or } Titration)}}{S_{1/2 \text{ graphene}}} = 6.022 \times 10^{17} \quad \text{Eq. 2.48}$$

Where $N_A = 6.022 \cdot 10^{23} \text{ at/mol}$ and $S_{1/2 \text{ graphene}} = 1000 \text{ m}^2/\text{g}$.

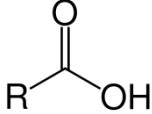
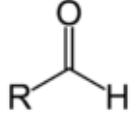
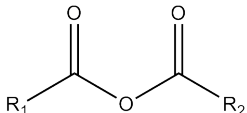
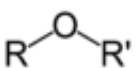
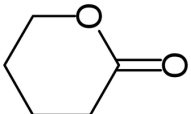
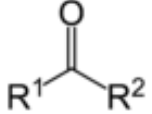
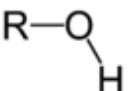

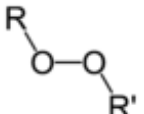
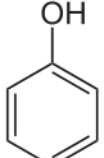
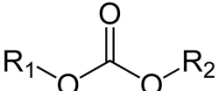
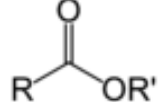
2.7.2 Oxygen surface groups

The reaction of oxygen with carbon at edge site or vacancy will form carbon-oxygen functional group represented as:



On carbon surfaces, different types of oxygen-containing surface groups as CO(ads) in the above reaction can be observed [¹⁰²][¹⁰³][¹⁰⁴]. The most common are listed in the Table 2.1 with a representation of their structural formula. It is also possible to observe epoxy group formation by atomic oxygen on a highly oxidised graphene layer [¹⁰⁵].

Table 2.1: Typical surface functional groups present on oxidised carbon surface.

Structural formula	Group and formula	Structural formula	Group and formula
	Carboxylic acid RCOOH		Aldehyde RCHO
	Anhydride (R ₁ CO)O(OCR ₂)		Ether ROR'
	Lactone		Ketone R ₁ COR ₂
	Hydroxyl ROH		Quinone
	Peroxide ROOR'		Phenol
	Carbonate R ₁ O(C=O)OR ₂		Ester RCOOR'

Carbon-oxygen functional groups are those which influence the most adsorption behaviour and surface physicochemical properties such as surface acidity and wetting. This multitude of oxygen-containing surface groups can be explained by different reactivity of active site and also the use of different oxidising agents. They are formed from chemical reaction with oxidising gases (such as oxygen, ozone, carbon dioxide and air) and also with oxidising solutions such as nitric acid, hydrogen peroxide, sodium hypochlorite and ammonium persulfate. These treatments are usually carried out at room temperature but high temperature can be preferable during the oxidation process [106][107][108][109]. The final properties of the material can be controlled with temperature, treatment time and concentration.

Nevertheless, oxidation treatment can also affect the bulk carbon network. Moreno-Castilla et al. [110] reported that HNO₃ treatment on activated carbon affected more the surface area and porosity than any of the other treatments. They also found that treatment with ammonium persulfate fixed stronger acid groups than HNO₃ treatment in spite of the fact that this latter treatment fixed the largest amount of oxygen complexes evolving as CO₂ (during desorption). For Wu et al. [111], nitric acid oxidation created effectively significant amount of acidic functional groups on carbon fibre surface but also caused a decrease of tensile strength and a carbon fibre weight loss.

2.7.3 Analysis techniques

Several methods are available to determine the amount of oxygen surface groups and some of these methods give also really important information about the type of functional groups present on the carbon surface. Temperature Programmed Desorption (TPD) is nowadays becoming a very popular technique to quantify the different oxygen complexes of a carbon material whether inside the material or on the external surface. The controlled heating of the oxidised carbon under vacuum gives useful information about the kind of oxygen groups which are being decomposed. It is an alternative to XPS measurements and is usually combined with thermogravimetry analysis.

By heating the carbon material under vacuum, functional oxygen groups will decompose at different temperatures and release oxygen atoms in the form of two gases: carbon dioxide and carbon monoxide. By monitoring the gas phase of desorbed species, usually with a Gas Chromatograph/Mass Spectrometer (GC/MS), one can get important information about the amount and types of different species, kinetics of the desorption process and enthalpy of desorption. The temperatures at which CO and CO₂ are being desorbed from the surface are then compared to experimental reference values found in the literature [112][113][114][115] and given in the Table 2.2. But it is important to note that TPD peak temperature may be affected by the texture of the materials (different types of

carbon materials, activated carbon and carbon nanotubes for example), chemical treatment and experimental parameters such as geometry design of the reactor or heating rate.

Table 2.2: Oxygen surface groups and their pyrolytic elimination temperatures.

Surface groups	Decomposition product	Temperature range of decomposition	References
Carboxylic acid	CO ₂	473-523°K	116
		453-573°K	117, 54
Lactone	CO ₂	463-923°K	118
		900°K	119
Carbonyl	CO	973-1253°K	119,120
		900°K	119, 117
Anhydride	CO, CO ₂	673-723°K	121
Phenol	CO	873-973°K	116
Quinone and ketone	CO	1073-1173°K	118
		973-1253°K	116
Ether	CO	973°K	122

Another method for determining these groups is the Boehm titration which was developed by Boehm in 1964 [¹²³][¹²⁴]. This method gives good results but the major constraint is that it is very time consuming.

An alternative to these methods is X-ray Photoelectron Spectroscopy (XPS) which presents some certain advantages: rapidity of scanning, ease of use and possible determination of the type of functional groups. But because the analysis surface is very small (about 1 mm²), 3 scans are preferred for statistic purpose and limit the errors.

All the techniques mentioned before have limitations to identify the type of surface functional groups and are generally used in combination with each other to give the right information.

Table 2.3: O1s binding energy and C1s chemical shifts related to primary C1s peak at 284.6eV and for different chemical groups.

Functional group	C1s chemical shift (ev)	O1s binding energy (ev)	References
C-O ¹ H/C-O ² R	1.6 ±0.1	¹ 532.9-533.6	125,126
		² 532.6-533.3	127, 128
ph-C=O	2.4	/	125
Quinone/enol	2.1±0.1	/	127, 126
-O ² -C(=O ¹)-O ² -	5.4	¹ 532.3	125
		² 533.9	
-C(=O ¹)-O ² -C(=O ¹)-	4.4	¹ 532.6	125
		² 533.9	
-C(=O ¹)-O ²	4.2±0.2	¹ 531.7-532.6	125,126,127,128
		² 533.1-534.0	
ph-C(=O)-O	3.6±0.1	/	125
C=O	3.0±0.1	531.3-532.3	125,127,128
C-N	0.94	/	125

X-ray photoelectron spectroscopy uses the O1s binding energies to identify the nature of the chemical groups. In addition, the C1s chemical shifts related to the primary C1s peak at 284.6 eV can also be really useful to determine the functional groups. The Table 2.3 indicates these data for the most common oxygen-containing groups present on carbon surface. In this work, the focus was limited to oxygen-containing functional groups but surface groups containing other elements exist such as nitrogen and sulphur groups.

References

- ¹ *Orange book: IUPAC compendium of analytical nomenclature* (Blackwell Scientific Publications, Oxford, 1987). p. 85
- ² F. London. Properties and applications of molecular forces. *Z. phys. Chem.* **B11** (1930) 222-251.
- ³ F. London. Theory and system of molecular forces. *Z. phys. Chem.* **63** (1930) 245.
- ⁴ D. M. Young and A. D. Crowell. *Physical adsorption of gases* (Butterworths, London, 1962).
- ⁵ J. E. Lennard-Jones. in *Proceedings of the physical society* 461-482 (1931).
- ⁶ J. E. Lennard-Jones. The equation of state of gases and critical phenomena. *Physica* **4** (1937) 941.
- ⁷ S. J. Gregg and K. S. W. Sing. *Adsorption, surface area and porosity* (Academic Press, London, 1982).
- ⁸ K. S. W. Sing. Physisorption of gases by carbon blacks. *Carbon* **32** (1994) 1311-1317.
- ⁹ A. W. Adamson. *Physical chemistry of surfaces* (John Wiley, New York, 1990). Ch. 16
- ¹⁰ S. Brunauer, L. S. Deming, W. S. Deming and E. Teller. On a theory of the Van der Waals adsorption of gases. *J. Am. Chem. Soc.* **62** (1940) 1723-1730.
- ¹¹ K. S. W. Sing et al. IUPAC Recommendations - Reporting physisorption data for gas/solid systems with special reference to the determination of surface area and porosity. *Pure & Appl. Chem.* **57** (1985) 603-619.
- ¹² A. V. Kiselev. Adsorption properties of hydrophobic surfaces. *J. Colloid Interface Sci.* **28** (1968) 430.
- ¹³ W. Kratschmer, J. Rathousky and A. Zukal. Adsorption of krypton at 77°K on fullerene C60, graphitized carbon black and diamond. *Carbon* **37** (1999) 301-305.
- ¹⁴ M. D. Donohue and G. L. Aranovich. A new classification of isotherms for Gibbs adsorption of gases on solids. *Fluid Phase Equilibria* **158-160** (1999) 557-563.

-
- ¹⁵ K. Murata and K. Kaneko. The general equation of supercritical gas adsorption isotherm. *J. Phys. Chem. B* **105** (2001) 8498-8503.
- ¹⁶ J. Rouquerol et al. IUPAC Recommendations - Recommendations for the characterization of porous solids. *Pure & Appl. Chem.* **66** (1994) 1739-1758.
- ¹⁷ T. Ohba, T. Suzuki and K. Kaneko. Preformed monolayer-induced filling of molecules in micropores. *Chemical Physics Letters* **326** (2000) 158-162.
- ¹⁸ I. Langmuir. The constitution and fundamental properties of solids and liquids. Part I. Solids. *J. Am. Chem. Soc.* **38** (1916) 2221-2295.
- ¹⁹ I. Langmuir. The adsorption of gases on plane surfaces of glass, mica and platinum. *J. Am. Chem. Soc.* **40** (1918) 1361-1403.
- ²⁰ S. Brunauer, P. H. Emmett and E. Teller. Adsorption of gases in multimolecular layers. *J. Am. Chem. Soc.* **60** (1938) 309-319.
- ²¹ M. M. Dubinin. *Progress in surface science and membrane science* (Academic Press, New York, 1975).
- ²² M. M. Dubinin. The potential theory of adsorption of gases and vapors for adsorbents with energetically non-uniform surfaces. *Chem. Rev.* **60** (1960) 235-241.
- ²³ F. Stoeckli. Dubinin's theory for the volume filling of micropores: an historical approach. *Adsorption Science & Technology* **10** (1993) 3-16.
- ²⁴ M. Polanyi. Causes of forces of adsorption. *Z Elektrochem* **26** (1920) 370-374.
- ²⁵ M. Polanyi. Theories of adsorption of gases. General survey and some additional remarks. *Trans. Farad. Soc.* **28** (1932) 316-333.
- ²⁶ M. M. Dubinin, E. D. Zaverina and L. V. Radushkevich. Sorption and structure of active carbons. I. Adsorption of organic vapors. *Zh. Fiz. Khim.* **21** (1947) 1351-1362.
- ²⁷ M. M. Dubinin and E. D. Zaverina. *Zh. Fiz. Khim.* **23** (1949) 1129-1140.
- ²⁸ M. M. Dubinin and L. V. Radushkevich. The equation of the characteristic curve of activated charcoal. *Proc. Acad. Sci. USSR* **55** (1947) 331-333.
-

- ²⁹ M. M. Dubinin. Fundamentals of the theory of adsorption in micropores of carbon adsorbents: Characteristics of their adsorption properties and microporous structures. *Carbon* **27** (1989) 457-467.
- ³⁰ M. M. Dubinin and V. A. Astakhov. Description of adsorption equilibrium of vapors on zeolites over wide ranges of temperatures and pressure. *Adv. Chem. Ser.* **102** (1971) 69-85.
- ³¹ J. W. Patrick. *Porosity in carbons* (Edward Arnold, London, 1995).
- ³² H. F. Stoeckli, P. Rebstein and L. Ballerini. On the assessment of microporosity in active carbons, a comparison of theoretical and experimental data. *Carbon* **28** (1990) 907-909.
- ³³ M. M. Dubinin, G. M. Plavnik and E. D. Zaverina. Integrated study of the porous structure of active carbons from carbonized sucrose. *Carbon* **2** (1964) 261-268.
- ³⁴ F. Stoeckli. Microporous carbons and their characterization: the present state of the art. *Carbon* **28** (1990) 1-6.
- ³⁵ F. Kraehenbuehl, H. F. Stoeckli, A. Addoun, P. Ehrburger and J. B. Donnet. The use of immersion calorimetry in the determination of micropore distribution of carbons in the course of activation. *Carbon* **24** (1986) 483-488.
- ³⁶ D. Burevski. Structural and energetic heterogeneities of microporous active carbons. *Carbon* **35** (1997) 1001-1004.
- ³⁷ M. Polanyi. Theories of adsorption of gases. General survey and some additional remarks. *Trans. Farad. Soc.* **28** (1932) 316-333.
- ³⁸ M. M. Dubinin and E. Zaverina. Charakter der porositats- und sorptionseigenschaften aktiver kohle. *Acta Physicochemica URSS* **4** (1936) 647-674.
- ³⁹ M. M. Dubinin and P. Tomofeyev. Adsorption of vapors on active carbons in relation to the properties of the adsorbate. *Dokl. Akad. Nauk. S.S.S.R.* **54** (1946) 701-704.
- ⁴⁰ Vaskovsky B. A. cited in "M. M. Dubinin and E. D. Zaverina. Adsorption of gases by activated carbons. *Dokl. Akad. Nauk. S.S.S.R.* **72** (1950)".
- ⁴¹ D. B. Macleod. On a relation between surface tension and density. *Trans. Faraday Soc.* **19** (1923) 38-42.
- ⁴² S. Sugden. *The parachor and valency* (George Routledge and Sons Ltd., London, 1930).
-

- ⁴³ O. Exner. Conception and significance of the parachor. *Nature* **196** (1962) 890 - 891.
- ⁴⁴ S. N. Balasubrahmanyam. Einstein, 'parachor' and molecular volume: Some history and a suggestion. *Current Science* **94** (2008) 1650-1658.
- ⁴⁵ G. O. Wood. Affinity coefficients of the Polanyi /Dubinin adsorption isotherm equations. A review with compilations and correlations. *Carbon* **39** (2001) 343–356.
- ⁴⁶ P. J. Reucroft, W. H. Simpson and J. L. A. Sorption properties of activated carbon. *J. Phys. Chem.* **75** (1971) 3526-3531.
- ⁴⁷ K. E. Noll, D. Wang and S. T. Comparison of three methods to predict adsorption isotherms for organic vapors from similar polarity and non similar polarity reference vapors. *Carbon* **27** (1989) 239-245.
- ⁴⁸ A. Golovoy and J. Braslaw. Adsorption of automobile paint solvents on activated carbon I. Equilibrium adsorption of single vapors. *JAPCA* **31** (1981) 861-865.
- ⁴⁹ G. O. Wood. Activated carbon adsorption capacities for vapors. *Carbon* **30** (1992) 593-599.
- ⁵⁰ J. Wu, M. E. Stromqvist, O. Claesson, I. E. Fangmark and L.-G. Hammarstrom. A systematic approach for modelling the affinity coefficient in the Dubinin–Radushkevich equation. *Carbon* **40** (2002) 2587-2596.
- ⁵¹ F. Stoeckli, A. Lavanchy and D. Hugi-Cleary. *Fundamentals of adsorption*. p75 (ed. Meunier F.) (Elsevier, Paris, 1998).
- ⁵² M. G. Kaganer. A method for the determination of specific surfaces from the adsorption of gases. *Proc. Acad. Sci. USSR* **116** (1957) 603-605.
- ⁵³ M. M. Dubinin. Water vapor adsorption and the microporous structures of carbonaceous adsorbents. *Carbon* **18** (1980) 355-364.
- ⁵⁴ B. R. Puri. *Chemistry and physics of carbon* (P. J. Walker, Jr., Marcel Dekker, New York, 1970).
- ⁵⁵ M. M. Dubinin, E. D. Zaverina and V. V. Serpinsky. The sorption of water vapour by active carbon. *J. Chem. Soc. London* **2** (1955) 1760–1766.
- ⁵⁶ M. M. Dubinin and V. V. Serpinsky. Letter to the Editor. Isotherm equation for water vapor adsorption by microporous carbonaceous adsorbents. *Carbon* **19** (1981) 402-403.
-

-
- ⁵⁷ S. S. Barton, M. J. B. Evans and J. A. F. MacDonald. The adsorption of water vapor by porous carbon. *Carbon* **29** (1991) 1099-1105.
- ⁵⁸ S. S. Barton, M. J. B. Evans, S. Liang and J. A. F. Macdonald. The influence of surface modification of BPL carbons on aging. *Carbon* **34** (1996) 975-982.
- ⁵⁹ S. Furmaniak, P. A. Gauden, A. P. Terzyk, R. P. Wesolowski and G. Rychlicki. 151-182 (Universitatis Mariae Curie - Sklodowska, Lublin–Polonia, 2005).
- ⁶⁰ R. L. D'Arcy and I. C. Watt. Analysis of sorption isotherms of non-homogeneous sorbents. *Trans. Faraday Soc.* **66** (1970) 1236 - 1245.
- ⁶¹ S. S. Barton, M. J. B. Evans and J. A. F. MacDonald. Adsorption of water vapor on nonporous carbon. *Langmuir* **10** (1994) 4250–4252.
- ⁶² F. Carrasco-Marin, A. Mueden, T. A. Centeno, F. Stoeckli and C. Moreno-Castilla. Water adsorption on activated carbons with different degrees of oxidation. *J. Chem. Soc., Faraday Trans.* **93** (1997) 2211-2215.
- ⁶³ F. Stoeckli, L. Currit, A. Laederach and T. A. Centeno. Water adsorption in carbons described by the dubinin-astakhov and dubinin-serpinski equations. *J. Chem. Soc., Faraday Trans.* **90** (1994) 3689-3691.
- ⁶⁴ S. Furmaniak, P. A. Gauden, A. P. Terzyk and G. Rychlicki. Water adsorption on carbons — Critical review of the most popular analytical approaches. *Advances in Colloid and Interface Science* **137** (2008) 82-143.
- ⁶⁵ R. C. Bansal, J. B. Donnet and F. Stoeckli. *Active carbon* (Marcel Dekker, New York, 1988).
- ⁶⁶ A. J. Groszek. Characterization of microporous carbons by flow microcalorimetry. *Carbon* **27** (1989) 33-39.
- ⁶⁷ F. Stoeckli, F. Kraehenbuehl and D. Morel. The adsorption of water by active carbons, in relation to the enthalpy of immersion. *Carbon* **21** (1983) 589-591.
- ⁶⁸ F. Kraehenbuehl. *Etude des charbons actifs par la calorimétrie d'immersion et les cinétiques d'adsorption gaz-solide*. PhD thesis. Université de Neuchâtel, Suisse, 1983.
- ⁶⁹ S. S. Barton, M. J. B. Evans and B. H. Harrison. Surface studies on carbon: water adsorption on polyvinylidene chloride carbon. *J. Colloid Interface Sci.* **45** (1973) 542-548.
-

-
- ⁷⁰ S. J. Gregg and J. F. Langford. Evaluation of microporosity, with special reference to a carbon black. *Trans. Faraday Soc.* **65** (1969) 1394-1400.
- ⁷¹ B. C. Lippens and J. H. d. Boer. Studies on pore systems in catalysts : V. The t method. *J. Catalysis* **4** (1965) 319-323.
- ⁷² K. S. W. Sing. *Surface area determination, Proc. Int. Symp. 1969* (ed. D.H. Everett and R.H. Otervill) (Butterworths, London, 1970). p.25
- ⁷³ P. J. M. Carrott, R. A. Roberts and K. S. W. Sing. Standard nitrogen adsorption data for nonporous carbons. *Carbon* **25** (1987) 769-770.
- ⁷⁴ F. Rodriguez-Reinoso, J. M. Martin-Martinez, C. Prado-Burguete and B. McEnaney. A standard adsorption isotherm for the characterization of activated carbons. *J. Phys. Chem.* **91** (1987) 515–516.
- ⁷⁵ P. J. M. Carrott, M. M. L. R. Carrott, I. P. P. Cansado and J. M. V. Nabais. Reference data for the adsorption of benzene on carbon materials. *Carbon* **38** (2000) 465–474.
- ⁷⁶ P. J. M. Carrott, M. M. L. R. Carrott and I. P. P. Cansado. Reference data for the adsorption of methanol on carbon materials. *Carbon* **39** (2001) 193–200.
- ⁷⁷ A. Guillot and F. Stoeckli. Reference isotherm for high pressure adsorption of CO₂ by carbons at 273 K. *Carbon* **39** (2001) 2059–2064.
- ⁷⁸ Website: <http://www.cabot-corp.com/>, accessed 23/10/2007.
- ⁷⁹ Website: <http://www.degussa.com/>, accessed 24/10/2007.
- ⁸⁰ Norit Activated Carbon, Brochure: *Introduction to Norit Activated Carbon*, 2004.
- ⁸¹ H. F. Stoeckli, F. Krähenbühl, A. Lavanchy and U. Huber. The physical and chemical characterization of active carbons. *J. Chimie Physique* **81** (1984) 785-790.
- ⁸² W. N. Reynolds. *Physical properties of graphite* (Elsevier, Amsterdam, 1968).
- ⁸³ B. McEnaney. *Carbon materials for advanced technologies. (Chapter I)* (ed. T. D. Burchell) (Pergamon, Amsterdam, 1999). Chap.1
- ⁸⁴ S. Iijima. Helical microtubules of graphitic carbon. *Nature* **354** (1991) 56-58.
- ⁸⁵ A. Oberlin, M. Endo and T. Koyama. Filamentous growth of carbon through benzene decomposition. *J. Cryst. Growth* **32** (1976) 335-349.
-

-
- ⁸⁶ M. Monthieux and V. L. Kuznetsov. Who should be given the credit for the discovery of carbon nanotubes? *Carbon* **449** (2006) 1621-1623.
- ⁸⁷ L. V. Radushkevich and V. M. Lukyanovich. O strukture ugleroda, obrazujucesja pri termiceskom razlozenii okisi ugleroda na zeleznom kontakte. *Zurn. Fisic. Chim.* **26** (1952) 88-95.
- ⁸⁸ Y. Murakami, Y. Miyauchi, S. Chiashi and S. Maruyama. Direct synthesis of high-quality single-walled carbon nanotubes on silicon and quartz substrates. *Chem. Phys. Lett.* **377** (2003) 49-54.
- ⁸⁹ R. Saito, G. Dresselhaus and M. S. Dresselhaus. Trigonal warping effect of carbon nanotubes. *Phys. Rev. B* **61** (2000) 2981-2990.
- ⁹⁰ M. S. Dresselhaus, G. Dresselhaus and P. Eklund. *Science of fullerenes and carbon nanotubes* (Academic Press, New York, 1996).
- ⁹¹ S. Iijima. Growth of carbon nanotubes. *Mater. Sci. Eng. B* **19** (1993) 172-180.
- ⁹² X. Sun et al. Stacking characteristics of graphene shells in carbon nanotubes. *Phys. Rev. B* **54** (1996) R12629–R12632.
- ⁹³ C. A. Leon y leon and L. R. Radovic. in *Chemistry and physics of carbon* (ed. P. A. Thrower) 215-311 (Marcel Dekker, New York, 1994).
- ⁹⁴ R. A. Smith. The absorption of gases by charcoal. I. *Proceedings of the Royal Society of London. Series A, Containing Papers of a Mathematical and Physical Character* **112** (1926) 296-303.
- ⁹⁵ R. A. Smith. Absorption of gases by charcoal. Part II. On a new series of equivalents or molecules. *Proceedings of the Royal Society of London* **78** (1878-1879) 322-324.
- ⁹⁶ T. F. E. Rhead and R. V. Wheeler. LIII - The mode of combustion of carbon. *J. Chem. Soc., Trans.* **103** (1913) 461 - 489.
- ⁹⁷ U. Hofmann and G. Ohlerich. Oberflachenchemie des Kohlenstoffes. *Angew. Chem.* **62** (1950) 16-21.
- ⁹⁸ M. L. Studebaker, E. W. D. Huffman, A. C. Wolfe and L. G. Nabors. Oxygen-containing groups on the surface of carbon black. *Ind. Eng. Chem.* **48** (1956) 162–166.
-

-
- ⁹⁹ N. R. Laine, F. J. Vastola and P. L. J. Walker. The importance of active surface area in the carbon-oxygen reaction. *J. Phys. Chem.* **67** (1963) 2030–2034.
- ¹⁰⁰ B. R. Puri and R. C. Bansal. Studies in surface chemistry of carbon blacks. Part II. surface acidity in relation to chemisorbed oxygen. *Carbon* **1** (1964) 457-464.
- ¹⁰¹ B. R. Puri and R. C. Bansal. Studies in surface chemistry of carbon blacks. Part I. High temperature evacuation. *Carbon* **1** (1964) 451-455.
- ¹⁰² H.-P. Boehm, E. Diehl and W. Heck. in *Identification of functional groups in surface oxides of carbon*. 2nd International London Carbon and Graphite Conference (ed. Society of Chemical Industry) 369-379 (London, 1966).
- ¹⁰³ J. B. Donnet. The chemical reactivity of carbons. *Carbon* **6** (1968) 161-176.
- ¹⁰⁴ R. Schlögl, M. Che, O. Clause and C. Marchilly. *Preparation of solid catalysts*. (Wiley-VCH, Weinheim, 1999). *Chap. 3 and 4*.
- ¹⁰⁵ A. Sánchez and F. Mondragón. Role of the epoxy group in the heterogeneous CO₂ evolution in carbon oxidation reactions. *J. Phys. Chem. C* **111** (2007) 612-617.
- ¹⁰⁶ I. Sutherland, E. Sheng, R. H. Bradley and P. K. Freakley. Effects of ozone oxidation on carbon black surfaces. *J. Mater. Sci.* **31** (1996) 5651-5655.
- ¹⁰⁷ C. Moreno-Castilla, M. V. Lopez-Ramon and F. Carrasco-Marin. Changes in surface chemistry of activated carbons by wet oxidation. *Carbon* **38** (2000) 1995–2001.
- ¹⁰⁸ H.-P. Boehm. Some aspects of the surface chemistry of carbon blacks and other carbons. *Carbon* **32** (1994) 759-769.
- ¹⁰⁹ H. Valdés, M. Sánchez-Polo, J. Rivera-Utrilla and C. A. Zaror. Effect of ozone treatment on surface properties of activated carbon. *Langmuir* **18** (2002) 2111–2116.
- ¹¹⁰ C. Moreno-Castilla et al. Activated carbon surface modifications by nitric acid, hydrogen peroxide, and ammonium peroxydisulfate treatments. *Langmuir* **11** (1995) 4386-4392.
- ¹¹¹ Z. Wu, C. U. Pittman Jr. and S. D. Gardner. Nitric acid oxidation of carbon fibers and the effects of subsequent treatment in refluxing aqueous NaOH. *Carbon* **33** (1995) 597-605.
- ¹¹² J. L. Figueiredo, M. F. R. Pereira, M. M. A. Freitas and J. J. M. Orfao. Modification of the surface chemistry of activated carbons. *Carbon* **37** (1999) 1379–1389.
-

-
- ¹¹³ G. de la Puente, J. J. Pis, J. A. Menendez and P. Grange. Thermal stability of oxygenated functions in activated carbons. *J. Anal. Appl. Pyrol.* **43** (1997) 125-138.
- ¹¹⁴ M. F. R. Pereira, S. F. Soares, J. J. M. Órfão and J. L. Figueiredo. Adsorption of dyes on activated carbons: influence of surface chemical groups. *Carbon* **41** (2003) 811–821.
- ¹¹⁵ J.-H. Zhou et al. Characterization of surface oxygen complexes on carbon nanofibers by TPD, XPS and FT-IR. *Carbon* **45** (2007) 785–796.
- ¹¹⁶ U. Zielke, K. J. Hüttinger and W. P. Hoffman. Surface-oxidized carbon fibers: I. Surface structure and chemistry. *Carbon* **34** (1996) 983-998.
- ¹¹⁷ Y. Otake and R. G. Jenkins. Characterization of oxygen-containing surface complexes created on a microporous carbon by air and nitric acid treatment. *Carbon* **31** (1993) 109-121.
- ¹¹⁸ B. Marchon, J. Carrazza, H. Heinemann and G. A. Somorjai. TPD and XPS studies of O₂, CO₂, and H₂O adsorption on clean polycrystalline graphite. *Carbon* **26** (1988) 507-514.
- ¹¹⁹ Q.-L. Zhuang, T. Kyotani and A. Tomita. DRIFT and TK/TPD analyses of surface oxygen complexes formed during carbon gasification. *Energy & fuels* **8** (1994) 714-718.
- ¹²⁰ E. Papirer, S. Li and J. B. Donnet. Contribution to the study of basic surface groups on carbons. *Carbon* **25** (1987) 243-247.
- ¹²¹ C. Moreno-Castilla, F. Carrasco-Marín, F. J. Maldonado-Hódar and J. Rivera-Utrilla. Effects of non-oxidant and oxidant acid treatments on the surface properties of an activated carbon with very low ash content. *Carbon* **36** (1998) 145-151.
- ¹²² Q.-L. Zhuang, T. Kyotani and A. Tomita. in *Carbon '94* 466 (Granada, Spain, 1994). p.466
- ¹²³ H. P. Boehm, E. Diehl, W. Heck and R. Sappok. Surface oxides of carbon. *Angew. Chem., Int. Ed. Engl.* **3** (1964) 669-678.
- ¹²⁴ H. P. Boehm. *Graphite and precursors. (p141–178)* (ed. P. Delhaës) (Gordon and Breach, Amsterdam, 2001). p.141-178
- ¹²⁵ G. Beamson and D. Briggs. *High resolution XPS of organic polymers* (John Wiley and Sons, Chichester, U.K., 1992).
- ¹²⁶ C. Kozłowski and P. M. A. Sherwood. X-ray photoelectron-spectroscopic studies of carbon-fibre surfaces. Part 5.—The effect of pH on surface oxidation. *J. Chem. Soc., Faraday Trans. 1* **81** (1985) 2745 - 2756.
-

- ¹²⁷ C. Kozlowski and P. M. A. Sherwood. X-ray photoelectron spectroscopic studies of carbon fiber surfaces VIII—A comparison of type I and type II fibers and their interaction with thin resin films. *Carbon* **25** (1987) 751-760.
- ¹²⁸ Y. Xie and P. M. A. Sherwood. X-ray photoelectron spectroscopic studies of carbon fibers. Part XIV: Electrochemical treatment of pitch-based fibers and the surface and bulk structure changes monitored by XPS, XRD, and SEM. *Appl. Spectrosc.* **44** (1990) 1621-1628.

3

Chapter 3 Experimental

3.1 Adsorption measurement

3.1.1 Isotherm measurement by gravimetric method

The gravimetric method also known as McBain method [¹] is based on the adsorbent weight increase during adsorption experiment. The adsorption isotherm is determined by measuring the amount adsorbed as a function of the equilibrium pressure p/p_0 for a given temperature T . This technique has been used to measure the adsorption isotherms of water, carbon dioxide, toluene and alcohols (methanol, ethanol and isopropanol) at different temperature. Adsorption measurements of gases and vapours have been carried out using the IGA (Intelligent Gravimetric Analyser) (Hiden Isochema, UK). The IGA, represented in Figure 3.1, is a fully automated gravimetric system in which the environment around the sample is actively controlled over a wide range of conditions. This system is housed in a stainless steel vessel allowing temperature of the sample between -196°C and 500°C).

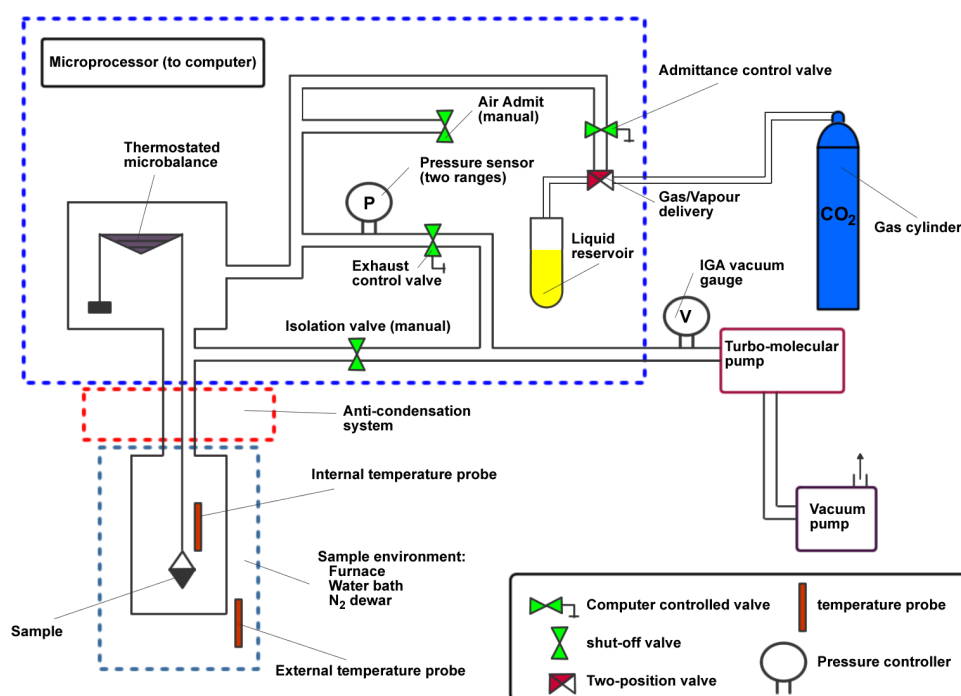


Figure 3.1: Schematic diagram of the IGA (Intelligent Gravimetric Analyser).

The sample to characterise is placed inside a metallic mesh nacelle that is suspended from a microbalance with a very thin chain. Before each experiment, samples are outgassed at the required temperature with a furnace (Severn Furnace Ltd, UK) specially designed to accommodate the stainless steel vessel. The degassing is carried out until the weight becomes constant (usually between 2 and 4 h or longer for high temperature) in a residual vacuum better than 10^{-6} mbar. The vacuum system is composed of primary diaphragm vacuum pump (Vacubrand, Germany) connected in serial with a turbo molecular pump (Balzers Pfeiffer, Germany). A vacuum better than 10^{-7} mbar can be achieved at the sample position and is monitored with a compact full range gauge (Balzers, Germany) having a pressure range up to 1 bar. The sample temperature is maintained constant ($\pm 0.05^\circ\text{C}$) during adsorption/desorption runs using a recirculating water bath (Lauda Ecoline RE 104, Germany).

The vapour adsorptive or gas is then injected into the system. After the pressure change and at constant temperature, the gravimetric analyser determines in real-time the

equilibrium mass uptake and kinetics parameter. The isotherm plot is built with these equilibrium values.

On the other hand, all the adsorption isotherms for nitrogen at 77°K were measured using the Micromeritics ASAP 2010 volumetric apparatus (Micromeritics, UK) after outgassing as above.

3.2 Immersion calorimetry

Immersion calorimetry consists in the determination of the enthalpy of immersion $-AH_i$ (J/g or mJ/m²) obtained from the heat release during the immersion of a solid in a liquid (or a mixture of liquid). This technique is a complementary technique to adsorption method in the characterisation of surfaces and provide information about surface area (external and internal), porosity distribution (by employing molecular probes) [2] and surface chemistry [3][4][5].

Immersion calorimetry experiments have been carried out at room temperature (24.6°C ± 0.01°C) using a C80 II Calvet type calorimeter (Setaram, France) shown in Figure 3.2 a).

In that case, the most reproducible and simplest method to get the immersion heat is to use sealed glass ampoule as described by Harkins and Jura [6] and Partyka et al. [7]. This method is based on the preparation of a glass ampoule with a brittle end. Thus, it is also possible, prior to the immersion, to do pre heat treatment during the degassing of the sample in order to clean the surface or remove surface groups for example. The immersion cell containing the glass ampoule is detailed in Figure 3.2 b).

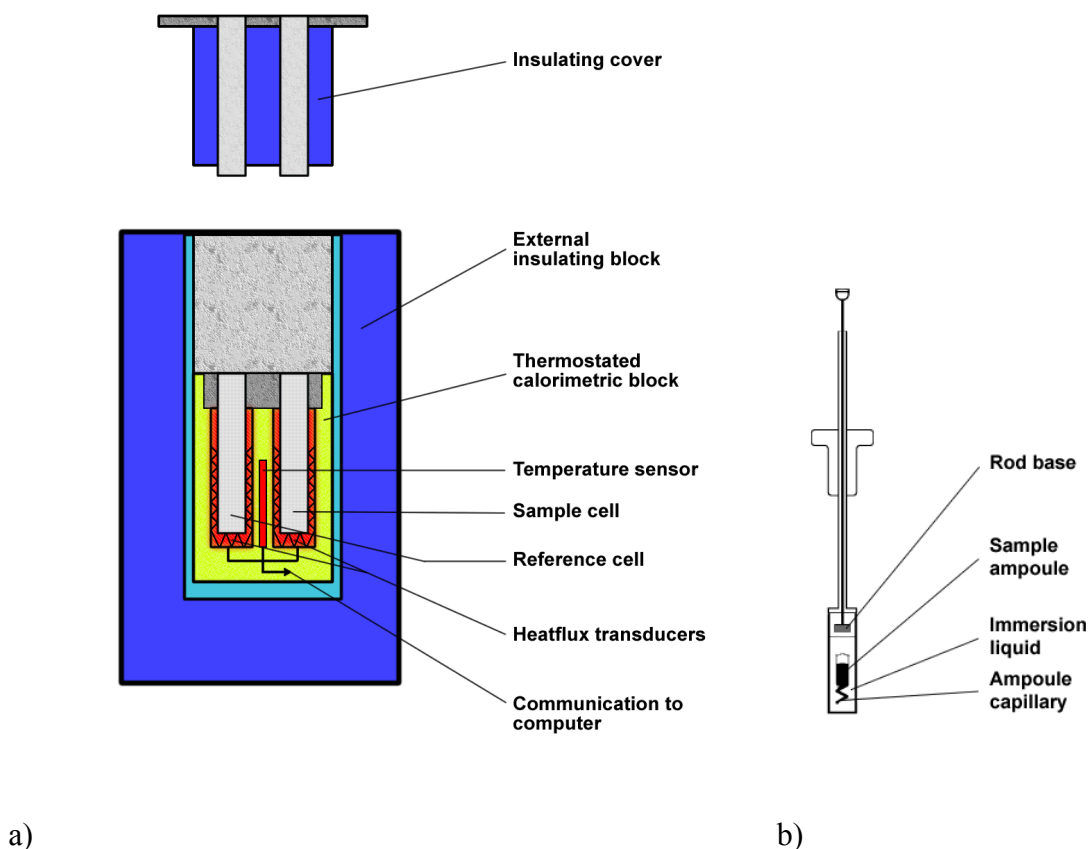


Figure 3.2: Schematic representation of: a) the C80 II Tian-Calvet type calorimeter and b) the immersion cell containing the ampoule used to determine enthalpies of immersion.

3.2.1 Measure of enthalpy of immersion

The first step before the immersion is to outgas the sample. At this effect, 0.2 g of solid is introduced in a glass ampoule and then the sample is outgassed in a vacuum of $10^{-3} \sim 10^{-2}$ mbar for 2 hours. Finally the ampoule is sealed using a butane/propane compact blowlamp (Taymar, UK). The weight loss after the degassing is usually negligible.

The ampoule is then placed in the immersion cell containing 7 mL of the test wetting liquid. Once thermally equilibrated at 24.6°C inside the calorimeter chamber, the capillary of the ampoule is gently broken by pushing down the metal rod. This allows the sample immersion to take place as the liquid will vaporise due to the pressure difference and will then penetrate inside the glass ampoule. The heat flow rise, due to the

immersion, is measured by a thermistor and recorded as a thermogram (Figure 3.3) from which $-\Delta H_i$ (J/g) is automatically calculated using Eq. 3.1.

$$-\Delta H_i(\text{exp}) = \frac{E}{m} = \frac{\int_0^t P \cdot dt}{m} \quad \text{Eq. 3.1}$$

where E is the peak area in mJ (mW.s) and m is the sample weight in g.

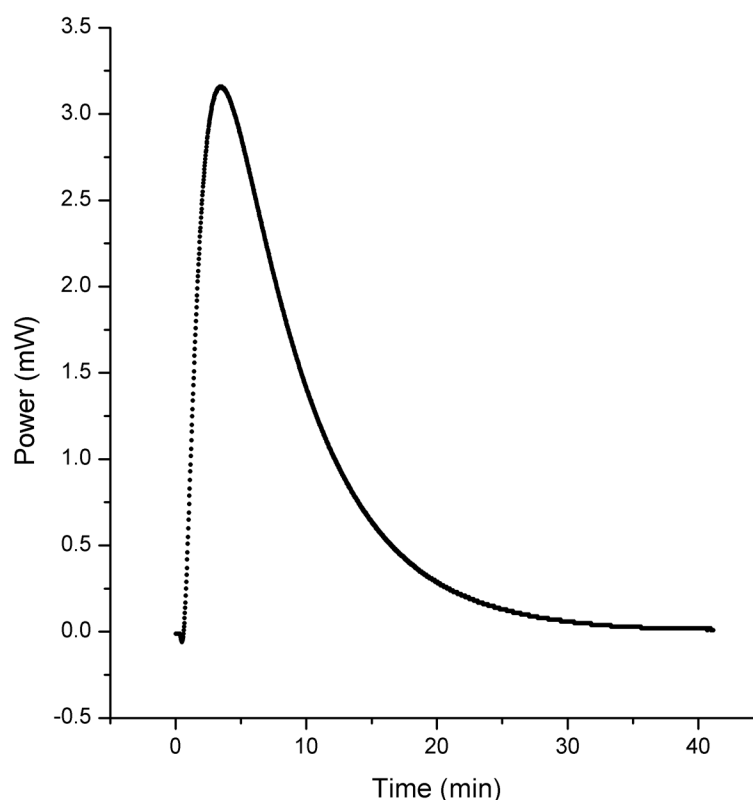


Figure 3.3: Characteristic thermogram of a measure of enthalpy of immersion. (Sample: CB N330 O₃ 30min in isopropanol).

The heat terms due to both the breakage of the brittle end and the vaporisation of the liquid inside the ampoule have usually small contributions to the experimentally

measured heat. But in order to correct rigorously the sample experiment, it is possible to subtract a blank experiment realised with one empty ampoule.

Another way to reduce the effect of the breakage is to have a very brittle end in order to minimize the energy needed to break it. This reason led us to make our own glass ampoule because it was found that the ampoules available commercially were very difficult to break and expensive as well (see Figure 3.4). The energy resulting from the breakage of the commercial ampoule is around 300 mJ whereas for the in-house prepared ampoule, this value drops to 80~90 mJ.

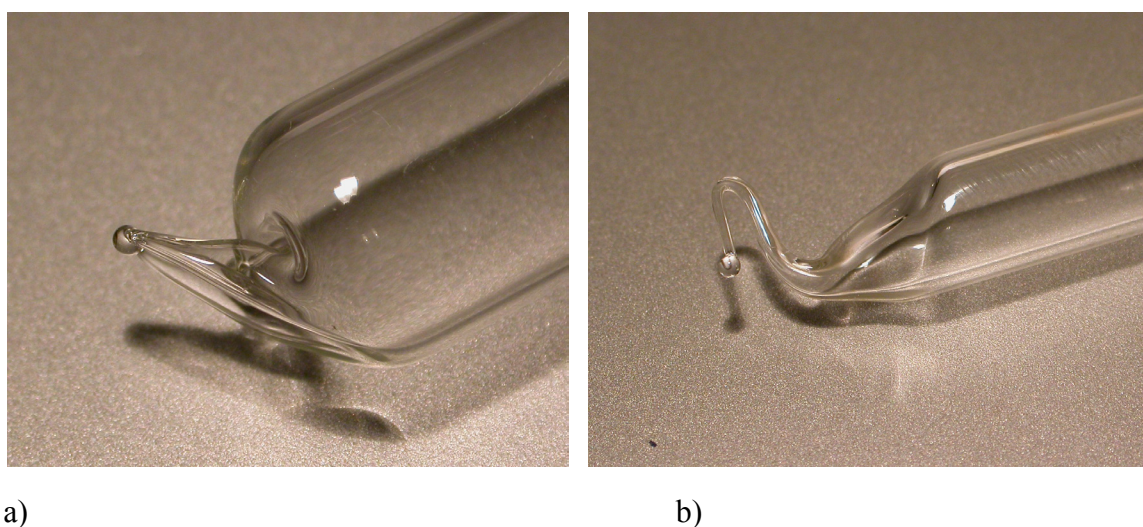


Figure 3.4: Photographs of a) commercial ampoule and b) lab-made glass ampoule with thin capillary.

The procedure to make glass ampoule with thin capillary is detailed in Appendix A.

3.3 X-ray photoelectron spectroscopy (XPS)

3.3.1 Theoretical principle of XPS technique

Surface analysis by XPS is realised by irradiating a material with a beam of monochromatic or polychromatic X-rays and by measure of the energy of emitted electrons. The X-ray sources such as $\text{MgK}\alpha$ (1253.6 eV) or $\text{AlK}\alpha$ (1286.6 eV) are

generally used. The photons which enter the solid interact with the surface atoms of the material (penetration depth 1~10 nm) and electrons are emitted by photoelectric effect.

Because the energy of a particular wavelength equals a known quantity, the kinetic energy of the ejected electrons can be determined using the following equation that is based on the work of Rutherford (1914) [⁸][⁹]:

$$E_K = h \cdot \nu - E_B - \Phi_S \qquad \text{Eq. 3.2}$$

Where E_K is the kinetic energy of the emitted electron, $h \cdot \nu$ is the energy of the incident photon, E_B is the binding energy to the atomic orbital where the emitted electron comes from and Φ_S is the extraction work of the electrons of the sample.

In the case of a solid, binding energy is defined in respect to the Fermi level. The sample and spectrometer being at the same potential, their Fermi levels are equal. So the extraction work of the sample squares with the extraction work of the spectrometer and represents the energy necessary to bring one Fermi level electron to the vacuum level.

During the photo-electronic process, photoelectrons are emitted but Auger electrons can also be ejected as seen in the Figure 3.5.

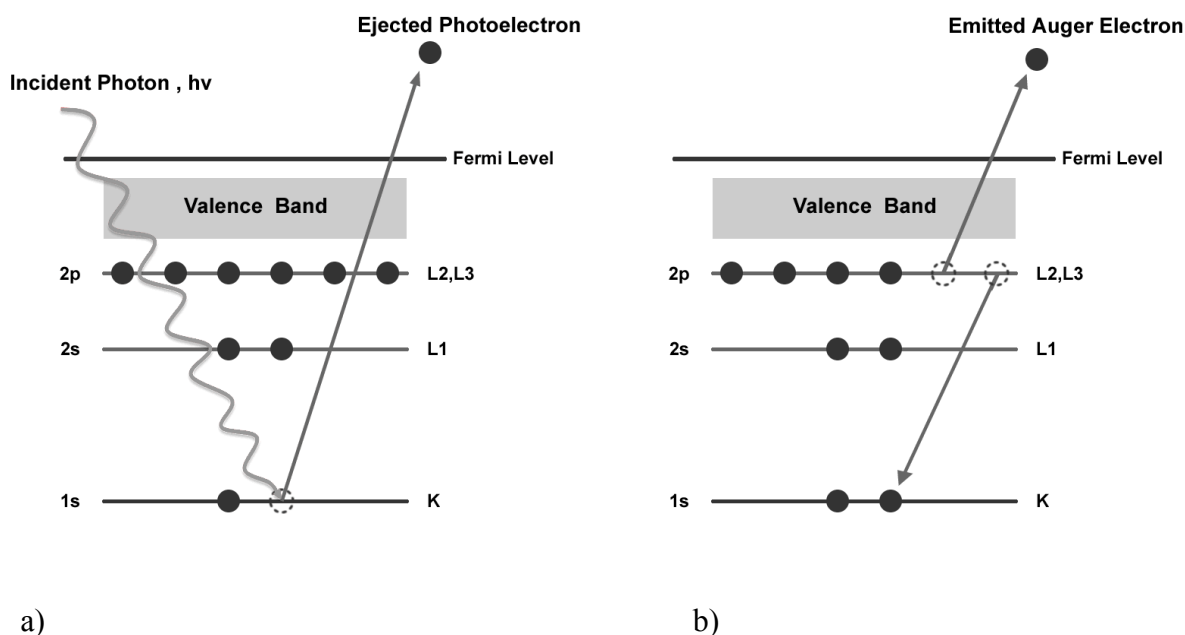


Figure 3.5: a) Atomic model for the XPS emission process. An incoming photon causes the ejection of the photoelectron. b) Atomic model for the relaxation process resulting in the emission of a 2p auger electron. The instantaneous rearrangement of atomic levels results in a final state with two electrons vacancies on the L2,3 or 2p level.

This type of emission occurs 10^{-14} second after the photoelectronic effect. In the Auger process, an outer shell electron comes to fill core state hole (“gap”) just created by the emitted photoelectron. In the same time, one Auger electron is simultaneously ejected. Its kinetic energy is equal to the difference between the energy of the initial ion (excited ion decaying) and the final ion (doubly charged ion) which has been ionised twice.

So photoionisation leads to emission of two electrons, one photoelectron and one Auger electron. The sum of the energy of both emitted electrons cannot exceed the energy of the photon which is the source of the ionisation.

3.3.2 Electron interaction with matter

The probabilities of interaction of electrons with matter are greater than those of photons. The mean free path of one photon in matter is micrometer order whereas it is nanometre

order for the electron. So it is possible to ionise one atom within 10 micrometer depth. Therefore, only electrons coming from the first nanometres of the material surface could be extracted without energy loss. Those electrons that leave the surface without energy loss are the most useful and are responsible for the peaks measured in XPS spectra.

3.3.3 Quantification of XPS

After a qualitative analysis of the XPS spectra, it is important to determine the relative concentrations of the different chemical elements present in the sample. Methods, using the area under the XPS peaks and its height, have been developed. For a homogeneous sample, the intensity of the peak associated to the element i is given by the relation:

$$I_i = N_i \cdot J_0 \cdot \sigma_i \cdot (h \cdot \nu) \cdot \lambda_i \cdot \cos \theta \cdot T_i \quad \text{Eq. 3.3}$$

where N_i is the number of atoms of element i per cm^3 , J_0 is the flux of X-rays per unit area ($\text{photon}/(\text{cm}^2 \cdot \text{s})$), $\sigma_i(h \cdot \nu)$ is the photoelectron cross-section (from the relevant inner shell per atom of i by a photon energy $h \cdot \nu$ for emission of a photoelectron), λ_i is the inelastic mean free path of electron extracted from element i , θ_{emi} is the angle of emission from the surface normal and T_i is the analyser transmission (for element i).

From Eq. 3.3, one may write:

$$N_i = \frac{I_i}{J_0 \cdot \sigma_i \cdot (h \cdot \nu) \cdot \lambda_i \cdot \cos \theta_{emi} \cdot T_i} \quad \text{Eq. 3.4}$$

The denominator of this equation is usually defined as the relative sensitivity factor of element i , S_i :

$$S_i = J_0 \cdot \sigma_i \cdot (h \cdot \nu) \cdot \lambda_i \cdot \cos \theta_{emi} \cdot T_i \quad \text{Eq. 3.5}$$

By measuring the ratio of intensities of peaks associated to both chemical elements A and B , one can access to the ratio of elemental concentration with the relation:

$$\frac{N_A}{N_B} = \frac{I_A}{I_B} \cdot \left(\frac{S_B}{S_A} \right) \quad \text{Eq. 3.6}$$

This expression can be used in the case of homogeneous samples if the ratio S_A/S_B is independent of the materials' matrix. $\sigma_i \cdot (h \cdot \nu)$ and λ_i are often changing from one material to another one, but the ratios $\sigma_A \cdot (h \cdot \nu) / \sigma_B \cdot (h \cdot \nu)$ and λ_A/λ_B remain equals.

So for any spectrometer, it is possible to calculate a group a relative values of S_i for all the elements.

A general relation to determine the atomic fraction of any element can be written as an extension of the last equation:

$$C_x = \frac{N_x}{\sum_i N_i} = \frac{I_x/S_x}{\sum_i I_i/S_i} \quad \text{Eq. 3.7}$$

where C_x is the atomic fraction of the element x .

The values of sensitivity factor S_i are based on measures and calculations of peak area, spectrometer characteristics and transmission function. These values can be found in the Kratos user manual but also in the literature with for example the tables of Scofield and Wagner [¹⁰].

Practically, analysis of XPS spectra is only semi-quantitative due to extreme sensitivity of electron emission to surface state. As an example, typical XPS spectra from a multi-walled carbon nanotube sample (both survey scan and narrow scans of carbon and oxygen elements) are represented in Figure 3.6.

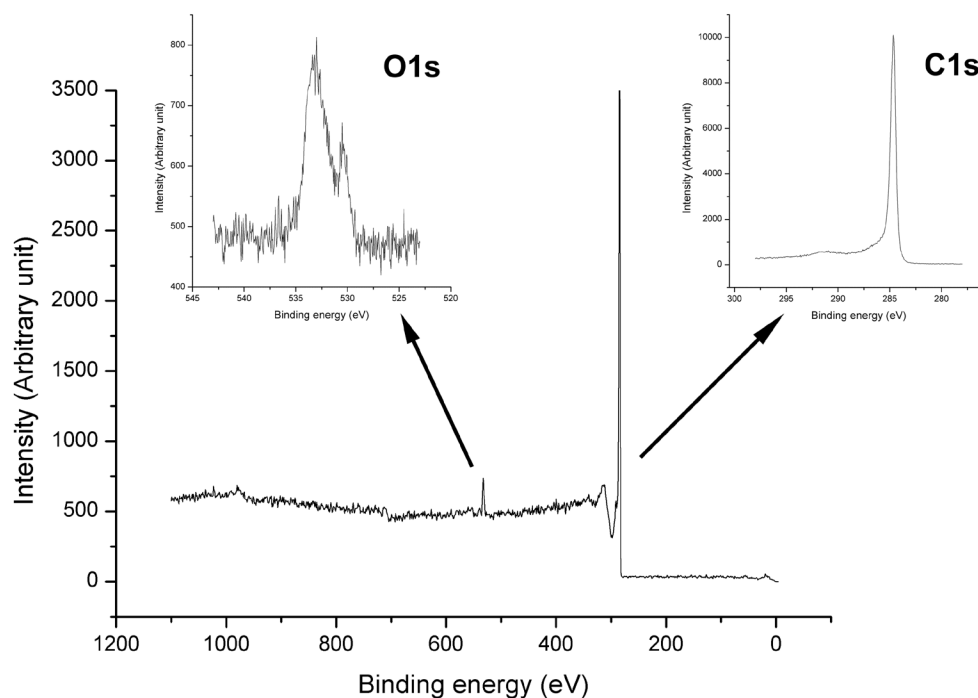


Figure 3.6: Typical X-ray photoelectron survey spectrum of multi walled carbon nanotubes as-produced excited by Al $K\alpha$ (1486.6 eV). Are also represented the narrow scans for oxygen and carbon element, O1s and C1s peaks respectively.

3.3.4 Instrumentation

Surface chemical composition of carbon materials were measured by X-ray photoelectron spectroscopy (XPS) using a Kratos Axis Hsi 5-channel instrument (Kratos Analytical Ltd, UK) with monochromatic Al $K\alpha$ (1486.6 eV) X-rays. In addition, the charge neutralizer was used to minimize the surface charge accumulation in the case of insulating samples. The photograph and schematic diagram of the XPS apparatus used for this work is represented in Figure 3.7 and Figure 3.8 respectively.

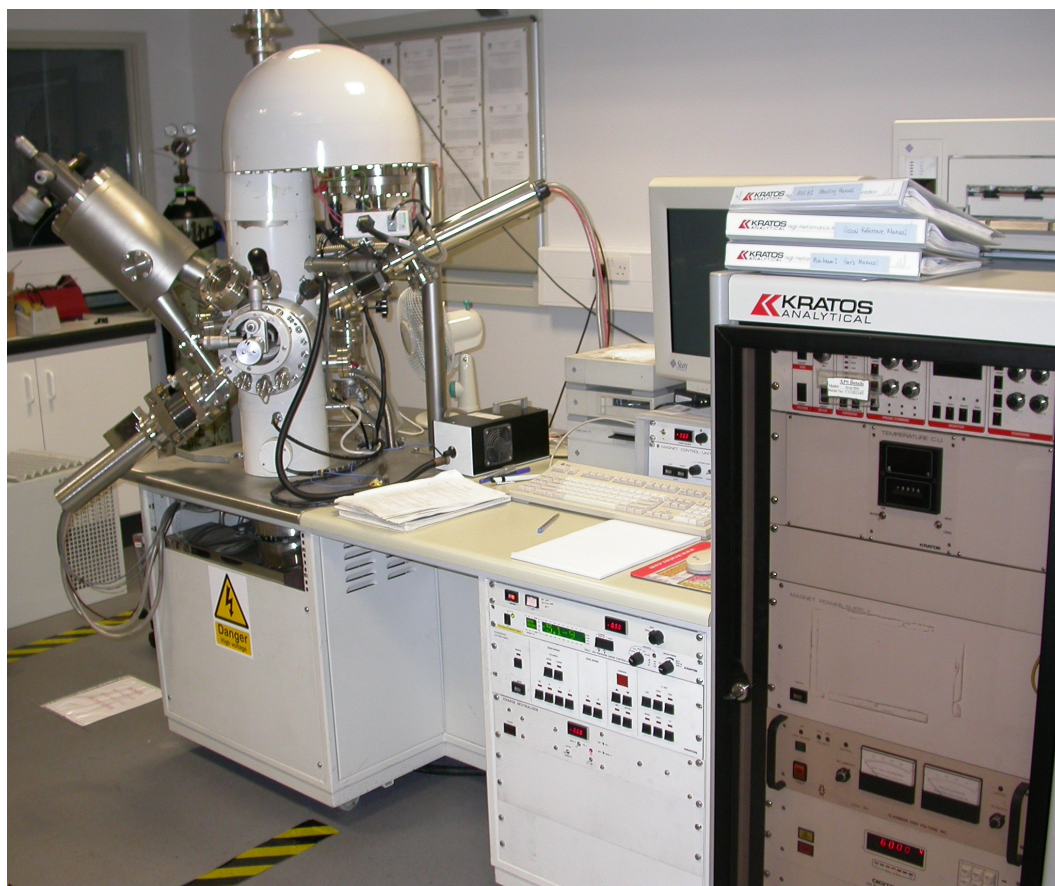


Figure 3.7: Photograph of the XPS apparatus used in this work.

An XPS instrument consists in three main components: an X-ray source (preferably monochromatic), an energy analyser and an electron detector containing a multiplier, amplifier and ratemeter. The analysis chamber is maintained permanently under ultra high vacuum (better than 10^{-9} mbar) via a turbo molecular pump and an ion pump, to avoid any obstruction to be present on the path of the emitted electrons.

As mentioned before, the most common X-ray sources used in commercial XPS systems are the $\text{AlK}\alpha$ (1486.6 eV, width 0.85 eV) and $\text{MgK}\alpha$ (1253.6 eV, width 0.70 eV). In our system, monochromatic $\text{AlK}\alpha$ X-rays operated at 135 W (emission current of 10 mA with a corresponding voltage of 13.5 kV) have been used.

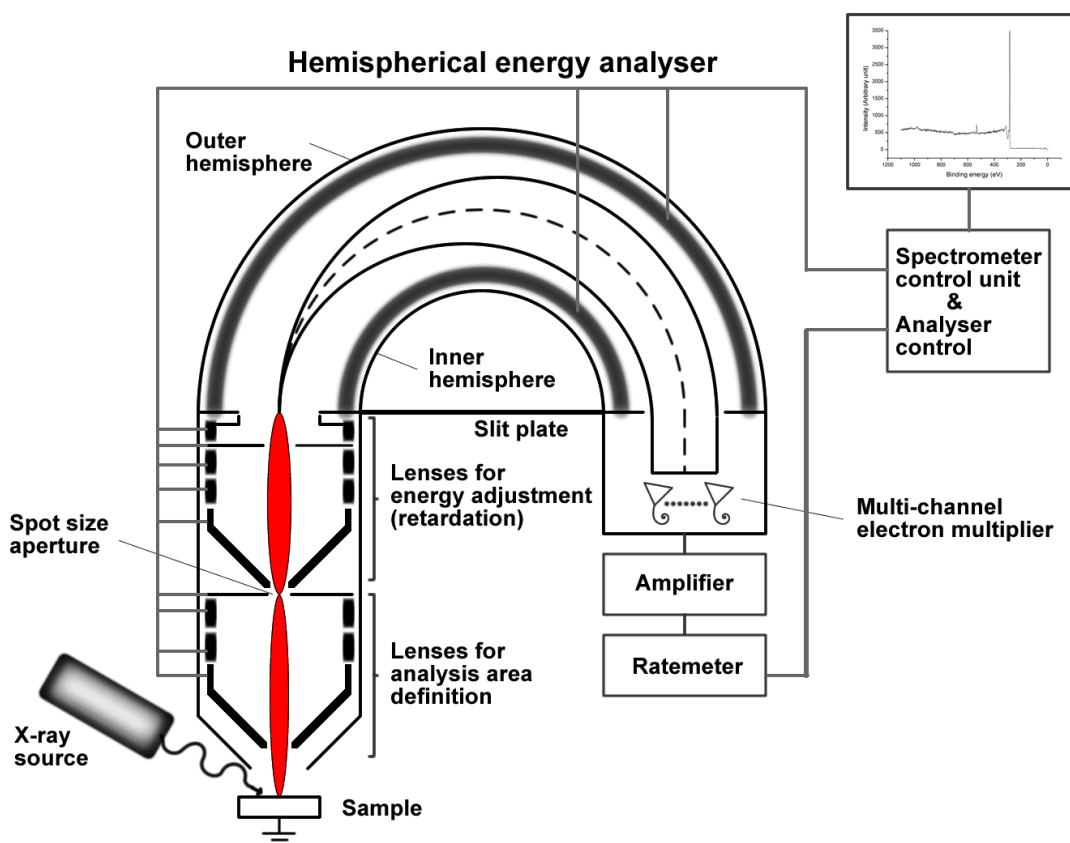


Figure 3.8: Schematic diagram of the Kratos Hsi Axis spectrometer.

The scanning and adjustment of electron kinetic energy is achieved with a series of lenses. Each lens has an electrode and by varying the voltage of this electrode, electrons with different kinetic energies are allowed to reach the energy analyser. Two operating modes exist: fixed retarding ratio (FRR) and fixed analyser transmission (FAT). The last mode was used in this work. In this mode, the electrons are slowed down in order to enter the energy analyser with an energy equal to the pass energy which is fixed in this case.

The hemispherical energy analyser consists of two concentric hemispheres with a potential difference between them. It allows only electrons with the desired kinetic energy (pass energy) to go through and reach the multi-channel electron multiplier at the

other end. The widths of the entrance and exit slits determine the energy resolution of this analyser.

The electron detection is realised by the channeltron type electron multiplier placed just after the exit slit of the analyser. Each pulse will be amplified before to be transmitted to an external conventional pulse counting electronics and then into the computer. The photoelectron spectrum is built from the electron pulse counted against analyser-lenses voltage. The analyser and lenses voltage are also controlled by the computer.

The reproducibility of XPS is usually within $\pm 5\%$ and in addition, for each sample, the measurements were taken at three different places and the mean values were used for the quantification results. This allows an extremely accurate and reliable comparison of data and trends.

3.3.5 Design and manufacture of XPS stubs for granular and powered samples

XPS is a highly surface sensitive technique and for that reason samples which have not been subjected to contamination after processing, mounting, preparation or sample handling (which is the principal source of contamination) are necessary to obtain the maximum information.

Regarding the mounting of the carbon material samples, different mounting techniques and stubs can be used depending of the size and characteristic of the sample. The most common stub for the Axis Hsi instrument is the flat 15mm diameter stainless steel stub. This stub is generally the preferred choice for sample mounting (most thin flat samples) and has been used to analyse graphite sample and the first activated carbon granules and carbon black powder. The graphite sample can be attached to the stub with double sided adhesive tape (high vacuum adhesive tape manufactured by 3M, UK). Analysis in the $10^{-9}\sim 10^{-8}$ mbar range was possible and the outgassing has not been found

to be problem. But the preferred method is to use standard stub with metal retaining clip (as shown in Figure 3.9) to avoid any contamination or charging issue.



Figure 3.9: Standard stub with additional metal retaining clip.

Regarding the analysis of carbon material in granule or powder form such as activated carbon (hard granules), carbon black (powder or easy to break granules), the initial analysis has been done by pressing the sample onto double sided tape and shaking to remove loose material. This method to analyse these kinds of powdered samples was found to be inadequate due to the contamination or background of the tape during analysis, pressure rising due to the deterioration/degassing of the tape by the X-rays and loose attachment of the granules on the stub (lots of empty spaces between the granules). So for all these reasons, a new stub was designed and manufactured in-house by the RGU workshop technicians from standard Kratos stubs. These stubs include a conic hole in the middle to accommodate the powder or granules as shown in Figure 3.10. The results obtained were of better quality with no background spectra from the tape (i.e. Si peaks).



Figure 3.10: New designed stub for granular and powdered samples.

However, for both method described above, the outgassing stage of this kind of sample represents a major risk for the machine if it is not carried out properly. This depressurisation during the degassing has to be carried out very slowly in order to avoid damage to the turbo molecular pump which is at this stage, particularly vulnerable (turbine blades and bearings) to fine powders [11].

Concerning the carbon fibres, they can be mounted as a thick bundle above a standard stub with a screw top ring or as a group of fibres above a hole drilled in the centre of the stub to minimize background signal from the stub surface. An alternative mounting of fibres exists but is rarely used.

3.4 Thermogravimetry analysis (TGA)

Thermogravimetry Analysis (TGA) is part of the family of thermal analysis techniques. TGA provides quantitative measurement of weight change in the carbon material as a function of temperature (or time if temperature increase rate is constant). The technique can characterise materials that lose or gain mass due to decomposition, oxidation or loss of volatiles such as water molecules.

Our TGA analyses were determined using the IGA gravimetric system described before. A 50 mg sample was introduced into a metallic nacelle suspended to a microbalance. Then, the sample was heated up 450°C at a rate of 1°C/min under a residual vacuum of $10^{-8}\sim 10^{-7}$ mbar. This high vacuum needs to be sustained throughout the course of the experiment in order to avoid oxidation of the sample. This can also be done by heating the sample with a continuous flow of inert gas such as nitrogen or argon). The weight of the sample is recorded until it reaches a constant weight, then the weight loss can be determined for each temperature range.

3.5 Microscopy Techniques

On most of the studies looking at characterisation of solid surface such as surface structure and porosity, different kinds of microscopy are usually being used. In the case of carbon materials (especially for activated carbon fibres (or clothes) (ACF)), from the literature, SEM is the most common technique due to its lower cost compared to other instruments. For example, Oya et al. [12] have observed the mesoporosity of certain ACFs. Brasquet et al. [13] have correlated observations obtained on ACFs by SEM and AFM with adsorption data. SEM was also used by Alcaniz-Monge et al. [14] to compare porosity of activated carbon fibres prepared by CO₂ and steam activation.

TEM is another microscopy technique relatively used to characterise carbon fibres and nanotubes offering a better resolution than SEM. In the 90s, Huttepain and Oberlin [15] managed to observe the slit shape of micropores of activated carbon samples using HRTEM. Few years later, Oshida et al. [16] made significant progress in pore structure determination of ACF materials using HRTEM combined with computer image processing. Marsh and Rodriguez-Reinoso [17] published a good review focused on the use of SEM and TEM to observe the structure of activated carbon materials.

However, the atomic force microscopy (AFM) and scanning tunnelling microscopy (STM) which are more recent techniques have been very little used for carbon material

characterisation with the huge exceptions of nanotubes which have been extensively described using this technique [18]. It is possible to do 3D nanotopography and morphology profiles of the nanostructure and to obtain as well dispersability and homogeneity information of the CNTs.

Regarding activated carbon and carbon black materials, very few studies include data and images from AFM characterisation. This can be explained in first instance by technical difficulties due to the morphology of the sample. It is relatively easier to observe flat surface such as graphite or even carbon fibre. In 1998, Stoeckli et al. [19] compared structural data derived from adsorption and immersion techniques to direct observation of the surface by AFM and STM. They also considered the relation with the fractal character D of the surface [20]. This very small number of studies is also true in the case of SEM studies for carbon black materials [21] as confirmed by the very low hits (“SEM OR *Scanning Electron Microscopy*” AND “*Carbon Black*”) when searching on Science-Direct/Elsevier and other online databases.

In this work, AFM images of graphite, both untreated and oxidised are shown but observations of activated carbon and carbon black materials were unsuccessful due to the non flatness and roughness of the samples. On the other hand, SEM micrographs of activated carbon, carbon black and carbon nanotubes which have been used in this study will also be presented. Finally, HRTEM images of mainly carbon nanotubes, which were realised externally, will also be shown in this work.

3.5.1 Scanning Electron Microscopy (SEM)

Scanning Electron Microscopy (SEM) is a widely used technique in materials science. It gives information about the morphology and topography of solid surfaces that is necessary for a better understanding of the surface behaviour or for deductions of structural significance [22][23]. The wave nature of the electron is exploited to get a much

better resolution than in optical microscopy. The microscope used in this work was the LEO S430 digital SEM located in the School of Life Sciences.

A beam of electrons, emitted from the filament in the electron gun, is accelerated towards the specimen and finely focused by the condenser lenses into a fine probe that is rastered over the specimen surface. A high vacuum is maintained inside the SEM column and analysis chamber to allow a smooth (unaccidented) travel for the electrons composing the beam. As the focused beam strikes each point of the sample, numerous interactions occur between the electrons from the beam and the sample atoms. As a result, electrons are emitted from the first few nm of the surface and are then collected by the detectors. Two types of electrons are emitted: secondary electrons which are low energy electrons (< 50 eV) and ejected at random angles, primary electrons (or backscattered electrons) which escape the surface without losing much of their original energy.

In our case, the secondary electron detector has been used to create the image. At each point of the sample, the detector counts the number of electrons emitted from the spot and the result is displayed as a point on the screen. These results are collected sequentially and displayed to give a magnified image of the sample. Under ideal conditions, the resolution of SEM lies in the range of 2 to 10 nm and it can operate at magnification that may exceed 300,000x.

The resulting image is similar to ordinary photograph due shadows and perspective. One other advantage is the great depth of focus allowing rough surfaces to be imaged in sharp focus.

SEM is one of the most important techniques used to study and elucidate the surface features and structure of carbon materials [17] and is usually used in conjunction with other imaging techniques such as atomic force microscopy (AFM), scanning tunnelling microscopy (STM) or transmission electron microscopy (TEM) as described in the next sub-chapters. Applications of scanning electron microscopy includes measures of carbon fibre diameters and studies of the fracture surface of carbon fibre composites, influence

of oxidation or heat treatment on surface morphology of carbon materials, growth of carbon nanotubes [24].

3.5.2 High Resolution Transmission Electron Microscopy (HRTEM)

High resolution transmission electron microscopy (HRTEM) is a unique technique for directly imaging crystallographic structures at an atomic scale and can be defined as a special imaging mode of the TEM. This technique has always been extensively used in materials science [25]. Regarding the field of carbon materials, it can be used for example to observe the shape of carbon nanotube or fullerene, their structures, number of wall layers forming a MWCNT, and defects on the graphitic surfaces.

As a brief description, a TEM operates on the same basic principles of a light microscope but using electron instead of light. Therefore it has a significantly higher resolution due to the small wavelength of the electron. Typically, a TEM is composed of three main components: a vacuum system, an electron source which emits the electron stream and a series of electromagnetic lenses to allow the operator to focus the electrons into a very thin beam. The electron beam travels through the ultra thin specimen. Interaction with the specimen occurs as the electrons pass through. Depending on the material, some of the electrons are scattered and lost in the chamber. The other ones, the unscattered electrons, are transmitted through the sample and will reach and hit the imaging device such as a fluorescent screen or a sensor type CCD camera. After magnification and focus adjustments, this will give rise to an image which will also depend on the imaging mode. The most common TEM imaging method [26] is the bright field imaging mode but in our case, all our images were obtained in “*phase contrast mode*” as HRTEM equipment was used.

The HRTEM images of our samples of carbon black and carbon nanotubes presented in this work have been produced by Prof W. Zhou from the Electron Microscopy Group at University of St Andrews (collaboration with Advanced Materials

Group at The Robert Gordon University (RGU)) using the Jeol JEM 2011 HRTEM. This group has substantial experiences of research in the field of nanoscale carbon materials and in the last 10 years, Prof. W. Zhou has published many papers in this topic, including detailed structures of CNT-like carbon fibres and their field emission properties [²⁷][²⁸], CNT-supported catalysts [²⁹] and recently study of the preferential growth of buckminsterfullerene (*C60*) nanowires [³⁰]. The microscope used to observe our samples was the high resolution transmission electron microscope JEOL JEM-2011 which has a resolution of 0.18 nm with a magnification of up to 1,200,000x.

3.5.3 Atomic Force Microscopy (AFM)

Atomic force microscopy is a high resolution form of scanning probe microscopy where sub-nanometre resolution can be attained. The first AFM was developed by Binnig, Quate and Gerber in 1986 [³¹]. In the same year, Binnig and Rohrer earned the Nobel Prize for Physics for their earlier work and development of the scanning tunnelling microscope (STM) [³²], which is considered as the ancestor of the AFM. Nowadays, AFM is not only used to observe nano-objects but also for measuring, modelling and manipulating matter and molecules at the nanoscale and fabricate nanomaterials (system) with unique properties [³³][³⁴].

The microscope consists in a cantilever with a sharp built-in pyramidal tip at its end, defined as the probe. This cantilever beam is connected to the controller electronics and will scan the sample surface across a selected area. As the tip approaches the sample surface, multiple forces between the probe and the surface arise and will make the cantilever to deflect as the surface topography changes. Other properties changes across the surface such as magnetic, electrostatic, chemical, etc... can be monitored using AFM. As the probe is scanning the surface, a laser spot reflected from the top surface of the cantilever end into photodiode sensors measures the respective deflexion of the cantilever. To avoid collision between the tip and the surface which could cause serious

damage to the tip and the sample surface, the scan is usually not carried out at constant height. So in most cases, the distance between the tip and the sample is kept constant and a feedback mechanism is used to restore the original cantilever deflexion (\sim constant force) during the scanning process. These information are sent back to the detector and feedback electronics which will generate a map of the topography of the sample or the property studied.

Different imaging modes can be used depending on the applications. They are divided into two main groups: contact mode known also as static mode and non-contact modes also called dynamic mode as the cantilever is vibrating over the surface. The AFM used in this work was the Digital Instruments (DI) Nanoscope SPM IIIa under ambient conditions. The AFM images on graphite have been obtained using the tapping mode which is an intermittent contact mode (i.e. “*improved*” contact mode which avoids damaging the surface).

As an example, the Figure 3.11 shows the AFM images of CD sample (data film) which were used to check the tip quality and response prior to observe the graphite samples. On the Figure 3.11 a), it is interesting to note that the data bits (which will be recognised as 0 or 1 by computer) are clearly visible and take the shape of crenels with a height of 150 nm. Each line is spaced of $\sim 1 \mu\text{m}$ with the following and has a thickness of $\sim 1 \mu\text{m}$ as well as shown on the section profile.

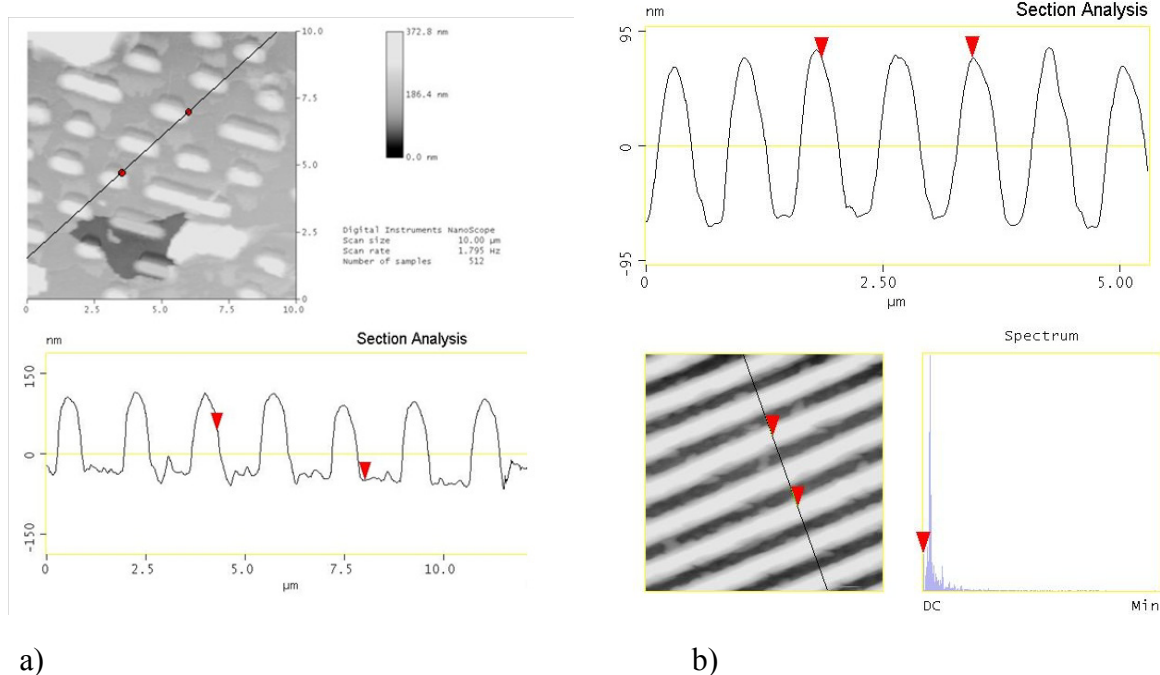


Figure 3.11: AFM image and depth profile of a) CD sample used for preliminary check-up and b) comparison with DVD data film sample.

Figure 3.11 b) shows AFM images of a DVD film sample. Given an identical surface, the data lines appear to be more concentrated. From the section profile, the height between top and hole is approximately 125 nm whereas the space between the lines is 380 nm which is smaller than for the CD sample. This is to be expected because the DVD capacity is larger than for a normal CD.

3.6 Oxidation and reduction of carbon materials

For the study of adsorption isotherms and enthalpies of immersion of polar and non-polar liquids, it is interesting to use carbon materials with different oxygen surface concentration. For this reason, the base material is usually oxidised (or reduced) to increase (or decrease) gradually the oxygen group amount. It is well known that surface oxygen functional groups are formed on activated carbon or carbon black when the materials are exposed to oxidizing agents. A multitude of oxidation methods have been

reported in the literature, either in a gas phase process or in acidic solution. To create a suite of adsorbents with increasing oxygen level, several solutions can be adopted:

- ✓ Treat in acidic solution during different time [35]
- ✓ Oxidise the material until saturation then heat treat in inert atmosphere to eliminate gradually the oxygen groups [36]
- ✓ Oxidise with ozone during different treatment time [37] [42].

The first method is the most commonly used due to its simplicity. But it presents some disadvantages. Usually liquid-phase oxidation with nitric acid or hydrogen peroxide is really strong and will damage the carbon structure. This will create carbon samples within a whole range of porous structure depending on the treatment time. This one major problem when investigation of the effects of surface chemistry on vapour adsorption is only desired. This kind of treatment can also introduced impurities such as nitrogen groups.

The second method, like the first one, uses also an acidic treatment to create a new base material saturated with oxygen groups. Then the suite of adsorbents with varying oxygen content is produced by heat treated this material in the range of 373~1000°K. This method gives *“very similar porous structure characteristics, thereby minimizing effects due to changes in porous structure”* [36].

The third solution is the method used in this work. This method presents some advantages: it is really efficient for short-time treatment and does not alter the structure of the carbon material. It is not a widespread technique because of the high cost of the ozone generator.

Other suitable techniques such as thermal treatment in air or oxygen, O₂ plasma treatment [38][39] or electrochemical oxidation [40] can be used to modify the nature and concentration of surface oxygen complexes.

3.6.1 Ozone treatment

Carbon materials were treated with ozone in a laboratory-scale fluidized bed-type reactor, as schematically represented in Figure 3.12. The material to be treated, usually powder or granule was inserted inside the glass reactor and oxidised with ozone by passing the controlled ozone/oxygen mixture through the carbon material bed.

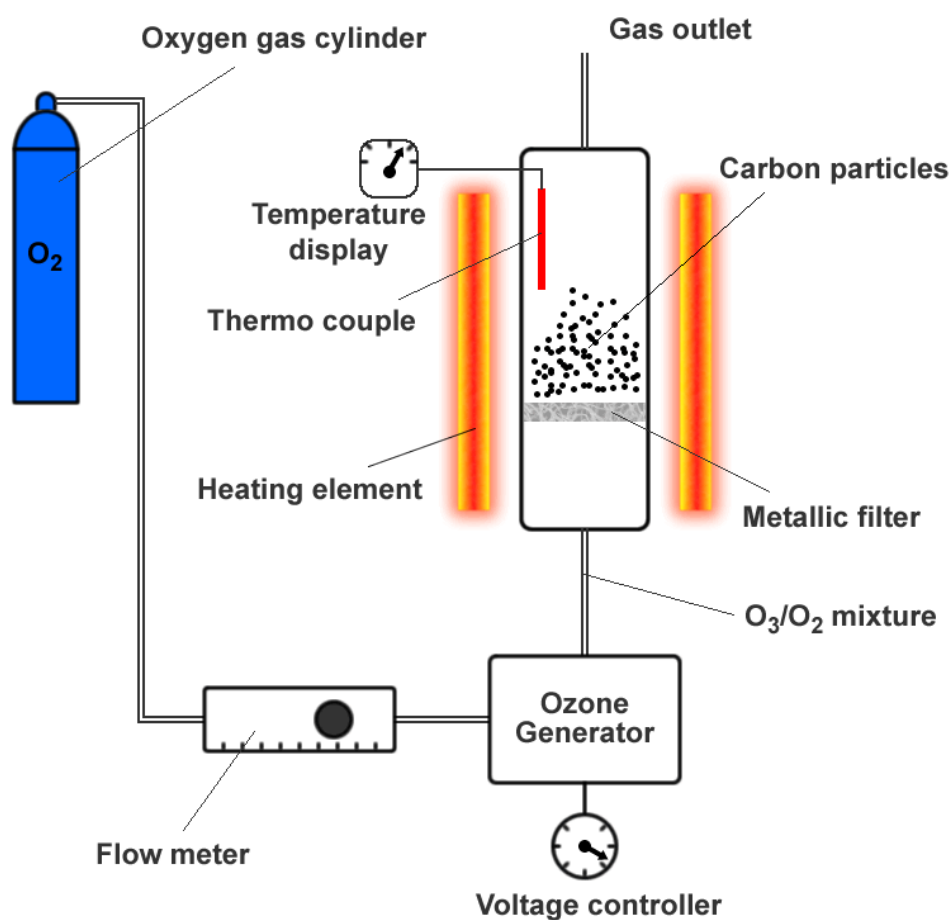


Figure 3.12: Fluidised bed-type reactor used for ozone treatment.

The ozone was produced from oxygen gas (BOC, UK) by the TOGC2 ozone generator (Ozonía Triogen, Scotland). This ozone generator incorporates a high voltage/high frequency power supply unit and a ceramic dielectric ozone production module. This module consists of a ceramic dielectric tube around a stainless steel anode

(and is cooled with ambient air (fan assisted) during production). Basically, the ozone is produced when air or oxygen is passed over the ceramic dielectric. The ozone production rate is controlled via a control knob (voltage/frequency) and also by adjusting the feed gas flow rate.

The importance of the choice of the feed gas, voltage/frequency and feed gas flow rate are shown in the following plots (Figure 3.13) [41].

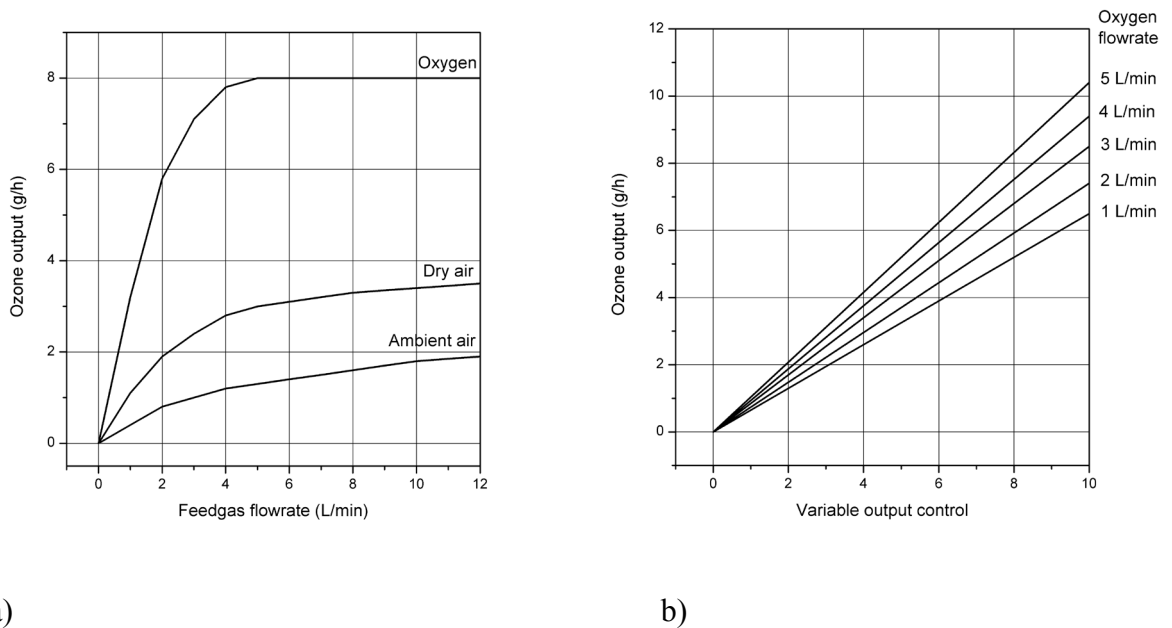


Figure 3.13: a) Influence of the feed gas flow rate on the ozone concentration for the three different feed gas: oxygen, dry air and ambient air. b) Influence of the voltage/frequency and also flow rate on the ozone concentration in the case of oxygen chosen as feed gas.

Sutherland et al. [42] investigated the effects of ozone treatment parameters i.e. ozonation voltage/frequency, oxygen flow rate and treatment time. They used a carbon black as base material. Each parameter was studied by keeping others constant. They reported that an increase of the ozonation voltage leads to an increase of ozone concentration, the surface oxygen concentration of carbon black also increased. They also found that increasing the oxygen flow rate increase the carbon black oxygen concentration but the ozone concentration in the O_3/O_2 mixture decreased. Finally, they

noticed that the carbon black surface oxygen concentration was significantly affected by the treatment time. The concentration was increasing steadily with longer treatment time when the voltage/frequency and flow rate were kept constant.

Similar results were found while investigating these ozone-treatment parameters on activated carbon BPL and carbon black N330. For this work, we decided to adjust the surface oxygen concentration by only varying the treatment time (more easy and accurate to control). Oxygen was chosen as a feed gas with a flow rate of 5 L/min and the control knob setting of 5.

3.6.2 Liquid-phase oxidation

Carbon materials have also been submitted to chemical treatment in liquid phase as a comparison to ozone oxidation. The experimental procedures are detailed as follow.

3.6.2.1 Hydrogen peroxide oxidation

About 5 g of carbon black N330 or activated carbon BPL was placed in a 100 mL solution of H₂O₂ (Sigma-Aldrich, ACS reagent, 30 wt.% in H₂O). The mixture was let under mechanical stirring in an incubator for 24 h. Then, in order to remove residual H₂O₂ and any water soluble materials, it was filtered and washed with water (portions of 1 L) until a constant pH is reached (the pH meter used was a Piccolo plus (Hanna Instruments, UK)). The resulting solid was dried in air in an oven (Genlab Ltd, England) at 80°C (353°K) for 48h and designated N330 H₂O₂ or BPL N330 H₂O₂.

3.6.2.2 Nitric acid oxidation

Carbon black N330 and activated carbon BPL have been oxidised with nitric acid in a similar way. About 5 g of carbon material was placed in 100 mL of pure HNO₃ (Sigma-Aldrich, Puriss, p.a. ≥ 65%). The mixture was let in the oven at 80°C during 24 h. Then, the mixture is filtered and washed with water to constant pH, until the washing waters are

exempts of residual HNO_3 and any water soluble materials. The resulting solid was dried in air at 80°C for 48 h and designated as either N330 HNO_3 or BPL HNO_3 .

3.6.2.3 Ammonium persulfate oxidation

The ammonium persulfate oxidation was only carried out for carbon black materials. 5 g of ammonium persulfate powder was dissolved in 100 mL of deionised water. About 5 g of carbon black N330 was placed in the mixture $\text{H}_2\text{O}/\text{H}_2\text{SO}_4$ (Sigma-Aldrich, Puriss, p.a. $\geq 97\%$). The mixture was let in an incubator under mechanical stirring for 24 h. Then, one filters and washes with water (portions of 1 L) to constant pH in order to remove residual sulphate and any water soluble materials. The resulting carbon material is finally dried in air at 80°C for 48 h and designated as N330 Amm Per .

3.6.3 Reduction

On the other hand, heat treatment of the carbon material under inert atmosphere (Helium, argon, nitrogen flow and even hydrogen) can be carried out in order to selectively remove some of these oxygen functional groups. Each type of groups has different pyrolytic decomposition temperature ranges. This method can also be used to remove some other groups like chlorinated, fluorinated or nitrogen groups. In our case, the reduction process was carried out using a tubular furnace (Carbolite, UK) where the carbon sample was heated at the selected temperature (typically between 400 and 1100°C) for 4 h under a flow (≈ 200 mL/min) of oxygen-free nitrogen (BOC, UK).

References

- ¹ J. W. McBain and A. M. Bakr. A new sorption balance. *J. Am. Chem. Soc.* **48** (1926) 690–695.
- ² F. Kraehenbuehl, H. F. Stoeckli, A. Addoun, P. Ehrburger and J. B. Donnet. The use of immersion calorimetry in the determination of micropore distribution of carbons in the course of activation. *Carbon* **24** (1986) 483-488.
- ³ S. S. Barton, J. R. Dacey and M. J. B. Evans. Surface oxides on porous carbon. *Colloid Polym. Sci.* **206** (1982) 726-730.
- ⁴ Barton S. S., Evans M. J. B., Holland J. and Koresh J. E. (1984) *Carbon* **22**, 265
- ⁵ H. F. Stoeckli and F. Kraehenbuehl. The enthalpies of immersion of active carbons, in relation to the Dubinin theory for the volume filling of micropores. *Carbon* **19** (1981) 353-356.
- ⁶ W. D. Harkins and G. Jura. Surfaces of solids. XII. An absolute method for the determination of the area of a finely divided crystalline solid. *J. Am. Chem. Soc.* **66** (1944) 1362-1366.
- ⁷ S. Partyka, F. Rouquerol and J. Rouquerol. Calorimetric determination of surface areas: Possibilities of a modified Harkins and Jura procedure. *J. Colloid Interface Sci.* **68** (1979) 21-31.
- ⁸ E. Rutherford. The structure of the atom. *Phil. Mag.* **27** (1914) 488 - 498.
- ⁹ E. Rutherford. The connexion between the beta and gamma ray spectra. *Phil. Mag.* **28** (1914) 305-319.
- ¹⁰ C. D. Wagner, L. E. Davis, M. V. Zeller, J. A. Taylor, R. H. Raymond and L. H. Gale. Empirical atomic sensitivity factors for quantitative analysis by electron spectroscopy for chemical analysis. *Surf. Interface Anal.* **3** (1981) 211–225.
- ¹¹ *AXIS HSi*, 165, Ultra, Operating *Manual*, KRATOS Manchester UK, 2000.
- ¹² A. Oya, S. Yoshida, J. Alcaniz-Monge and A. Linares-Solano. Formation of mesopores in phenolic resin-derived carbon fiber by catalytic activation using cobalt. *Carbon* **33** (1995) 1085-1090.

- ¹³ C. Brasquet, B. Rousseau, H. Estrade-Szwarcopf and P. L. Cloirec. Observation of activated carbon fibres with SEM and AFM correlation with adsorption data in aqueous solution. *Carbon* **38** (2000) 407-422.
- ¹⁴ J. Alcañiz-Monge, D. Cazorla-Amorós, A. Linares-Solano, S. Yoshida and A. Oya. Effect of the activating gas on tensile strength and pore structure of pitch-based carbon fibres. *Carbon* **32** (1994) 1277-1283.
- ¹⁵ M. Huttepain and A. Oberlin. Microtexture of nongraphitizing carbons and tem studies of some activated samples. *Carbon* **28** (1990) 103-111.
- ¹⁶ K. Oshida, K. Kogiso, K. Matsubayashi, S. Kobayashi, M. Endo, M. S. Dresselhaus and G. Dresselhaus. Analysis of pore structure of activated carbon fibers using high resolution transmission electron microscopy and image processing. *J. Mater. Res.* **10** (1995) 2507-2517.
- ¹⁷ H. Marsh and F. Rodríguez-Reinoso. in *Activated Carbon* (Elsevier Science & Technology, Amsterdam, 2006). Chap. 7 - SEM and TEM Images of Structures in Activated Carbons, Pages 366-382
- ¹⁸ E. T. Thostenson, Z. Ren and T.-W. Chou. Advances in the science and technology of carbon nanotubes and their composites: a review. *Compos. Sci. Technol.* **61** (2001) 1899-1912.
- ¹⁹ H. F. Stoeckli, D. Hugi-Cleary and T. A. Centeno. The characterisation of solids by adsorption and immersion techniques and by AFM/STM. *J. Eur. Ceram. Soc.* **18** (1998) 1177-1185.
- ²⁰ H. F. Stoeckli and L. Currit. The fractal character of carbon surfaces determined by Fourier analysis of STM data. *Carbon* **33** (1995) 338-340.
- ²¹ S. Iijima. Direct observation of the tetrahedral bonding in graphitized carbon-black by high-resolution electron-microscopy. *J. Cryst. Growth* **50** (1980) 675-683.
- ²² J. I. Goldstein. *Scanning electron microscopy and X-ray microanalysis: a text for biologists, materials scientists and geologists* (Plenum Press, New York, 1981).
- ²³ I. M. Watt. *The principles and practice of electron microscopy* (Cambridge University Press, Cambridge, 1985).

- ²⁴ N. A. Kiselev, A. P. Moravsky, A. B. Ormont and D. N. Zakharov. SEM and HREM study of the internal structure of nanotube rich carbon arc cathodic deposits. *Carbon* **37** (1999) 1093-1103.
- ²⁵ D. B. Williams and C. B. Carter. *Transmission electron microscopy: a textbook for materials science* (Springer, New York, 1996).
- ²⁶ L. Reimer and H. Kohl. *Transmission electron microscopy: physics of image formation* (Springer, New York, 2008).
- ²⁷ X. Ma et al. Polymerised carbon nanobells and their field emission properties. *Appl. Phys. Lett.* **75** (1999) 3105-3107.
- ²⁸ X. Ma, E. G. Wang, R. D. Tilley, D. A. Jefferson and W. Zhou. Size-controlled short nanofibres and nanobells: growth and formation mechanism. *Appl. Phys. Lett.* **77** (2000) 4136-4138.
- ²⁹ Z. J. Liu, Z. Y. Yuan, W. Zhou, L. M. Peng and Z. D. Xu. Co/carbon-nanotube monometallic system: the effects of oxidation by nitric acid. *Phys. Chem. Chem. Phys.* **3** (2001) 2518-2521.
- ³⁰ J. F. Geng, I. A. Solov'yov, W. Zhou and A. V. Solov'yov. Uncovering a solvent-controlled preferential growth of buckminsterfullerene (C60) nanowires. *J. Phys. Chem. C* **113** (2009) 6390-6397.
- ³¹ G. Binnig, C. F. Quate and C. Gerber. Atomic force microscope. *Phys. Rev. Lett.* **56** (1986) 930-933.
- ³² G. Binnig, H. Rohrer, C. Gerber and E. Weibel. Surface studies by scanning tunneling microscopy. *Phys. Rev. Lett.* **49** (1982) 57-61.
- ³³ T. Junno, K. Deppert, L. Montelius and L. Samuelson. Controlled manipulation of nanoparticles with an atomic force microscope. *Appl. Phys. Lett.* **66** (1995) 3627-3629.
- ³⁴ T. Fukuda, F. Arai and D. L. X. Assembly of nanodevices with carbon nanotubes through nanorobotic manipulations. *Proceedings of the IEEE* **91** (2003) 1803-1818.
- ³⁵ F. Carrasco-Marin, A. Mueden, T. A. Centeno, F. Stoeckli and C. Moreno-Castilla. Water adsorption on activated carbons with different degrees of oxidation. *J. Chem. Soc., Faraday Trans.* **93** (1997) 2211-2215.
-

- ³⁶ A. J. Fletcher, Y. Uygur and K. M. Thomas. Role of surface functional groups in the adsorption kinetics of water vapor on microporous activated carbons. *J. Phys. Chem. C* **111** (2007) 8349-8359.
- ³⁷ R. H. Bradley, R. Daley and F. Le Goff. Polar and dispersion interactions at carbon surfaces: further development of the XPS-based model. *Carbon* **40** (2002) 1173–1179.
- ³⁸ T. Xu, J. Yang, J. Liu and Q. Fu. Surface modification of multi-walled carbon nanotubes by O² plasma. *Applied Surface Science* **253** (2007) 8945–8951.
- ³⁹ J. B. Donnet, M. Brendle, T. L. Dhami and O. P. Bahl. Plasma treatment effect on the surface energy of carbon and carbon fibers. *Carbon* **24** (1986) 757-770.
- ⁴⁰ G. U. Sumanasekera et al. Electrochemical oxidation of single wall carbon nanotube bundles in sulfuric acid. *J. Phys. Chem. B* **103** (1999) 4292-4297.
- ⁴¹ Ozonia Triogen website: <http://www.ozonia.com/> accessed 08/02/2005 and user manual.
- ⁴² I. Sutherland, E. Sheng, R. H. Bradley and P. K. Freakley. Effects of ozone oxidation on carbon black surfaces. *J. Mater. Sci.* **31** (1996) 5651-5655.

4

Chapter 4 Initial investigations and characterisation of graphite, carbon black and activated carbon

4.1 Introduction

In order to understand the relationships between carbon structure, surface chemistry and physical adsorption (i.e. specific interactions), it was important to carry out some initial and basic characterization on the different carbon materials: graphite, activated carbon, carbon black and multi-walled carbon nanotubes which were studied in this work.

Untreated carbon materials and those submitted to various oxidation treatments (ozone and liquid-phase oxidation) were studied by means of the two following microscopy techniques: Scanning Electron Microscopy (SEM) and Atomic Force Microscopy (AFM). These initial observations give us a visual aspect of the effects of the different oxidation treatments on the carbon structure of each material. Thermogravimetric analysis was also carried out on both activated carbon and carbon black as a first qualitative tool to investigate the oxygen-containing functional groups present on these surfaces and to obtain information about their thermal decomposition temperatures. Finally, heat treatment in an inert atmosphere and at different temperatures was shown to have a significant influence on the surface oxygen concentration of the base activated carbon BPL but left the porous structure almost unchanged.

4.2 AFM observations on base and oxidised graphite materials

A series of oxidised graphite samples have been observed using AFM in order to study the influence of this treatment on the physical structure of a most ordered carbon surface. The structure of graphite has been discussed on paragraph 2.6.3 including the ABA stacking of graphene sheets in Figure 2.8. The Figure 4.1 shows the AFM photograph of the base material. The scale is 100 μm x 100 μm which is considered a low magnification for AFM. The higher magnification photo will be discussed afterwards. On the image, a multitude of particles (impurities, carbon dust and debris) can still be observed on the surface even after passing a gentle flow of N_2 on the sample before observation.

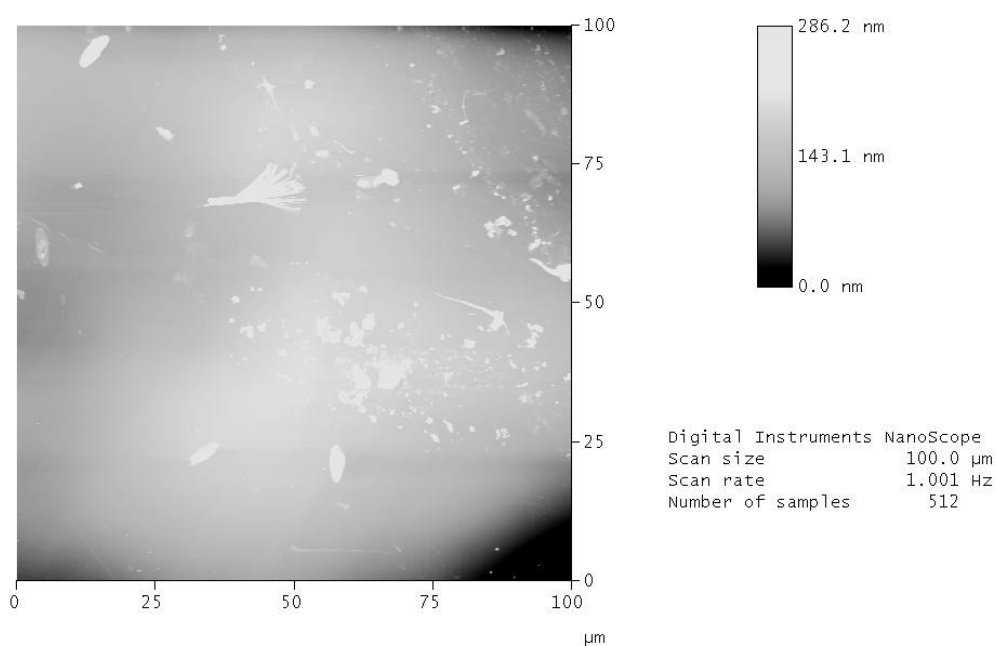
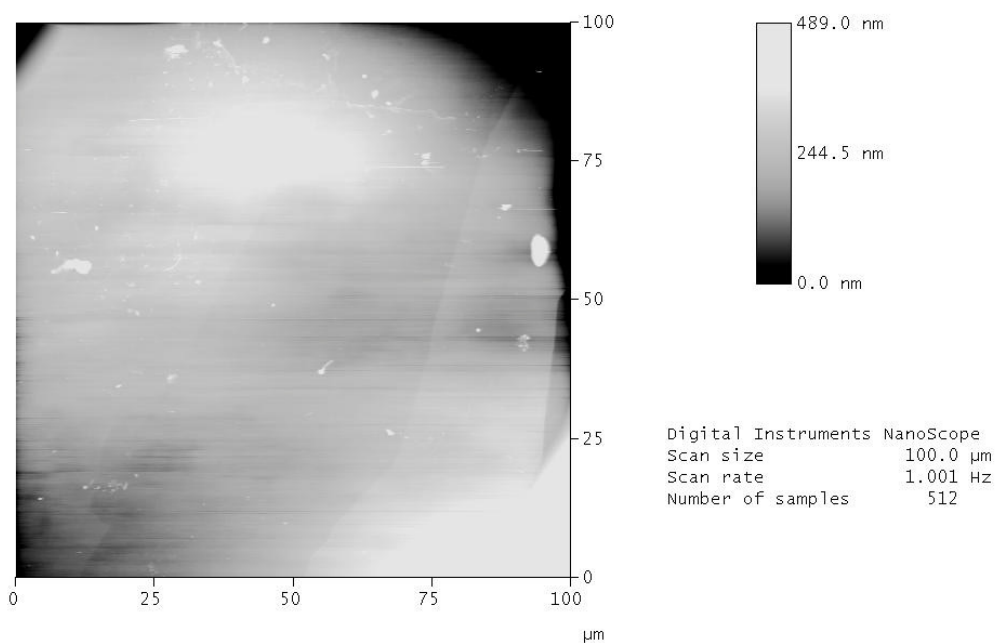


Figure 4.1: AFM image of the untreated graphite surface at low magnification.

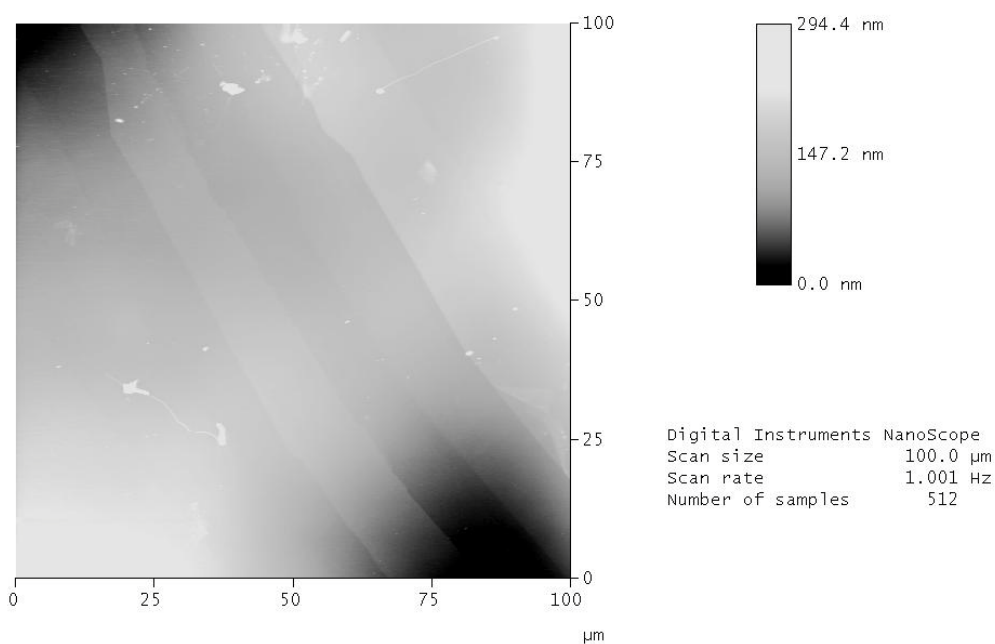
Regarding the graphite sample oxidised with ozone, some particles are still present on the surface (Figure 4.2 a)) but in lower quantity than for the base material. It seems that the ozone treatment has not strongly affected (in terms of damage) the physical

structure of the graphite surface. It has just cleared and removed most of the impurity particles from the surface. At this magnification, the graphene sheets are almost visible and can be guessed by the diagonal lines across the photo. It should be pointed out that few other groups have managed to observe mono and multilayer graphene sheet using microscopy techniques [1][2][3][4][5]. Identical observations can be taken from the surface of the H₂O₂ treated graphite represented in Figure 4.2 b). As one may expect, the impurities are almost completely removed because the H₂O₂ is carried out in aqueous phase so the very small particles are flushed away more easily. The graphene sheets are also clearly visible on this photo. The section analysis (profile) indicates the presence of multi-sheet of graphene as the elevation between two consecutive terraces is of the order of 10~25 nm. The graphene sheets are very straight and give an impression of stairs shape.

Graphite surfaces treated with nitric acid HNO₃ and ammonium persulfate have also been observed and are similar to H₂O₂ treated graphite sample. So for that reason, their photographs were not included.



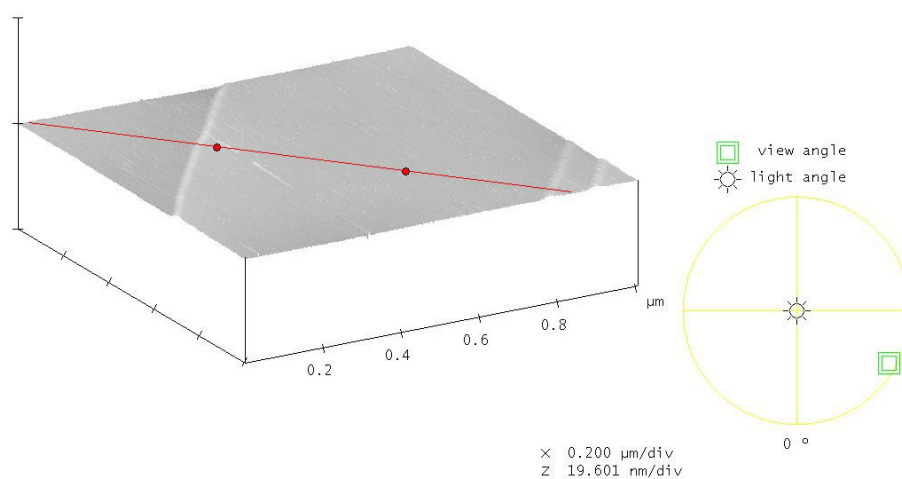
a)



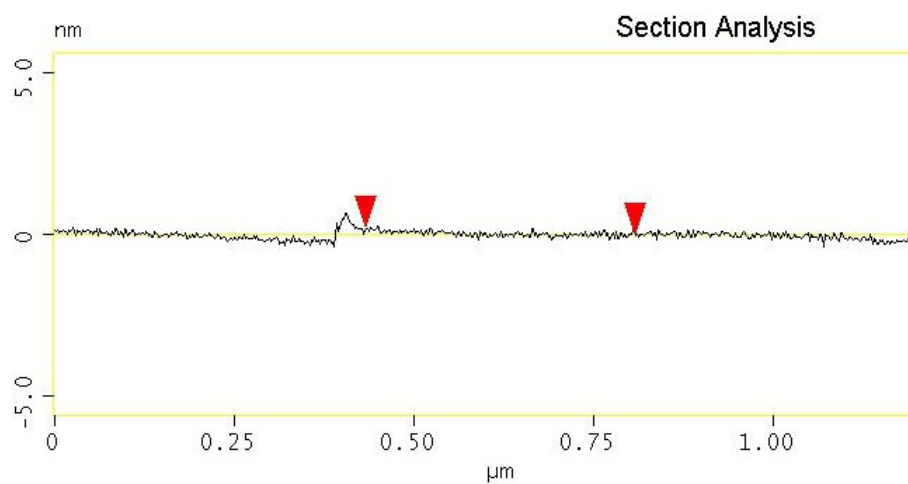
b)

Figure 4.2: AFM images of the surface of: a) the ozone oxidised graphite and b) H_2O_2 treated graphite at low magnification.

The Figure 4.3 shows a really interested feature at high magnification (1 μm x 1 μm) of the ozonated graphite surface. Three straight steps can be seen on the 3D topography and are believed to be monosheet of graphene because their step height is below 0.5 nm (the theoretical interlayer spacing in the graphite structure is $c/2 = 0.335$ nm). It is also interesting to note that the area is incredibly flat (RMS roughness of 0.080 nm) which makes it ideal for AFM observation.



a)



b)

Figure 4.3: a) AFM 3D topography of the surface of the ozone oxidised graphite and b) depth profile perpendicularly to the graphene sheet at high magnification.

This AFM study indicates to us that ozone treatment in gas phase and liquid-phase oxidation do not appear to damage the integrity and physical structure of the graphite surface in the observable central region but they seems to play a role in term of cleaning of the graphite surface as they removed very small particles (impurities and/or debris). This can be explained because of the hardness of the graphite material (in particular the middle part of every graphene sheet) but the edges of the sheet and also the defect sites may be eroded away or oxidised by these treatment. Unfortunately, this is very difficult to observe with the normal AFM as it does not give any chemical aspect of the surface. This also how bring another technical problem of how to mount the sample in order to observe the edges while keeping a relatively flat surface. Beyond scope of this adsorption study, treatment in-situ over long time period or combination with other characterisation technique could be a solution to these issues.

4.3 TEM observations of the untreated carbon black N330

The internal structure of the untreated carbon black N330 was investigated using high resolution transmission electron microscopy (HRTEM). As mentioned before, Prof W. Zhou from the Electron Microscopy Group at University of St Andrews carried out the HRTEM observations on our samples. These HRTEM images obtained (see Figure 4.4) represent the inside of a primary particle at different magnifications. They were created by imaging of *002* lattice fringes of graphite-like structures. The average size of the primary N330 carbon black particles is around 50 nm from visual approximation and is in agreement with the observation made by Kohls and Beaucage [6].

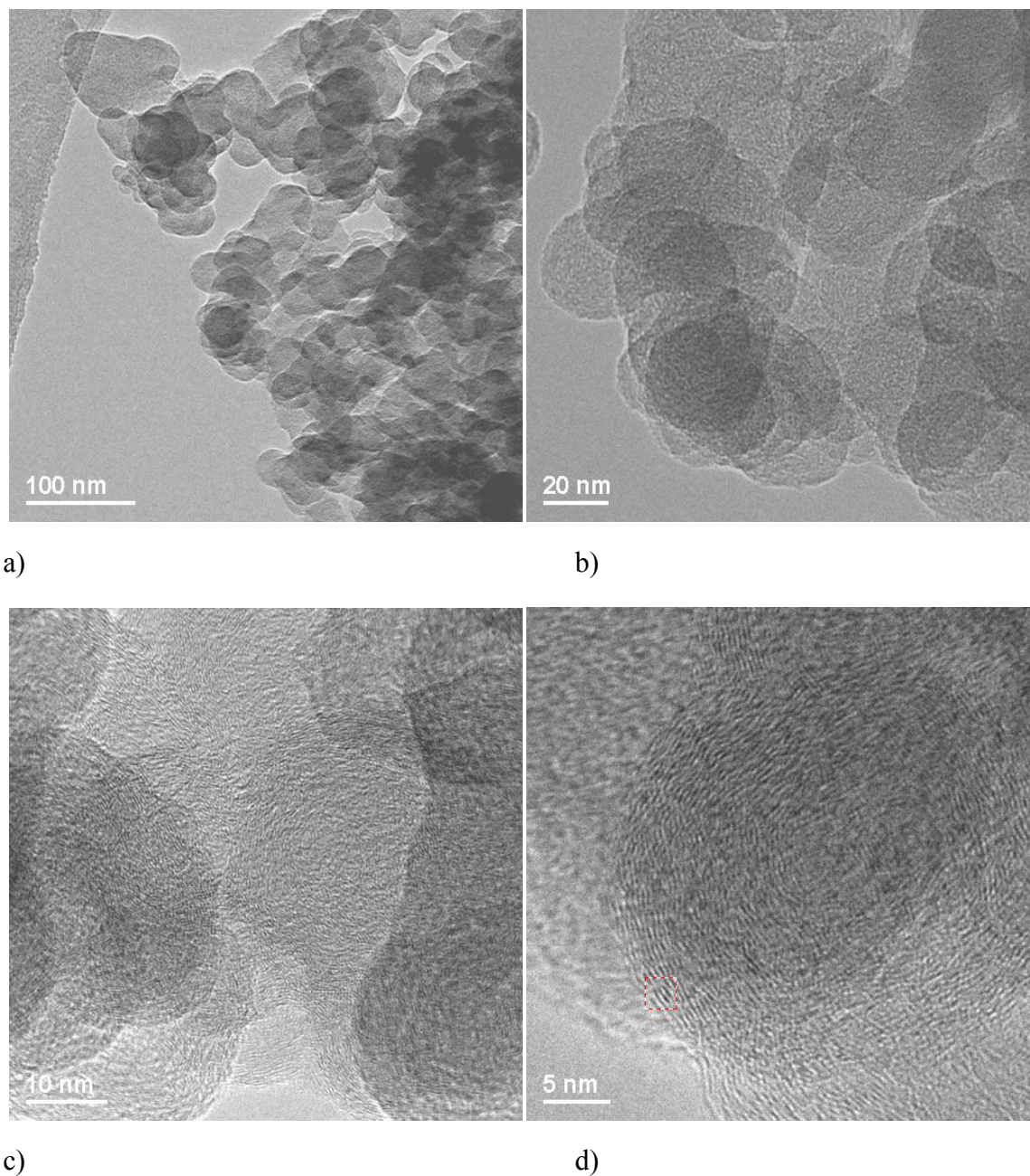


Figure 4.4: TEM high resolution phase contrast images of the base material N330 carbon black at different magnifications.

On the Figure 4.4 b) and d), the onion-like or capsular structure reported by Jager et al. [7] and Heckman [8] is quite visible. The light and dark lines represent the graphitic layers (or “*graphitic segments*”) and the distance between two consecutive dark (or light) lines represents the d-spacing. The d-spacing has been measured from the

diffractograms (not represented here) at different positions (see the red square area in Figure 4.4 d)) and is comprised between 0.3450 and 0.3902 nm. This value is in agreement with the interlayer spacing value (0.34 nm) obtained by Li et al. [9] for another N330 carbon black and also in the same range than the one measured by Hess and Herd [10] for carbon black N220 which was heated at 2700°C. The graphitic layer tends to be continuous and can be compared to the paracrystalline model from Heidenreich et al. [11] and Heckman and Harling [12].

The ozone oxidised carbon blacks have not been observed with TEM as the internal structure should in theory remain the same with only the edges or defects being affected by the ozonation treatment.

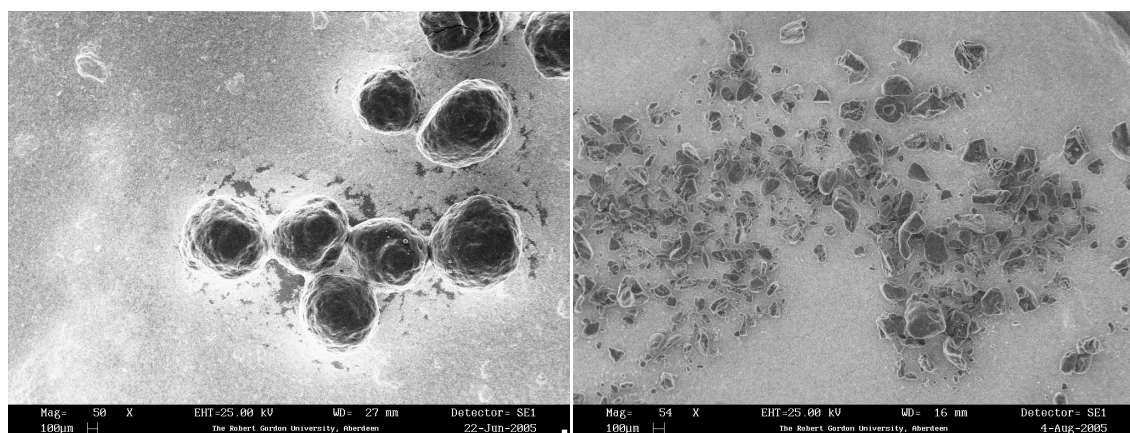
For comparison with the N330 material, the graphitized carbon black N234G, even though not directly observed by ourselves, has clear, more ordered graphitic structure as it has been observed in the literature. As the temperature (and duration) of the thermal treatment increases, the growth and order of the graphitic structure become more and more apparent as it was observed by Vander Wal et al. [13]. This is characterised by an increase of the stacked graphitic segments together with a better alignment and extended length. These induced faceted polygons created from the carbon black particles tend to also have hollow interiors similar to MWCNTs.

4.4 SEM observations of the effects of the oxidation treatments on various carbon surfaces

4.4.1 Carbon black materials

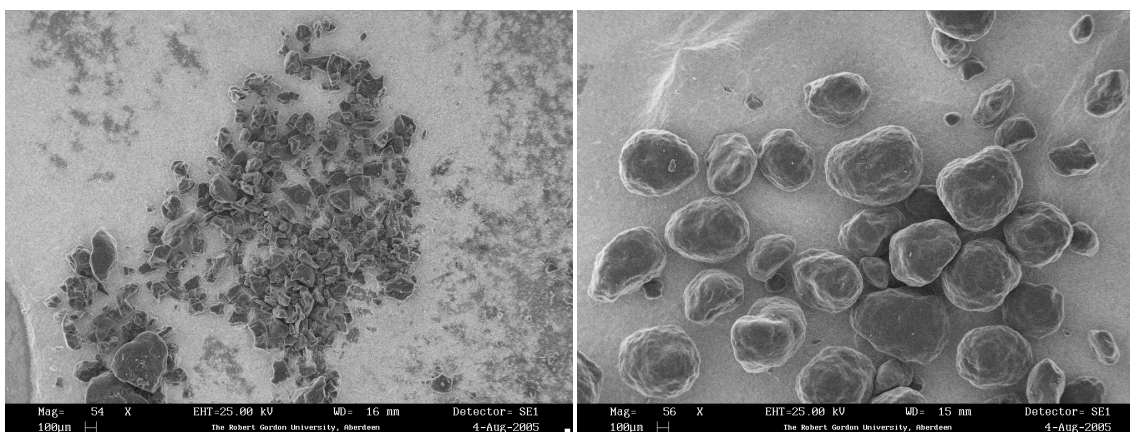
Figure 4.5 shows the SEM micrographs at low magnification of N330 carbon black samples: a) base material, b) after ammonium persulfate modification, c) after nitric acid modification and d) after ozone treatment. On this whole view, one can notice that carbon black granules oxidised in the liquid phase (Amm Per and HNO₃) have been

severely damaged resulting in particles of smaller size (20 to 100 μm) compared to the base and ozonated N330. These particles have irregular sharp shapes completely different from the original almost spherical granules. The ozone treatment does not change the morphology of the carbon black granules. The very fine dust (particles) present on the granules of the original material and around them has been removed by the ozone treatment, leading to very clean and neat carbon particles.



a)

b)



c)

d)

Figure 4.5: SEM micrographs (at x50) of base and selected modified N330 carbon black samples: a) base material, b) after ammonium persulfate modification, c) after nitric acid modification and d) after ozone treatment.

Figure 4.6 shows the SEM micrographs of the same samples but at higher magnification (x1000). It demonstrates that SEM images of untreated N330, N330 O₃ and N330 Amm Per are similar in appearance at this magnification. Very fine particles attached over the carbon black surface can be observed. On the other hand the oxidation of N330 with nitric acid has a visual impact on the surface morphology. The surface has lost its smooth aspect and looks seriously damaged by the treatment. A lot of cavities have appeared and even some cracks have been created.

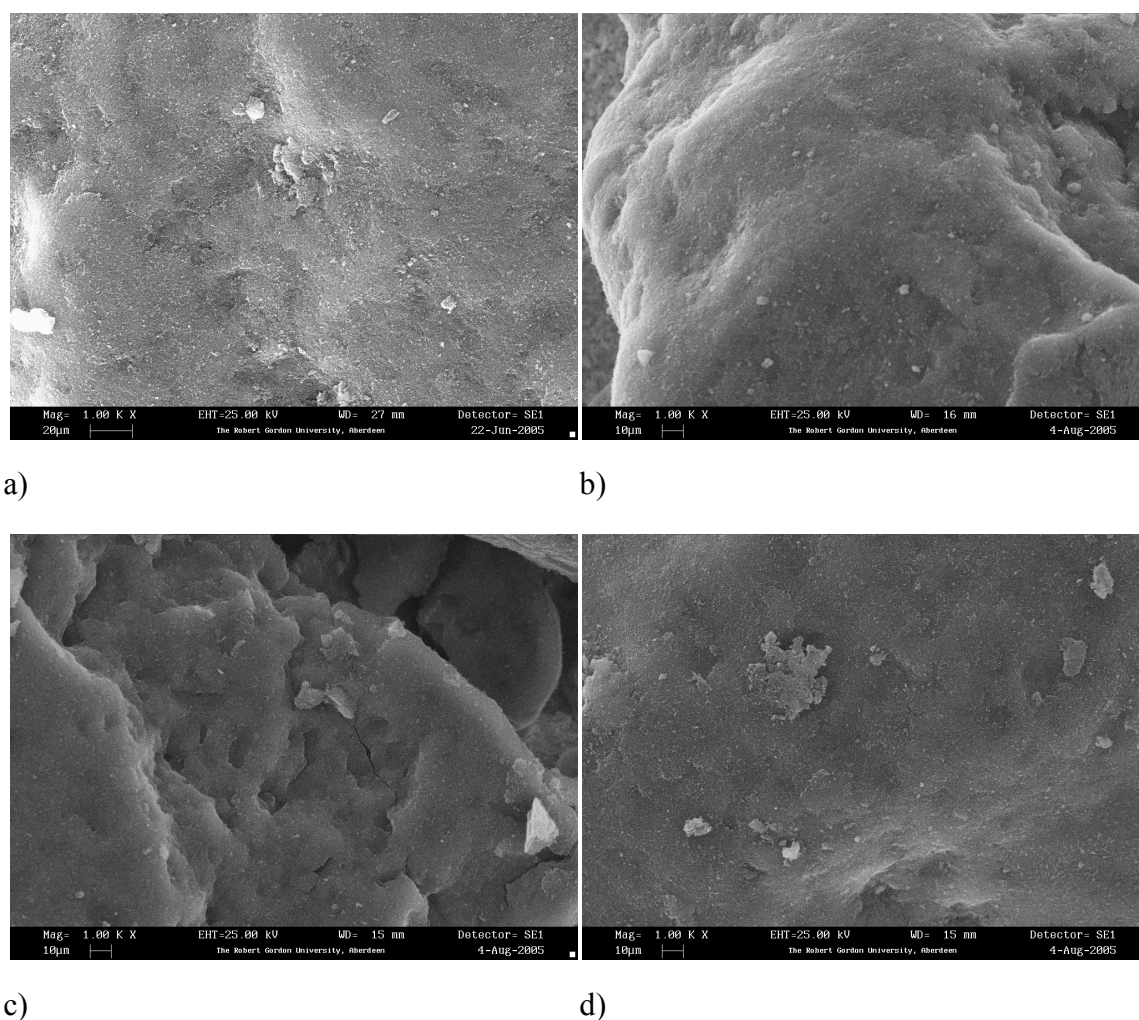
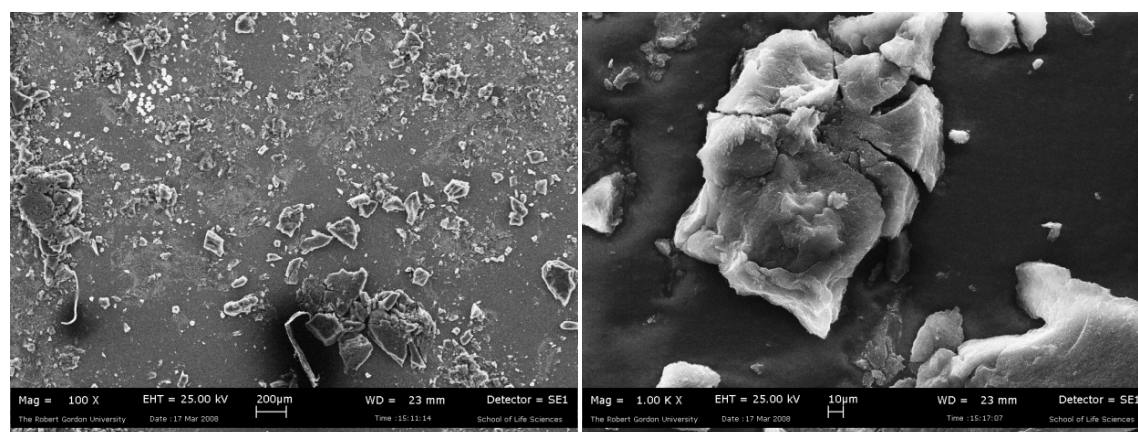


Figure 4.6: SEM micrographs at higher magnification (x1000) of base and selected modified N330 carbon black samples: a) base material, b) after ammonium persulfate modification, c) after nitric acid modification and d) after ozone treatment.

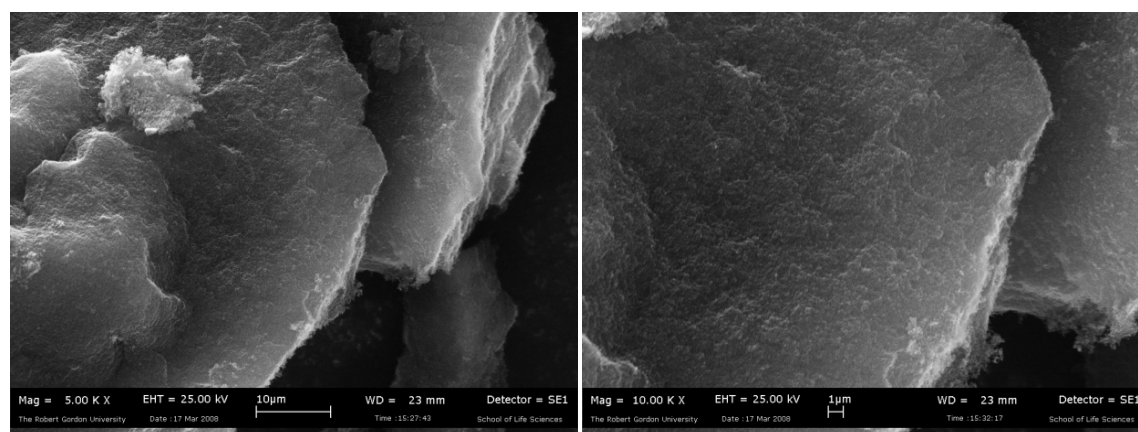
One can say that ozone treatment does not significantly change the morphology of the carbon black surface. SEM micrographs of these samples and even ammonium persulfate sample show typical non porous surface as expecting for carbon black sample. On the contrary, nitric acid oxidation does significantly change the surface morphology of the carbon.

SEM was also used to observe the surface morphology of the untreated N234 carbon black. At low magnification (Figure 4.7 a) and b)), the N234 granules appear to be significantly different from the N330 carbon black granules. They have various sizes and also display very sharp edges possibly due to the more ordered graphitic structure.



a)

b)



c)

d)

Figure 4.7: SEM micrographs of base N234 carbon black samples: a) x100, b) x1k, c) x5k and d) x10k.

The high magnification SEM micrographs from Figure 4.7 c) and d) reveal that this carbon black has some similarity with the N330. The surface looks quite smooth and it is interesting to note the presence of primary carbon black particles on the edge of the surface (bottom right corner of Figure 4.7 d)). These very small particles are forming carbon black agglomerates.

4.4.2 Activated carbon materials

Figure 4.8 shows the SEM micrographs at low magnification of BPL activated carbon samples: a) base material, b) after ammonium persulfate modification, c) after nitric acid modification, d) after ozone treatment and e) after hydrogen peroxide treatment. On this whole view, one can notice that activated carbon granules appear extremely similar. They all look like the untreated material and do not show oxidation damages unlike the previous carbon black samples. This can be explained by the fact that the hardness of activated carbon granules is greater than for carbon black granules which are easily breakable. The typical size of an AC granule is between 500 μm and 1 mm. These particles have irregular shapes and are quite eroded. They also have a rough external surface completely different from the smooth surface of carbon black granules. It is interesting to note that the innumerable entrances of the macropore channels can even be observed at this magnification.

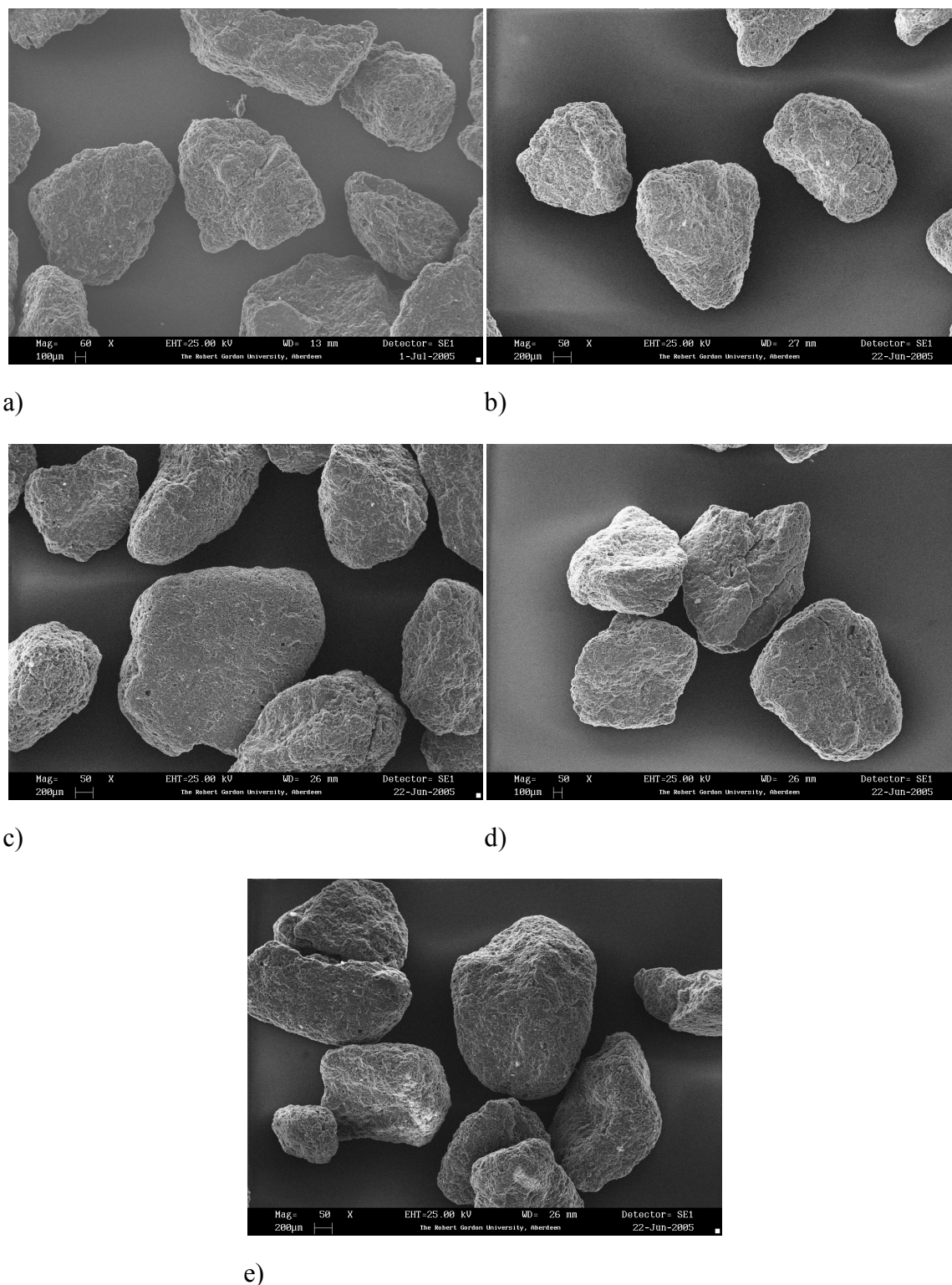


Figure 4.8: SEM micrographs (at x50) of base and selected modified BPL activated carbon samples: a) base material, b) after ammonium persulfate modification, c) after nitric acid modification, d) after ozone treatment and e) after hydrogen peroxide treatment.

Figure 4.9 shows the SEM micrographs of the same AC samples but at higher magnification (x1000). It demonstrates that SEM images of untreated BPL and BPL O₃ are similar in appearance at this magnification. Very fine carbon particles can be observed on the surface. On the other hand, the oxidation in liquid-phase whether it be with nitric acid, hydrogen peroxide or ammonium persulfate, has a major effect on the surface morphology. The surface became rough with many sharp edges and it looks like all the very fine carbon particles (or dust) have been washed away by the treatment.

On a global view, liquid-phase oxidation of activated carbon does not seem to disrupt considerably the material but at high magnification one can notice a major impact on the surface morphology of the particles. On the contrary, the ozone oxidation does not change the external structure of the activated carbon.

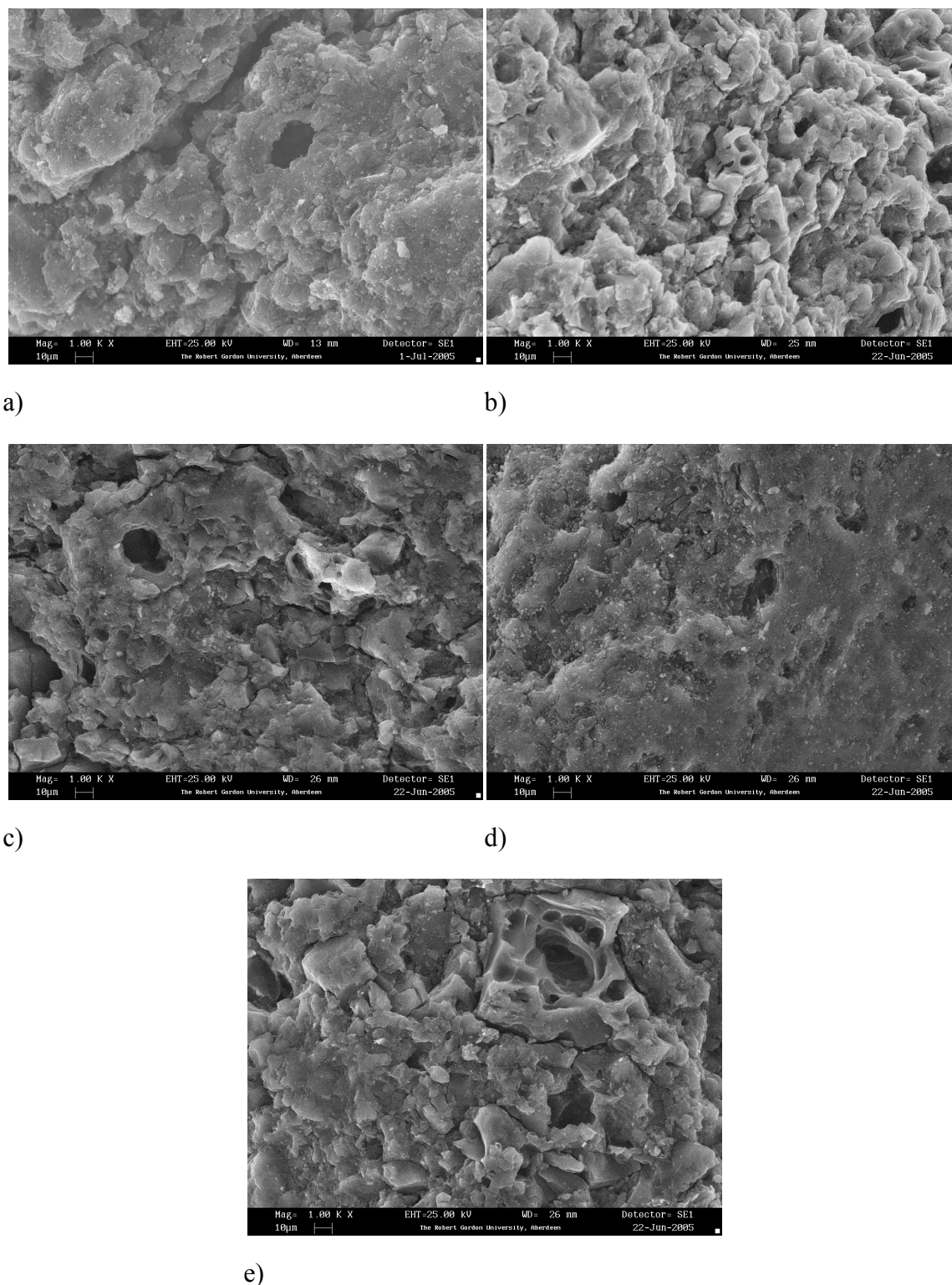


Figure 4.9: SEM micrographs at higher magnification (at x1000) of base and selected modified BPL activated carbon samples: a) base material, b) after ammonium persulfate modification, c) after nitric acid modification, d) after ozone treatment and e) after hydrogen peroxide treatment.

For both carbon material types, the SEM observations show that nitric acid and hydrogen peroxide oxidation appear to be the most severe treatments in term of structural disruption. On the other hand, ozone oxidation seems to be an adequate treatment route in order to change only the surface chemistry of a solid and not its external or internal structure as it was later confirmed by our N_2 and toluene adsorption data. Hence, for this reason, this technique was used to create the series of oxidized carbon black N330 materials used in the next two chapters. Moreover, AC and CB materials oxidized with these acids were also studied using XPS and water adsorption in Chapter 6 as a comparison to ozone treatment.

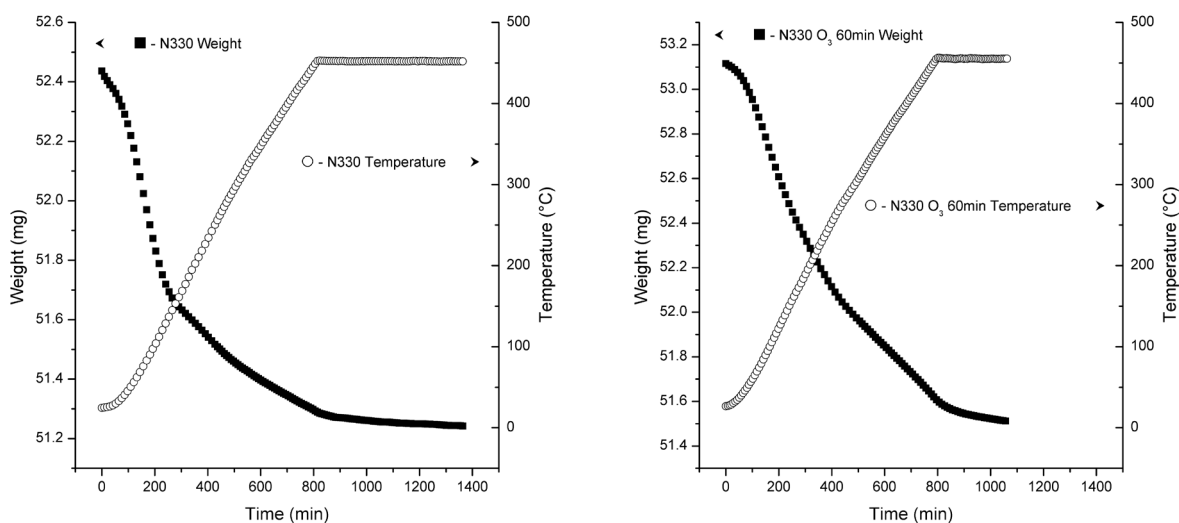
4.5 Thermogravimetric analysis (TGA) and differential thermal gravimetry (DTG) on oxidised carbon materials

4.5.1 Carbon black materials

The thermogravimetric analysis of the carbon black materials was conducted inside the TGA chamber under vacuum to allow the species removed from the surface to be completely evacuated. This device provides a very good resolution in terms of weight reading as the same micro balance than for the adsorption measurement is being used. The only disadvantage is that the maximum temperature is limited. However, qualitative information can be drawn back from these TGA and DTG profiles.

For our experiments, the temperature range studied was between 20 and 460°C with a very slow heating rate of 0.5°C/min. This sort of value is typical from thermogravimetric analysis in order to let enough time for the elimination/removal of the species being desorbed.

The TGA and DTG curves for the base and oxidised carbon black are represented in Figure 4.10 and Figure 4.11 respectively.



a)

b)

Figure 4.10: Weight loss and temperature profile during the TGA experiment for a) the base N330 carbon black and b) the N330 oxidised with ozone.

On the first look, one can notice that the DTG plot for the N330 HNO₃ is significantly higher than all the other plots which indicates that a larger quantity of surface groups has been eliminated. It is quite difficult to conclude on this behaviour but it is believed this is due to the elimination of the residual nitrate groups left from the nitric acid treatment and possibly weaker bonding of the oxygen groups on the carbon surface (damage resulting from the treatment). On the other plots, the main peak, corresponding to the maximum weight loss (and highest slope on the TGA plots) is centred on $t = 175$ min (~ 90 – 100°C). This is usually associated with the release of the physisorbed water molecules from the carbon surface. Szymanski et al. [14] observed the same kind of behaviour on oxidised porous carbon. The DTG plots of the N330 treated with nitric acid and ammonium persulfate have a different shape as their main peak is broader and is composed of additional peak centred at around 350 min ($T = 215^\circ\text{C}$) which may result from nitrate groups.

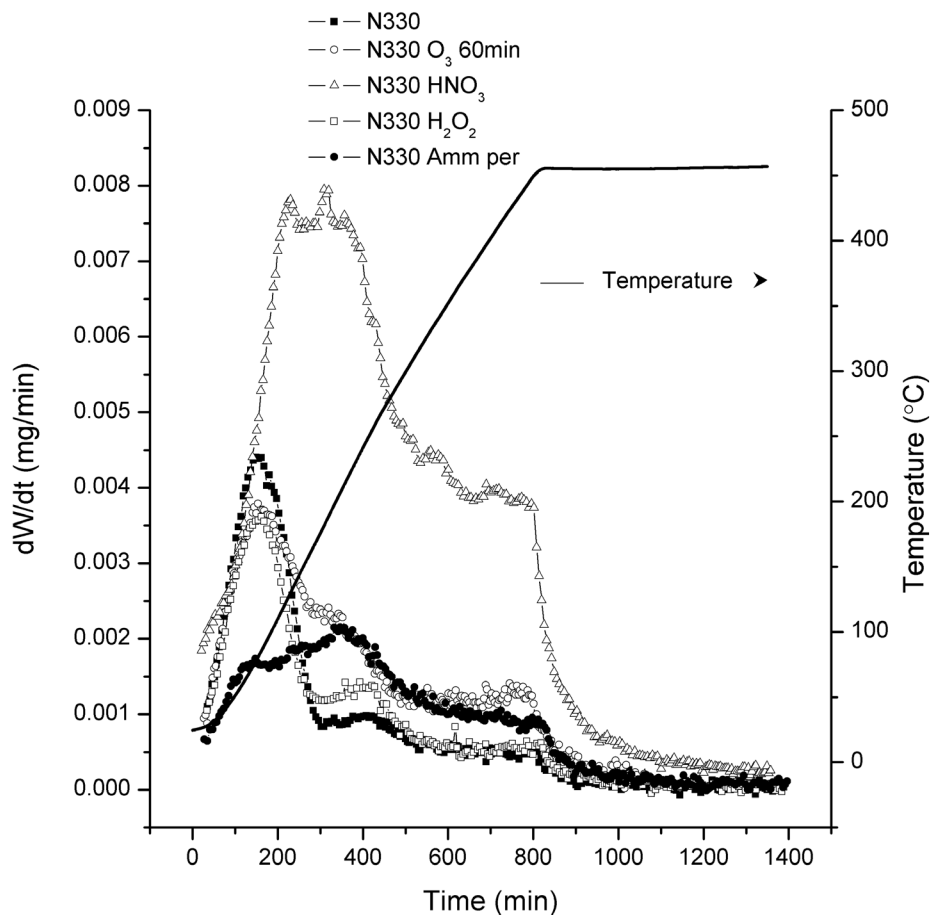


Figure 4.11: DTG and temperature profiles on the base and modified carbon black materials.

On all the DTG profiles, a sharp drop can be observed at around 850min which corresponds to the time when the temperature reaches its maximum value and stays constant.

4.5.2 Activated carbon materials

The TGA and DTG plots for the untreated and oxidised activated carbon BPL are represented in Figure 4.12 and Figure 4.13 respectively. The curve for the BPL material oxidised with ozone is significantly higher than the other plots and in particular the base

activated carbon. The figure indicates that the main peaks corresponding to the maximum weight loss (removal of physisorbed water molecules) are all centred on $t = 300\sim 400$ min (which correspond to a temperature of approximately 175°C). This temperature is slightly higher than for carbon black materials as more energy is necessary to remove the water from the porous structure. As for carbon black, the analysis of the activated carbon treated with nitric acid is more complex than for the other treatments. A first peak appears after 190 min (90°C) then a second peak at $t = 250$ min (125°C), a third peak at $t = 400$ min (225°C) and two other peaks between 650 and 850 min ($325\text{-}400^{\circ}\text{C}$).

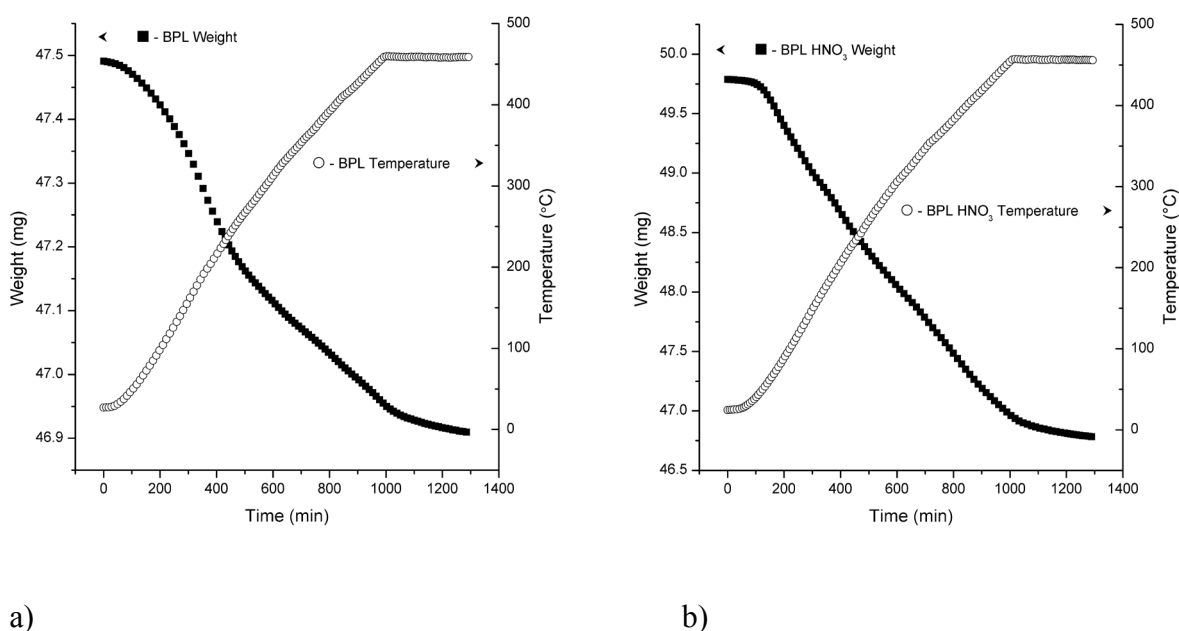


Figure 4.12: Weight loss and temperature profile during the TGA experiment for a) the base BPL activated carbon and b) the BPL treated with nitric acid.

The sharp decrease on the DTG profiles at $t = 1000$ min indicates that the temperature reached its limiting value.

For both carbon black and activated carbon, most of the weight loss after 500min ($> 180\sim 200^{\circ}\text{C}$) corresponds to the removal of oxygen atoms from carboxylic groups and maybe lactone groups as discussed in the Theory chapter (see Table 2.2: Oxygen surface

groups and their pyrolytic elimination temperatures.). As said before, the limitation in temperature did not allow us to investigate the presence of oxygen-containing groups with higher elimination temperature such as ketone or peroxide groups for example.

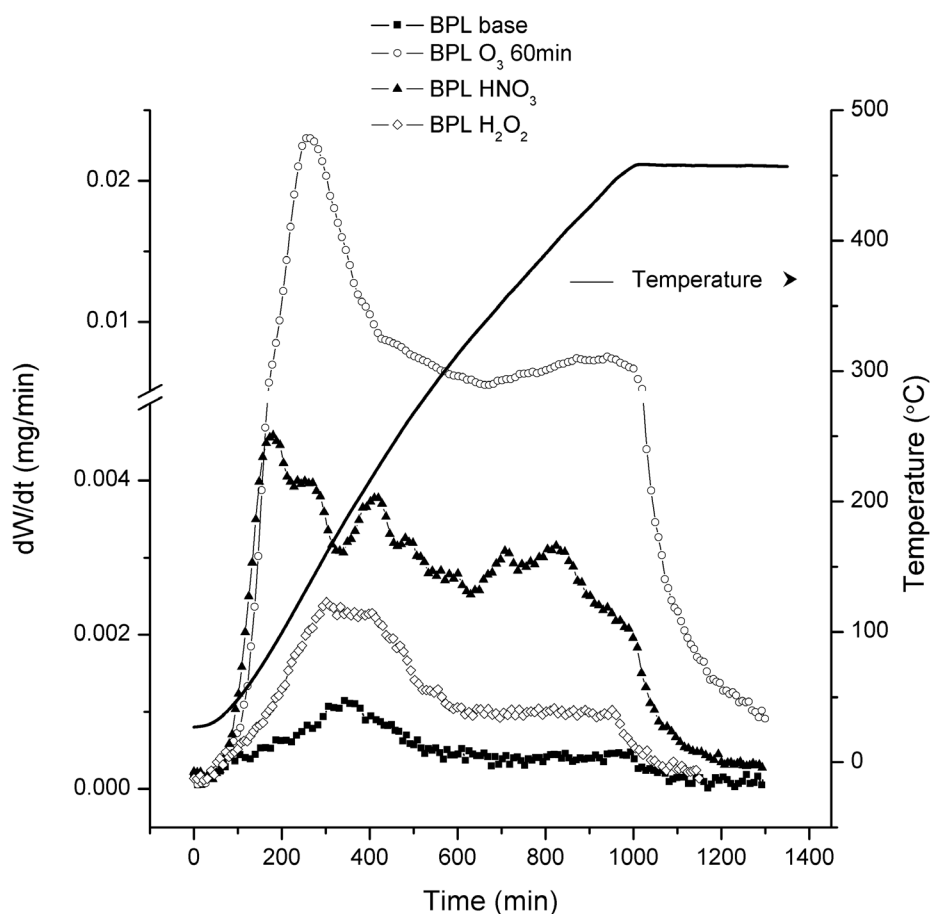


Figure 4.13: DTG and temperature profiles on the base and modified activated carbon materials.

4.6 Thermal reduction on activated carbon BPL

It has previously been shown that the effect of heat treatment on activated carbon is to thermally desorb surface oxygen functionalities [¹⁵][¹⁶], resulting in a more hydrophobic carbon surface. In terms of water adsorption, this will result in a displacement of the

isotherms to higher relative pressure and lower uptakes [16][17]. These effects are usually reversible with time and re-oxidation of the carbon surface is observed unless the material is kept using controlled (dry) storage conditions or if a hydrophobic protection method is applied [18]. The effects of heat treatment on the external surface compositions of the carbon granules are represented by the XPS data given in Figure 4.14. This graph clearly illustrates the decrease of oxygen levels for the BPL carbon series within the heat treatment temperature (HTT) range from 400 to 1100°C.

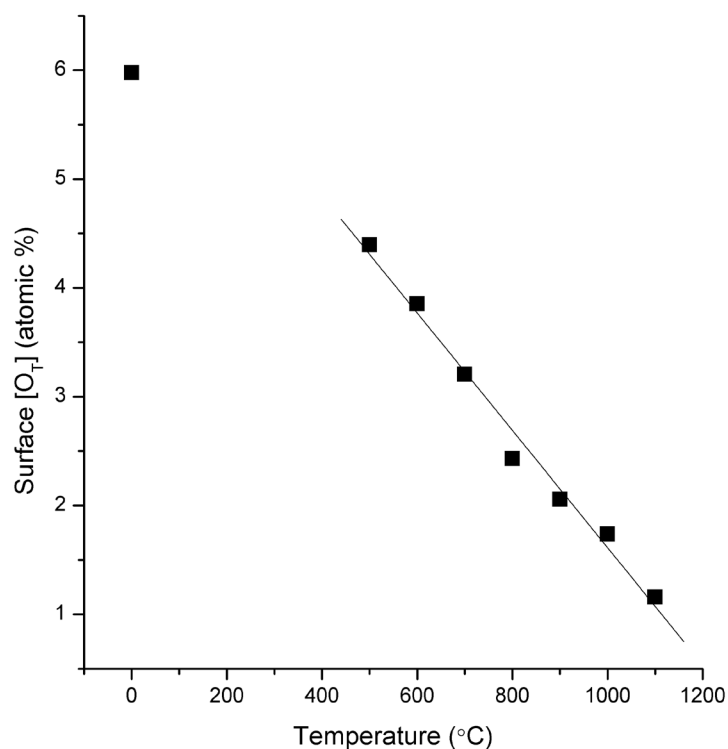


Figure 4.14: Effects of heat-treatment on XPS measured surface oxygen levels for BPL carbon. Linear fitting within the temperature range of 400 to 1100°C is also included.

The Eq. 4.1 was obtained by regression analysis of the XPS data from the heat treated activated carbons shown in Figure 4.14. The fitting was carried out for data above

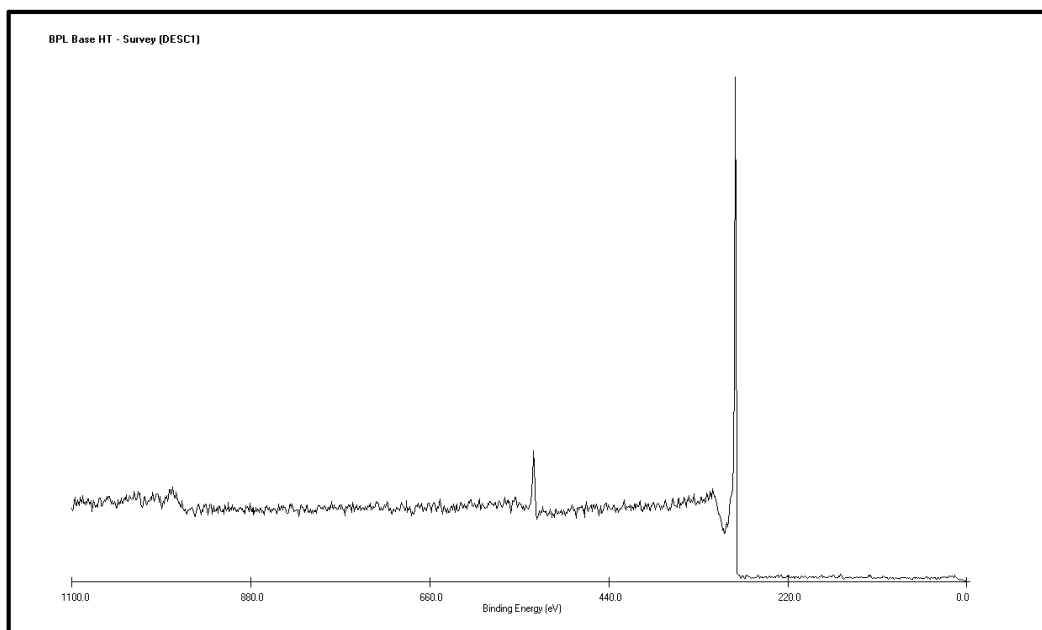
400°C to 1100°C so the y-intercept value of 7.00 at.% (theoretical oxygen level for untreated BPL) is slightly higher than the one measured experimentally and the correlation coefficient, R^2 , obtained is equal to 0.986.

$$[O]_T(\text{at. \%}) = 7.00 - 5.39 \cdot 10^{-3} \cdot T(^{\circ}\text{C}) \quad \text{Eq. 4.1}$$

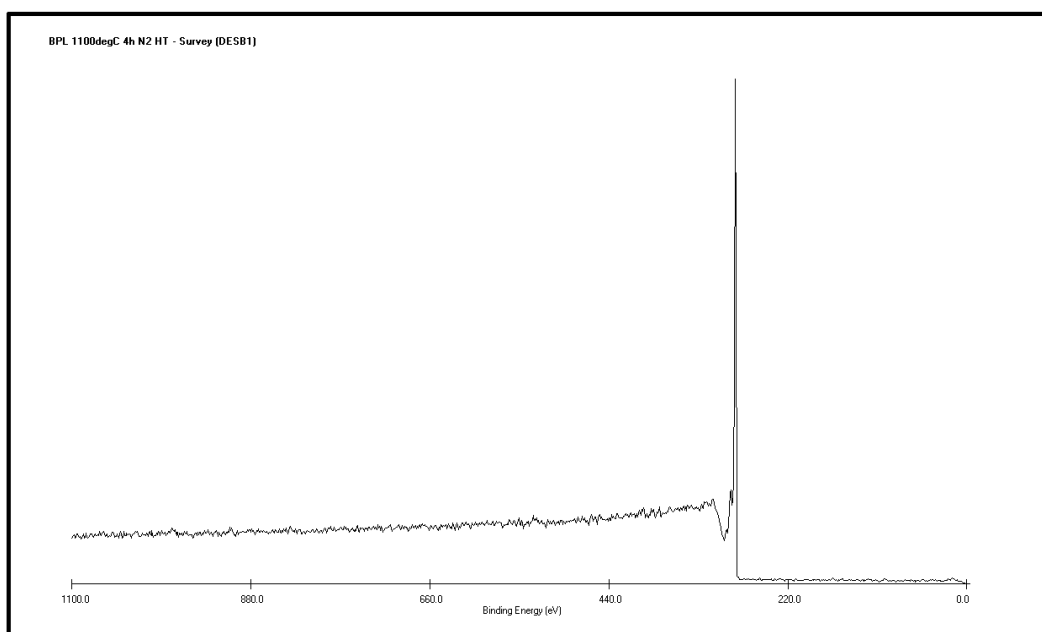
This equation, which describes the behaviour of our samples, may provide a basis for predicting the surface oxygen concentration left after heat treatment (within the range of 300 to 1200°C) for any activated carbon having similar characteristics than BPL.

The Figure 4.15 contains the survey XPS spectra recorded for the base material and for the material treated at the highest temperature. The spectrum from the base material (Figure 4.15 a)) shows two peaks corresponding to the Carbon1s peak at a binding energy 284.6 eV and Oxygen1s peak at binding energy 532 eV whereas only the C1s peak is visible on the spectra of the heat treated BPL (Figure 4.15 b)). The quantification of the surface composition has been done using the O1s and C1s narrow scan spectra.

The Carbon1s peak envelope for this series, which have not been represented here, have been fitted with five components: a main C–C/C–H peak at 284.6 eV, three lower intensity peaks at shifts of +0.9, +2.3 and +4.1 eV which have been assigned respectively to [phenolic, alcohol, ether], [carbonyl or quinone] and [carboxyl or ester] groups and a fifth peak at +6.5 eV which is usually associated with the shake-up of π electrons in the aromatic structure of the graphene rings. The proportion of each component seems to remain almost the same as the temperature of the heat treatment increases. But a slight decrease for the Peak II to IV (peaks from oxygen-containing functional groups) associated to a small increase of the peak V (shake-up satellite peak) (from 10 to 14% of the C–C/C–H intensity) is observed. This is most likely due to thermal desorption of (sp³ hybridised) low molecular weight carbon surface contamination which reveals more aromatic carbon as significant structural rearrangement of the carbon aromaticity is not expected at these temperatures.



a)



b)

Figure 4.15: Survey scans obtained for activated carbon BPL. a) Base material and b) carbon heat treated at 1100°C under N₂.

From the O1s narrow scan spectra represented on Figure 4.16, one observes that the O1s peak area is diminishing as the heat treatment temperature increases (up to 1373°K) which illustrates clearly the effects of heat treatment in terms of thermal desorption of surface oxygen groups. It must be remembered that the photoelectrons excited in the XPS experiment have a maximum escape depth (attenuation length) of 5~10 nm and so only reflect the surface and very near surface oxygen levels of the carbon granules however, based on other thermal desorption studies which used mass spectrometer detection of desorbing oxide species [¹⁹], it is reasonable to assume that similar oxygen loss occurs pretty much uniformly throughout the pore structure; the only differences being the differing diffusion constants for species originating from external surface and within pores of differing widths. Correction of the peak areas, using the relevant relative sensitivity factors, shows that the surface oxygen level falls from 5.98 at.% for the base BPL to respectively 4.40, 2.06 and 1.16 at.% on the BPL 500°C BPL, 900°C and BPL 1100°C materials.

As for carbon black material, the O1s peak can be fitted using two individual component peaks: Peak I {~531.5 eV} for carbonyl groups and Peak II {~533.3 eV} for hydroxyl or ether groups. Another interesting point is the fact that the heat treatment seems to have a clear effect on the proportion of these two peaks. The contribution of the carbonyl groups decreases from 51% for the base BPL to 36 and 43% for the heat treated BPL at 500 and 900°C. For the BPL 1100°C, as the intensity of the oxygen peak is very low, the analysis (computation) needs to be taken with precaution as the two individual are not really distinguishable from each other. It still results in two components but the position of peak I (present at 532.3 eV) is shifted compared to its usual position.

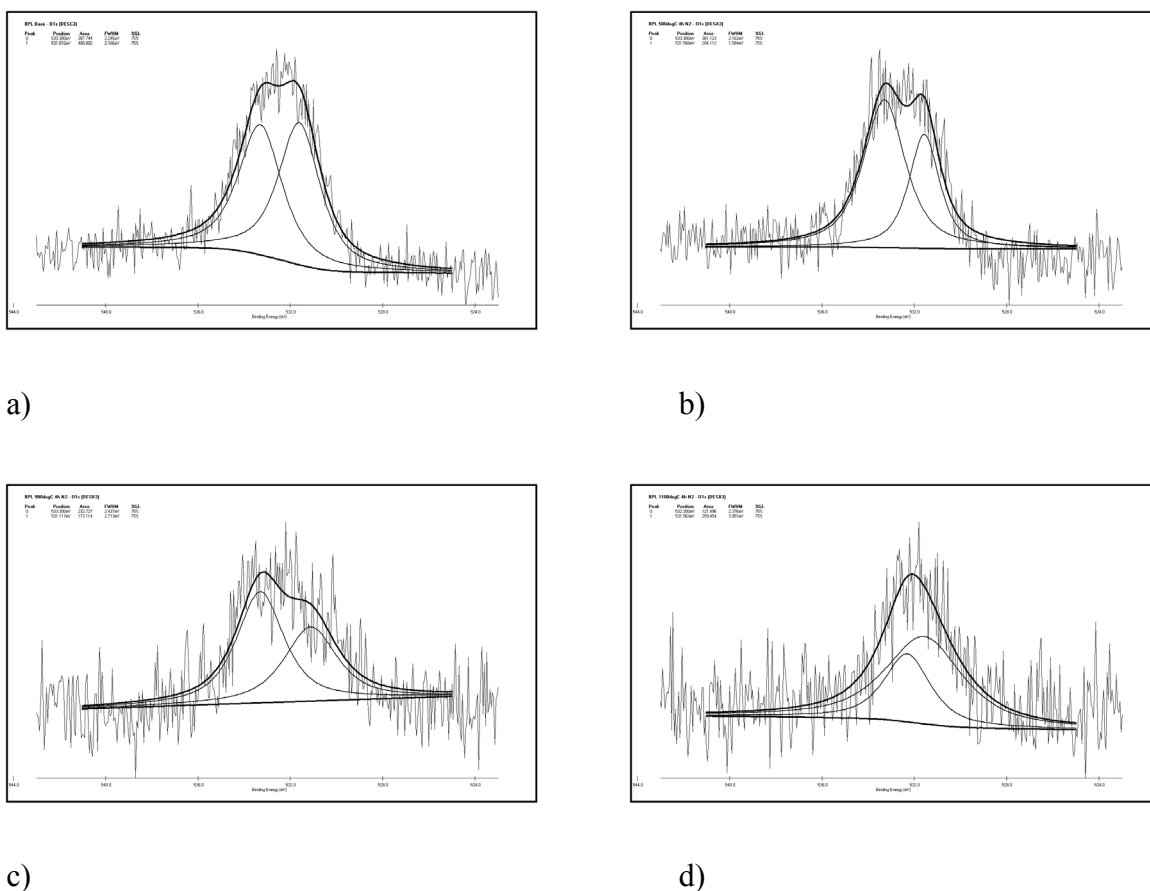
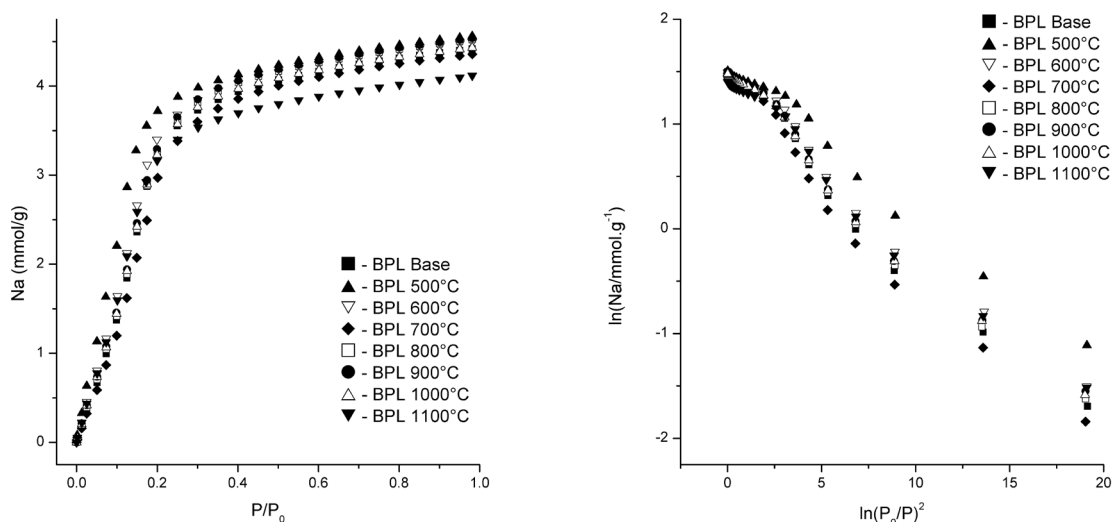


Figure 4.16: O1s narrow scan spectra for the heat treated activated carbon series. a) BPL base, b) BPL 500°C N₂, c) BPL 900°C N₂ and d) BPL 1100°C N₂.

The effect of heat treatment on porosity was checked using toluene adsorption at 303°K. Except for the BPL 1100°C which seems to have lower total pore volume, it appears that the structural integrity of the materials has not been affected strongly by the heat treatment as all the adsorption isotherms have a similar Type I shape as shown on Figure 4.17 a).



a)

b)

Figure 4.17: a) Toluene adsorption isotherms on the heat treated BPL carbons at 303°K and b) corresponding DR plots.

The DR plots are represented in Figure 4.17 b) and show that two linear regions are present in the low pressure domain. Heat treatments at temperature above 800°C are reducing marginally the porosity but care should be taken into account as the DR plots were not evident to fit due to the two linear zones which may indicate the presence of two different sized micropore groups.

References

- ¹ H. Wang, X. Wang, X. Li and H. Dai. Chemical self-assembly of graphene sheets. *Nano Research* **2** (2009) 336-342.
 - ² D. Pandey, R. Reifenger and R. Piner. Scanning probe microscopy study of exfoliated oxidized graphene sheets. *Surface Science* **602** (2008) 1607-1613.
 - ³ F. Atamny, T. F. Fassler, A. Baiker and R. Schlogl. On the imaging mechanism of monatomic steps in graphite. *Appl. Phys. A* **71** (2000) 441-447.
 - ⁴ T. Tsukamoto and T. Ogino. Morphology of graphene on step-controlled sapphire surfaces. *Applied Physics Express* **2** (2009) 075502 1-3.
 - ⁵ P. Nemes-Incze, Z. Osvath, K. Kamaras and L. P. Biro. Anomalies in thickness measurements of graphene and few layer graphite crystals by tapping mode atomic force microscopy. *Carbon* **46** (2008) 1435-1442.
 - ⁶ D. J. Kohls and G. Beaucage. Rational design of reinforced rubber. *Curr. Opin. Solid State Mat. Sci.* **6** (2002) 183-194.
 - ⁷ C. Jäger, T. Henning, O. Spillecke and R. Schlögl. Spectral properties of carbon black. *J. Non-Cryst. Solids* **258** (1999) 161-179.
 - ⁸ F. A. Heckman. Microstructure of carbon black. *Rubber Chem. Technol.* **37** (1964) 1245-1298.
 - ⁹ Q. Li, X. Zhang, G. Wu, S. Xu and C. Wu. Sonochemical preparation of carbon nanosheet from carbon black. *Ultrasonics Sonochemistry* **14** (2007) 225-228.
 - ¹⁰ W. M. Hess and C. R. Herd. *Carbon black* (eds. J. B. Donnet, R. C. Bansal and M. J. Wang) (Marcel Dekker, New York, 1993).
 - ¹¹ R. D. Heidenreich, W. M. Hess and L. L. Ban. A test object and criteria for high resolution electron microscopy. *J. Appl. Cryst.* **1** (1968) 1-19.
 - ¹² F. A. Heckman and D. F. Harling. Progressive oxidation of selected particles of carbon black: further evidence for a new microstructural model. *Rubber Chem. Technol.* **39** (1966) 1-3.
-

- ¹³ R. L. Vander Wal, A. J. Tomasek, K. Street, D. R. Hull and W. K. Thompson. Carbon nanostructure examined by lattice fringe analysis of high-resolution transmission electron microscopy images. *Appl. Spectrosc.* **58** (2004) 230-237.
- ¹⁴ G. S. Szymaski, Z. Karpiski, S. Biniak and A. Witkowskic. The effect of the gradual thermal decomposition of surface oxygen species on the chemical and catalytic properties of oxidized activated carbon. *Carbon* **40** (2002) 2627-2639.
- ¹⁵ S. S. Barton, M. J. B. Evans and B. H. Harrison. Surface studies on carbon: water adsorption on polyvinylidene chloride carbon. *J. Colloid Interface Sci.* **45** (1973) 542-548.
- ¹⁶ F. Stoeckli, F. Kraehenbuehl and D. Morel. The adsorption of water by active carbons, in relation to the enthalpy of immersion. *Carbon* **21** (1983) 589-591.
- ¹⁷ R. H. Bradley and B. Rand. The adsorption of vapours by activated and heat-treated microporous carbons. Part 2. Assessment of surface polarity using water adsorption. *Carbon* **31** (1993) 269-272.
- ¹⁸ L. B. Adams, C. R. Hall, R. J. Holmes and R. A. Newton. An examination of how exposure to humid air can result in changes in the adsorption properties of activated carbons. *Carbon* **26** (1988) 451-459.
- ¹⁹ S. S. Barton, M. J. B. Evans and J. A. F. MacDonald. The adsorption of water vapor by porous carbon. *Carbon* **29** (1991) 1099-1105.

5

Chapter 5 Specific and non-specific interactions (during the adsorption of alcohols) on non-porous carbon black surfaces

Abstract

The interactions which take place between the methanol, ethanol or isopropanol molecules and the surfaces of non-porous carbon blacks with increasing concentrations of oxygen atoms have been studied using immersion calorimetry and adsorption isotherm analysis. The surface oxygen level has been controlled by ozone treatment and characterised using X-ray photoelectron spectroscopy (XPS), which gives a quick, direct and quantitative measurement of the surface composition. This technique can be considered novel in the case of detailed carbon adsorption studies as it has not yet been extensively employed in this field. The physical structure of the carbon black material has not been modified by the ozone treatment as shown by the results of nitrogen adsorption at 77°K and enthalpy (heat) of immersion $-AH_i$ (mJ/g or mJ/m²) data for toluene. As the total oxygen concentration $[O]_T$ (at.%) on the carbon black surface increases, a systematic shift to higher adsorption values is observed on each alcohol isotherms. This can be explained because of the increasing specific hydrogen bonding interactions between the alcohol –OH groups and surface oxygen atoms. This effect is most significant in the case of methanol confirming that the mechanism of adsorption is dominated by hydrogen bonding and in consequence strongly dependant on the content of oxygen sites present on the surface. The same effect is also observed but less marked for ethanol and isopropanol because of the increasing non-specific (dispersion) interactions of the alkyl chain with the non-polar function of the carbon surface. This description is consistent with the specific enthalpies of immersion $-AH_i$ (mJ/m²) data obtained for alcohols, water and toluene. These measurements allow a semi-quantitative assessment of the relative polar and dispersion contributions to the overall interactions as function of both carbon surface oxygen composition and the molecular structure of the alcohols. An overall correlation exists between oxygen level $[O]_T$ (at.%) from XPS, heat of immersion $-AH_i$ (mJ/m²) values and the adsorption behaviour with the characteristic energy E (kJ/mol) of the DRK equation. It is also observed that the values of the affinity coefficient β_{DRK} increase directly as a function of $[O]_T$ indicating that this latter parameter may provide a initial basis for the prediction of the adsorption isotherms of certain polar vapours on non-porous carbon surfaces and possibly on porous carbon material. The variation of the adsorption mechanism brought to the fore by the change of isotherm shape from Type III for the base N330 (and also for the graphitised carbon black N234G) to type II for the oxidised N330 materials due to the effects of carbon surface chemistry is discussed in this chapter and the resulting effects on the surface area parameters S_{DRK} and S_{BET} (m²/g) are also considered.

5.1 Introduction and theoretical

The interaction between carbon surfaces with most organic molecules is dominated by dispersion forces which are considered as “*non-specific interactions*”. In contrast, when active sites are present on the carbon surface, relatively strong interactions may occur through hydrogen bonding between these sites and polar molecules adsorbing on the surface. These specific sites which are usually oxygen-containing surface groups located mainly on the edges or defects of the graphene layer-planes of the carbon structure, gave their name to these interactions: “*specific interactions*”. As discussed by a number of researchers, this phenomenon is observed in the case of water [1][2][3][4][5][6] and to some extent for the alcohols [7][8][9]. In the case of non-porous carbons, direct evidence of this is provided by the linear increase of the specific enthalpy of immersion - $\Delta H_i(\text{water})$ with the surface oxygen content from the lower limit of approximately 35 mJ/m² which defines the non-specific (dispersion) interaction of an oxygen free carbon surface. In the instance of interactions of polar molecules with porous carbons, the same type of behaviour does of course occur but the precise relationship is much more complex to quantify since new difficulties arise due to: the positions of the polar sites, which may be located within the complex pore structure of the carbon, making them less readily available to direct interrogation, for example, by spectroscopic means such as XPS which was used in this study; and kinetic effects, which may appear due to the slow diffusion of water in hydrophobic regions of microporosity.

Define a correlation or find a relationship between the surface chemistry of carbon, the well defined structure of the adsorbent and the character of the resulting adsorption isotherm represents an important challenge in the field of gas and vapours adsorption on carbon materials. The idea is to allow predictions of adsorption behaviour on the basis of simple structural and chemical parameters for most carbon (or porous) materials and different gas or vapours. Stoeckli [4][7] has shown that this can be achieved for activated

carbons using the framework of the adsorption theory of Dubinin and its extension to immersion calorimetry which provides complementary information on the specific interactions. In his work, coherent descriptions have been offered for the water isotherm and the isotherms of methanol and ethanol using the classical Dubinin-Radushkevich approach as described previously in the literature review and theory chapter. The affinity coefficient β_i for the adsorbate i , (calculated using the molar volume ratio $\beta_i = M_{V,i}/M_{V,REF}$) was found to vary directly with the degree of the specific interactions and therefore the surface chemistry of the activated carbon.

Regarding non-porous surfaces and more specially graphitized and non-graphitized carbon blacks, the adsorption process can be described by an alternative to the classical Dubinin-Radushkevich equation [¹⁰][¹¹], called the Dubinin-Radushkevich-Kaganer (DRK) equation [¹²] in which the equilibrium adsorption volume W (cm³/g) and the micropore volume W_0 (cm³/g) of the former expression are replaced respectively with the amount adsorbed N_a (mmol/g) and the monolayer capacity N_{am} (mmol/g). Moreover the term E_{DRK} corresponds to the characteristic energy of the first monolayer rather than micropore filling. If one considers its modern formulation and for the submonolayer region, the equation can be written:

$$N_a = N_{am}(DRK) \cdot \exp \left[- \left(\frac{A}{E_{DRK}} \right)^2 \right] \quad \text{Eq. 5.1}$$

where N_a is the amount adsorbed at temperature T and pressure P and N_{am} is the monolayer capacity. The quantity $A = R \cdot T \cdot \ln(p_0/p)$ is the adsorption potential $-\Delta G$, also used in the classical DR equation for the theory of volume filling of micropores (TVFM) [¹⁰][¹¹], p is the equilibrium pressure, p_0 the saturated vapour pressure at T . E_{DRK} is the characteristic energy.

In comparison with the BET approach [13], $N_{am}(DRK)$ and the corresponding surface area S_{DRK} (m^2/g) for many non-porous materials obtained from Eq. 5.1 are frequently different from $N_{am}(BET)$ and S_{BET} obtained from the same isotherm, but at higher relative pressures ($0.05 < p/p_0 < 0.30 \sim 0.35$). As discussed by Hugi-Cleary, Wermeille and Stoekli [14], this can be explained by the fact that the exponent, fixed to the value 2, corresponds to a distribution of the adsorption energy (surface heterogeneity) which does not reflect reality for a given solid. Therefore it was suggested that the classical DRK equation (Eq. 5.1) could be replaced by a flexible expression with a variable exponent n and by substituting $N_{am}(DRK)$ by $N_{am}(BET)$. The latter named could be considered as the real surface area of a non-porous solid but it should be noted that, as discussed by Stoekli and Centeno [15], this is not necessarily the case for porous solids. One then obtains a reasonable general working equation:

$$Na = Nam(BET) \cdot \exp \left[- \left(\frac{A}{E_{DRK}} \right)^n \right] \quad Eq. 5.2$$

In the case of carbon black materials, a value of $n \approx 2$, which is similar from the classical DR value has been found to be appropriate as suggested in different studies [16][8]. Under these conditions and as a first approximation, one may use the following working expression:

$$Na = Nam(BET) \cdot \exp \left[- \left(\frac{A}{E_{DRK}} \right)^2 \right] \quad Eq. 5.3$$

As indicated in the work of Stoekli et al. [17], the adsorption of non-specific vapours such as C_6H_6 , N_2 , CCl_4 , CH_2Cl_2 and CO_2 onto microporous carbon blacks XC-72 and XC-72-16 gives relatively good linear logarithmic plots for the low-pressure data with the corresponding characteristic values of E_{DRK} . It also appears, from data obtained at different temperatures, that the principle of temperature-invariance of E_{DRK} , required

by Dubinin's theory, is fulfilled. However the affinity coefficient β of a vapour i derived for a non-porous carbon surface using the DRK method i.e. $\beta_{DRK}(i)$ does not seem to be necessarily equal to the value for the volume filling of micropores suggested by Wood [18]. As a reminder, the coefficient $\beta_{DRK}(i)$ is given by the following expression:

$$\beta_{DRK}(i) = \frac{E_{DRK}(i)}{E_{DRK}(Ref)} \quad \text{Eq. 5.4}$$

where $E_{DRK}(i)$ is the characteristic energy derived from the slope of the DRK plot for the vapour i and $E_{DRK}(Ref)$ is the energy for the reference vapour which is usually benzene.

So the actual determination of the isotherm for benzene is required, as well as the isotherms of other vapours (nitrogen, alcohols, etc...) if one wants to keep benzene as a reference. Hence, taking nitrogen adsorbed at 77°K as the reference instead of benzene may be a wise choice since it is frequently used for adsorption characterisation studies but also for health and safety issues regarding benzene. Therefore reference isotherms are often readily available but $E_{0,DRK} = E_{DRK}(C_6H_6)$ is not necessarily given by the simple expression $0.33 \cdot E_{0,DRK}(N_2)$ i.e. by assuming that $\beta(N_2) = 0.33$.

From the above, it is tempting to correlate β_{DRK} for alcohols, or other polar adsorptives, adsorbed on non-porous carbons with the amount of surface oxygen $[O]_T$ measured by X-ray photoelectron spectroscopy (XPS) or by other techniques such as TPD or titration. Following this reasoning could make possible to predict the adsorption isotherm for a specific and well characterised material on the basis of Eq. 5.1 to Eq. 5.3 and with the help of the parameters $N_{am}(BET)$, $E_{0,DRK}$ and the function $\beta_{DRK}(alcohols) = f([O]_T)$.

This chapter describes the adsorption of the following alcohols: *methanol, ethanol and isopropanol* on a series of non-porous carbon black surfaces which have the same

physical characteristics but increasing levels of oxygen controlled by ozone oxidation and quantified by XPS. It is shown that this approach allows a systematic study of the effects of surface oxygen chemistry on the dominant mechanisms of adsorption and on the resulting vapour adsorption isotherms. The adsorption data are analysed using the classical BET and Dubinin-Radushkevich-Kaganer equations designed for adsorption on non-porous carbon surface. A particular interest in this work is the fact that the affinity coefficient (β_{DRK}) values for polar molecules such as alcohols and water on the different surfaces have, as mentioned above, previously been observed to change with the degree of surface polarity but for which no quantitative relationship using direct measure of surface oxygen content currently exists. In addition, calorimetric data obtained from the immersion of the modified carbon materials in the corresponding liquid phases of the adsorptive was used. It gives a complementary indication of the relative specific and non-specific interactions for each system to help us to comment the observed behaviour. In this work, water has also been used as a probe for immersion calorimetry, but the more complex relationships between adsorption of water vapour and the varying oxygen levels of the carbon black surface have been investigated separately and the details of this study are reported in the next chapter of this thesis.

5.2 Experimental

Although the characterisation techniques and chemical treatments have already been described in the experimental Chapter, more experimental details related to this particular study are given in the paragraphs below.

The non-porous carbon black N330 (Cabot Co., USA) has been used as the base material for treatment in order to produce a small range of materials with increasing and controlled surface oxygen levels. N330 has a quoted surface area of 77 m²/g and has been used in several previous adsorption studies where areas of 80.0 m²/g (± 8 m²/g) have

been reported from nitrogen adsorption isotherm analysis using both BET and α_s methods [19][20]. The material used in this study has an intrinsic surface oxygen level of 1.7 at.% measured by X-ray photoelectron spectroscopy (XPS). Ozonation of this material has been carried out in a fluidised bed system of the type described in previous publications [20] for duration times of 5, 10, 30, 60 and 120 min. Adsorption of the alcohols onto a graphitized (2973°K) carbon black N234G (Cabot Co., USA) has also been investigated. This material has a BET surface area of 92 m²/g (\pm 4 m²/g), a surface oxygen level of 0.5 at.% and an enthalpy of immersion in water of $-\Delta H_i(H_2O) = 28.0$ mJ/m². This material was used as the reference for the construction of the α_s plots. Vapour adsorption and immersion calorimetry work was carried out using Analar grade liquids: methanol (Acros Organics, UK), ethanol, isopropanol and toluene (Fisher Scientific, UK). Toluene was chosen as a non-polar probe with which to carry out immersion in preference to benzene which is a known carcinogen.

XPS measurements have been made using the Kratos HSi 5-channel monochromated instrument, at a residual vacuum of 10⁻⁸ mBar with AlK α radiation of energy 1486.6 eV and with the analyser in FAT mode. The carbon samples were presented in shallow sample dishes in the specially made stud. Surface compositions have been calculated from the areas of elemental peaks, after subtraction of a linear background, using Kratos relative sensitivity factors i.e. 0.25 for C1s and 0.66 for O1s photoelectron peak areas (absolute error of \pm <10%).

Immersion calorimetry has been carried out in a Setaram/Calvet C80 Instrument on samples that had been sealed in glass ampoules after being out gassed to 10⁻³~10⁻² mbar at room temperature. Enthalpy values, $-\Delta H_i$ (mJ/m²) have been calculated using $S_{BET}(N_2)$ values.

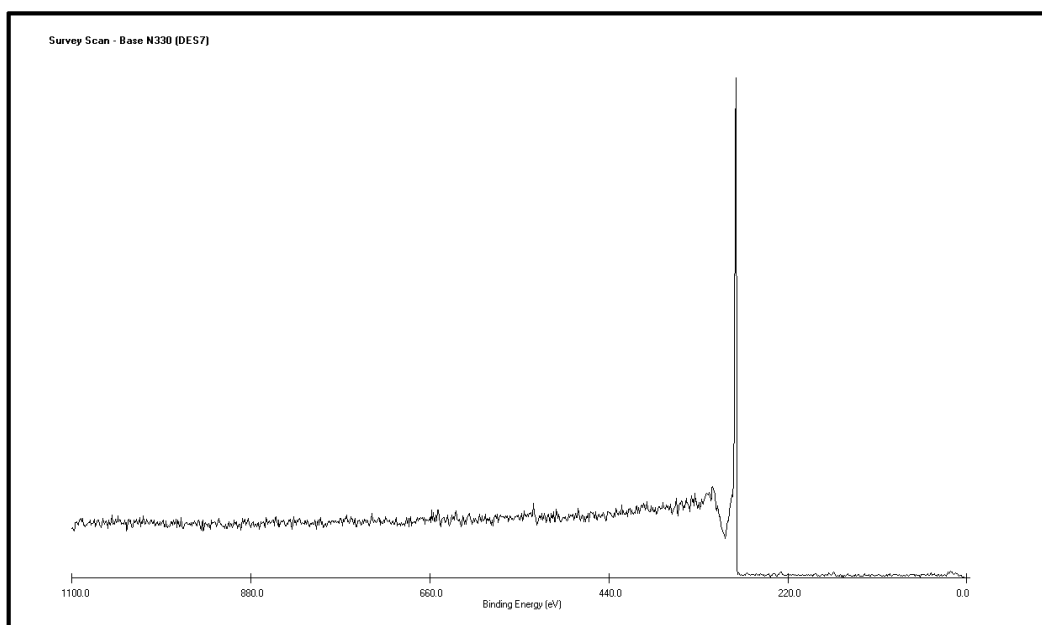
Adsorption isotherms for methanol, ethanol and isopropanol at 303°K have been measured using a Hiden/IGA gravimetric system after out gassing to constant weight at 353°K (which was chosen in order to minimise thermal rearrangement and

decomposition of surface oxygen groups i.e. significantly below the first thermal desorption peak usually observed in TPD data at 450°K [21]). Equilibrium adsorption for each point of P/p_0 was defined from kinetic data such that no effective weight changes occurred. Isotherms for nitrogen at 77°K were measured using a Micromeritics ASAP2010 Volumetric apparatus, after out gassing as above, assuming a molecular area of 0.162 nm² and a P₀ value of 987 mbar. For the alcohols, molecular areas of (0.180 nm²) methanol (0.229 nm²) ethanol and (0.274 nm²) isopropanol have been calculated using the method described by Gregg and Sing [22] and respective saturated vapour pressure (P₀) values of 218, 105 and 78 mbar derived using the Antoine equation [23]. Isotherm data were fitted to the classical BET equation or to the DRK equation, the later using a value of n=2.

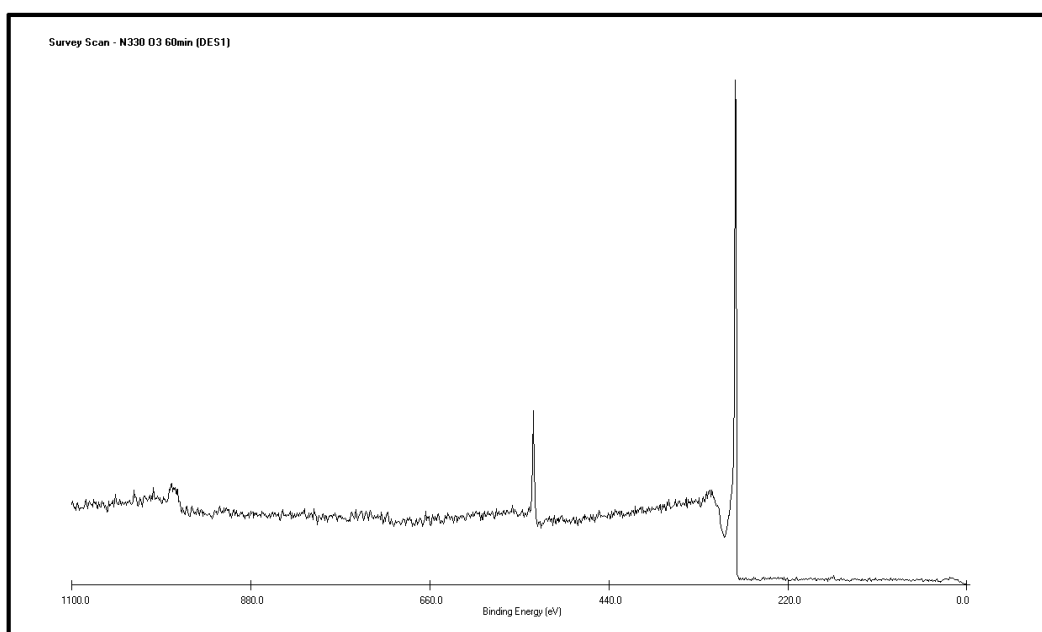
5.3 Results and discussion

5.3.1 XPS results

In this study, the ozone fluidized bed system has been used in order to produce carbon black surface of increasing oxygen concentration. The carbon black N330 was oxidised for various period of time (up to 120 min). The surface chemistry of the oxidised materials was then analysed using XPS. As the treatment time becomes longer, one observes on the survey spectra a gradual increase of the size of oxygen peak O1s. As an example, the survey spectra for the untreated carbon black and the oxidised with ozone for 60min are represented in the Figure 5.1. On the spectrum of the oxidised material, the apparition of a large oxygen 1s peak at a binding energy of 532eV is visible.

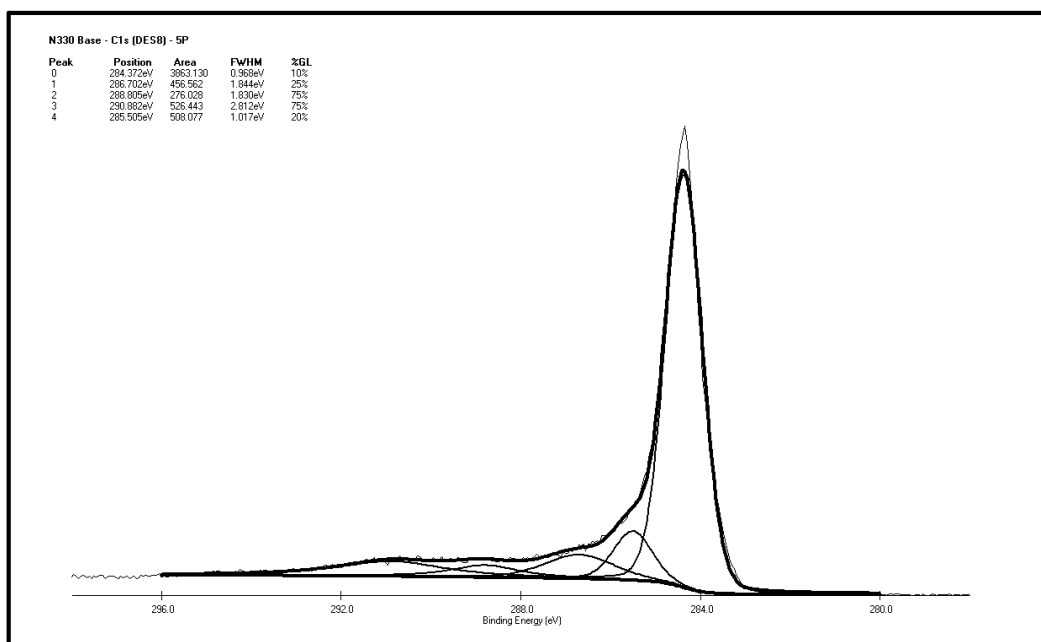


a)

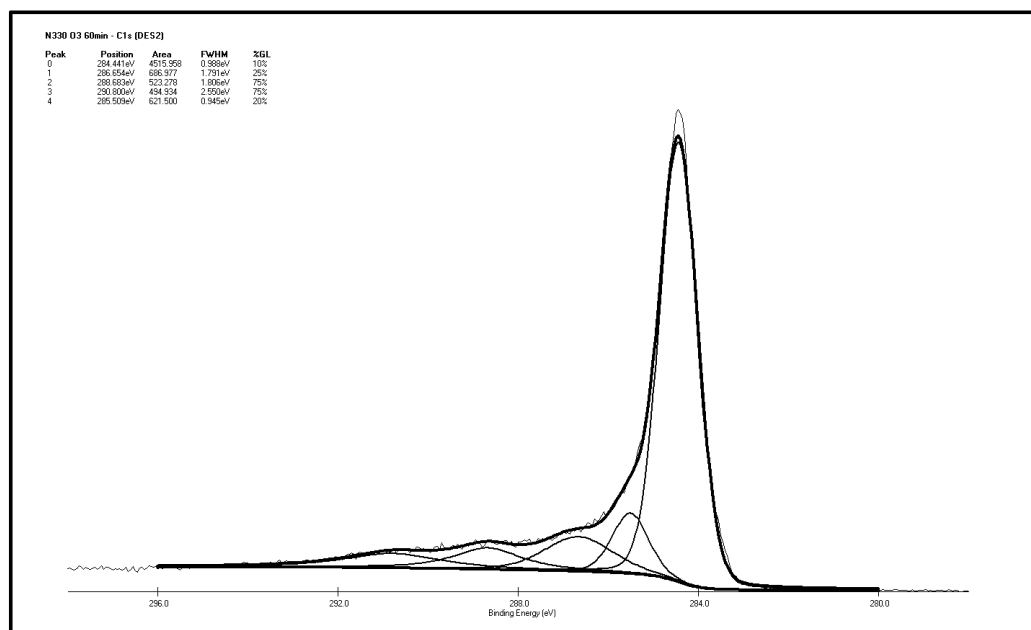


b)

Figure 5.1: Survey scans obtained for both a) untreated and b) ozone oxidized (60min) carbon black.



a)



b)

Figure 5.2: C1s narrow scan spectra for a) untreated and b) ozone oxidized (60min) carbon black.

For a better accuracy, the narrow scans O1s and C1s (area) were used to determine the relative atomic concentration of oxygen and carbon for each materials. Additionally, they were also used to determine the type and proportion of the diverse oxygen groups present on the surface.

The C1s narrow scan spectra for the base and ozone oxidised (60min) carbon black are represented in Figure 5.2. The deconvolution of the C1s gives us five individual peaks representing: Peak I graphitic carbon {~284.4eV}, Peak II carbon atoms present in phenolic, alcohol, ether {~285.0–286.0eV}, Peak III carbonyl or quinone groups {~286.3–287.1eV}, Peak IV carboxyl or ester groups {~288.1–289.1eV} and Peak V shake-up satellite peaks due to a π - π^* transitions in aromatic rings {~290.8–291.6eV} [24]. The main characteristics of these peaks for these two samples are summarised in Table 5.1.

Table 5.1: C1s decomposition results for base and 60-min ozonated carbon black.

Base N330				N330 O ₃ 60min			
Peak	Position (eV)	FWHM (eV)	Concentration (%)	Peak	Position (eV)	FWHM (eV)	Concentration (%)
I	284.4	0.97	69%	I	284.4	0.99	66%
II	285.5	1.02	9%	II	285.5	0.95	9%
III	286.7	1.84	8%	III	286.7	1.79	10%
IV	288.8	1.83	5%	IV	288.7	1.81	8%
V	290.9	2.81	9%	V	290.8	2.55	7%

The carbonyl/quinone groups and carboxyl/ester group surface concentrations increase significantly due to the effect of the ozone treatment. This compartment has already been observed by Yue et al. [25] during the electrochemical oxidation of carbon fibres. On the contrary, carbon in graphitic surface structures is reduced from 69 to 66% as a result of the increase in the oxidation level. The concentration of phenolic, alcohol and ether groups remains unchanged after the treatment.

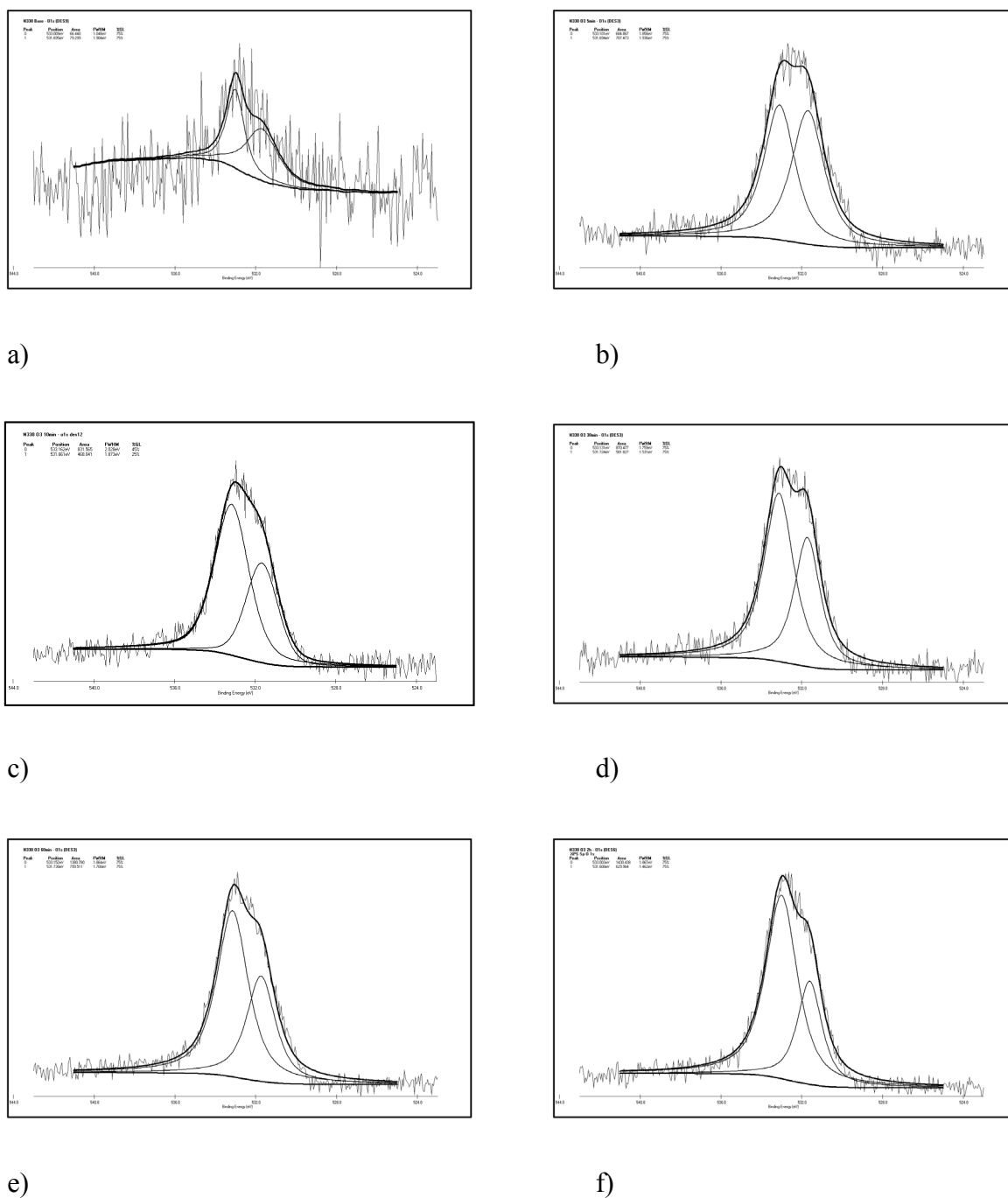


Figure 5.3: O1s narrow scan spectra for the oxidized carbon black series. a) untreated, b) N330 O₃ 5min, c) N330 O₃ 10min, d) N330 O₃ 30min, e) N330 O₃ 60min and f) N330 O₃ 2h.

On the other hand, as illustrated in Figure 5.3, the high resolution oxygen spectra can be resolved into only two individual component peaks: Peak I { $\sim 530.7\text{eV}$ } oxygen atoms from carbonyl groups (C=O) and Peak II { $\sim 533.1\text{eV}$ } oxygen atoms from

hydroxyl or ether groups (C–OH or C–O–C). It is common to find in the literature [25][26][24] a third peak {534.6–535.6eV} of low intensity corresponding to chemisorbed O₂ and/or water but for our oxidised carbon blacks, this peak was not detected (or was of very low intensity). Additionally, the oxygen peak for the base material is significantly smaller than for the oxidised materials and displays a high noise level.

The main characteristics of the O1s peak decomposition for the base and oxidised carbon blacks are summarised in Table 5.2.

Table 5.2: O1s decomposition results for base and oxidised carbon blacks.

Materials	Position (eV)		FWHM (eV)		Concentration (%)	
	Peak I	Peak II	Peak I	Peak II	Peak I	Peak II
Base N330	533.0	531.7	1.05	1.90	46%	54%
N330 O ₃ 5min	533.1	531.7	1.86	1.94	49%	51%
N330 O ₃ 10min	533.0	531.5	1.99	1.32	64%	36%
N330 O ₃ 30min	533.1	531.7	1.76	1.53	60%	40%
N330 O ₃ 60min	533.2	531.7	1.86	1.70	63%	37%
N330 O ₃ 2h	533.0	531.6	1.87	1.46	69%	31%

Regarding the respective concentration of these two peaks, a rise (from 46 to 69%) of the contribution of the peak I (carbonyl groups) is observed as the treatment time increases while the contribution of the peak II (hydroxyl or ether groups) decreases in the opposite way.

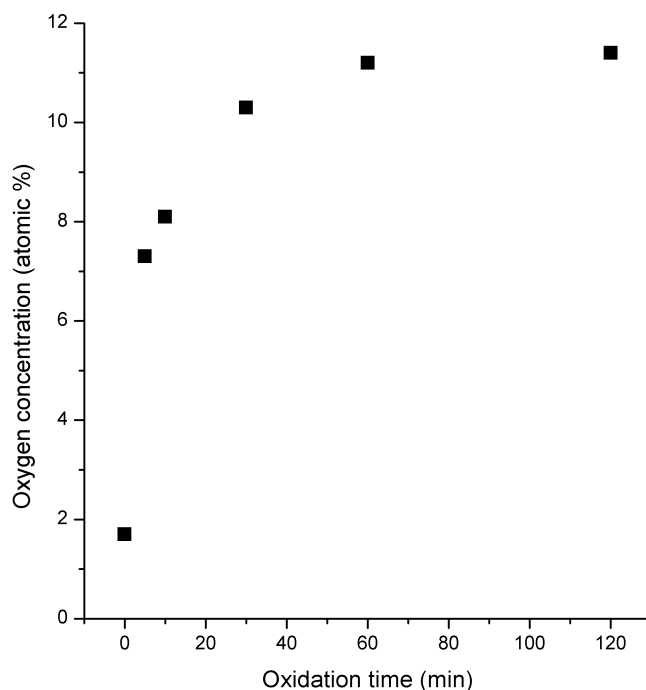


Figure 5.4: Oxygen level $[O]_T$ (at.%) measured by XPS for ozone-treated carbon black N330 as a function of oxidation time.

The increase of the surface oxygen concentration (chemisorbed oxygen atoms) as a function of the treatment time is represented in Figure 5.4. The plot shows a sharp increase in the first 10min from 1.7 at.% which is the level of the base material to 8.1 at.% then the increase slows down until the oxygen concentration reaches a plateau (~ 11.2 at.%) after 1h of oxidation. The oxygen concentrations of the oxidised N330 carbon blacks and other base carbon blacks (N234 and N234G) are summarised in the Table 5.3.

5.3.2 Characterisation with nitrogen adsorption and immersion calorimetry

Figure 5.5 a) shows isotherms for the adsorption of nitrogen at 77°K by the five carbon blacks and b) shows the low pressure regions ($P/P_0 < 0.1$) of the isotherm. Extended ozone treatment duration leads to higher adsorption level characterised by the relative position of the plots (lower for base material and upper position for 30 and 60 min O₃ treated materials).

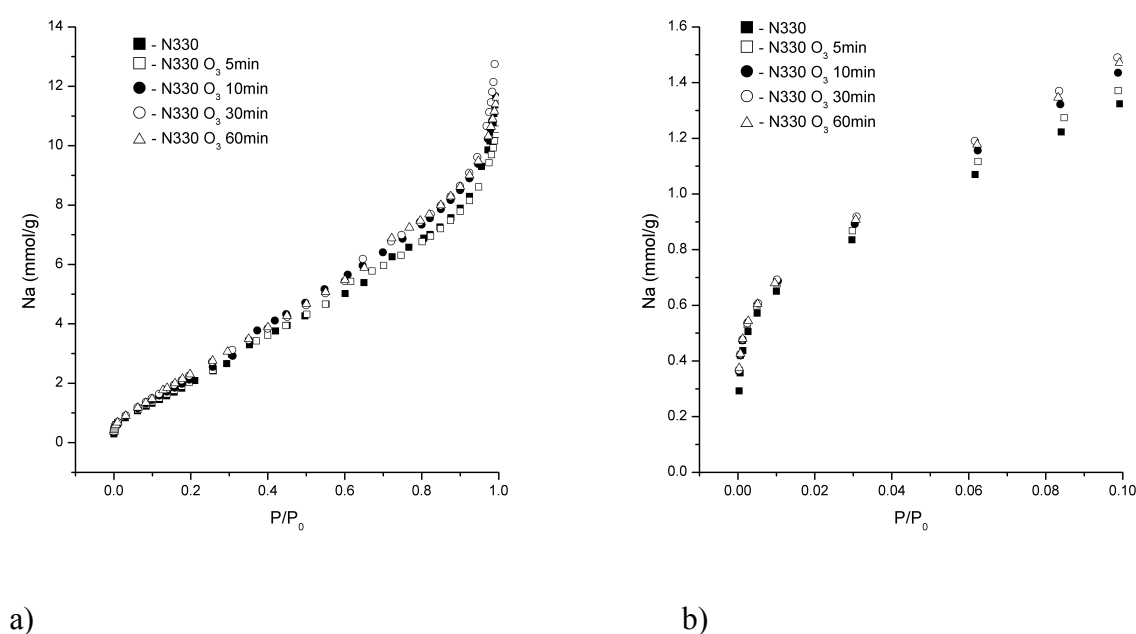
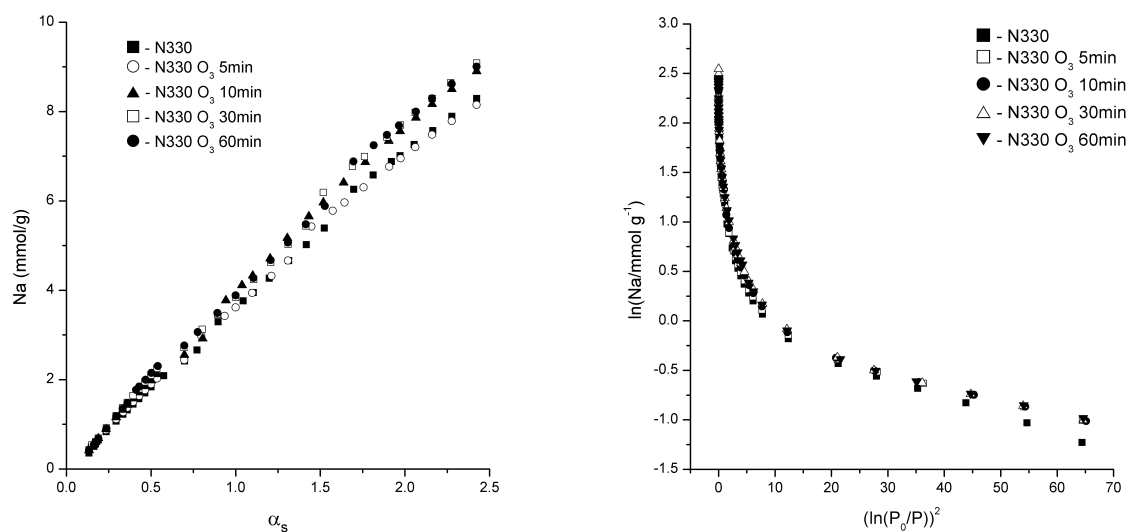


Figure 5.5: a) Nitrogen adsorption isotherms at 77°K for carbon blacks and b) expanded low pressure domains ($p/p_0 < 0.1$).

Figure 5.6 contains corresponding analyses obtained using: a) the α_s method [27][28] and b) the DRK method. Table 5.3 contains the relevant physicochemical data for the carbon blacks and one can infer that there is minimal change in the physical structure of the CBs as reflected by S_{BET} or S_{α_s} whilst the oxygen levels range from 1.7 to 11.2 at.%.



a)

b)

Figure 5.6: Nitrogen adsorption data analysis with a) α_s method and b) DRK method.

On the other hand, from Figure 5.7 a), the observed values of $-\Delta H_i(Tol)$ do not change significantly across the series of carbon blacks, hence it is concluded that neither nitrogen nor toluene is sensitive to the oxygen chemistry changes induced in the carbon black surfaces by the ozone treatment. The absolute values of $-\Delta H_i(Tol)$ observed are similar to those found in the literature for benzene [15] and for *n*-heptane [19]. Previous calculations of surface free energy values from nitrogen spreading pressures [19][29] for non-porous carbons with varying surface oxygen levels have also demonstrated that surface chemistry modification does not influence nitrogen adsorption. In those instances the absolute free energy values were found to be in the range 100~110 mJ/m² and therefore similar to the $-\Delta H_i(Tol)$ values shown here. Hence it was decided that nitrogen may conveniently be used as the reference vapour in place of benzene for the determination of $\beta_{DRK}(alcohol)$ using Eq. 5.4.

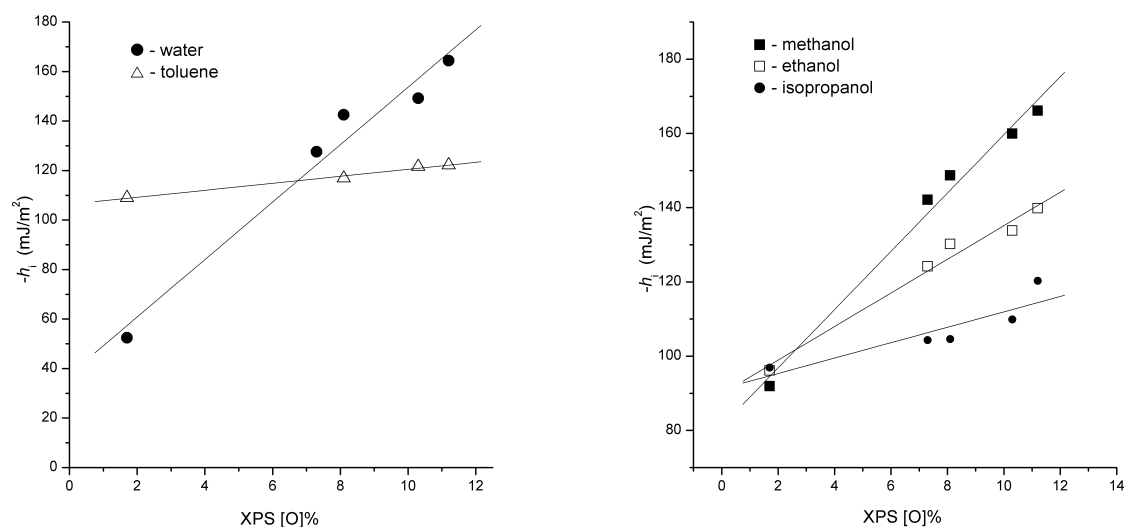
Table 5.3: Physicochemical characteristics of carbon blacks.

Materials	$S_{BET}(N_2)$ (m ² /g)	$S\alpha_s(N_2)$ (m ² /g)	$S_{DRK}(N_2)$ (m ² /g)	$E_{DRK}(N_2)$ (kJ/mol)	$[O]_T$ (at.%)	$-\Delta H_i(Tol)$ (mJ/m ²)	$-\Delta H_i(H_2O)$ (mJ/m ²)
Base N330	81.3	82.0	93.6	4.0	1.7	109.0	52.4
N330 O ₃ 5min	83.9	82.6	86.8	4.6	7.3	/	127.6
N330 O ₃ 10min	86.2	89.1	88.1	4.6	8.1	116.9	142.5
N330 O ₃ 30min	89.0	90.0	88.7	4.6	10.3	121.6	149.2
N330 O ₃ 60min	88.0	90.2	86.8	4.7	11.2	122.2	164.4
N234	107.6	98.6	121.8	4.0	1.5	i	68.6
N234G	90.9	92.0	94.6	5.1	0.5	i	28.0

Nitrogen surface areas from BET (S_{BET}), α_s ($S\alpha_s$) and DRK (S_{DRK}) methods, total surface oxygen level from XPS $[O]_T$ (at.%) and enthalpy of immersion for toluene $-\Delta H_i(Tol)$ and water $-\Delta H_i(H_2O)$.

ⁱ Enthalpy of immersion in toluene not measured for this sample.

From Figure 5.7 a), one can see that the enthalpy of immersion in water $-\Delta H_i(H_2O)$ increases in direct proportion to the surface oxygen levels of the CBs. This behaviour is in complete contrast with what is observed in the case of toluene $-\Delta H_i(Tol)$. The water values are in the same order than those previously reported for a wide range of carbon blacks of various types and levels of oxidation measured directly by XPS [20] and are also in agreement with studies by other groups based on the pH at the point of zero charge pH_{pzc} and temperature programmed desorption of oxygen complexes [4][30][31].



a)

b)

Figure 5.7: a) $-\Delta H_i$ (displayed as $-h_i$ on the graphs) values as a function of surface oxygen levels for water and toluene and b) for methanol, ethanol and isopropanol.

The regression analysis of water and toluene data leads to the following equations which are consistent with previously reported relationships [⁹][²⁰][³²][³³]:

$$-\Delta H_i(\text{H}_2\text{O})_{exp}(\text{mJ/m}^2) = 37.6 + 11.61 \cdot [\text{O}]_T \quad \text{Eq. 5.5}$$

$$-\Delta H_i(\text{C}_7\text{H}_8)_{exp}(\text{mJ/m}^2) = 106.4 + 1.41 \cdot [\text{O}]_T \quad \text{Eq. 5.6}$$

5.3.3 Adsorption of alcohols on oxidized carbon black surfaces

Adsorption isotherms for methanol, ethanol and isopropanol, represented in Figure 5.8, are all Type III for the untreated N330 and become Type II for the oxidised materials. Figure 5.8 a), b) and c) show clearly that the Type II isotherms are displaced gradually to higher adsorption values as the CB surface oxygen levels increase. For clarity, the low pressure ($p/p_0 < 0.6$) data are expanded on Figure 5.8 d), e) and f) and show that the

displacement occurring for all three alcohols as a function of surface oxidation is most marked for methanol whose the relative contribution of the polar –OH group is most prominent than the dispersion interaction of the alkyl chain. For methanol and ethanol, the displaced isotherms converge at a respective relative pressure p/p_0 of 0.5 and 0.3 with the isotherm of the base material whereas for isopropanol the convergence location is slightly broader since it takes place over the range of p/p_0 values: 0.17 to 0.24. At these relative pressure values correspond respective areas of 77 m²/g for methanol, 69 m²/g ethanol and 66~70 m²/g for isopropanol which indicates that overall these shifts are confined within the monolayer capacity for each adsorptive and therefore relates directly to specific interactions with carbon surface groups.

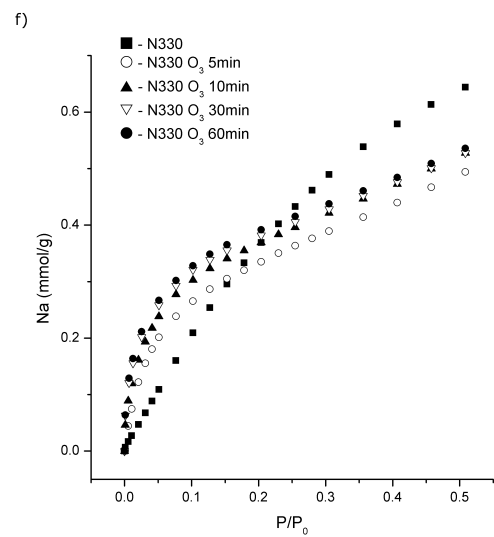
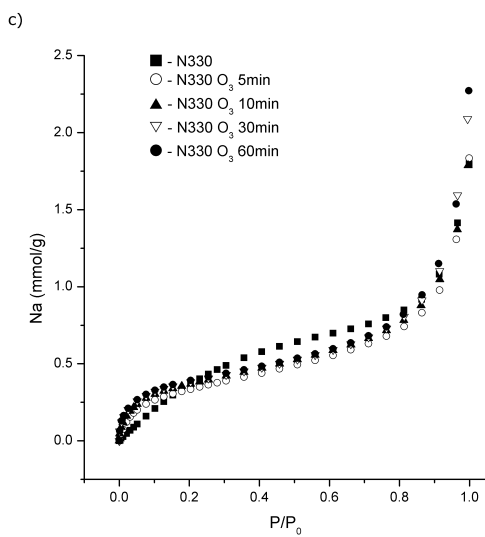
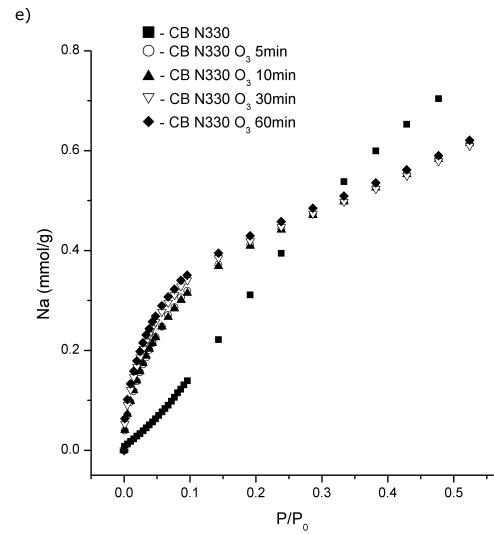
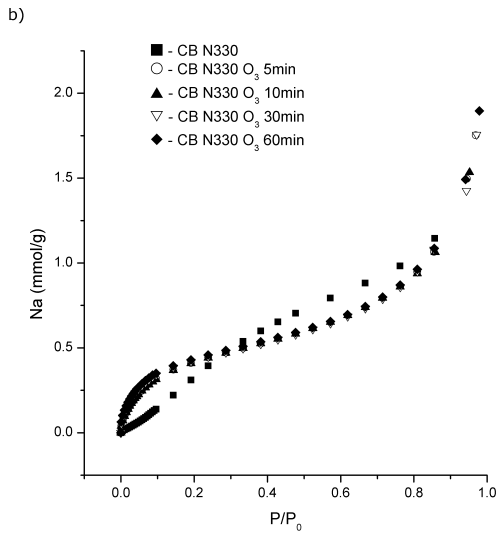
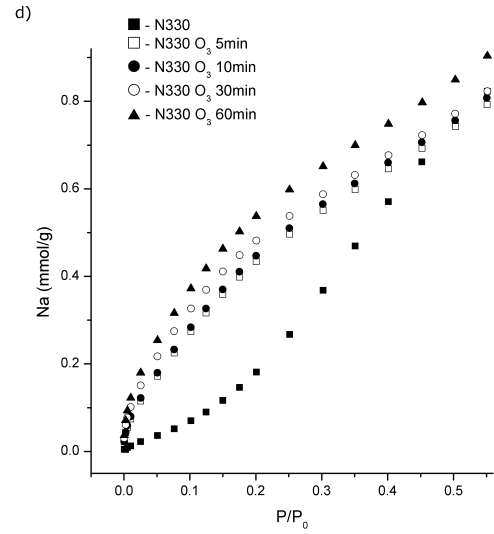
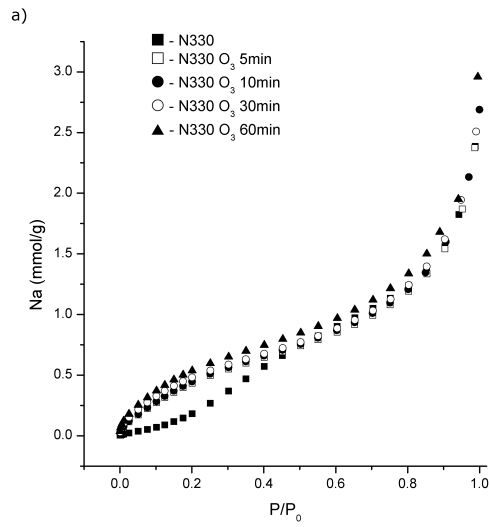


Figure 5.8: a), b) and c) Adsorption isotherms for methanol, ethanol and isopropanol including in d), e) and f) the expanded low pressure domains ($p/p_0 < 0.6$) showing displacement due to increasing specific interactions in sub-monolayer region and isotherm convergence near monolayer capacity.

Table 5.4 shows the increases in $-\Delta H_i(\text{alcohol})$ resulting from the increases in carbon black surface oxygen. The greater effect is observed for methanol which is the most polar of the three and whose smaller molecular size allows a higher proportion of $-\text{OH}$ interactions per unit area of surface. As shown in Figure 5.7 (b), the slopes of the plots decrease as expected as the alcohol chain length is increasing. From regression analysis of the experimental data one obtains the following expressions:

$$-\Delta H_i(\text{CH}_3\text{OH})_{exp}(\text{mJ}/\text{m}^2) = 81.2 + 7.85 \cdot [\text{O}]_T \quad \text{Eq. 5.7}$$

$$-\Delta H_i(\text{C}_2\text{H}_5\text{OH})_{exp}(\text{mJ}/\text{m}^2) = 89.9 + 4.53 \cdot [\text{O}]_T \quad \text{Eq. 5.8}$$

$$-\Delta H_i(\text{C}_3\text{H}_7\text{OH})_{exp}(\text{mJ}/\text{m}^2) = 91.2 + 2.07 \cdot [\text{O}]_T \quad \text{Eq. 5.9}$$

The limiting values between $81 \text{ mJ}/\text{m}^2$ and $91 \text{ mJ}/\text{m}^2$ correspond to the non-specific, dispersion, interaction between the alcohols and an ideal non-oxidised carbon surface. The difference can easily be attributed to the higher proportion of oxygen per unit surface area in the case of methanol (CH_3OH) and by the fact that carbon shows less affinity toward oxygen than for organic groups. As the alkyl chain length increases the contribution from specific interactions with oxygen groups decreases and the limiting value comes closer to $100\sim 110 \text{ mJ}/\text{m}^2$ obtained for pure hydrocarbons such as benzene, hexane and in our case toluene. The significant differences in the terms of each expression given in Eq. 5.5 to Eq. 5.9 clearly reflect the systematic change from hydrogen bonded dominated interactions for water through to non-specific, dispersion dominated, for toluene. Moreover, the BET analysis is in agreement with the immersion

data and the displacement of the adsorption isotherm and give C_{BET} values increasing with surface polarity of each alcohols (within the ranges 9 to 16 for methanol and 31 to 56 for ethanol and 41 to 99 for isopropanol as indicated in Table 5.4).

Table 5.4: Surface area (S_{BET} and S_{DRK}), characteristic energy E_{DRK} , C_{BET} constant values and enthalpy parameters from alcohol data.

Materials	Methanol				
	S_{BET} (m ² /g)	S_{DRK} (m ² /g)	E_{DRK} (kJ/mol)	C_{BET}	$-\Delta H_i$ (mJ/m ²)
N330 Base	-	-	8.4	-	91.9
N330 O ₃ 5min	52.9	24.9	11.0	9	142.1
N330 O ₃ 10min	54.0	26.1	11.1	10	148.7
N330 O ₃ 30min	52.0	30.6	11.6	14	159.9
N330 O ₃ 60min	57.4	36.0	11.7	16	166.1
Materials	Ethanol				
	S_{BET} (m ² /g)	S_{DRK} (m ² /g)	E_{DRK} (kJ/mol)	C_{BET}	$-\Delta H_i$ (mJ/m ²)
N330 Base	-	-	7.4	-	96.1
N330 O ₃ 5min	49.9	69.7	8.6	31	124.2
N330 O ₃ 10min	51.0	67.8	8.8	30	130.2
N330 O ₃ 30min	49.8	69.0	9.4	50	133.8
N330 O ₃ 60min	50.6	69.9	9.7	56	139.8
Materials	Isopropanol				
	S_{BET} (m ² /g)	S_{DRK} (m ² /g)	E_{DRK} (kJ/mol)	C_{BET}	$-\Delta H_i$ (mJ/m ²)
N330 Base	-	-	7.4	-	96.9
N330 O ₃ 5min	47.9	67.7	8.8	41	104.3
N330 O ₃ 10min	51.4	66.4	10.5	62	104.6
N330 O ₃ 30min	51.9	67.9	11.3	94	109.9
N330 O ₃ 60min	53.1	69.2	11.5	99	120.3

The plots representing the isotherm data for nitrogen and the alcohols in the form of Eq. 5.1 are given in Figure 5.9 where a) confirms that the nitrogen data coincide across all of the pressure range studied except for a very small deviation observed for the three lowest pressure points measured on the base material (see later). As a result of this, the calculated $S_{DRK}(\text{nitrogen})$ and $E_{DRK}(\text{nitrogen})$ values remains almost the same across the carbon black series as shown in Table 5.3. Regarding the alcohol plots represented in

Figure 5.8 b, c and d), a different behaviour than from nitrogen was observed. All the graphs superimpose nicely in the high pressure regions (low adsorption potential regions) but in the low pressure “*submonolayer*” domain (high adsorption potential region), the effects of the surface chemistry i.e. the differing levels of specific interactions are clearly observed and lead to S_{DRK} values given in Table 5.4. As a consequence of surface oxidation, the increase of adsorbed amount within the initial regions of the type II isotherms seen in Figure 5.8 and corresponding to a decrease of slope in the low pressure regions of the DRK plots, results in $E_{DRK}(\text{alcohols})$ values which are increasing with oxygen concentration on the carbon surface as shown in Table 5.4. An important point to note is the fact that the overall linearity of the plots is slightly variable and that the energy values are only given for comparative purpose as they do not relate directly to those derived from the classical form of the DR equation describing micropore filling. In the case of the adsorption of methanol on the base N330 material, the linearity of the data is quite poor and reflects the relatively weak non-specific interaction of the alkyl group coupled with the low level of surface oxygen and hence specific interactions with the polar –OH group of the methanol as described by Carrott [8]. It results that the isotherm has effectively a type II character but with a slight positive inflexion in the middle pressure region ($0.4 < p/p_0 < 0.5$) as the adsorbate-adsorbate hydrogen bonding becomes significant. Generally, the low pressure linearity of the DRK plots improves significantly as the carbon surface oxygen content increases and the initial region of the isotherm (Figure 5.8 a) and d)) becomes concave to the pressure axis typical of type II isotherm. As the vapour changes from methanol to ethanol and then isopropanol, one gradually observes a better low pressure fit as well as a better degree of linearity as a consequence of the increasing contribution of the non-specific interaction of the alkyl chains which produces the tightening of the knee on the corresponding isotherms.

If one now looks at both surface areas, S_{BET} and S_{DRK} (shown in Table 5.4) the values from alcohols data obtained using both method are lower than those derived using the

nitrogen data as it was previously observed by Carrott [8]. Firstly for methanol, S_{BET} seems to be always higher than S_{DRK} but as soon as the surface oxygen content (i.e. the number of specific adsorption sites) increases, S_{DRK} increases considerably. Secondly for ethanol and isopropanol, S_{BET} values are much lower than those for S_{DRK} , are similar, within error, for both adsorptives and are not influenced by the surface chemistry changes of the carbon showing the influence of non-specific interactions of the alkyl chains on the adsorption process. The work of Carrott et al. [8] indicates that the adsorption of methanol onto carbon blacks at low pressures (sub-monolayer region) is strongly influenced by hydrogen bonds which form with polar groups on the carbon surface and also that the methanol adsorption is limited when the levels of surface oxygen are low. As a confirmation of previous observations, our study shows that methanol adsorption onto the base N330 containing 1.7 at.% oxygen gives rise to a type III isotherm whilst the adsorption of the same alcohol on the N234G graphitized carbon which has of course a distinct structure and less oxygen (only 0.5 at.%) than the N330, adsorbs even less methanol at low pressures and hence behaves in a similar way to the Sterling FT graphitized black reported in [8]. On the other hand, our results show clearly that an increase of oxygen concentrations on the carbon black surface leads to a shift of the methanol adsorption isotherm to higher adsorption values. In that way, the low pressure (sub-monolayer) regions become more and more concave toward to the pressure axis, characteristic of a type II isotherm. It is interesting to note that S_{BET} values obtained for methanol (see Table 5.4) are significantly lower than the “true” surface area of the N330 carbon black (quoted area of 80 m²/g) regardless of the oxygen levels studied whereas the S_{DRK} values are also lower but increase with the surface oxygen level. Neither equation seems to provide a coherent description of the methanol data but surprisingly enough the DRK method, which places emphasis on the very low pressure data point, produces surface areas which reflect the increase of the adsorbed amount as a function of carbon surface polarity.

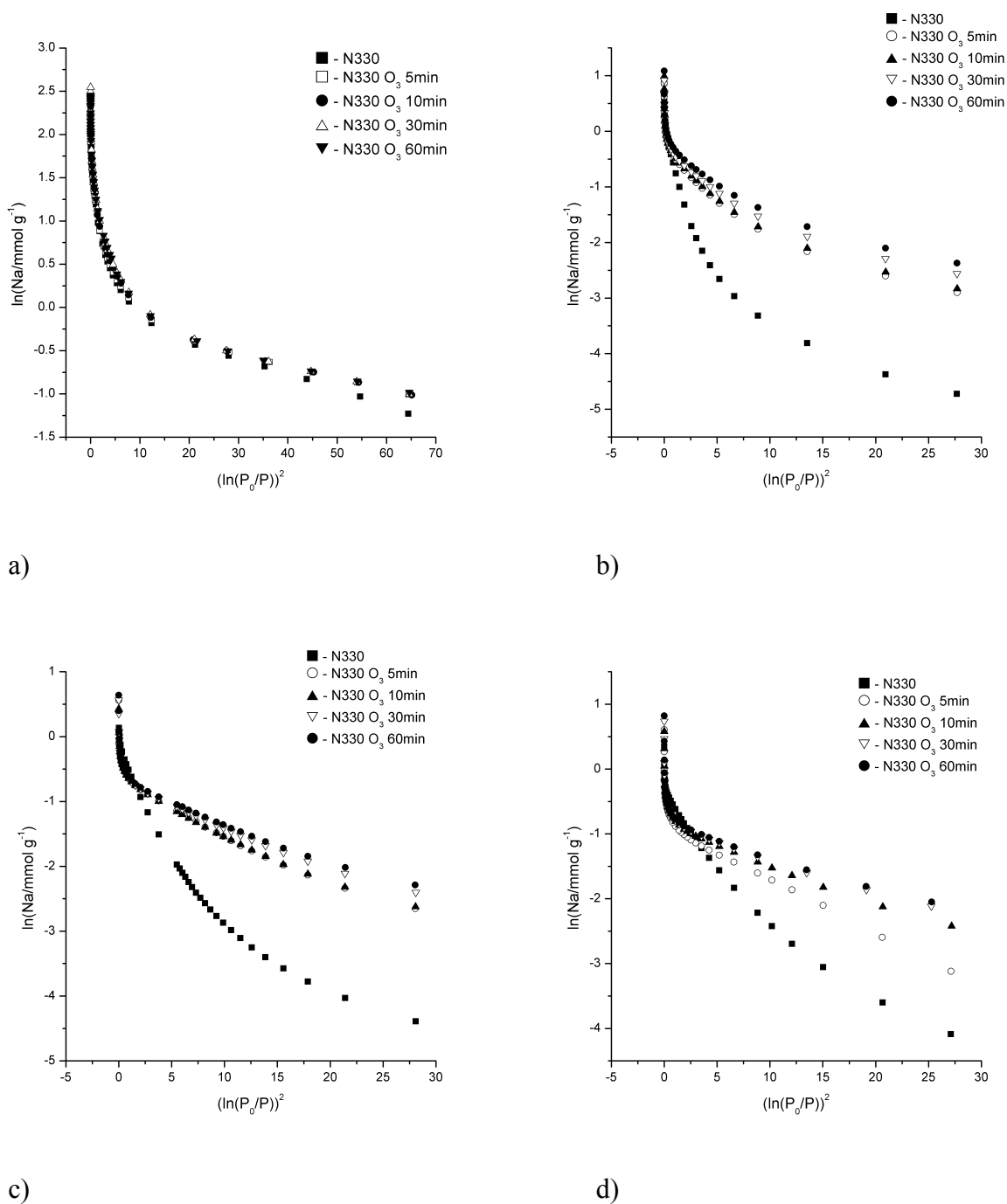


Figure 5.9: DRK plots for the adsorption of: a) nitrogen at 77°K, b) methanol, c) ethanol and d) isopropanol at 303°K.ⁱ

ⁱ Note: marked differences in the low pressure region ($[\ln(P_0/P)]^2 > 5$) of the adsorption of the alcohols due to specific interactions with active surface groups.

Carrott has argued [8] that the mechanism of methanol adsorption on carbon blacks is similar to the one of water. This has already been discussed by a number of workers [34][35][36][37] and it was suggested that at low pressures and surface coverage, hydrogen bonding occurs between methanol and polar surface groups which can be considered as primary adsorption sites. The methanol adsorbed on the primary sites will then act as secondary sites as the surface coverage increase, especially at higher pressures, thus starting the second and following layer of adsorbed molecules on the surface. The overall process, represented in the next chapter (see Figure 6.3: *Schematic representation of the growth mode occurring during the adsorption of water at different coverage regimes.*), could be synthesised by two steps: the initial formation of adsorbed cluster on polar sites such as chemisorbed oxygen molecules followed by the construction of an extended network structure. In this network, the adsorbed polar molecules are constrained although the absolute structure and density of both clusters and network in relation to liquid adsorptive are not currently known. As typified by our data, the methanol (and other alcohols) isotherm could be described by the following expression $Na = f(P, [O]_T)|_T$ where the additional term $[O]_T$ describes the surface concentration of oxygen groups, in our case measured by XPS. Since specific interactions occur at fixed polar sites and the non-specific dispersion forces are present all over the surface creating a mobile adsorbed layer, the entropic contribution to the adsorption process is likely to be significantly more important in the case of methanol where the adsorbed layer has a greater “*structure*”. For the ethanol and isopropanol, the hydrogen bonding effect can still be clearly observed in the isotherm data although it becomes less and less dominant as the emphasis changes from specific to dispersion interaction with increasing alkyl chain length. These non-polar molecules (such as toluene, benzene, long-chain alcohols, etc...) follow the mechanism of adsorption known as layer-by-layer or Frank-van der Merve (FM) growth. In this adsorption process represented in Figure 5.10 for various surface coverage, each new layer starts to grow only after the underlying layer is complete. This type of growth

is usually observed when the interaction between the adsorbate and the surface is stronger than that between the adsorbate molecules. As seen on the schematic illustration, the non-polar molecules are not really influenced by the active sites present on the carbon surface. For these last two adsorptives, the S_{BET} values are still lower than the nitrogen values but the S_{DRK} values show an important increase to between 66.4~69.9 m²/g.

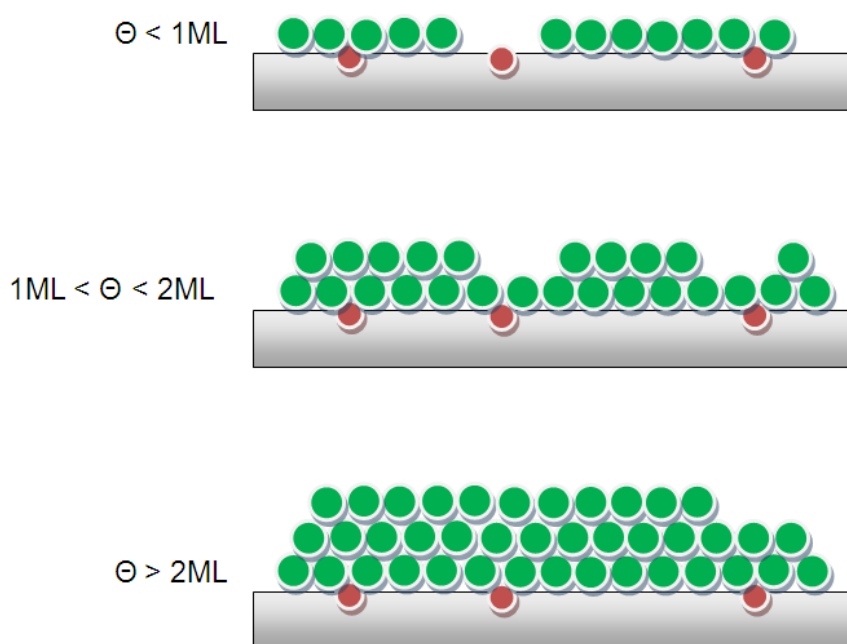


Figure 5.10: Schematic representation of the growth mode occurring during the adsorption of non-polar molecules at different coverage regimes. This mode is also known as Layer-by-layer growth or Frank - van der Merve mode. The surface active sites are represented as red spheres whereas the non-polar molecules (such as toluene or in long-chain alcohols) are represented by the green spheres.

A mixed mode of adsorption called Stranski-Krastanov (SK) growth also exists. This mode where both islands and complete monolayers are observed occurs when the nature of the adsorbate layer becomes dependant to the chemical and physical properties,

such as surface energies and lattice parameters of the substrate [38]. An example of the phenomenon is the adsorption of rare gases on graphite sheet.

Figure 5.8 and Figure 5.9 have shown the effects of the “*adsorbent*” on the alcohol isotherms i.e. that increasing the surface oxygen levels of the carbons leads to systematic increases in the hydrogen bonding interactions and marked differences in sub-monolayer regions of the isotherms for the individual alcohols.

In terms of the “*adsorbate*” effects, the isotherm data for the three alcohols on each carbon black were plotted and are shown in Figure 5.11. The most marked differences appear for the base N330 material (1.7 at.% oxygen) where the initial, sub-monolayer region of the methanol curve is convex to the pressure axis showing similarity with water and indicative of relatively weak overall interaction whilst the isopropanol isotherm tends to have a Type I character indicating stronger interaction. In this instance, the ethanol isotherm appears to follow an intermediate behaviour and displays an isotherm almost linear at low pressure.

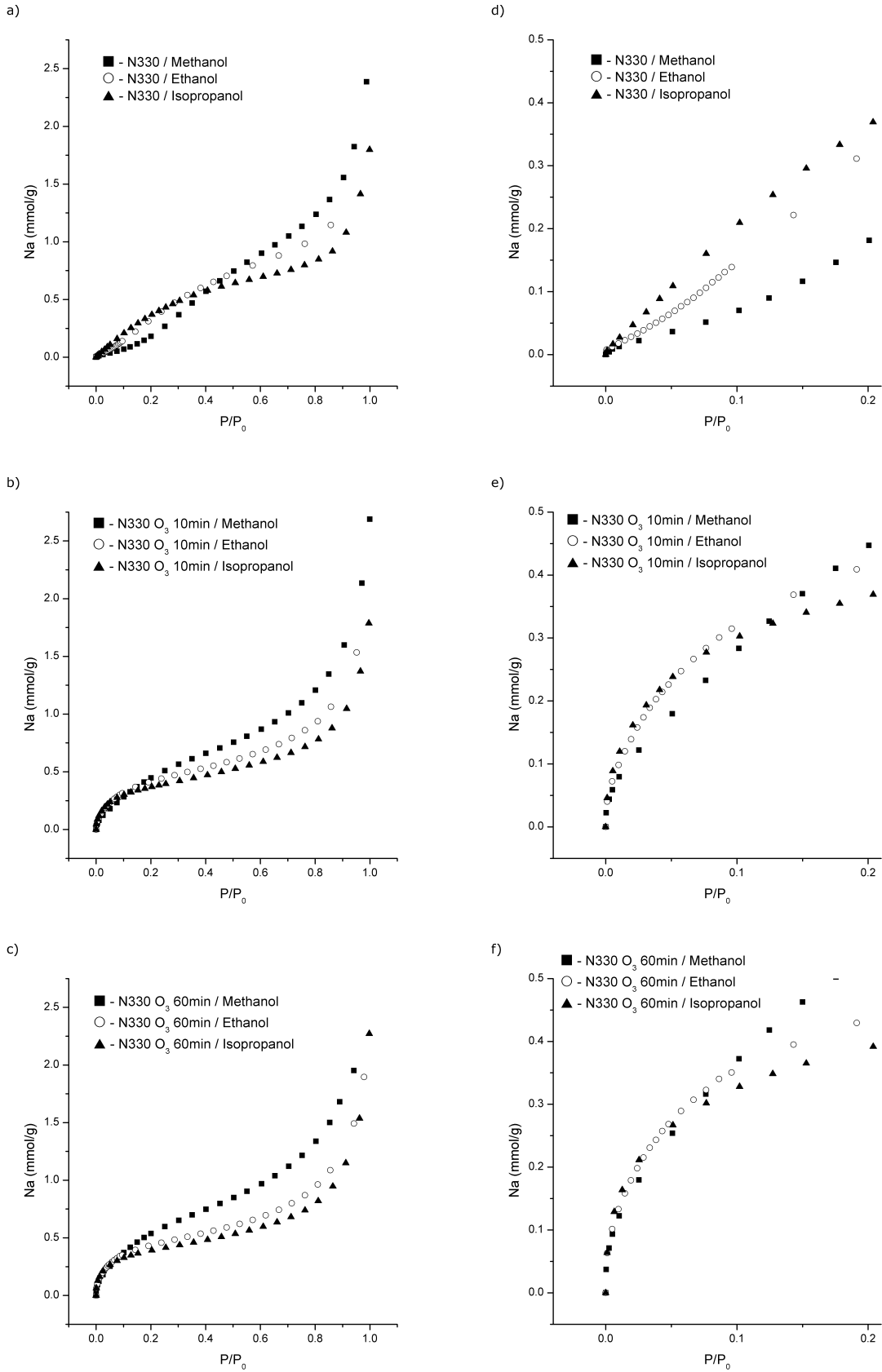


Figure 5.11: Alcohol isotherms plotted on: a) the base N330, b) N330 O₃ 10min (8.1 at.% oxygen) and c) N330 O₃ 60min (11.2 at.% oxygen) showing effects of adsorbate chemistry. Zooms on the low pressure region are also included in d), e) and f) respectively.

In addition, the Figure 5.12 represents the limiting behaviour for an oxygen free surface obtained by adsorbing the three alcohols onto the graphitized carbon black N234G. The low pressure data for each alcohol follow closely the pressure axis (methanol being the most pronounced). This clearly indicates that specific interactions play a significant role in the initial stages of adsorption for these adsorbates.

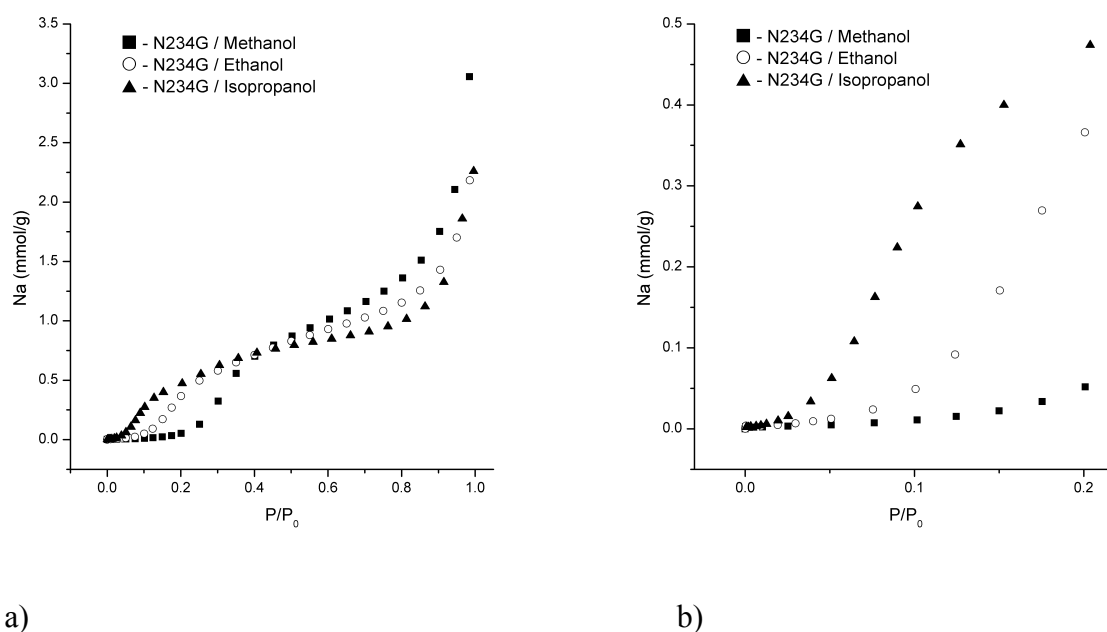


Figure 5.12: Alcohols adsorbed on graphitized carbon black N234G showing type III/V character of initial regions of isotherms. a) Full adsorption isotherm and b) zoom in the very low pressure region.

On each of the other carbons containing higher oxygen levels (Figure 5.11 b) and c) for oxygen level of 8.1 and 11.2 at.% oxygen respectively) the isotherms for the three alcohols coincide very well in the initial region and display a strong positive curvature to the pressure axis. This behaviour shows that at high oxygen levels, within the low

pressure region, the “adsorbate” chemistry does not play a significant role to influence the isotherm character. But as soon as the multilayer region is reached, the isotherms start to diverge due to the different adsorbate-adsorbate interactions which are strongest for methanol and weakest for isopropanol.

Regarding the β_{DRK} values, it appears from Figure 5.8 and Figure 5.9 that the surface chemistry of the carbon material will affect this parameter, which will therefore differ from those derived assuming a single liquid density for the adsorbed phase. This was confirmed by our experimental data in Figure 5.13 which shows the relationship between β_{DRK} values for each alcohols obtained using nitrogen as the non-polar reference adsorptive and the surface oxygen level $[O]_T$ directly measured by XPS. $E_{\text{DRK}}(\text{N}_2)$ was substituted into Eq. 5.4 in place of $E_{\text{DRK}}(\text{C}_6\text{H}_6)$. One notes in this respect a very slight decrease in slope of the nitrogen DRK plots for the oxidised carbons relative to the base material which leads to a β value of 0.38 for the oxidised materials rather than 0.33, reference for nitrogen, observed for the base N330. This β_{DRK} average value (for the oxidised solids) was obtained by multiplying the $\beta_{\text{DRK}}(\text{N}_2)$ for these materials (as displayed on the Figure 5.13) by the β_{DRK} reference value for nitrogen.

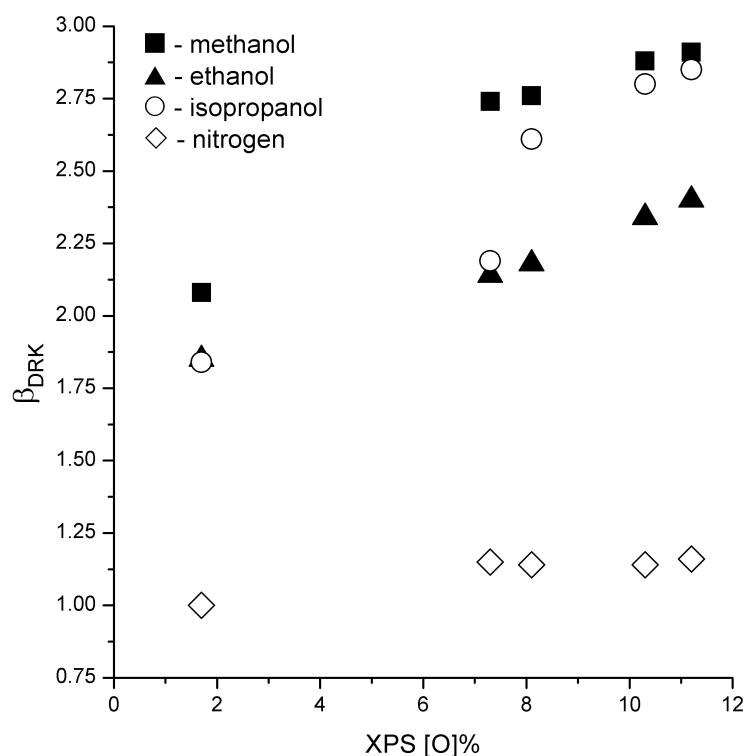


Figure 5.13: Values of $\beta_{DRK}(\text{alcohols})$ (with N_2 as reference) as a function of total surface oxygen $[O]_T$ (at.%).

Since β_{DRK} appears to be available from a quick and direct XPS measurement of carbon surface compositions, one believes that this approach may become, in the future, beneficial for both isotherm prediction (especially for non-porous material and polar vapours) and refining computer modelling methods.

5.4 Conclusions

The carbon black N330 has been oxidized in a fluidized bed using the ozonation technique to create a series of carbon blacks with increasing surface oxygen level $[O]_T$ (at.%) which was measured by XPS. The interactions of methanol, ethanol and

isopropanol with these surfaces have been studied using vapour adsorption and immersion calorimetry.

Strong correlations between $[O]_T$ and the structure of the adsorbate molecules were observed, which allow interpretation of the mechanisms of interaction with the carbon. In particular, the low pressure adsorption of the alcohols is highly sensitive to $[O]_T$ and the isotherms for these vapours are significantly displaced to higher adsorption values as the oxygen level increases.

The data show a transitional behaviour limited by water at one end with interactions mainly dominated by hydrogen bonding at polar surface sites (oxygen groups) and toluene at the other end with much weaker dispersion interaction with the non-polar carbon surface. This shift from specific dominated interactions to more significant dispersion interactions is observed with a series of alcohols of increasing chain length.

Two types of isotherms were observed depending on the surface chemistry of the carbon black. Type III isotherms for the un-oxidised N330 with only 1.7 at.% oxygen were obtained but the character of the isotherm changes to Type II for the oxidised materials confirming that the low pressure, low coverage, domains of the isotherms are still dominated by specific interactions which increase as a function of $[O]_T$.

A semi-quantitative analysis of the relative influence of the specific to non-specific interactions is possible from the heat of immersion data. These values show that both the relative sensitivity of each alcohol to $[O]_T$ and also the shift from specific to non-specific interaction as the alkyl chain length of the alcohols increases.

These specific (sub-monolayer) interactions are also reflected in the C_{BET} constant values derived by application of the BET equation to the alcohol adsorption data although some difficulty was encountered in fitting the data especially that for the un-oxidised N330 carbon black which gives Type III isotherms. Non-linearity was also observed in the low pressure, high A (kJ/mol) domains of the DRK plots for the base material samples but better fits were obtained for the alcohols on the oxidised surfaces

which gave Type II isotherms. E_{DRK} (kJ/mol) and $\beta_{\text{DRK}}(\text{alcohols})$ are shown to be sensitive to the level of specific interaction and consequently a dependence on $[O]_T$ is observed.

References

- ¹ R. H. Bradley and B. Rand. *Adsorption of alcohols and water vapour onto active carbons* 18th Biennial Conf. on Carbon 94-95 (American Carbon Society, Worcester, Mass., USA, 1987).
- ² R. H. Bradley and B. Rand. A comparison of the adsorption behaviour of nitrogen, alcohols, and water towards active carbons. *Carbon* **29** (1991) 1165-1172.
- ³ F. Rodriguez-Reinoso, M. Molina-Sabio and M. T. Gonzalez. Effect of oxygen surface groups on the immersion enthalpy of activated carbons in liquids of different polarity. *Langmuir* **13** (1997) 2354-2358.
- ⁴ M. V. Lopez-Ramon, F. Stoeckli, C. Moreno-Castilla and F. Carrasco-Marin. On the characterization of acidic and basic surface sites on carbons by various techniques. *Carbon* **37** (1999) 1215-1221.
- ⁵ F. Stoeckli and A. Lavanchy. The adsorption of water by active carbons, in relation to their chemical and structural properties. *Carbon* **38** (2000) 475-494.
- ⁶ Y. I. Tarasevich and E. V. Aksenenko. Interaction of water, methanol and benzene molecules with hydrophilic centres at a partially oxidised model graphite surface. *Colloids and Surfaces A: Physicochem. Eng. Aspects* **215** (2003) 285-291.
- ⁷ M. V. Lopez-Ramon, F. Stoeckli, C. Moreno-Castilla and F. Carrasco-Marin. Specific and nonspecific interactions between methanol and ethanol and active carbons. *Langmuir* **16** (2000) 5967-5972.
- ⁸ P. J. M. Carrott, M. M. L. R. Carrott and I. P. P. Cansado. Reference data for the adsorption of methanol on carbon materials. *Carbon* **39** (2001) 193-200.
- ⁹ R. H. Bradley and B. Rand. On the physical adsorption of vapors by microporous carbons. *J. Colloid Interface Sci.* **169** (1995) 168-176.
- ¹⁰ M. M. Dubinin and L. V. Radushkevich. The equation of the characteristic curve of activated charcoal. *Proc. Acad. Sci. USSR* **55** (1947) 331-333.

- ¹¹ M. M. Dubinin. Fundamentals of the theory of adsorption in micropores of carbon adsorbents: Characteristics of their adsorption properties and microporous structures. *Carbon* **27** (1989) 457-467.
- ¹² M. G. Kaganer. A method for the determination of specific surfaces from the adsorption of gases. *Proc. Acad. Sci. USSR* **116** (1957) 603-605.
- ¹³ S. Brunauer, P. H. Emmett and E. Teller. Adsorption of gases in multimolecular layers. *J. Am. Chem. Soc.* **60** (1938) 309-319.
- ¹⁴ D. Hugi-Cleary, S. Wermeille and F. Stoeckli. The characterization of non-porous surfaces by a combination of the BET and the DRK theories. *Chimia* **57** (2003) 611-615.
- ¹⁵ F. Stoeckli and T. A. Centeno. On the determination of surface areas in activated carbons. *Carbon* **43** (2005) 1184-1190.
- ¹⁶ P. J. M. Carrott, M. M. L. R. Carrott, I. P. P. Cansado and J. M. V. Nabais. Reference data for the adsorption of benzene on carbon materials. *Carbon* **38** (2000) 465-474.
- ¹⁷ F. Stoeckli, A. Guillot, A. M. Slasli and D. Hugi-Cleary. Microporosity in carbon blacks. *Carbon* **40** (2002) 211-215.
- ¹⁸ G. O. Wood. Affinity coefficients of the Polanyi /Dubinin adsorption isotherm equations. A review with compilations and correlations. *Carbon* **39** (2001) 343-356.
- ¹⁹ R. H. Bradley, I. Sutherland and E. Sheng. Relationship between carbon black surface chemistry and energy. *J. Chem. Soc., Faraday Trans.* **91** (1995) 3201-3207.
- ²⁰ R. H. Bradley, R. Daley and F. Le Goff. Polar and dispersion interactions at carbon surfaces: further development of the XPS-based model. *Carbon* **40** (2002) 1173-1179.
- ²¹ G. de la Puente, J. J. Pis, J. A. Menendez and P. Grange. Thermal stability of oxygenated functions in activated carbons. *J. Anal. Appl. Pyrol.* **43** (1997) 125-138.
- ²² S. J. Gregg and K. S. W. Sing. *Adsorption, surface area and porosity* (Academic Press, London, 1982). p.61-66.
- ²³ S. Ohe. *Computer aided data book of vapor pressures* (Data Book Publishing Co., Tokyo, Japan, 1976).
-

- ²⁴ S. Biniak, G. Szymanski, J. Siedlewski and A. Swiatkowski. The characterization of activated carbons with oxygen and nitrogen surface groups. *Carbon* **35** (1997) 1799-1810.
- ²⁵ Z. R. Yue, W. Jiang, L. Wang, S. D. Gardner and C. U. P. Jr. Surface characterization of electrochemically oxidized carbon fibers. *Carbon* **37** (1999) 1785–1796.
- ²⁶ H. Valdés, M. Sánchez-Polo, J. Rivera-Utrilla and C. A. Zaror. Effect of ozone treatment on surface properties of activated carbon. *Langmuir* **18** (2002) 2111–2116.
- ²⁷ K. S. W. Sing. *Surface area determination, Proc. Int. Symp. 1969* (ed. D.H. Everett and R.H. Otervill) (Butterworths, London, 1970).
- ²⁸ K. S. W. Sing. Physisorption of gases by carbon blacks. *Carbon* **32** (1994) 1311-1317.
- ²⁹ A. C. Zettlemoyer. *Hydrophobic surfaces* (ed. F. M. Fowkes) (Academic Press, New York, 1969).
- ³⁰ F. Carrasco-Marin, A. Mueden, T. A. Centeno, F. Stoeckli and C. Moreno-Castilla. Water adsorption on activated carbons with different degrees of oxidation. *J. Chem. Soc., Faraday Trans.* **93** (1997) 2211-2215.
- ³¹ J. Kamierczak, S. Biniak, A. Swiatkowski and K.-H. Radeke. Interdependence of different parameters characterizing the chemistry of an activated carbon surface. *J. Chem. Soc., Faraday Trans.* **87** (1991) 3557 - 3561.
- ³² S. S. Barton, M. J. B. Evans and B. H. Harrison. Surface studies on carbon: water adsorption on polyvinylidene chloride carbon. *J. Colloid Interface Sci.* **45** (1973) 542-548.
- ³³ S. S. Barton and B. H. Harrison. Surface studies on graphite: Immersional energetics. *Carbon* **10** (1972) 245-251.
- ³⁴ M. M. Dubinin and V. V. Serpinsky. Letter to the Editor. Isotherm equation for water vapor adsorption by microporous carbonaceous adsorbents. *Carbon* **19** (1981) 402-403.
- ³⁵ R. H. Bradley and B. Rand. The adsorption of vapours by activated and heat-treated microporous carbons. Part 2. Assessment of surface polarity using water adsorption. *Carbon* **31** (1993) 269-272.
- ³⁶ S. S. Barton, M. J. B. Evans and J. A. F. MacDonald. Adsorption of water vapor on nonporous carbon. *Langmuir* **10** (1994) 4250–4252.
-

- ³⁷ M. M. Dubinin, E. D. Zaverina and V. V. Serpinsky. The sorption of water vapour by active carbon. *J. Chem. Soc. London* **2** (1955) 1760–1766.
- ³⁸ H. Lüth. *Solid surfaces, interfaces and thin films* (Springer Verlag, Heidelberg, 2001).

6

Chapter 6 Correlation of water adsorption isotherms with oxygen groups on carbon surfaces

Abstract

The adsorption of polar molecules, such as water and short chain alcohols on carbon material is strongly influenced by the state of the surface which usually contains polar sites, oxygen functional groups in particular. Specific, hydrogen bonding, interactions take place at these sites, in addition to the normal non-specific, dispersion, interactions happening globally. In this chapter, the same series of ozonated non-porous carbon blacks with increasing surface oxygen levels was used to correlate the surface oxygen concentration quantified by XPS with the precise shape of the water adsorption isotherm observed and also with the enthalpies of immersion $-\Delta H_i$ (mJ/m²) for this adsorptive. Additionally, both activated carbon and carbon black materials submitted to liquid-phase oxidation (nitric acid, hydrogen peroxide and ammonium persulfate) were studied as a comparison to ozone treatment and non-porous surface. The water adsorption data were analysed using in particular the Dubinin-Serpinsky equation and also some of its recent variations such as Barton and D'Arcy & Watt equations for the materials subjected to liquid-phase oxidation. In a general way, the water isotherms are shifted to higher adsorption uptakes as the surface oxygen level $[O]_T$ increases. It was shown that the resulting parameter, a_0 (for the DS2 equation), describing the surface concentration of primary polar adsorption sites, was linked to the surface oxygen level $[O]_T$ measured by XPS, which also influences both the degree of fit to the equation and the limiting experimental water adsorption value a_s . Correlations between measurable physicochemical variables of various carbon materials, for example $[O]_T$ here, and parameters of water adsorption equations (a_0 and a_s in particular) can greatly contribute in the field of both isotherm prediction and refinement of adsorption models. For organic vapours as seen before, a better understanding of the adsorption process is given by the DRK approach and its terms E and β describing the carbon polarity.

6.1 Introduction and Theoretical

In contrast to the non-specific or dispersion interactions which occur for most organic species, the interaction of polar molecules with carbon surfaces takes place by relatively strong hydrogen bonding at the specific sites. These sites usually contain oxygen molecules and are mainly located on the edges of the graphene layer-planes of the carbon structure or near the defects of the surface structure (such as dislocations, etc...). Their surface concentration governs the overall interaction which occurs between carbon surfaces and molecules such alcohols [1][2] and most markedly water [3]. As a consequence, it affects the qualitative and quantitative characteristics of resulting adsorption isotherms as described in several other studies [4][5][6][7][8].

In terms of surface chemistry and polarity, while non-specific adsorption can be described by the Dubinin-Radushkevich-Kaganer (DRK) equation [9] as seen before, Dubinin et al. [10] presented in 1955 the first formal description of water adsorption on carbon surfaces based on the following mechanistic approach. Surface polar groups act as primary adsorption centres to which water molecules attach through hydrogen bonding and nucleate to form clusters at higher relative pressure. These clusters are considered as secondary adsorption centres. The initial equation has been slightly modified [11][12][13] and takes the form:

$$a = c(a_0 + a)(1 - ka)^{p/p_0} \quad \text{Eq. 6.1}$$

where a (mmol/g) is the equilibrium water adsorption value, a_0 (mmol/g) is the surface concentration of primary hydrophilic sites, c is the ratio of the rate constants for the adsorption and desorption processes (i.e. k_{ads}/k_{des}) and p and p_0 are respectively the equilibrium and saturation water pressures at the adsorption temperature. k represents the loss of secondary sites due to the cluster formation and its value therefore affects the limiting adsorption capacity, a_s , which is the value of a at $p/p_0 = 1$.

Over the years, the Eq. 6.1 has accumulated several derivations and extensions in order to improve the adsorption isotherm modelling as you can see for example in the review of Furmaniak et al. [14]. Using this equation and the two parameters a_0 and a_s , it is common practice to characterise the surface polarity of carbons from water adsorption data. It is implicit that with these approaches, the carbon surface of the studied material is defined in terms of hydrophobic or hydrophilic character but still an absolute definition of the carbon surface polarity is difficult to achieve. Hence, precise correlation between the physical structure of carbon surfaces, surface chemistry (concentration of oxygen containing functional groups) and the resulting water adsorption/desorption isotherms is still not firmly established in spite of the progress made.

This chapter describes the adsorption of water vapour on a series of non-porous carbon black surfaces which have the same physical characteristics but increasing levels of surface oxygen. The surface chemistry of the carbons has been modified in a fluidised bed using ozone oxidation. Most importantly, since the carbons are non-porous, these chemical modifications only affect the material surface and so can be directly quantified using X-ray photoelectron spectroscopy (XPS), moreover any physical modification consequently to these treatments can be identified using SEM. The effects of directly measured surface oxygen levels on the dominant mechanisms of adsorption and on the resulting vapour adsorption isotherms are discussed. Data for the adsorption of methanol is also included for comparison. The observed behaviour is also reflected in calorimetric data for immersion of the carbons in the corresponding liquid phases of the adsorptives which gives an indication of the relative specific and non-specific interactions for each system. The water adsorption data are analysed mainly within the framework of the Dubinin equations but an attempt to use other equations such as Barton and D'Arcy &

Watt equations has been made. Correlations between the resulting equation parameters and the real surface oxygen level $[O]_T$ (in at.%) measured by XPS were investigated.

This approach brings together the direct quantitative measurement of carbon surface chemistry and the resulting thermodynamic character of the surfaces which underlies the Dubinin approach to adsorption.

6.2 Experimental

Non-porous carbon black N330 (Cabot Co., USA) has been used as the base material for treatment using ozone in order to produce a small range of materials with increasing and controlled surface oxygen levels. Additionally, carbon black N330 and activated carbon BPL, treated with the following acids: nitric acid, hydrogen peroxide and ammonium persulfate, were also studied. The details regarding the oxidations in liquid phase are presented in paragraph 3.6.2.

The base CB N330 has an intrinsic surface oxygen level of 1.7 at.% measured by X-ray photoelectron spectroscopy (XPS). Ozonation of this material in a fluidised bed system of the type described in previous publications [17] for duration times of 5, 10, 30 and 60 min leads to surface oxygen levels of 7.3, 8.1, 10.3 and 11.2 at.%. Adsorption onto a graphitized (2973°K) carbon black, Cabot N234G and another carbon black, N234 has also been investigated. This graphitised CB N234G which represents a near-limiting, hydrophobic, surface in terms of water adsorption, has a BET surface area (S_{BET}) of 92 m²/g (± 4 m²/g), a surface oxygen level of 0.5 at.% and an enthalpy of immersion in water, $-\Delta H_i(H_2O)$, of 28.0 mJ/m². This material was also used as the reference for the construction of nitrogen α_s plots. On the other hand, N234 has a S_{BET} of 108 m²/g a surface oxygen level of 1.5 at.% and a $-\Delta H_i(H_2O) = 68.6$ mJ/m².

XPS measurements of carbon surface oxygen levels have been made using a Kratos HSi 5-channel monochromated instrument at a residual vacuum of 10⁻⁸ mbar with Alka

radiation of energy 1486.6 eV and with the analyser in FAT mode and carbon samples presented in shallow sample dishes. Surface compositions have been calculated from the areas of elemental peaks, after subtraction of a linear background, using Kratos relative sensitivity factors i.e. 0.25 for C1s and 0.66 for O1s photoelectron peak areas.

Vapour adsorption and immersion calorimetry work was carried out using analar grade methanol (Acros Organics, UK), toluene (Fisher Scientific, UK) and triple distilled water from the pharmacy department (RGU). Immersion calorimetry has been carried out in a Setaram/Calvet C80 Instrument on samples that had been sealed in glass ampoules after being out gassed to 10^{-2} mbar at room temperature. Enthalpy of immersion values, $- \Delta H_i$ (mJ/m²), have been calculated using $S_{BET}(N_2)$ values.

Adsorption isotherms for water have been measured using a Hiden/IGA gravimetric system after outgassing to constant weight at 353°K (which was chosen in order to avoid any elimination of surface oxygen groups [¹⁵]). Equilibrium adsorption for each point of p/p_0 was defined from kinetic data such that the weight remains constant. Saturated vapour pressure of 42 mbar for water vapour was derived using the Antoine equation [¹⁶]. Isotherms for nitrogen at 77°K were measured using a Micromeritics ASAP2010 Volumetric apparatus, after out gassing as above, assuming a molecular area of 0.162 nm² and a P_0 value of 987 mbar. Nitrogen surface areas have been calculated using the BET and DRK equations and the non-polar interactivity of the surfaces has been probed using immersion in toluene.

6.3 Results and discussion

Adsorption isotherm of nitrogen at 77°K on the five carbon blacks with different degrees of oxidation ($[O]_T$ ranging from 1.7 to 11.2 at.%) were all type II and exhibited very little variation among the different materials, indicating strong similarity with the base N330 in terms of surface homogeneity and structure. The surface areas shown in Table 5.3

from Chapter 5, were determined using the BET, DRK and Sing's α_s methods taking a value of 0.162 nm² for the nitrogen cross sectional area. Similarly, the isotherms of toluene on the oxidised carbon blacks (as shown in the previous chapter) are all type I and do not seem affected by the oxygen content on the carbon surface. This statement is supported by the enthalpy of immersion data for toluene, $-\Delta H_i(\text{Tol})$, which can be considered insensitive to surface chemical changes due to its non-polar character. But these enthalpy values should have been able to reveal any significant change in the physical structure of the CBs surface including development of surface porosity.

Figure 6.1 gives the enthalpy of immersion of water, methanol and toluene versus the carbon surface oxygen level. From these plots, it is clear that water and methanol interactions are strongly dependent of the carbon polarity as $-\Delta H_i(\text{H}_2\text{O})$ and $-\Delta H_i(\text{methanol})$ (polar dominated interaction) values increase in direct proportion to the surface oxygen levels of the CB surfaces. On the contrary, toluene is insensitive to the surface chemistry as the $-\Delta H_i(\text{Toluene})$ (dispersion dominated interaction) figures do not change significantly over the range of oxidized CBs.

The water values are similar to those previously reported for a wide range of carbon blacks of various types and levels of oxidation measured by XPS [17] and are also consistent with studies by other authors based on pH_{pzc} and temperature programmed desorption of oxygen complexes [18][19][20].

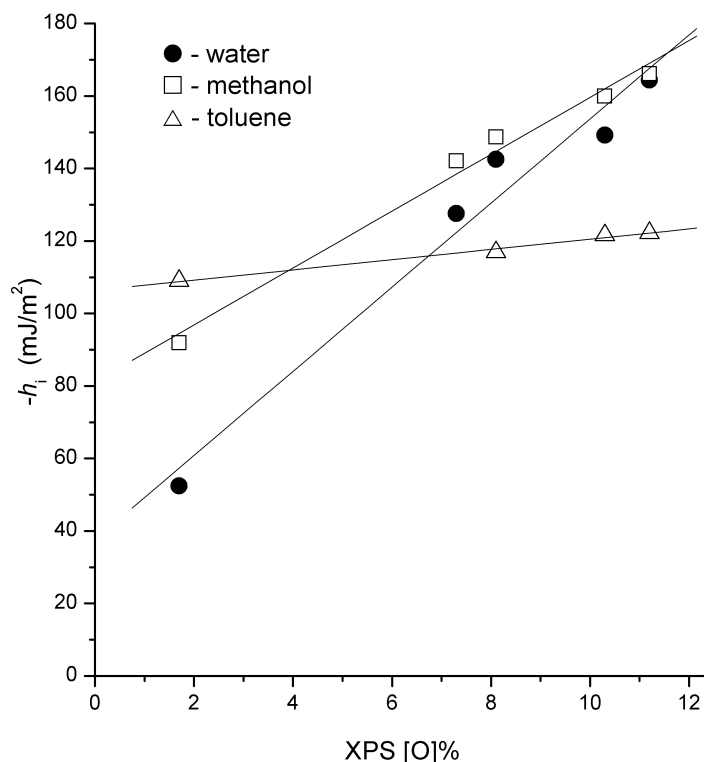


Figure 6.1: $-AH_i$ values as a function of surface oxygen levels for water, toluene and methanol.

The slope observed for the water data is greater than the one for methanol because water molecule is the most polar probe of both. The combined effect of the hydrogen bonding with the dispersion interaction of the methyl group leads to higher enthalpy values for methanol. At higher surface oxygen levels the plots for each liquid converge indicating that specific interactions become dominant. Another possible explanation could be that the dispersion interactivity of the carbon surface decreases as the number of oxygen-containing functional groups increases. This was observed for n-heptane by Bradley et al. [21] and may have two causes: a reduction in the total surface area available for dispersion interactivity and/or a loss of electrons, due to the formation of covalent bonds with oxygen atoms, which would otherwise be free to participate in dispersion

interactions. By regression analysis of the immersion data, one obtained the Eq. 6.2 to Eq. 6.4 written below (these equations have already been introduced in the previous chapter as Eq. 5.5, Eq. 5.7 and Eq. 5.6 respectively). The slope and y-intercept values show clearly the shift from the polar dominated interaction for water to the dispersion dominated interaction for toluene.

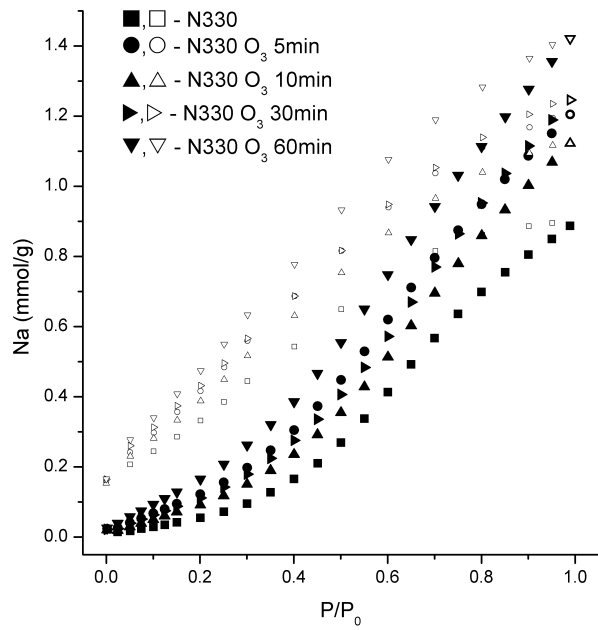
$$-\Delta H_i(H_2O)_{exp}(mJ/m^2) = 37.6 + 11.61 \cdot [O]_T \quad Eq. 6.2$$

$$-\Delta H_i(CH_3OH)_{exp}(mJ/m^2) = 81.2 + 7.85 \cdot [O]_T \quad Eq. 6.3$$

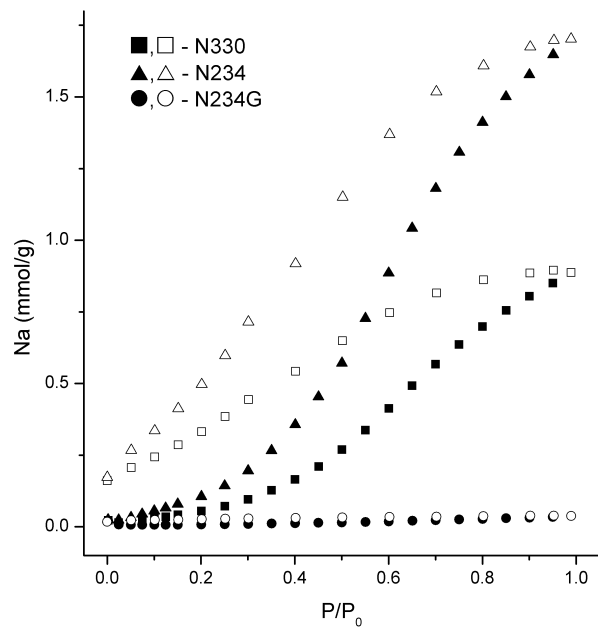
$$-\Delta H_i(C_7H_8)_{exp}(mJ/m^2) = 106.4 + 1.41 \cdot [O]_T \quad Eq. 6.4$$

Looking now at the adsorption data, one can see that water isotherms on N330 and the N330 oxidised carbon blacks are all Type III and are associated to significant displacement to higher adsorption uptakes over the whole pressure range as the surface oxygen level (in at.%) increases as shown in Figure 6.2 a). Water adsorption isotherms for the graphitized carbon black N234G and for the carbon black N234 are given in Figure 6.2 b). The carbon black N234G has a similar surface area ($90 \text{ m}^2/\text{g}$) than the N330 unoxidised but with its low surface oxygen level ($[O]_T \approx 0.5 \text{ at.}\%$), is a good example of a limiting hydrophobic surface in terms of water uptake. In the other way, the carbon black N234 has only a slightly higher surface area ($S_{BET} = 108 \text{ m}^2/\text{g}$) and a similar $[O]_T$ value ($\sim 1.5 \text{ at.}\%$ oxygen) than N330 but an a_s value of 1.71 is obtained compared to 0.90 for N330. This structural aspect could directly influence the distribution of primary sites on the carbon surface, their coordination with adsorbing water molecules, and also the entropic contribution to the adsorption process.

As seen in the previous chapter, isotherms for methanol on the unoxidised N330 are Type III but Type II isotherms are observed for the oxidised. This change being explained by the additional polar interactions as discussed for Figure 6.1.



a)



b)

Figure 6.2: Water adsorption isotherms at 303°K for a) N330 and N330 oxidised carbon blacks and b) N330, N234 and N234G (graphitized) and carbon blacks.

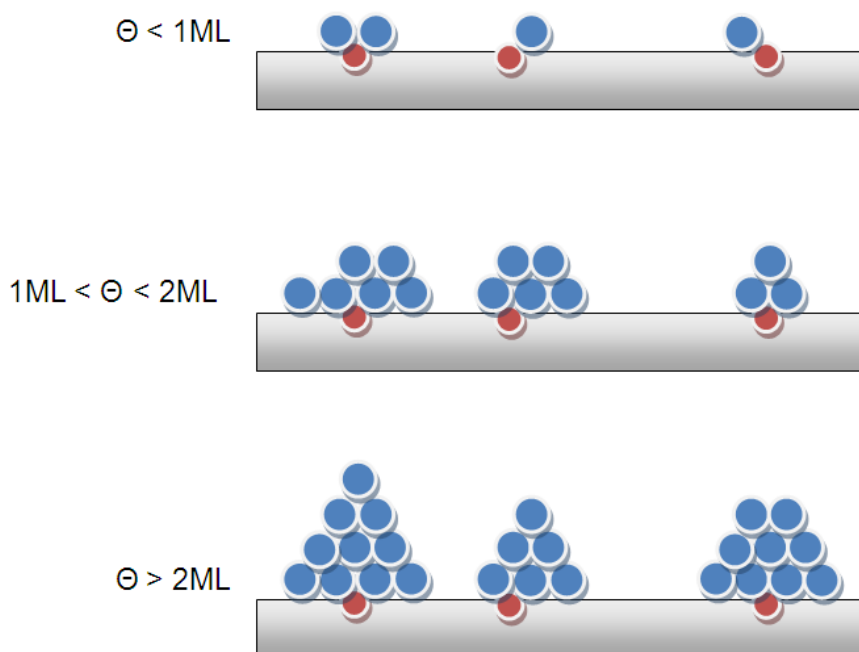


Figure 6.3: Schematic representation of the growth mode occurring during the adsorption of water at different coverage regimes. This mode is also known as island growth or Vollmer-Weber (VW) mode. The surface active sites are represented as red spheres whereas the water (or polar adsorptive) molecules are represented by the blue spheres.

Overall, the data confirm the strong specific hydrogen bonding dependence of both adsorptives and concentration of primary polar sites as reflected by the measured surface oxygen levels. At the difference of water, the additional interaction changes the isotherm type in the case of methanol. The mechanism of adsorption for these small polar molecules, represented in Figure 6.3, has been previously been discussed by a number of workers ^{[22][11][12][23][24]} and contrasts significantly with the adsorption mechanism described in Figure 5.10 for non-polar molecules. At low pressures, and surface coverage, θ , hydrogen bonding occurs between polar adsorptive and active sites present on the surface of the material. These sites are designated as primary adsorption sites. At higher pressures and as surface coverage increases, the molecules adsorbed on the primary sites act as secondary sites. The interaction between adsorbate molecules is

stronger than the interactions between the adsorbate molecule and the oxygen-free substrate. The overall process is therefore characterised by the formation of adsorbed “clusters” at chemisorbed oxygen, or other polar sites, followed by the formation of an extended network structure in which the adsorbed polar molecules are constrained. The absolute structure and density of the clusters and the network thus established are not currently fully understood but should be close to liquid water. Hence an attempt was made to describe the water isotherms by the expression $Na = f(P, [O]_{tot})|_T$ where the additional term to the normal isotherm expression $[O]_T$ describes the concentration of polar oxygen groups, obtained here by a quick and direct measure from XPS.

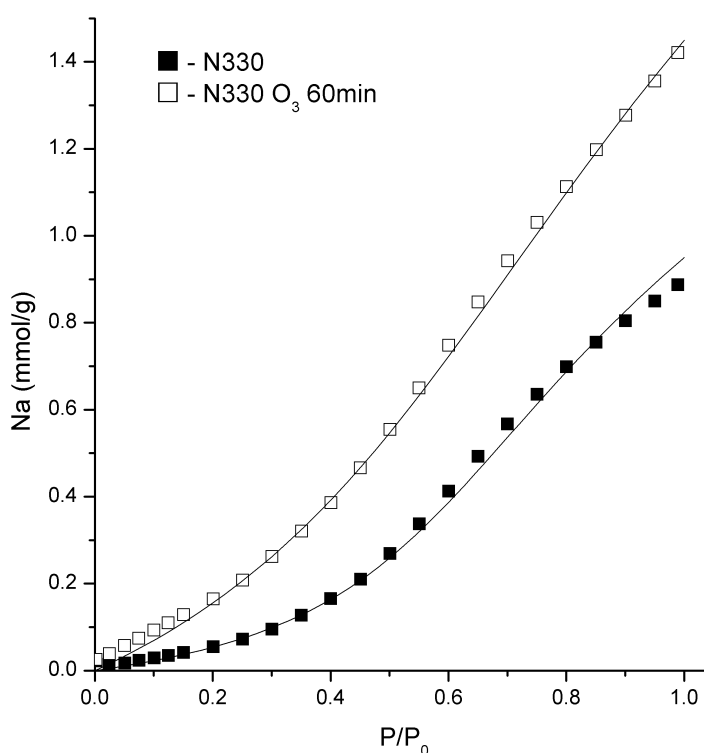


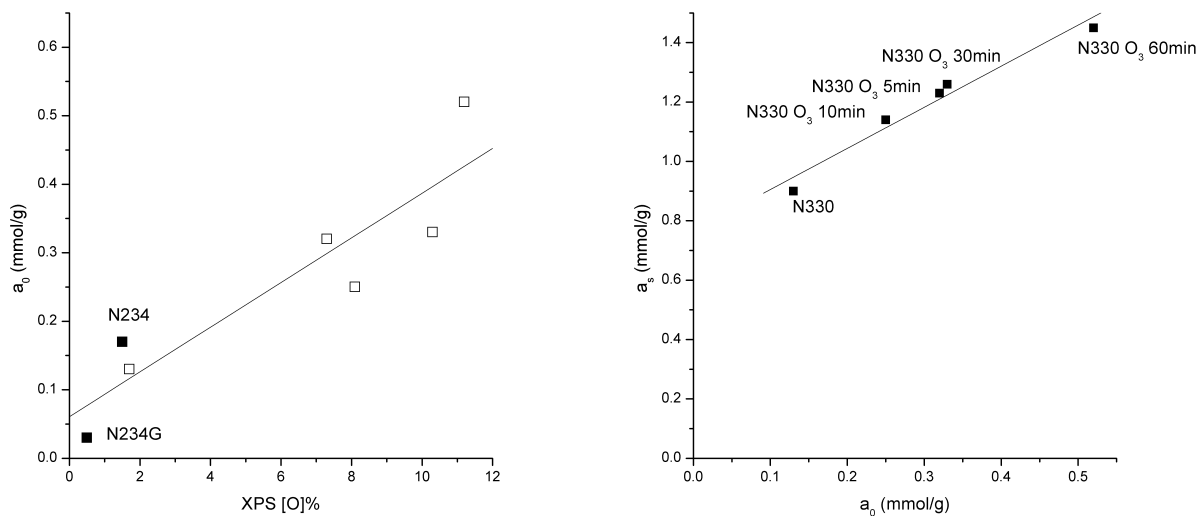
Figure 6.4: Fits of experimental data points to DS2 equation represented by solid lines for N330 base material (1.7 at.% oxygen) and N330 60 min. (11.2 at.% oxygen).

Water isotherm data from the CBs have been fitted to the modified DS equation (DS2) (examples are given in Figure 6.4 for the least and most oxidised surfaces). This equation gives a satisfactory description of the water adsorption on these materials across most of the pressure range. A slight over estimation of uptake at values of $p/p_0 > 0.9$ is visible for the untreated material. As discussed for example by Dubinin and Serpinsky [11][12] and Barton et al. [13] this is most probably due to the lack of availability of, or access to, the secondary sites at high surface coverage. For the 11.2 atom % oxygen surface a slight underestimation of uptake is observed in the low pressure region of the fit ($p/p_0 < 0.2$). The reason could be that the primary nucleation process is influenced in a positive way by the high concentration of surface sites.

As shown in Figure 6.5 a), the resulting a_0 values (calculated using the DS2 equation) are clearly increasing as the oxygen-containing groups become more numerous on the carbon surface. For this series of ozonated N330 CBs (without taking into account the two untreated CBs N234 and N234G), one obtained the Eq. 6.5 below by regression analysis of these data.

$$a_{0,DS2}(mmol/g) = 0.053 + 0.033 \cdot [O]_T \quad Eq. 6.5$$

The y-intercept value of 0.053 corresponds to an a_0 value for a “pure” carbon surface without any oxygen groups. It is interesting to note that this theoretical value is almost double than the value obtained ($a_0 = 0.029$) for the graphitized carbon black N234G. Another thing to point out was the difficulty to obtain adequate fits of the N234G water data using the DS or Barton equations so the DW equation was used instead for this particular case.



a)

b)

Figure 6.5: a) Relationship between $[O]_T$, the carbon black surface oxygen level in at.%, and the primary adsorption site parameter, a_0 , of the DS2 equation (correlation coefficient = 0.87) and b) the effect of a_0 on the measured limiting water adsorption parameter a_s .

From the Figure 6.5 b), one observes that the limiting water uptake, a_s , is also a function of a_0 . It demonstrates that the overall packing density of the adsorbed water is also dependent of the surface concentration of oxygen atoms (i.e. primary sites).

Carbon surface compositions can be measured from a one-off direct XPS measurement and the resulting values could be used for a quick estimation of β_{DRK} for organic vapours or a_0 and a_s for water. It seems reasonable to assume that this approach may, in the future, prove helpful in the fields of both isotherm prediction and in refining computer modelling methods.

6.3.1 Comparison with materials subjected to liquid-phase oxidation

6.3.1.1 XPS analysis of CBs subjected to liquid-phase oxidation

In this second part of the study, liquid-phase oxidations have been used in order to produce carbon black surface with different oxygen levels. The carbon black N330 was oxidised in liquid phase with the following chemicals: nitric acid (HNO_3), hydrogen peroxide (H_2O_2) and ammonium persulfate ($(\text{NH}_4)_2\text{S}_2\text{O}_8$) and details of the oxidation procedure can be found in the experimental section. The surface chemistry of the acid-oxidised materials was then analysed using XPS.

On the survey spectrum of each oxidised material, the presence of the oxygen 1s peak at a binding energy of 532 eV is clearly visible with the one for N330 HNO_3 being the largest. As an example, the survey spectra for the carbon black treated with ammonium persulfate is represented in the Figure 6.6 below.

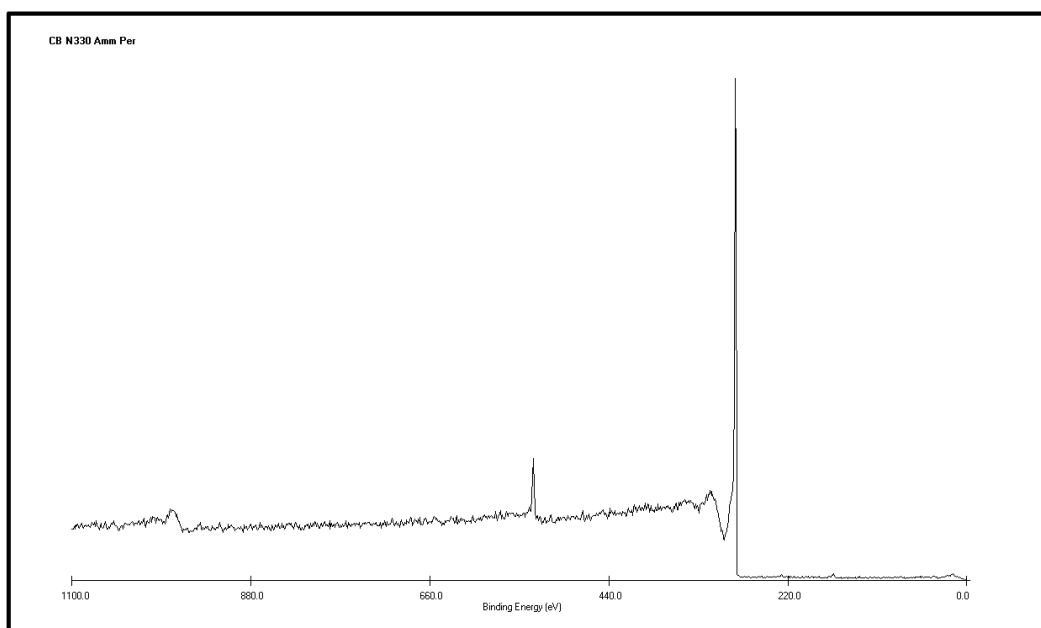


Figure 6.6: Survey scan obtained for N330 carbon black oxidized with ammonium persulfate.

For a better accuracy, the narrow scans O1s and C1s (and subsequent areas obtained from the data processing with the XPSpeak 4.1 software) were used to determine the relative atomic concentration of oxygen and carbon for each material. Additionally, they were also used to determine the type and proportion of the diverse oxygen groups present on the surface.

Table 6.1: Surface composition of N330 carbon blacks subjected to liquid-phase oxidation.

Materials	Surface composition	
	[C] at. %	[O] at. %
Base N330	98.6%	1.4%
N330 HNO ₃	88.8%	11.2%
N330 Amm Per	93.4%	6.6%
N330 H ₂ O ₂	96.7%	3.3%
N330 O ₃ 60min	88.8%	11.2%

The Table 6.1 summarises the surface composition obtained for these carbon blacks. The highest oxidation level was obtained for the carbon black treated with nitric acid with $[O]_{N330\ HNO_3} = 11.2\ at.\ %$, almost a tenfold increase compared to the oxygen level of the base N330 ($[O]_{Base\ N330} = 1.4\ at.\ %$).

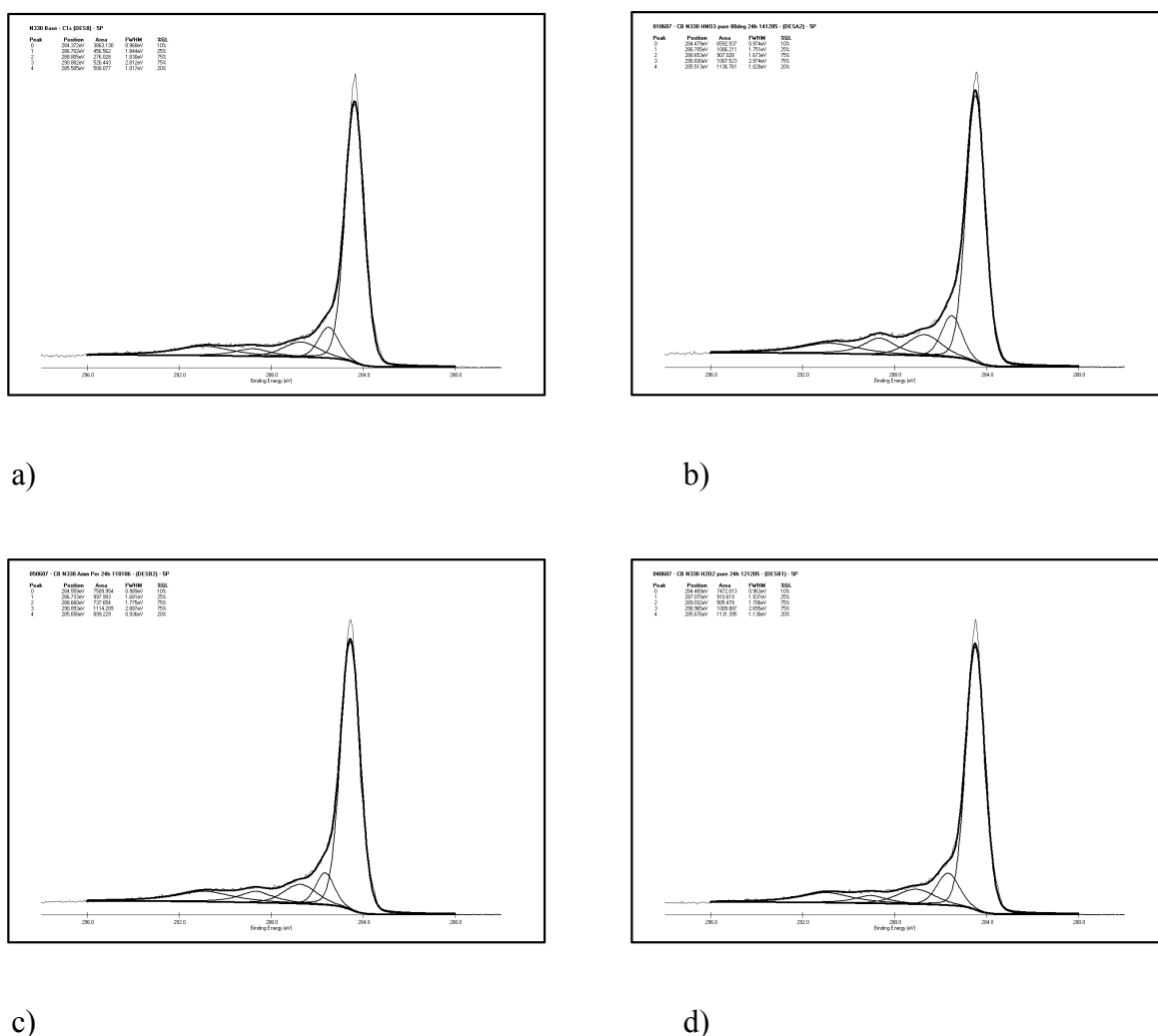


Figure 6.7: C1s narrow scan spectra for the carbon blacks subjected to liquid-phase oxidation. a) Base N330, b) N330 HNO₃, c) N330 Amm Per and d) N330 H₂O₂.

The C1s narrow scan spectra for the base and carbon black subjected to liquid-phase oxidation are represented in Figure 6.7. As in the case of the ozonated samples, the C1s peak was deconvoluted with five individual peaks representing: Peak I graphitic carbon, Peak II phenolic, alcohol, ether groups, Peak III carbonyl or quinone groups, Peak IV carboxyl or ester groups and Peak V shake-up satellite peaks due to a π - π^* transitions in aromatic rings [25]. The main characteristics of these peaks for these four samples are summarised in Table 6.2.

Table 6.2: C1s decomposition results for carbon blacks subjected to liquid-phase oxidation.

Base N330				N330 HNO ₃			
Peak	Position (eV)	FWHM (eV)	Concentration (%)	Peak	Position (eV)	FWHM (eV)	Concentration (%)
I	284.4	0.97	69%	I	284.5	0.97	62%
II	285.5	1.02	9%	II	285.5	1.03	11%
III	286.7	1.84	8%	III	286.7	1.75	9%
IV	288.8	1.83	5%	IV	288.7	1.67	9%
V	290.9	2.81	9%	V	290.9	2.97	9%

N330 Amm Per				N330 H ₂ O ₂			
Peak	Position (eV)	FWHM (eV)	Concentration (%)	Peak	Position (eV)	FWHM (eV)	Concentration (%)
I	284.6	0.99	67%	I	284.5	0.96	68%
II	285.7	0.94	8%	II	285.7	1.14	10%
III	286.7	1.68	9%	III	287.1	1.94	8%
IV	288.7	1.77	7%	IV	289.0	1.71	5%
V	290.9	2.89	10%	V	291.0	2.66	9%

As one can see from the values, the biggest change from the carbon in graphitic surface structures arises from the carbon treated with nitric acid where it is reduced from 69 to 62% while the level of Peak IV (carboxyl or ester groups) almost doubles for this material (from 5 to 9%). This aspect is much less pronounced for the two other oxidised carbons as the oxygen concentration is significantly lower than for the N330 HNO₃. As for the ozonated carbon blacks, the concentration of [phenolic, alcohol and ether groups] and [carbonyl or quinone groups] remains almost unchanged after the treatment.

On the other hand, as illustrated in Figure 6.8, the high resolution oxygen spectra were resolved using two individual component peaks: Peak I for carbonyl groups and Peak II for hydroxyl or ether groups. The same fitting parameters than for the ozone oxidised carbon black were used. The peak corresponding to chemisorbed O₂ and/or water was again not detected. For comparison purposes, the oxygen peak for the base material is redisplayed in Figure 6.8 a).

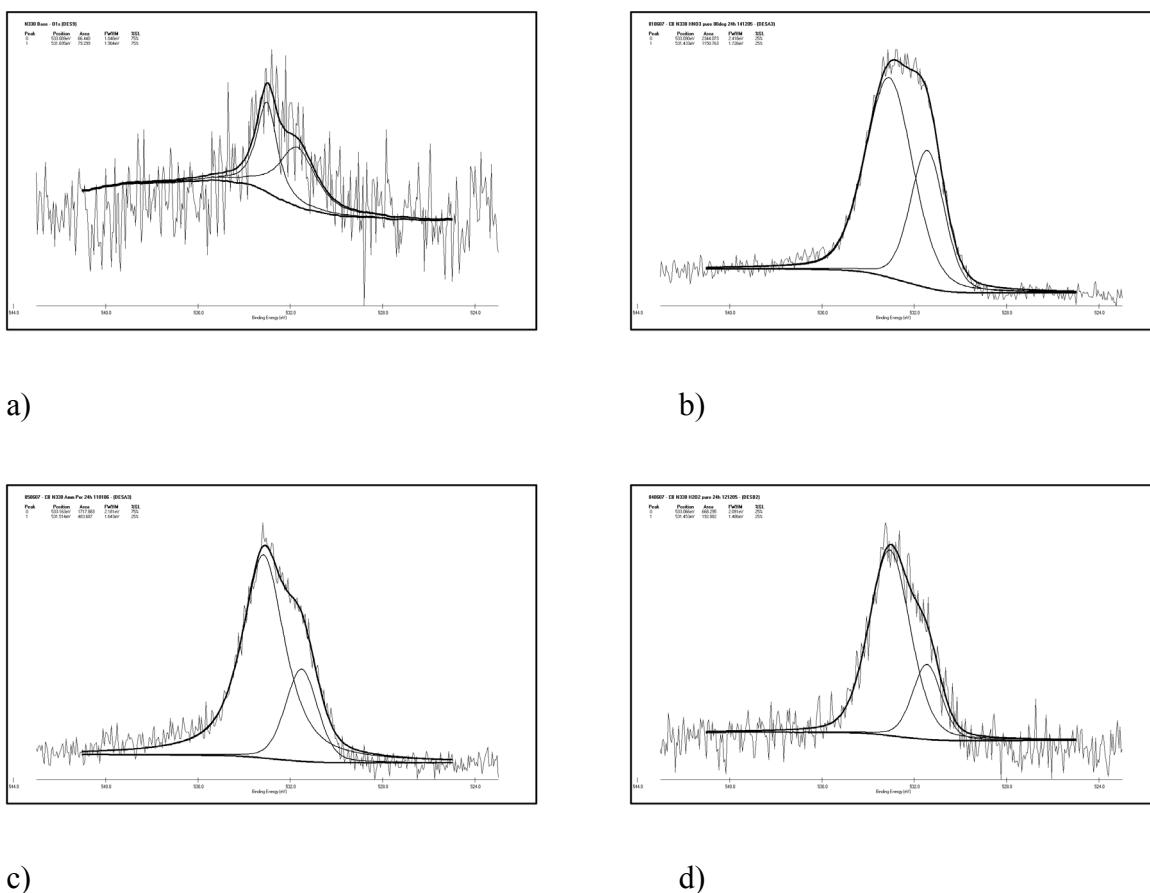


Figure 6.8: O1s narrow scan spectra for the carbon blacks subjected to liquid-phase oxidation. a) Base N330, b) N330 HNO₃, c) N330 Amm Per and d) N330 H₂O₂.

The main characteristics of the O1s peak decomposition for the base and carbon blacks subjected to liquid-phase oxidation are summarised in Table 6.3.

Table 6.3: O1s decomposition results for carbon blacks subjected to liquid-phase oxidation.

Materials	Position (eV)		FWHM (eV)		Concentration (%)	
	Peak I	Peak II	Peak I	Peak II	Peak I	Peak II
Base N330	533.0	531.7	1.05	1.90	46%	54%
N330 HNO ₃	533.1	531.4	2.42	1.73	67%	33%
N330 Amm Per	533.2	531.5	2.18	1.64	78%	22%
N330 H ₂ O ₂	533.1	531.5	2.09	1.49	78%	22%

Looking at the respective concentration of these two peaks, one can observe a rise of the contribution of the peak I (carbonyl groups) from 46% for the base carbon black to 67% for N330 HNO₃ and to 78% for both N330 Amm Per and N330 H₂O₂. In opposite way, the contribution of the peak II (hydroxyl or ether groups) decreases. While the positions of these two peaks hardly change, one observes from the FWHM values, a significant widening of the Peak I and a slight narrowing of the Peak II for the carbon blacks subjected to liquid-phase oxidation.

Regarding now the adsorption data, adsorption isotherm of nitrogen at 77°K (not represented here) on the carbon blacks subjected to the different liquid-phase oxidation were type II and were very similar to the one of the untreated material. The only difference was observed in the initial region where the isotherm of the N330 HNO₃ and N330 Amm Per were slightly displaced to higher adsorption values. Surface areas were also determined using the DRK method and taking a value of 0.162nm² for the nitrogen cross sectional area. The values obtained were quite close to each other with 87.4 m²/g for N330 HNO₃, 90.7 m²/g for N330 H₂O₂ and 89.1 m²/g for N330 Amm Per.

As illustrated in Figure 6.9 a), one notices that water isotherms on N330 Amm Per and N330 H₂O₂ carbon blacks are Type III and are similar, especially for N330 H₂O₂, to the isotherm of the base N330 while the water isotherm obtained for N330 HNO₃ is significantly different and can be considered as a type II. In the latter, this complete change to the isotherm shape indicates that the nitric acid treatment has not only modified the surface chemistry but also affected the carbon black structure. This is also confirmed by looking at the water isotherm of N330 O₃ 60min (see Figure 6.2) which has exactly the same oxygen level ($[O]_T = 11.2 \text{ at. } \%$) but has a typical type III isotherm shape.

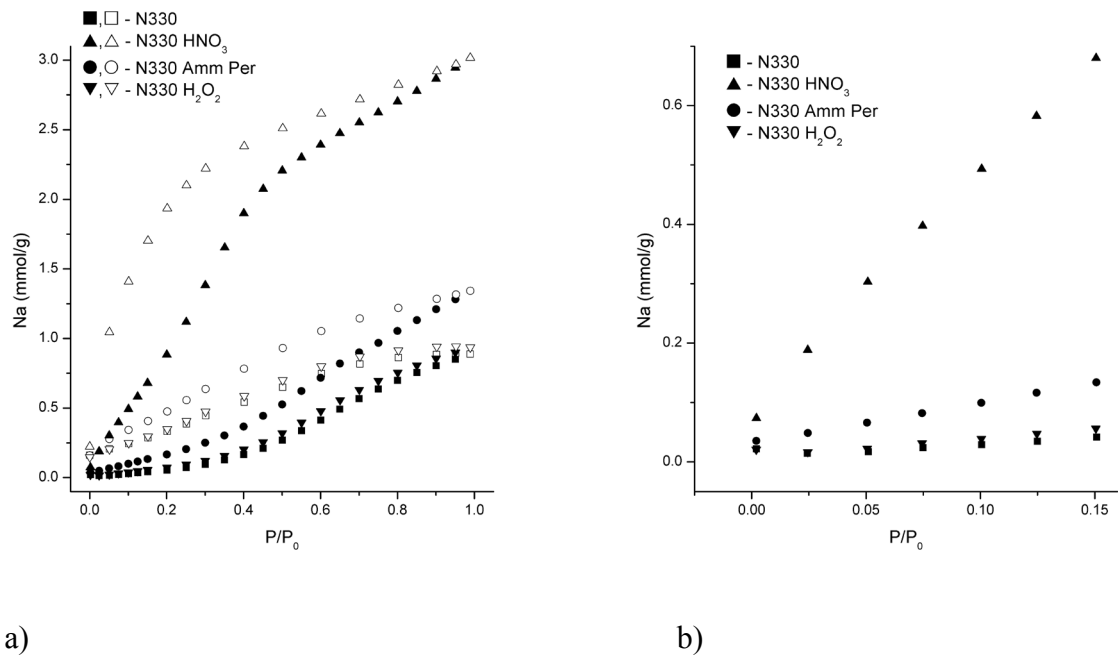


Figure 6.9: Water adsorption isotherms at 303°K for N330 carbon blacks subjected to liquid-phase oxidation. a) Whole isotherms with adsorption and desorption branches and b) expanded low pressure domains ($p/p_0 < 0.16$).

All isotherms of materials subjected to liquid-phase oxidation are associated to displacement to higher adsorption uptakes over the whole pressure range as the surface oxygen level (in at.%) increases ranging in terms of a_s values from a very little increase for N330 H₂O₂ ($a_s = 0.94 \text{ mmol/g}$) to almost a fourfold increase in the case of N330 HNO₃ ($a_s = 3.02 \text{ mmol/g}$). A zoom on the low pressure region is also represented on Figure 6.9 b).

Water isotherm data from the CBs subjected to liquid-phase oxidation have been fitted with the following equations: Dubinin-Serpinsky (DS1 (Eq. 2.30) and DS2 (Eq. 2.32)), Barton (B1 (Eq. 2.34), B2 (Eq. 2.35) and generalised equation GB (Eq. 2.36)) and D'Arcy & Watt (DW (Eq. 2.37) and generalised equation GDW (Eq. 2.38)). For the four materials, the best fits, calculated using the Excel solver, are represented in Figure 6.10.

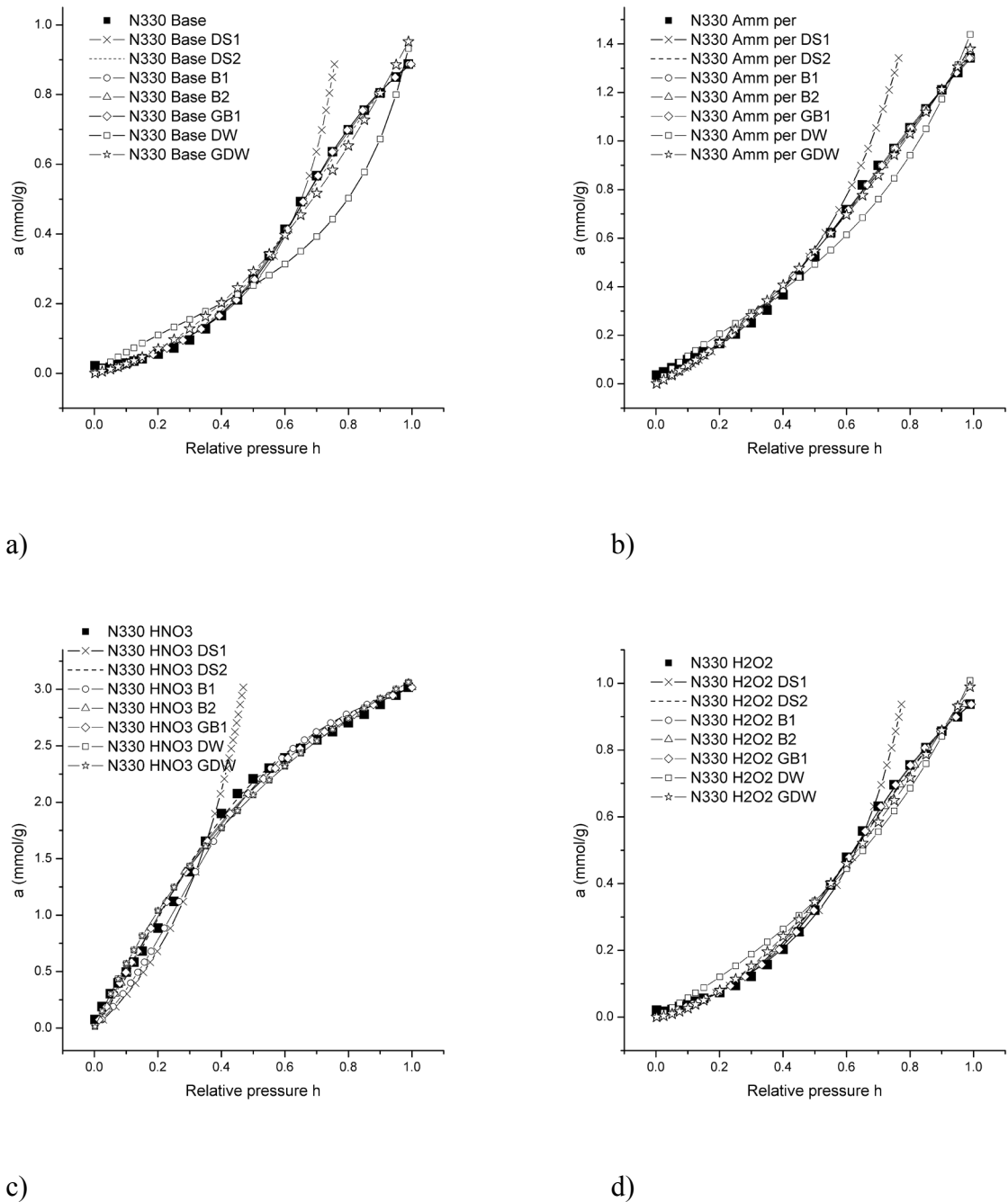


Figure 6.10: Water adsorption isotherm fits using the equations of Dubinin-Serpinsky, Barton and D'Arcy & Watt for the following materials: a) N330 Base, b) N330 Amm Per, c) N330 HNO₃ and d) N330 H₂O₂.

The DS1 equation, which represents the most simplified model, was not used to fit the water data up on the whole pressure range but only up to a relative pressure of 0.5.

This equation gives a reasonably description of the water adsorption on these materials (except for the CB treated with nitric acid) across the low pressure region but displays important deviation at higher pressure as expected. All the equations used give an excellent description of the water adsorption with an exception of the D'Arcy & Watt equation. This DW equation seems to slightly over-estimate the uptake at values of $p/p_0 < 0.4$ while giving an under estimation at high pressure region ($p/p_0 > 0.5$). This might be explained by the limitation of the Excel solver to calculate the best fit. A solution to overcome this issue would be to switch to a proper mathematical/modelling software with more computational capabilities.

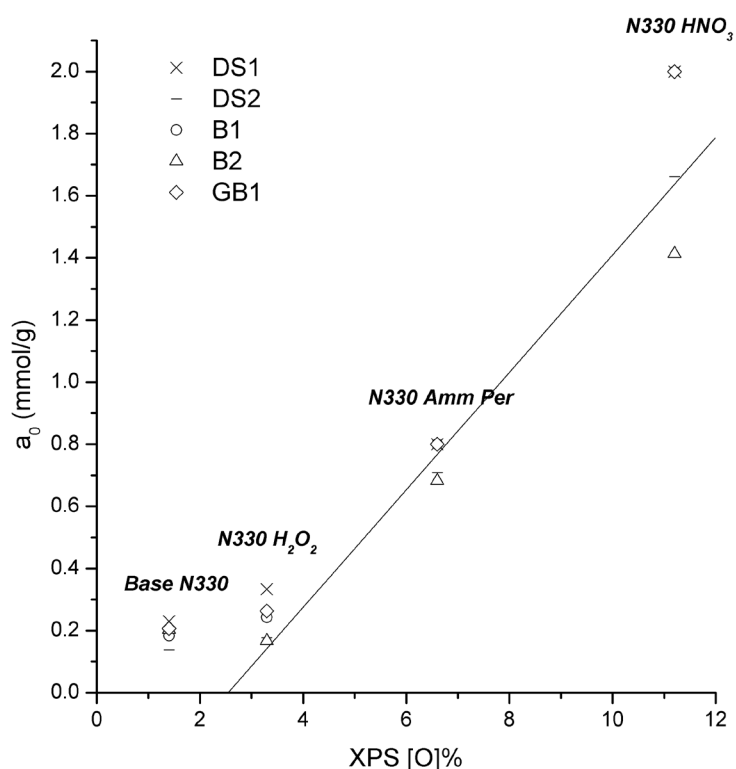


Figure 6.11: Relationship between $[O]_T$, the carbon black surface oxygen level (in at.%), and the primary adsorption site parameter, a_0 , obtained using the various water equations (except D'Arcy & Watt equations).

As shown in Figure 6.11, the resulting a_0 values obtained from the various water equations follow all the same trend and are, as for the ozonated CBs, strongly dependant from the amount of oxygen-containing groups present on the carbon black surface subjected to liquid-phase oxidation. From the regression analysis of these oxidised N330 CBs (DS2 data), one obtained the Eq. 6.6 below:

$$a_{0,DS2}(mmol/g) = -0.481 + 0.189 \cdot [O]_T \quad Eq. 6.6$$

For these oxidised carbon blacks, one obtained a slope value of 0.189 which is significantly higher than the value of 0.033 obtained in the case of the ozonated N330 series. This is most probably due to the different oxidation mechanisms occurring during ozone treatment and oxidation in liquid-phase with acid. This may also reflect the damage caused by these acids (especially nitric acid) on the physical structure while the ozone treatment has been shown to affect only the surface chemistry.

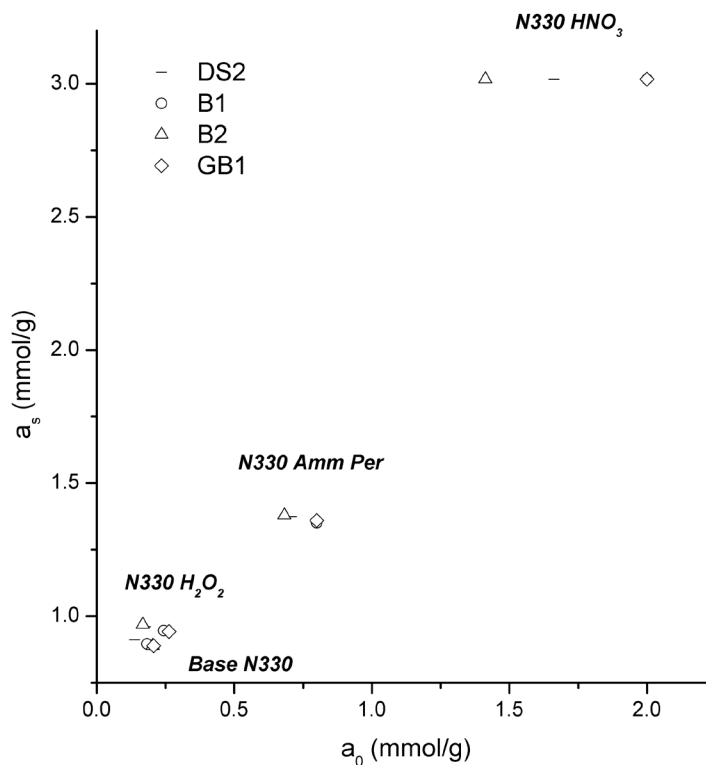


Figure 6.12: Relationship between the primary adsorption site parameter, a_0 , and the measured limiting water adsorption parameter, a_s .

From the Figure 6.12, the limiting water uptake, a_s , appears to be a function of a_0 . It demonstrates that the overall packing density of the adsorbed water is also dependent of the surface concentration of oxygen atoms (i.e. primary sites). For comparison with the ozonated N330, the a_s value obtained for N330 O₃ 60min is similar to the a_s of N330 Amm Per but only half of the a_s of N330 HNO₃. From these two plots, one can also observe that these different equations provide a wide range of a_0 values whereas the a_s values are quite close to each other. The B2 equation usually gives the lowest a_0 values and B1 and GB1 the highest while DS2 values are in the middle of the range. But this might also be influenced by the surface oxygen concentration of the material.

6.3.1.2 XPS analysis of ACs subjected to liquid-phase oxidation.

The effects of liquid-phase oxidation on the surface chemistry of activated carbon BPL were also investigated. Nitric acid (HNO_3) and hydrogen peroxide (H_2O_2) were used in order to produce activated carbon with different oxygen levels (both external surface and porosity). The details of the oxidation procedure can be found in the experimental section. The surface chemistry of the acid-oxidised materials was then analysed using XPS.

Observations of the survey spectra show the presence of the Oxygen1s peak for the two oxidised BPL but this peak is also clearly noticeable for the base BPL. As an example, the survey spectra for the carbon black treated with nitric acid is represented in the Figure 6.13.

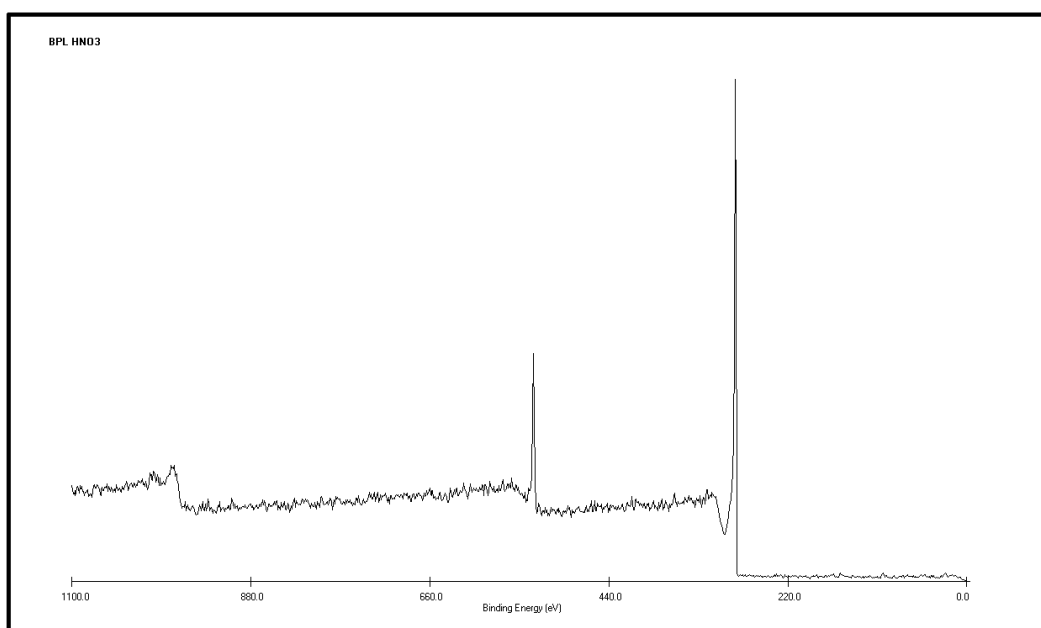


Figure 6.13: Survey scan obtained for BPL activated carbon oxidized with nitric acid.

Similarly to carbon black samples, the narrow scan O1s and C1s areas obtained from the data processing with the XPSpeak 4.1 software were used to determine the relative

atomic concentration of oxygen and carbon for each material. Additionally, the nitrogen element was also taken into account in the case of the activated carbon treated with nitric acid. These scans were also used to determine the type and proportion of the diverse oxygen groups present on the surface. The Table 6.4 summarizes the surface composition obtained for these activated carbons. The oxidation level measured for BPL HNO₃ ($[O]_{BPL\ HNO_3} = 15.6\ at.\ \%$) and BPL H₂O₂ ($[O]_{BPL\ H_2O_2} = 17.9\ at.\ \%$) were on the same order. This is more than twice the oxygen level of the base BPL ($[O]_{Base\ BPL} = 7.6\ at.\ \%$). It is interesting to note that the oxygen amount on the base activated carbon BPL is significantly higher than on the base carbon black N330 as activated carbon is more prone to oxidation due to more available sites (defects and edges) and less ordered graphitic structure than carbon black. Moreover the BPL material batch used in this study have been opened and stored for more than 5 years so its oxygen level is slightly higher than a “fresh” as-received BPL which should be around 5.5~6.0 at.% (see values obtained later in this work for heat-treated BPL series or published by Bradley et al. [26]). As said before, a nitrogen level of 1.9 at.% was measured for the material treated with nitric acid.

Table 6.4: Surface composition of BPL activated carbons subjected to liquid-phase oxidation.

Materials	Surface composition		
	[C] at.%	[O] at.%	[N] at.%
Base BPL	92.4%	7.6%	n.d.
BPL HNO ₃	83.8%	15.6%	1.9%
BPL H ₂ O ₂	82.1%	17.9%	n.d.

The C1s narrow scan spectra for the base and activated carbons subjected to liquid-phase oxidation are displayed in Figure 6.14. The deconvolution of the C1s peak has been carried out using the same five individual components than previously (see paragraph 6.3.1.1 for more details). The main characteristics of the carbon peaks for the

base and activated carbons subjected to liquid-phase oxidation are summarised in Table 6.5.

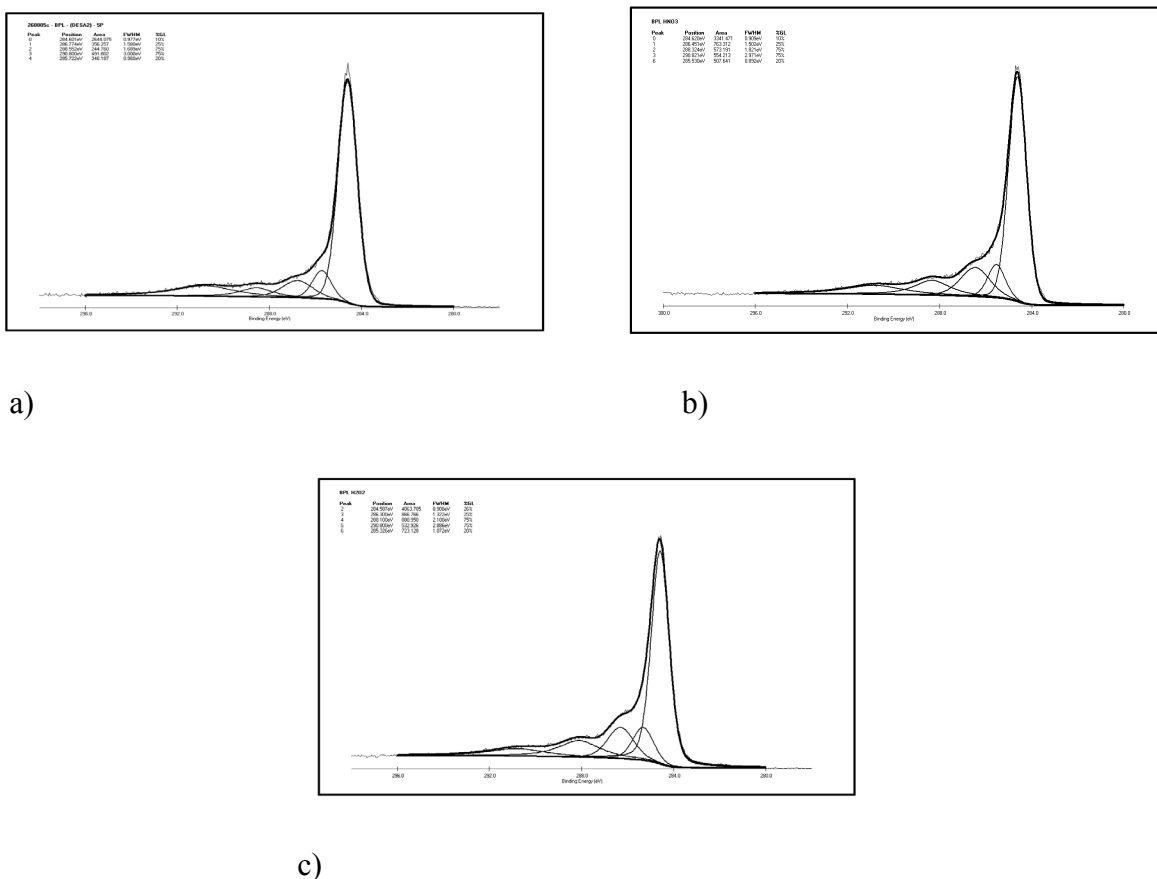


Figure 6.14: C1s narrow scan spectra for the activated carbons subjected to liquid-phase oxidation. a) Base BPL, b) BPL HNO₃ and c) BPL H₂O₂.

As seen from the XPS values, one observes a similar trend than for the carbon blacks subjected to liquid-phase oxidation. The carbon in graphitic surface structures reduced significantly from 65 to 58% after both treatments while the level of Peak IV (carboxyl or ester groups) doubles (from 6 to 10% for BPL HNO₃ and 12% for BPL H₂O₂). In addition, an increase in the level of Peak III (carbonyl or quinone groups) was observed for the oxidised materials. As for the ozonated and carbon blacks subjected to liquid-phase oxidation, it was observed that the concentration of [phenolic, alcohol and ether groups] remains almost unchanged after the treatment. The Peak V levels are also

reduced for oxidised materials as this peak is linked to the carbon present in the graphitic structure.

Table 6.5: C1s decomposition results for activated carbons subjected to liquid-phase oxidation.

Base BPL			
Peak	Position (eV)	FWHM (eV)	Concentration (%)
I	284.6	0.98	65%
II	285.7	0.96	8%
III	286.8	1.58	9%
IV	288.5	1.69	6%
V	290.8	3.00	12%

BPL HNO ₃			
Peak	Position (eV)	FWHM (eV)	Concentration (%)
I	284.6	0.90	58%
II	285.5	0.89	9%
III	286.5	1.50	13%
IV	288.3	1.82	10%
V	290.8	2.97	10%

BPL H ₂ O ₂			
Peak	Position (eV)	FWHM (eV)	Concentration (%)
I	284.6	0.91	58%
II	285.3	1.07	10%
III	286.3	1.32	12%
IV	288.1	2.10	12%
V	290.8	2.89	8%

On the other hand, as illustrated in Figure 6.15, the high resolution oxygen spectra were resolved using the two individual component peaks (as detailed above) and with similar fitting parameters than used for other materials. The main characteristics of the O1s peak decomposition for the base and activated carbons subjected to liquid-phase oxidation are summarised in Table 6.6.

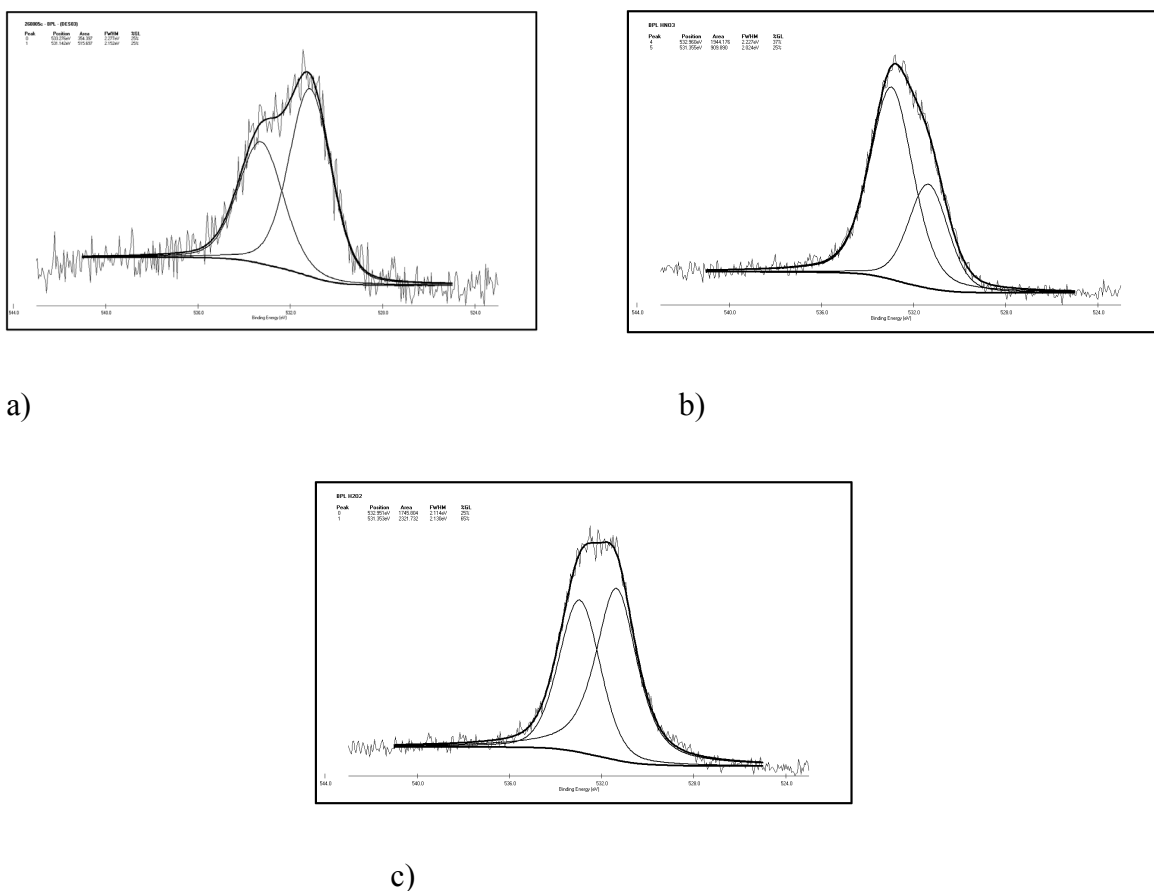


Figure 6.15: O1s narrow scan spectra for the activated carbons subjected to liquid-phase oxidation. a) Base BPL, b) BPL HNO₃ and c) BPL H₂O₂.

Looking at the respective concentration of these two peaks, one notices that although the peak profiles look different, the values are almost identical for the base and BPL H₂O₂. This can be explained by the much higher oxygen level on the BPL H₂O₂ bringing less influence to the Shirley background level. On the contrary, a rise of the contribution of the peak I (carbonyl groups) from 41% for the base carbon black to 68% for N330 HNO₃ was observed. The positions and FWHM values are hardly influenced by the liquid-phase oxidation (and also due to the intrinsically higher oxygen level for base BPL than for base N330).

Table 6.6: O1s decomposition results for activated carbons subjected to liquid-phase oxidation.

Materials	Position (eV)		FWHM (eV)		Concentration (%)	
	Peak I	Peak II	Peak I	Peak II	Peak I	Peak II
Base BPL	533.3	531.1	2.28	2.15	41%	59%
BPL HNO ₃	533.0	531.4	2.23	2.02	68%	32%
BPL H ₂ O ₂	533.0	531.4	2.11	2.13	43%	57%

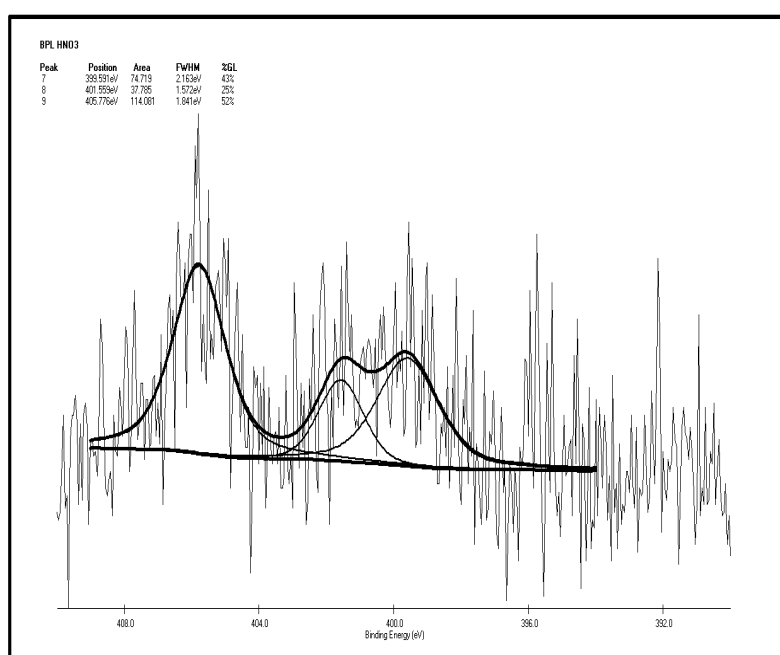


Figure 6.16: N1s narrow scan spectra for the activated carbons treated with nitric acid (HNO₃).

The deconvolution of the N1s peak from BPL HNO₃ is also included in Figure 6.16. For this carbon sample, both typical forms of nitrogen elements are observed at 399.6 eV for “pyrrolic nitrogen, pyridones or a mixture of both” and at 401.6 eV for “forms of quaternary nitrogen, protonated pyridinic ammonium ions, nitrogen atoms replacing carbon in graphene” [27]. In addition, one additional form of nitrogen elements was

found at 405.8 eV. This form is characteristic of oxidised nitrogen functionalities or NO₂ groups and has already been observed by Terzyk [28].

Regarding the water adsorption data represented in Figure 6.17 a), one observes that water isotherms on BPL HNO₃ and BPL H₂O₂ activated carbon have a similar type III shape than the isotherm of the base BPL but a significant displacement to higher adsorption uptakes (almost twofold increase) is observed over the whole pressure range.

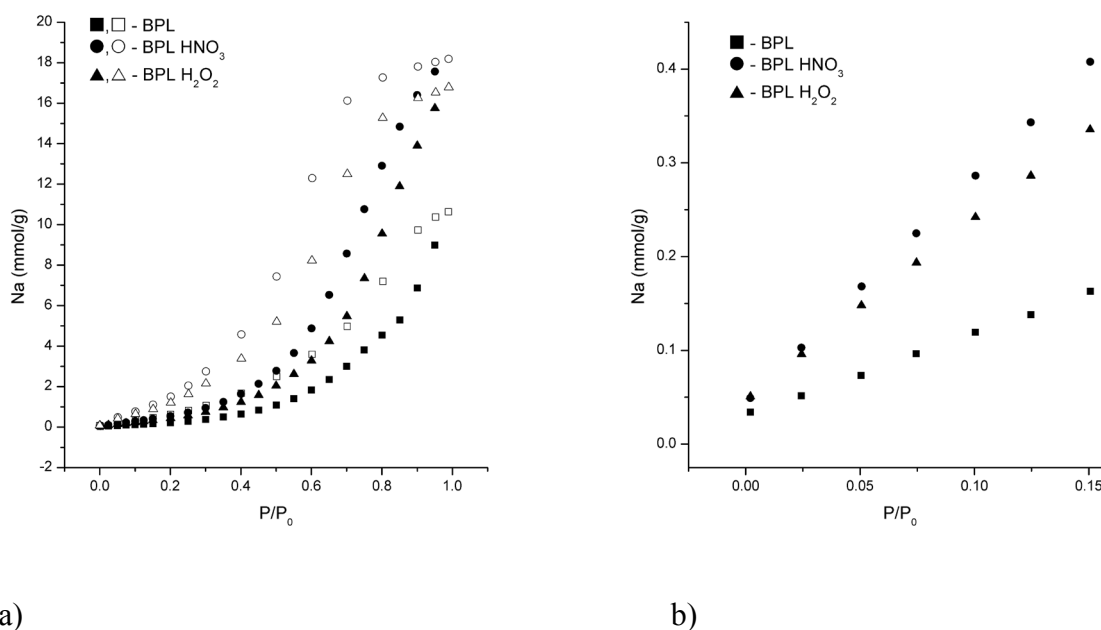


Figure 6.17: Water adsorption isotherms at 303°K for BPL activated carbons subjected to liquid-phase oxidation. a) Whole isotherms with adsorption and desorption branches and b) expanded low pressure domains ($p/p_0 < 0.16$).

This displacement results in the following a_s values: $a_s = 10.63 \text{ mmol/g}$ for the base BPL, $a_s = 16.79 \text{ mmol/g}$ for BPL H₂O₂ and $a_s = 18.19 \text{ mmol/g}$ for BPL HNO₃. A zoom on the low pressure region is also represented on Figure 6.17 b) and it is interesting to see the difference between the water adsorption behaviour (adsorption capacity, isotherm shape, etc...) of activated carbon or carbon black materials subjected to liquid-phase oxidation.

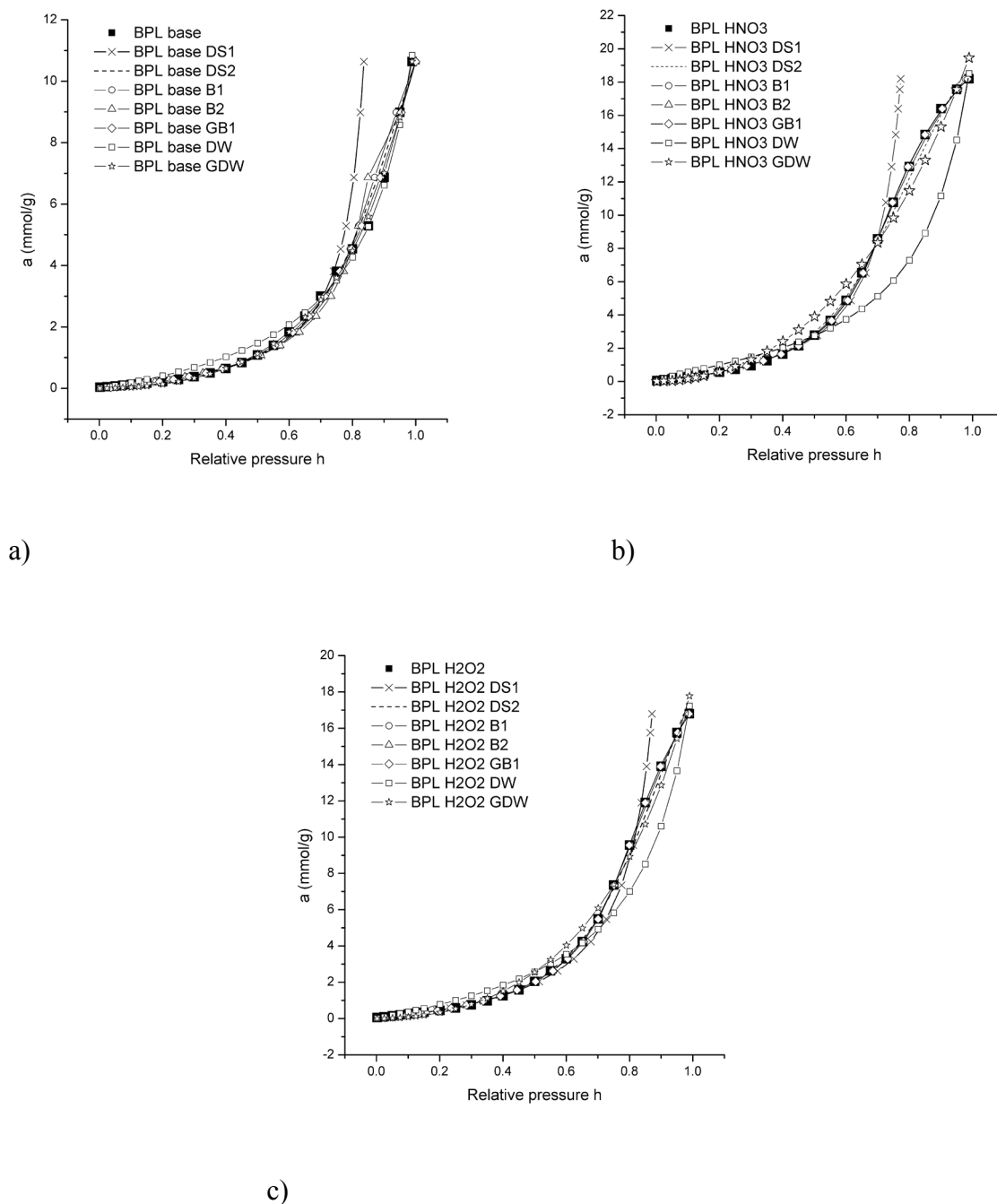


Figure 6.18: Water adsorption isotherm fits using the equations of Dubinin-Serpinsky, Barton and D’Arcy & Watt for the following materials: a) BPL Base, b) BPL HNO₃ and c) BPL H₂O₂.

Water isotherm data from the ACs subjected to liquid-phase oxidation have been fitted with the same equations than the oxidised CBs and the best fits are represented in

Figure 6.18. As for CB materials, the DS1 equation, was only used over a relative pressure range of $0 < p/p_0 < 0.5$. This equation gives a very good description of the water adsorption on these materials up to $p/p_0 = 0.7\sim 0.8$ which is higher than for CB materials. For the base AC material, all the equations used give an excellent description of the water adsorption. Now regarding the activated carbons subjected to liquid-phase oxidation, the Dubinin-Serpinsky and Barton equations give excellent fit to the data whereas deviations are observed with the D'Arcy & Watt equations both normal and generalised. The DW equation seems to under-estimate the uptake at values at high pressure region. As said below, the limitation of the Excel solver could be one reason for that.

The Figure 6.19 shows that the resulting a_0 values obtained for the ACs subjected to liquid-phase oxidation follow the same trend as for the CBs, i.e. increase with the amount of oxygen-containing groups present on the activated surface. From the regression analysis of these oxidised BPL ACs (DS2 data), one obtained the following equation:

$$a_{0,DS2}(\text{mmol} \cdot \text{g}^{-1}) = 0.300 + 0.063 \cdot [O]_T \quad \text{Eq. 6.7}$$

The first term of this equation gives an a_0 value of 0.300 mmol/g for a theoretical oxygen-free activated carbon material.

In addition, one obtained a slope value of 0.063 which is comparable to the value of 0.033 obtained in the case of the ozonated N330 series. The a_0 value calculated for BPL HNO₃ is slightly higher than for BPL H₂O₂ although having a lower surface oxygen concentration. A possible explanation could be that the nitric acid treatment has resulted in more damage to the physical structure of the AC than the hydrogen peroxide treatment.

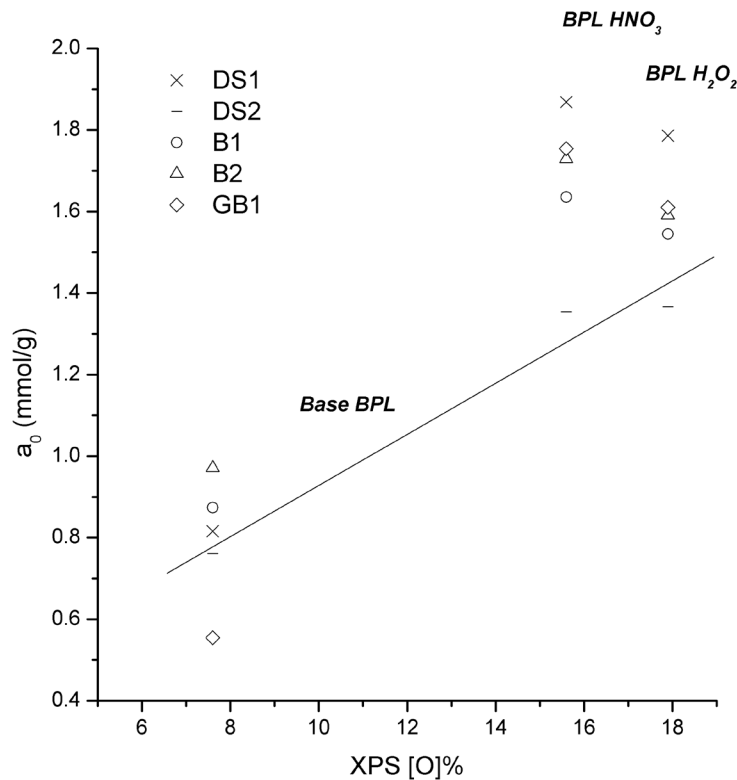


Figure 6.19: Relationship between $[O]_T$, the activated carbon surface oxygen level (in at.%), and the primary adsorption site parameter, a_0 , obtained using the various water equations (except D'Arcy & Watt equations). Solid line: regression analysis of the DS2 data points.

6.4 Conclusions

N330 carbon black has been oxidized in ozone (O_3) fluidised-bed system in order to produce a series of material with increasing oxygen concentrations on the surface. Alternatively, N330 carbon black and BPL activated carbon were treated in liquid-phase using nitric acid (HNO_3), hydrogen peroxide (H_2O_2) and ammonium persulfate. Direct measurement of surface oxygen levels $[O]_T$ (at.%) on the resulting materials has been carried out using XPS. For the ozonated series, the enthalpies of immersion data clearly indicate a shift from the dispersion dominated interaction for toluene to the polar

dominated interaction for water. For an oxygen free carbon black surface, water dispersion interactions (about 35 mJ/m^2) dominate adsorption process and the heat of adsorption is proportionate to the heat of condensation. In the case of the ozonated CB samples, Type III adsorption isotherms are observed and exhibit a displacement to higher adsorption values as the carbon total surface oxygen level $[O]_T$ (at.%), measured by XPS, increases. Regarding the carbon blacks subjected to liquid-phase oxidation, a similar behaviour is observed for the N330 treated with H_2O_2 and Amm Per with identical isotherm shapes but significant differences are visible for the sample treated with nitric acid where the isotherm shape shifts to a Type II associated with really high adsorption values. Type III isotherms are observed for activated carbon materials with almost twofold increase of water adsorption uptake over the whole pressure range for the ACs subjected to liquid-phase oxidation but differed significantly in terms of adsorption capacity and kinetics of adsorption in the low pressure region. While the ozone treatment is only modifying the surface chemistry of the material, the liquid-phase oxidations, in particular with HNO_3 , seem to affect both surface chemistry and physical structure of the carbon material as indicated in the literature [29]. The Dubinin-Serpinsky equation and other water equations (Barton and D'Arcy & Watt) give a reasonable description of the water isotherm data across much of the pressure range. Similarly to the alcohol study, a correlation is observed between the surface oxygen concentration $[O]_T$ and the following parameters: the primary polar adsorption sites a_0 and the limiting water uptake value a_s .

References

- ¹ M. V. Lopez-Ramon, F. Stoeckli, C. Moreno-Castilla and F. Carrasco-Marin. Specific and nonspecific interactions between methanol and ethanol and active carbons. *Langmuir* **16** (2000) 5967-5972.
- ² P. J. M. Carrott, M. M. L. R. Carrott and I. P. P. Cansado. Reference data for the adsorption of methanol on carbon materials. *Carbon* **39** (2001) 193–200.
- ³ F. Stoeckli and A. Lavanchy. The adsorption of water by active carbons, in relation to their chemical and structural properties. *Carbon* **38** (2000) 475–494.
- ⁴ R. H. Bradley and B. Rand. *Adsorption of alcohols and water vapour onto active carbons* 18th Biennial Conf. on Carbon 94-95 (American Carbon Society, Worcester, Mass., USA, 1987).
- ⁵ R. H. Bradley and B. Rand. A comparison of the adsorption behaviour of nitrogen, alcohols, and water towards active carbons. *Carbon* **29** (1991) 1165-1172.
- ⁶ R. H. Bradley and B. Rand. On the physical adsorption of vapors by microporous carbons. *J. Colloid Interface Sci.* **169** (1995) 168-176.
- ⁷ F. Rodriguez-Reinoso, M. Molina-Sabio and M. T. Gonzalez. Effect of oxygen surface groups on the immersion enthalpy of activated carbons in liquids of different polarity. *Langmuir* **13** (1997) 2354-2358.
- ⁸ Y. I. Tarasevich and E. V. Aksenenko. Interaction of water, methanol and benzene molecules with hydrophilic centres at a partially oxidised model graphite surface. *Colloids and Surfaces A: Physicochem. Eng. Aspects* **215** (2003) 285-291.
- ⁹ M. G. Kaganer. A method for the determination of specific surfaces from the adsorption of gases. *Proc. Acad. Sci. USSR* **116** (1957) 603-605.
- ¹⁰ M. M. Dubinin, E. D. Zaverina and V. V. Serpinsky. The sorption of water vapour by active carbon. *J. Chem. Soc. London* **2** (1955) 1760–1766.

- ¹¹ M. M. Dubinin and V. V. Serpinsky. Water vapour adsorption on microporous activated carbons. *Dokl. Akad. Nauk SSSR* **258** (1981) 1151-1157.
- ¹² M. M. Dubinin and V. V. Serpinsky. Letter to the Editor. Isotherm equation for water vapor adsorption by microporous carbonaceous adsorbents. *Carbon* **19** (1981) 402-403.
- ¹³ S. S. Barton, M. J. B. Evans and J. A. F. MacDonald. The adsorption of water vapor by porous carbon. *Carbon* **29** (1991) 1099-1105.
- ¹⁴ S. Furmaniak, P. A. Gauden, A. P. Terzyk, R. P. Wesolowski and G. Rychlicki. 151-182 (Universitatis Mariae Curie - Sklodowska, Lublin-Polonia, 2005).
- ¹⁵ G. de la Puente, J. J. Pis, J. A. Menendez and P. Grange. Thermal stability of oxygenated functions in activated carbons. *J. Anal. Appl. Pyrol.* **43** (1997) 125-138.
- ¹⁶ S. Ohe. *Computer aided data book of vapor pressures* (Data Book Publishing Co., Tokyo, Japan, 1976).
- ¹⁷ R. H. Bradley, R. Daley and F. Le Goff. Polar and dispersion interactions at carbon surfaces: further development of the XPS-based model. *Carbon* **40** (2002) 1173-1179.
- ¹⁸ M. V. Lopez-Ramon, F. Stoeckli, C. Moreno-Castilla and F. Carrasco-Marin. On the characterization of acidic and basic surface sites on carbons by various techniques. *Carbon* **37** (1999) 1215-1221.
- ¹⁹ F. Carrasco-Marin, A. Mueden, T. A. Centeno, F. Stoeckli and C. Moreno-Castilla. Water adsorption on activated carbons with different degrees of oxidation. *J. Chem. Soc., Faraday Trans.* **93** (1997) 2211-2215.
- ²⁰ J. Kazmierczak, S. Biniak, A. Swiatkowski and K.-H. Radeke. Interdependence of different parameters characterizing the chemistry of an activated carbon surface. *J. Chem. Soc., Faraday Trans.* **87** (1991) 3557 - 3561.
- ²¹ R. H. Bradley, I. Sutherland and E. Sheng. Relationship between carbon black surface chemistry and energy. *J. Chem. Soc., Faraday Trans.* **91** (1995) 3201-3207.
- ²² S. S. Barton, M. J. B. Evans and B. H. Harrison. Surface studies on carbon: water adsorption on polyvinylidene chloride carbon. *J. Colloid Interface Sci.* **45** (1973) 542-548.

- ²³ R. H. Bradley and B. Rand. The adsorption of vapours by activated and heat-treated microporous carbons. Part 2. Assessment of surface polarity using water adsorption. *Carbon* **31** (1993) 269-272.
- ²⁴ S. S. Barton, M. J. B. Evans and J. A. F. MacDonald. Adsorption of water vapor on nonporous carbon. *Langmuir* **10** (1994) 4250-4252.
- ²⁵ S. Biniak, G. Szymanski, J. Siedlewski and A. Swiatkowski. The characterization of activated carbons with oxygen and nitrogen surface groups. *Carbon* **35** (1997) 1799-1810.
- ²⁶ R. H. Bradley, I. Sutherland and E. Sheng. Carbon surface: area, porosity, chemistry, and energy. *J. Colloid Interface Sci.* **179** (1996) 561-569.
- ²⁷ J. R. Pels, F. Kapteijn, J. A. Moulijn, Q. Zhu and K. M. Thomas. Evolution of nitrogen functionalities in carbonaceous materials during pyrolysis. *Carbon* **33** (1995) 1641-1653.
- ²⁸ A. P. Terzyk. The influence of activated carbon surface chemical composition on the adsorption of acetaminophen (paracetamol) in vitro. Part II. TG, FTIR, and XPS analysis of carbons and the temperature dependence of adsorption kinetics at the neutral pH. *Colloids Surf. A* **177** (2001) 23-45.
- ²⁹ C. Moreno-Castilla et al. Activated carbon surface modifications by nitric acid, hydrogen peroxide, and ammonium peroxydisulfate treatments. *Langmuir* **11** (1995) 4386-4392.



Chapter 7 Surface studies of functionalised multi-wall carbon nanotubes

Abstract

In this work, controlled and specific functionalisation of the MWCNTs surfaces have been carried out in order to optimize both physical and chemical interactions with matrix materials used in composite manufacture process. The aim was to introduce and control the level of active functional groups on the outer graphene sheet of the MWCNTs while keeping their structure intact and therefore their mechanical properties. The resulting material surfaces have been characterised using SEM and high resolution TEM. XPS has been used to identify the chemistry of these surfaces and types of functional group present on these MWCNTs. Additionally, the reactivity of the active groups was probed by water vapour adsorption. The main objective is to get a better understanding of the relationship between surface chemistry, bonding (and stress transfer (future work)). This approach has led to a greater understanding of the specific interfacial interactions which contribute to, for example, adsorption and adhesion. This would also be beneficial for the development of a predictive model and/or improvement of the modelling approach to identify optimal bonding conditions (or tailor special bonding conditions).

7.1 Introduction

Since the discovery of the spherical fullerene structures C₆₀ and C₇₀ by Kroto et al. [1] in the 80s, work and research in the field of nanocarbons (SWCNT and MWCNT) has not stop to gain importance. However, it is now accepted that microfibrinous carbons were found well before that [2][3] whereas concerted research projects on carbon nanotubes (CNTs) began in the seventies. The intrinsic properties relatives to the structure of fullerene or CNT were on the centre of the initial studies. But it quickly becomes apparent that producing these materials with good structure uniformity, in a controllable way and with the required mechanical properties was an important challenge ahead. Another drawback regarding the commercial exploitation was the limitation in term of quantities required for most practical applications. Nowadays, CNTs are just beginning to be used in a limited range of commercial products but their main application remain in scientific research and also in replacement of electric grade carbon black. The major challenge in terms of mechanical properties is to try to exploit their low weight, high modulus and tensile strength in the next generation of composite structures for aerospace and related, high performance engineering applications.

Regarding their fabrication, CVD method [4] is one of the current methods which allows to produce substantial quantity of high quality and uniformity multiwall carbon nanotubes (MWCNTs). Typical dimensions of these materials are: length between 1 and 10 mm and diameters in the range of 5 to 100 nm associated with strength 100 times higher than conventional stainless steel with only 15~20% of the weight. MWCNTs are significantly larger than true nanotubes (the smallest of which have near molecular dimensions) but they are sufficiently small enough to become intimately mixed with polymer chain and matrix resin entanglements such that the types of structures and phases likely to be encountered in these new composites may be significantly different to those found in more conventional macro-fibre composites. Also, MWCNTs display significantly better measured modulus and tensile properties than carbon fibres currently

used in aerospace components [5]. This alone promises to yield exciting and new science but, ultimately, one of the major challenges would be to translate directly these fantastic properties into new generation composites or maybe use MWCNTs as filling agent.

However, MWCNTs are hydrophobic in character due to the presence of graphene surface and have a relatively low surface free energy. These can explain the poor dispersibility in polar solvents such as water and methanol and the low wettability and reactivity with matrix compounds. It will therefore be necessary to manipulate the specific properties of the MWCNT surfaces at the atomic and molecular level, in order to integrate their specific properties into the macrostructure. So a direct functionalisation (or oxidation) of the nanotube surfaces is possible to overcome these inherent problems. But it has also been shown that debris present on the surface could lead to a weak boundary layer at the interface between nanotubes and the matrix. Hence, in order to ensure a good transfer of the superior mechanical properties of the MWCNTs to the matrix compounds, a sufficient bonding should be achieved during the surface modification process. Interfacial control at this level, particularly the concept of making the modifier surface-specific to the matrix chemistry is unique and yet is essential if a holistic and predictive approach to high performance composite design is to be achieved.

7.2 Experimental: materials and methods

7.2.1 Materials used in this study

The MWCNTs used in the experiments were supplied by CAER UKY (Center for Applied Energy Research at the University of Kentucky) [6] and had the following dimensions: mean length 20 μm (max. length 70 μm) and 30 nm diameter with a corresponding mean aspect ratio $L_{mean}/\phi = 667$ approx. These nanotubes, available commercially, are a realistic material to study surface properties and behaviour in composite system and their future development.

Table 7.1: Mechanical properties of SWCNT and MWCNT compared to carbon fibres and stainless steel [7][8][9][10][11].

Materials	Young's Modulus (GPa)	Tensile strength (GPa)	Strain to failure (%)
SWCNT	920 – 1000	13 – 53	15 – 23
MWCNT	270 – 800	11 – 150	5 – 12
High strength carbon fibre	220 – 580	4.3 – 6.4	1 – 2
High modulus carbon fibre	520 – 827	1.9 – 3.3	0.3 – 0.6
Stainless steel	186 – 214	0.4 – 1.6	15 – 50

Table 7.1 shows the mechanical properties of the MWCNTs used in this study and also the characteristics of two types of PAN (Polyacrylonitrile) base carbon fibres: high strength and high modulus which are currently used in conventional fibre composites. The TEM photograph displayed in Figure 7.1 a) shows the uniform structure of the MWCNT obtained via CVD growth whereas the micrograph in Figure 7.1 b) shows clearly the multi-wall structure of a single tube. This HRTEM characterisation is an important step before carrying out the surface functionalisation as it allows us to determine the levels of perfection of the multi-wall graphene layers.

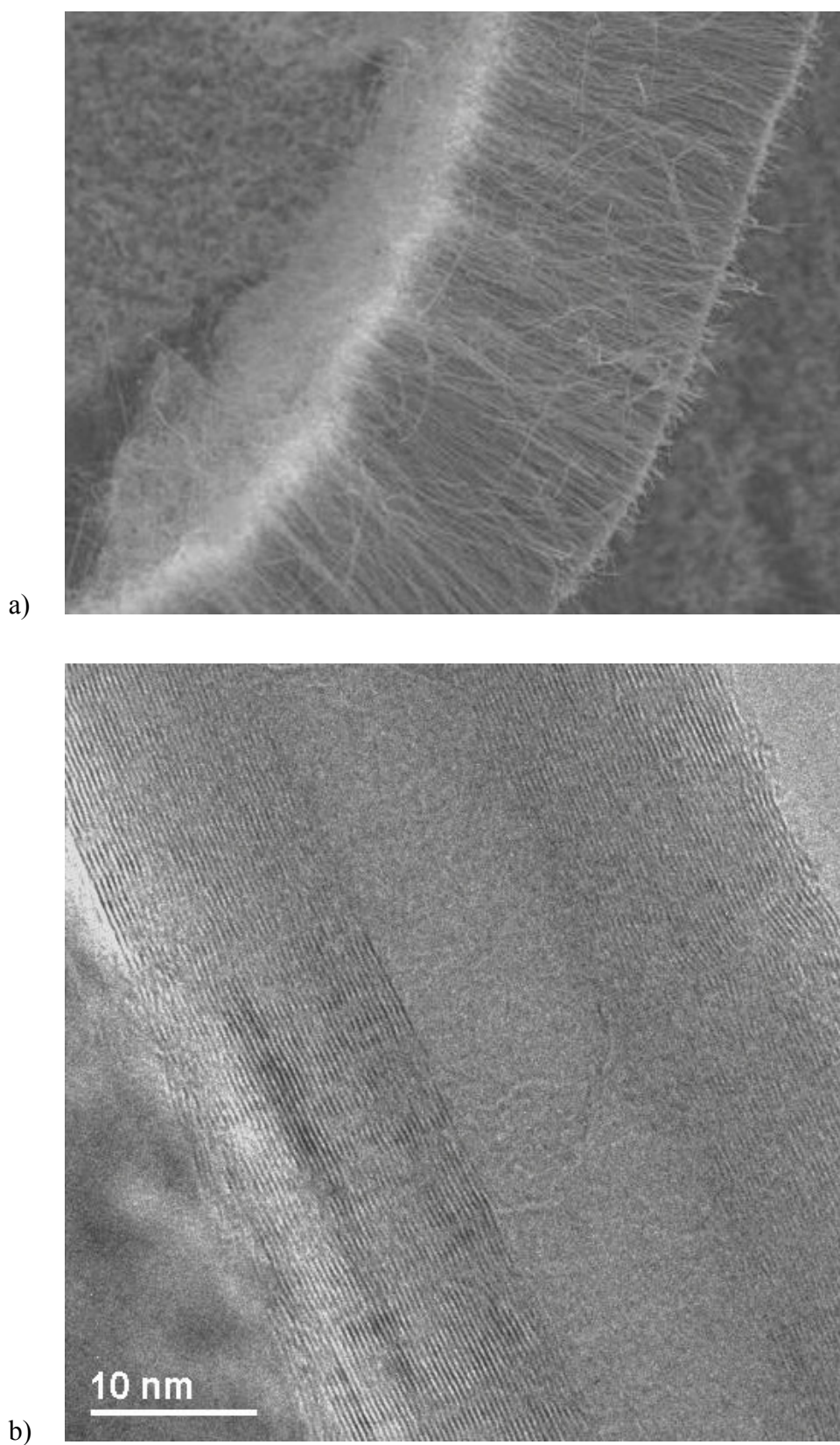


Figure 7.1: a) CVD deposited MWCNTs and b) example of HRTEM image showing multi-wall structure of one of the MWCNT studied in this work.

7.2.2 Surface Functionalisation

Different physical and chemical routes could be used to create specific functionalities required on the MWCNT surface to optimise the interaction with particular resin or polymer. Ether and ester groups can be formed by derivatising the oxygen functional groups introduced by the ozone treatment. Some of the initial XPS results show considerably high surface oxygen levels proving the potential of these routes. It should be taken into account that some of the oxygen could arise from the oxidation of the debris as mentioned in the introduction [12]. Therefore, the surface cleaning of the MWCNTs and its effect on the functionalisation of the graphene structure should be taken into consideration.

The Fenton oxidation ($\text{FeSO}_4/\text{H}_2\text{O}_2$) and the Birch reduction have been used in this work. Experimental details about these oxidation treatments carried out in the CAER UKY labs are given below. The first method allows the introduction of chemisorbed hydroxyl groups at the edges or defect sites encountered for example in discontinuities, dislocations and steps in nanotube shells whereas the second one can generate specific functional groups such as acids, esters or amines on the MWCNT surface from the alkylation of the nanotube anions. Both of these chemospecific methods are represented on Figure 7.2. The Fenton treatment procedure is as-follow: 6 g of as-produced MWCNTs were mixed with 680 cm³ of toluene for 45 min using an ultrasonic horn resulting in a 1 wt% suspension. The resulting suspension was filtered and washed with toluene then pentane, and dried under vacuum at 80°C. 3 g of these “*Horn sonicated*” MWCNTs were placed in 900 cm³ of deionised water and dispersed in an ultrasonic bath for 30 min. 1.5 g ferrous sulphate-7 hydrate and 300 cm³ of 30% H_2O_2 were then added to the solution. After stirring for 24 h, the suspension was washed with deionised water then ethanol, and dried under vacuum at 80°C.

The shatter milled Fenton nanotubes consist of as-produced nanotubes which have been mechanically grinded for 10min prior the Fenton reaction, breaking them from

~70um down to ~3um. This process produces a material with significantly more “edges” which can be considered as active sites for the hydroxylation reaction.

A brief description of the Birch reduction/alkylation procedure is included as follows: as-produced nanotubes are introduced into a liquid solution of NH_3 /Lithium metal in order to transfer many electrons inside the nanotubes then an excess of alkyl halide is added to the mixture in order to create the ester groups on the carbon surface.

XPS has been used to characterise and quantify these functionalities added on the surface to facilitate the bonding between the MWCNTs and the matrix compounds. This surface study is necessary to obtain a better control over the interfacial characteristics of the composite test materials such as bonding, stress transfer and mechanical properties.

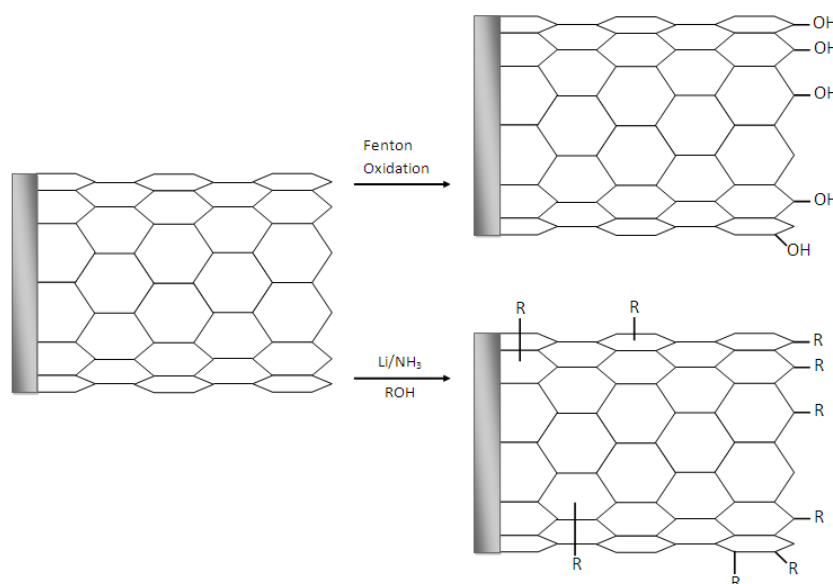


Figure 7.2: Examples of chemo-specific pathways to hydroxylated and esterified MWCNT surfaces.

Other methods such as ozone oxidation and plasma etching/oxidation have not been used in this specific work but could be used in the future. Ozone oxidation using an ozone generator or by UV/Ozone exposure, as described earlier for the oxidation of carbon black materials, is considered as a highly controllable method to oxidise carbon and other material surfaces. This method, developed by Mathieson and Bradley [¹³][¹⁴]

has been used in the past to generate hydroxylic and carboxylic groups on a number of surfaces [¹⁵][¹⁶][¹⁷]. This treatment has the advantage to produce uncontaminated surfaces when it is applied to standard carbon materials while achieving a generic control of the chemistry of surface. Thus, using this method, the resulting MWCNTs are expected to contain only carbon and oxygen elements leading to high wettability and reactivity toward the matrix compounds. On the other hand, plasma etching and plasma oxidation of the MWCNT could be used to create new sites on the graphene basal planes (which are not usually chemically reactive toward molecular species) which will serve to vary the physical distribution of reactive sites (away from existing edge sites).

In order to produce specially tailored surfaces for optimal interaction with a particular matrix formulation, any combination of the previously described methods could be investigated to check the influence of chemical functionalisation of the pre-oxidised or plasma-treated carbon surfaces.

7.2.3 Surface and structural characterisation

MWCNTs have been studied using a Kratos Axis HSi 5-channel monochromated X-ray photoelectron spectrometer (XPS). Surface elemental compositional data (in at.%), C/O ratios and chemical shift information have been obtained from the carbon 1s and oxygen 1s peaks of the survey spectra. Moreover high resolution scans have been used to identify surface functional groups. Detailed studies of MWCNTs containing XPS spectra and chemical shift data are quite rare in the literature so these data could be used to establish a database of XPS spectra for interpretation of surface chemical modification and functionalisation.

HRTEM has been used to study the effects of the different surface functionalisation reactions proposed here on the resulting structures of the MWCNTs. These observations were carried out by Prof W. Zhou from the Electron Microscopy Group at University of St Andrews using the Jeol JEM 2011 HRTEM. The samples are prepared in suspension

with acetone and are then treated in an ultrasonic bath for few minutes. Surface defects are considered as interesting artefacts to observe. The shape of pit defect can either be round or linear and can be determined by rotation around the CNT axis in both direction and also using the tilting angle to estimate its length.

Immersion calorimetry has been carried out in a Setaram/Calvet C80 instrument to check the influence of MWCNTs surface functionalisation on the thermodynamic properties. Different liquids could be used to allow interpretation of the fundamental polar and dispersion interactions with the surfaces and an extension to specific liquids simulating key composite matrix materials and/or new candidate materials is conceivable.

This approach was previously used and developed for carbon black reinforced elastomer [16] and also for the study of fundamental adsorption interactions at carbon surfaces [18][19]. This should allow in future studies to investigate the specific interactions of the modified MWCNT surfaces involving different types of resin cross-linking groups as you can see in Figure 7.3. A better control of the interfacial linking process and also identification of optimal surfaces for specific matrix formulations should be achievable.

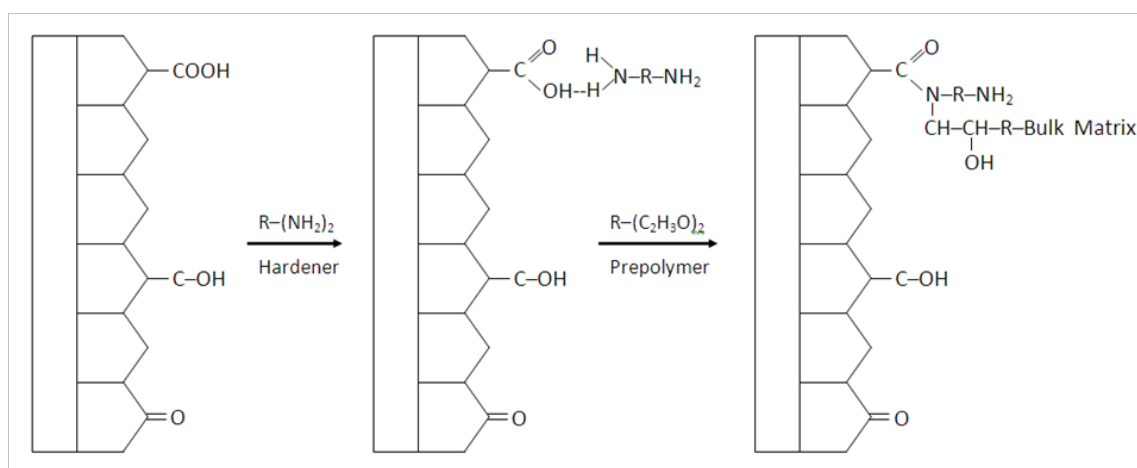


Figure 7.3: Possible cross-linking reaction of resin epoxide ring with carbon fibre surface carboxylic acid according to Fitzer et al. [20].

Water adsorption isotherms were determined at 303°K using a Hiden Analytical IGA instrument. BET and Dubinin methods (and suitable water isotherm equation such as Barton and D'Arcy & Watt) were used to analyse the adsorption data. Moreover the energy parameters (for example: C_{BET} constant or DR E_0 (kJ/mol)) from these equations will help us to characterise the chemical reactivity of the surfaces.

7.3 Results and discussion

7.3.1 Structural Effects

Figure 7.4 shows the SEM micrographs of untreated MWCNT samples. On the whole view, agglomerates of carbon nanotubes can be observed. Their size is quite homogeneous (from 50 to 400 μm) and they look like flat flakes with sharp edges. Another important characteristic can be seen on Figure 7.4 b) with the presence of two completely different morphologies. The left part represents a roughly flat surface composed of nanotubes whereas on the right, the surface looks like a hive and is composed of big holes (2~3 μm of diameter) created by the entanglement of the nanotubes.

At very high magnification (x50k, Figure 7.4 d)), the individual nanotubes are clearly visible but it not possible to tell about the structure of the nanotubes (single walled, multi walled, etc...). The nanotubes are entangled the ones with the others and their diameter measure approximately 50 nm.

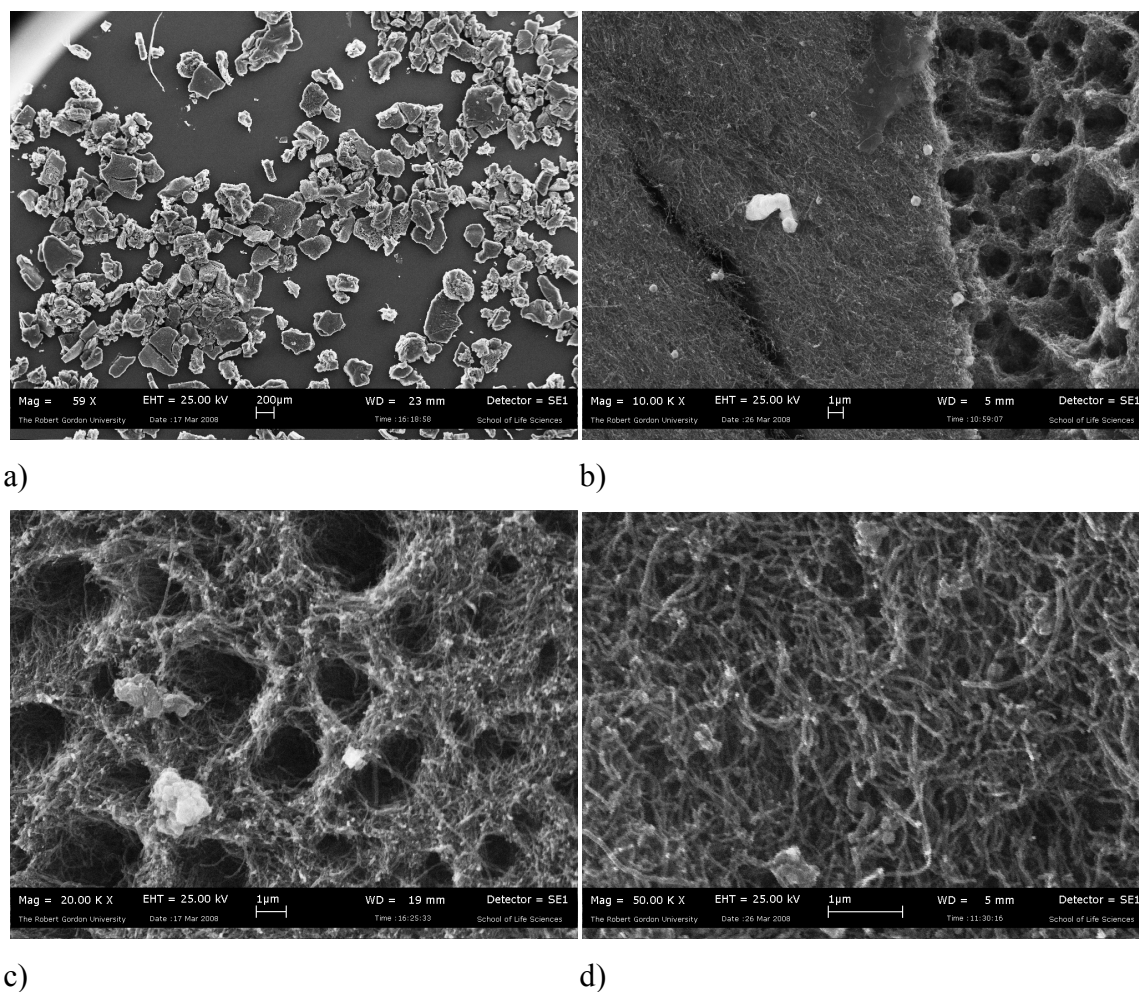


Figure 7.4: SEM micrographs of base MWCNT samples: a) x59, b) x10k, c) x20k and d) x50k.

The TEM images of the base MWCNTs are given in Figure 7.1 b) and Figure 7.5 a), b) and c). A typical heap of MWCNTs containing in the specimen is represented at very low magnification in the Figure 7.5 a). Whereas the Figure 7.1 b) and Figure 7.5 c) show clearly the multiple graphene layer structures of the tubes, typical of this kind of materials. In this study, the base material used is characterised by a multiwall structure of approximately 20 to 30 concentric graphene tubes. The internal tube diameter varies along the length of the CNT between 5 and 20 nm. The average inter-graphene layer spacing d for these nanotubes is in the range of 0.35~0.38 nm. The outer surfaces appear to be relatively clean without adsorbed physical contamination, as confirmed by XPS data.

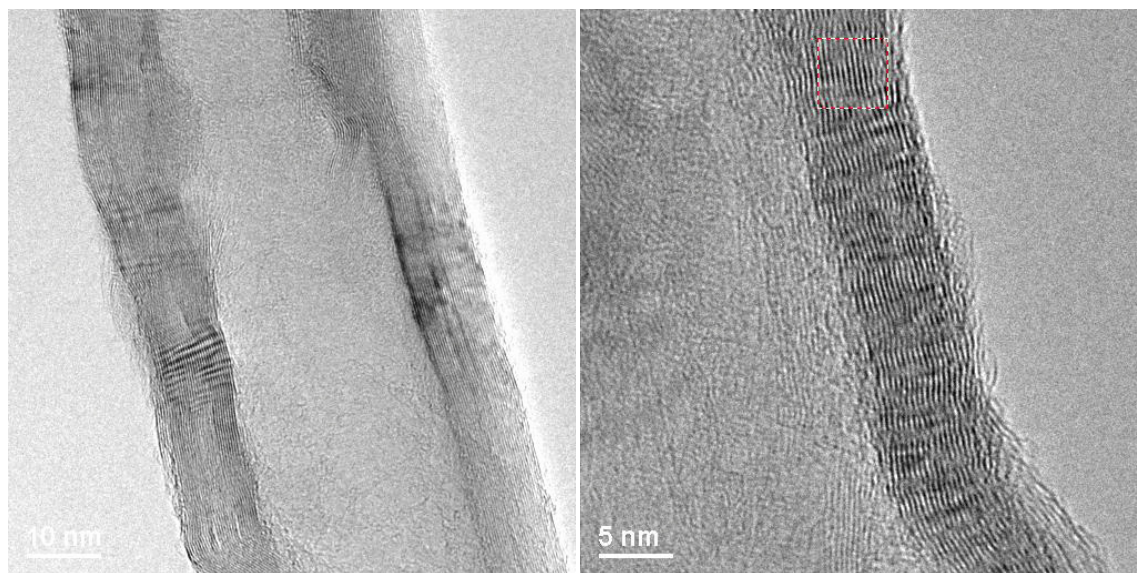
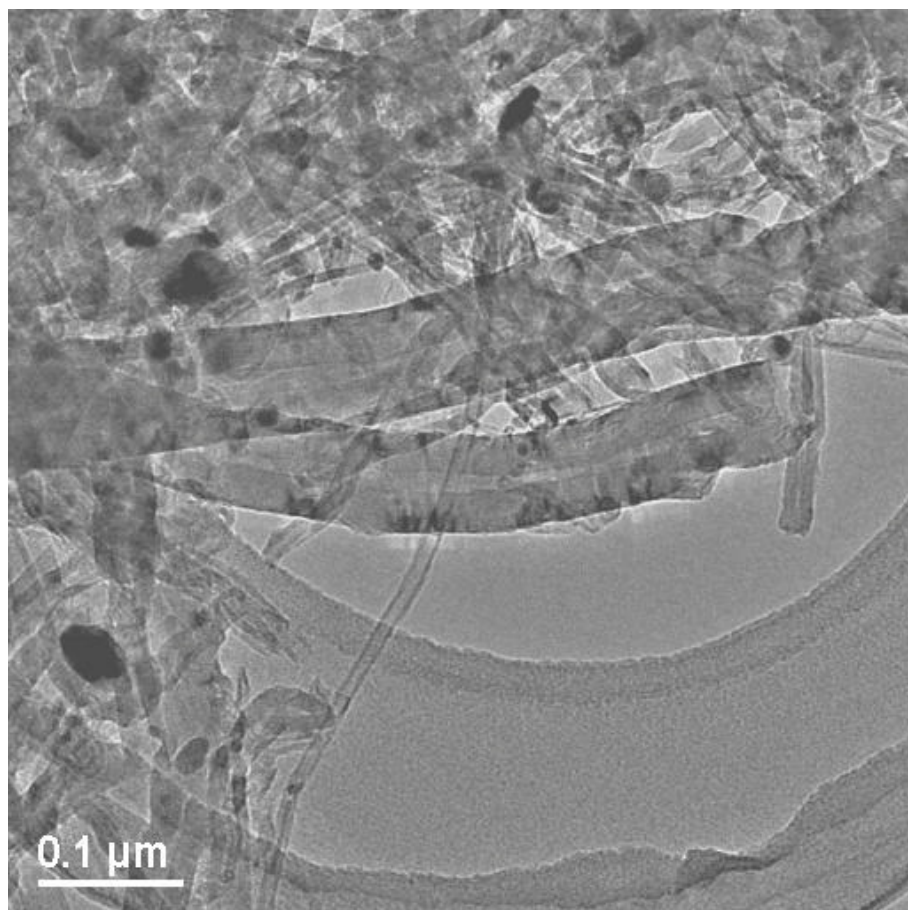


Figure 7.5: HRTEM images of the base MWCNT. a) Global view, b) and c) higher magnification images.

Figure 7.6 a) and b) represent the TEM micrographs of the Fenton oxidised materials. The treatment does not seem to disrupt significantly the internal multiwall structure of the tubes as the graphene layers are still clearly evident in the image at high magnification. In this material, the number of concentric graphene tube has been counted to be around 30 which is in the same order than for the untreated CNTs. But regarding the possible damage near the external surface, it is more difficult to comment. For example, inspection of Figure 7.6 b) suggests the presence of some smaller “*crystallites*” which may result from the disruption of the surface layers by oxidative cleavage of C–C bonds during the hydroxylation process but confirmation of this is difficult. Another aspect is that the inside wall of this particular tube seems less linear than the untreated tubes as seen before. It is again difficult to conclude if this is the result of the oxidation treatment which could have penetrated inside the tube via an open end or fracture. As discussed before, the CNTs usually possess debris and contamination particles on their surfaces. These were observed by other workers [21] on several materials resulting as a surface “*halo*” in the HRTEM images. But we could not find any clear evidence of this contamination in this study. The debris should be removed before any functionalisation treatment as they affect significantly the properties at the resulting interface with for example poor adhesion and stress transfer due to their weak bonding with the graphene layers.

In order to get a better understanding on the structure of MWCNT and the influence of chemical treatment, HRTEM images of graphitized MWCNTs, both untreated material (see Figure 7.7) and materials submitted to Fenton oxidation (Figure 7.8) and HNO₃ treatment (Figure 7.9) are also included.

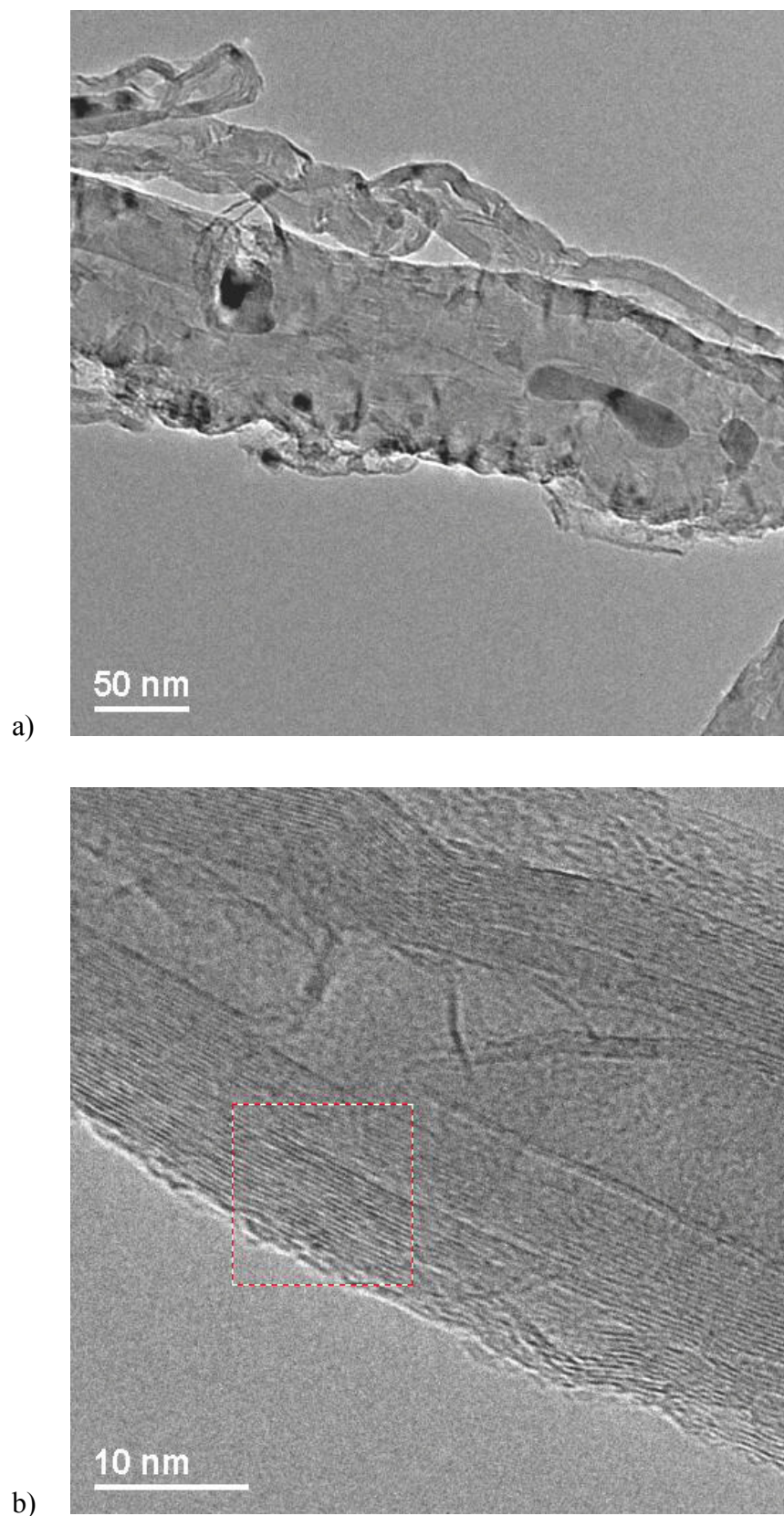
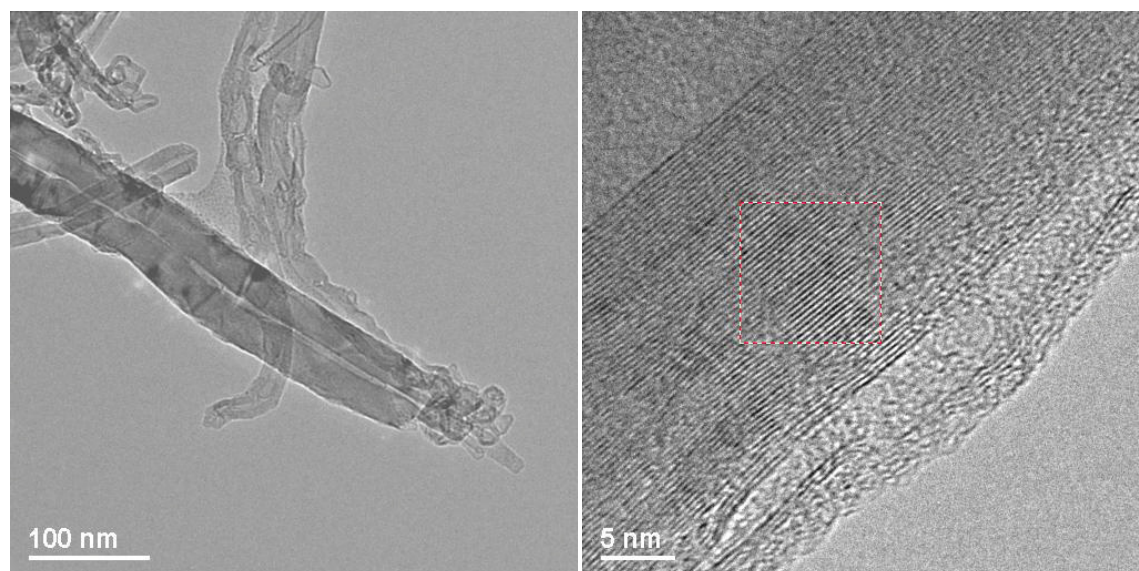
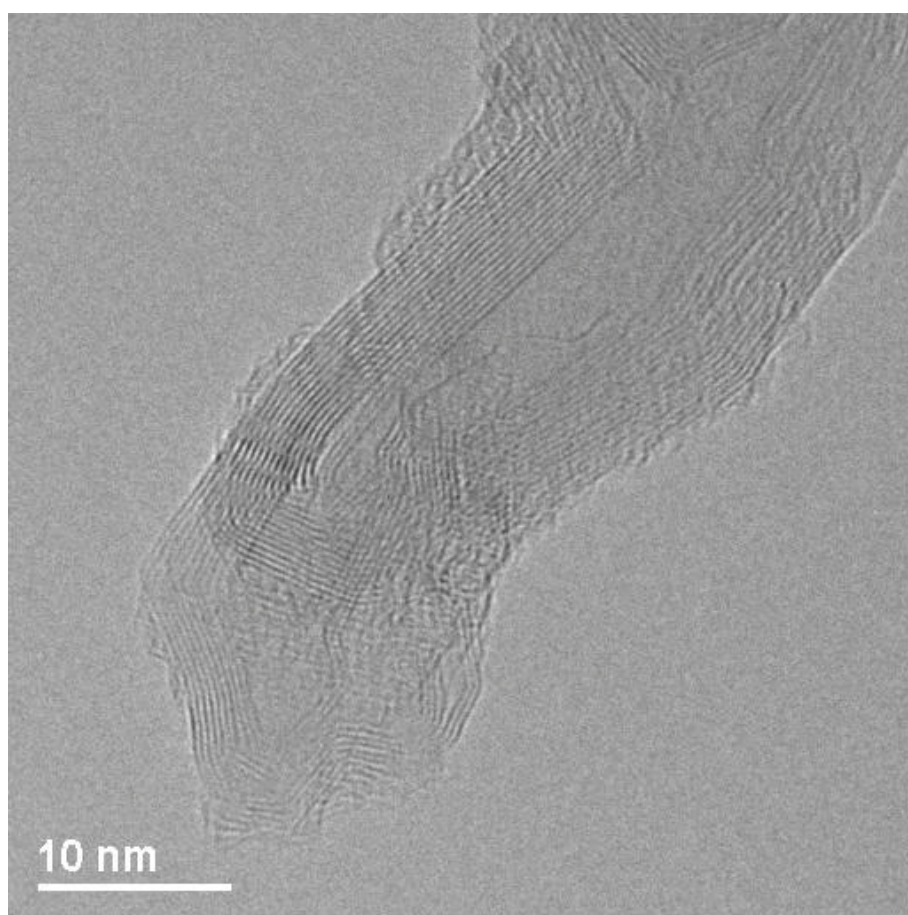


Figure 7.6: HRTEM images of the Fenton sonicated MWCNT: a) global view and b) higher magnification image.



a)

b)



c)

Figure 7.7: HRTEM images of the highly graphitized base MWCNT. a) Global view, b) higher magnification image showing the highly graphitic multilayer structure and c) interesting view of the termination of one MWCNT.

The Figure 7.7 a) shows a global view of the highly graphitized base MWCNT. One can observe on the diagonal one large tube having a very good linearity and an external diameter of 60~70 nm. The Figure 7.7 b) represents the multiwall structure of a graphitized tube which is composed from at least 70 (from a visual observation) concentric graphene tube with a perfect linearity. This can be explained by the rearrangement undergone by the carbon atoms during the graphitization process carried out at very high temperature ($> 3000^{\circ}\text{K}$) to form a more regular and graphitic structure. This is very similar to the graphitization process for carbon black material as seen with the carbon black N234G. Another interesting feature represented in Figure 7.7 c) is the photograph of the termination of one tube. This end seems to be closed by some sort of fullerene cap (C_{60} type). This is expected from the literature and already been observed by other researchers [22].

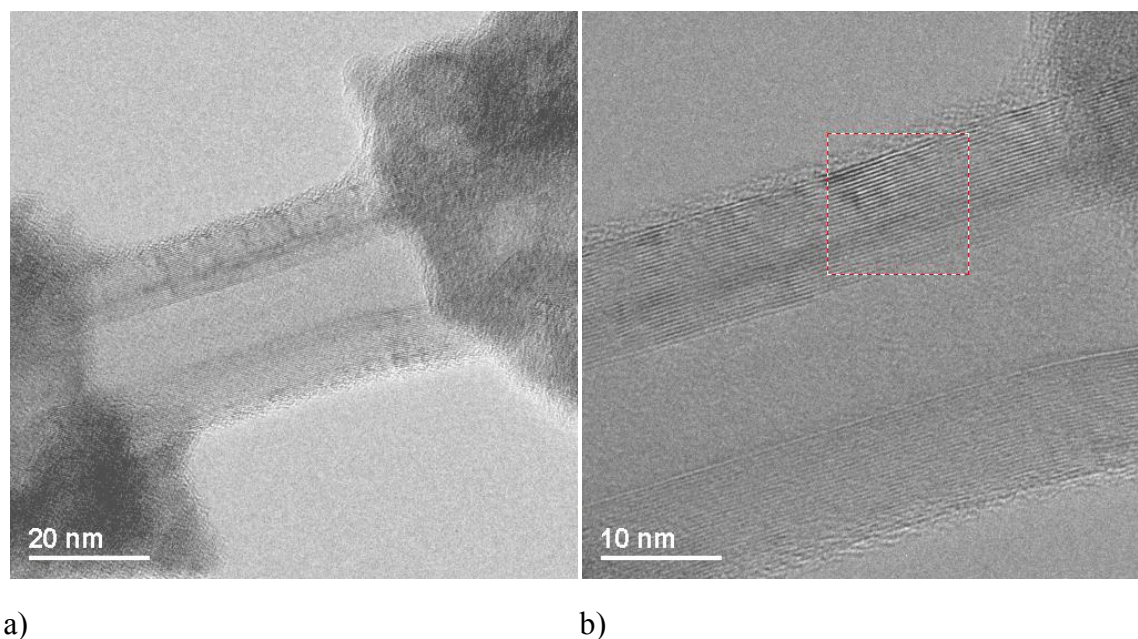


Figure 7.8: HRTEM images of the graphitized Fenton MWCNT (a) and (b) corresponding to lower and higher magnification images respectively.

Regarding the Fenton treatment on the graphitized nanotubes, it appears, from the HRTEM photographs, that the effect on the external structure seems minimal. The multiwall structure is clearly visible on Figure 7.8 b) and has a very nice linearity. This

might be expected as it was shown before that ozone treatment or liquid-phase oxidation on highly ordered pyrolytic graphite (HOPG) have minimal impact on the surface aspect. The Figure 7.9 shows the HRTEM images of the graphitized HNO₃ treated MWCNTs. Similarly, the liquid-phase oxidation does not appear to have damaged the external surface of the nanotubes (Figure 7.9 b)) but sharp changes in directions of the graphene layer can be observed inside the multiwall structure. The origin of this defect is unclear as it can be attributed to the HNO₃ treatment or it might originate from the intrinsic structure of the nanotube.

The nitrogen adsorption isotherms were measured at 77°K and lead to BET surface areas of 59.2 m²/g for the unsonicated base material, 60.4 m²/g for the sonicated sample and 71.8 m²/g for the Fenton treated and sonicated materials. The most plausible reason for this increase in surface area could be that during the functionalisation step, the MWCNTs start to separate from each other. Structural disruptions which open up the space inside the tube are less likely to occur. A decrease in the total porosity from 0.24 cm³/g to 0.18 cm³/g was also observed after treatment. This occurs mostly in the macroporous region and can be explained by a greater separation of the tubes after the functionalisation leading to a reduced capillarity between the tubes and new graphene surface available.

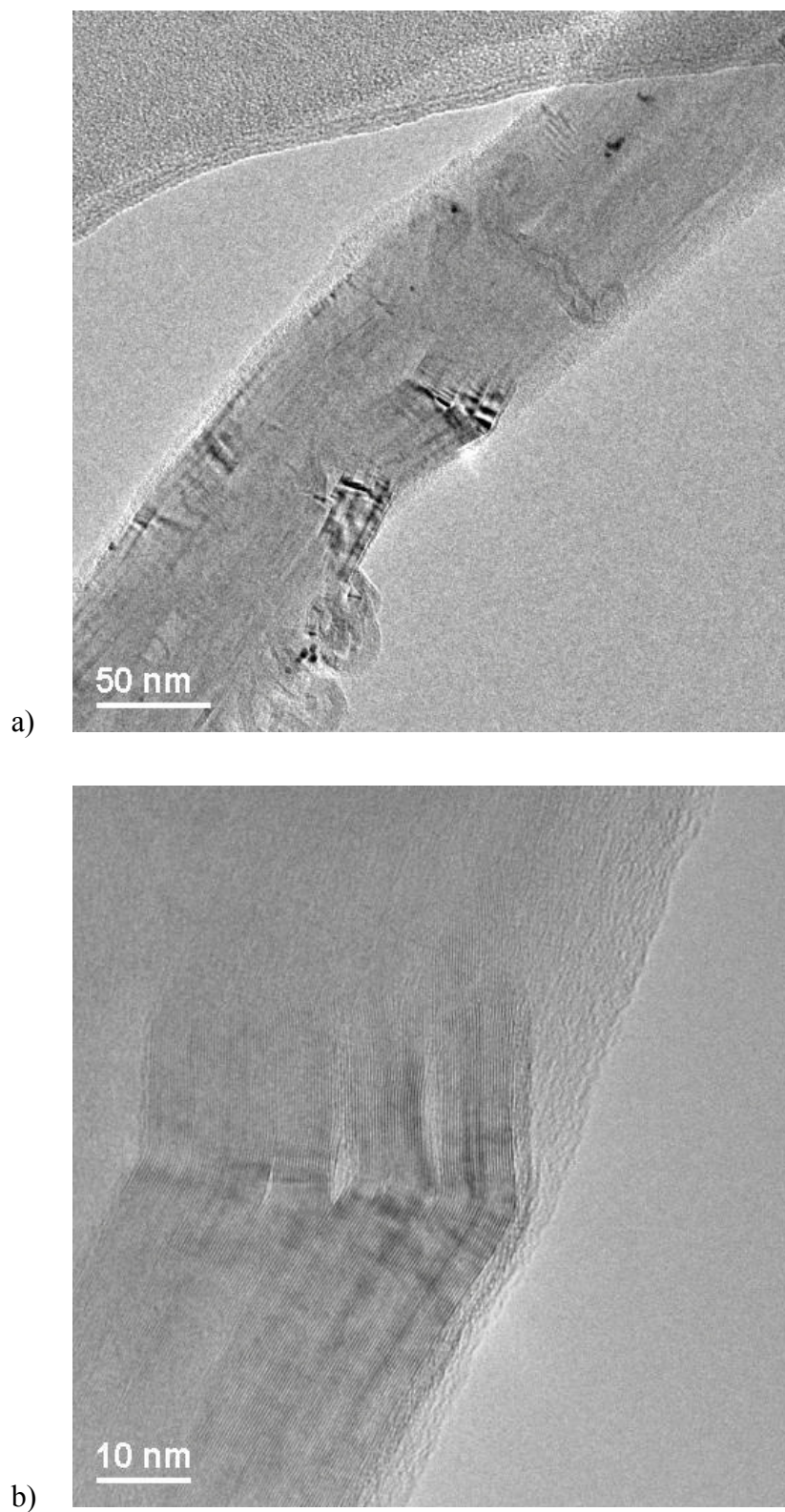


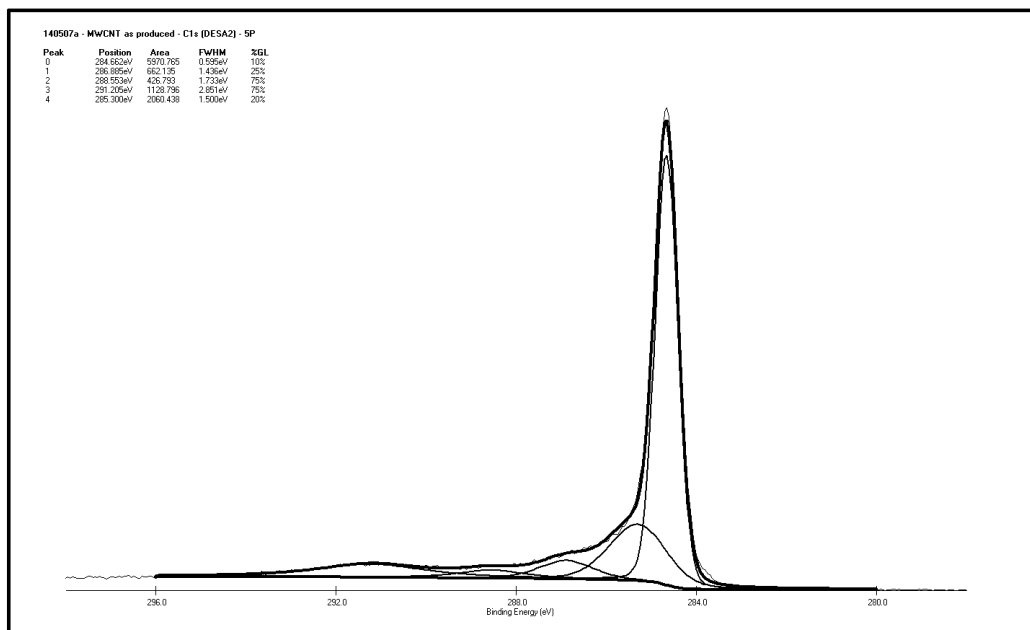
Figure 7.9: HRTEM images of the graphitized HNO₃ treated MWCNT. a) Global view of one tube and b) higher magnification image showing the change of direction of the graphene layers.

7.3.2 Surface Compositions and Chemistry

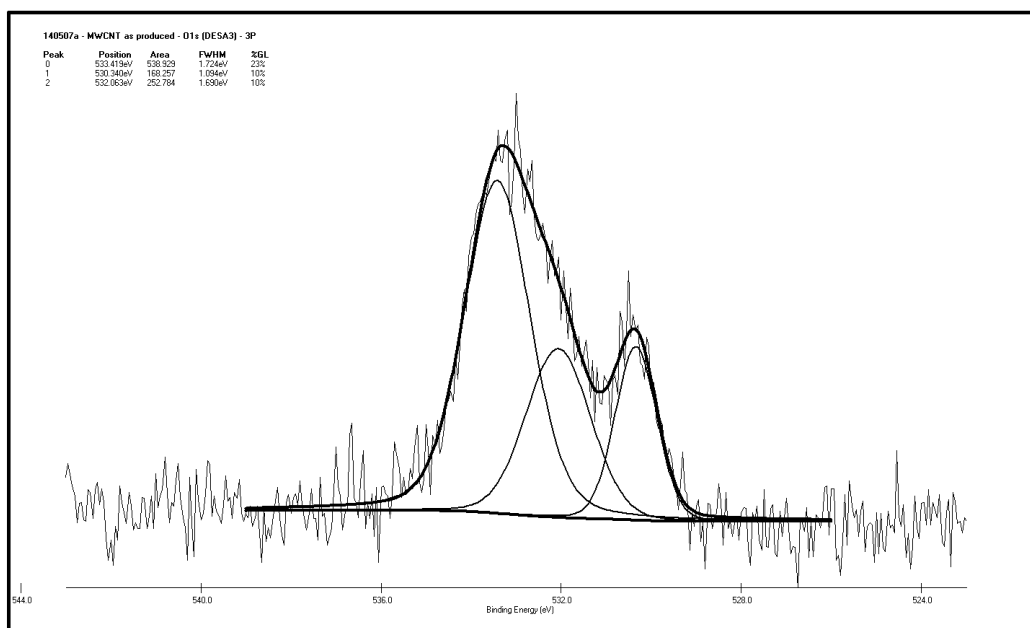
Typical carbon 1s and oxygen 1s peaks from the untreated MWCNTs are given in Figure 7.10 a) and b) respectively. The intrinsic oxygen level for the as-produced nanotubes was evaluated at 4.3 at.%. The global carbon 1s peak can be decomposed using 5 individual envelopes [23]. The main peak is assigned to C–C bonds within the graphene layers composing the multiwall structure of the nanotubes. This main peak is characterised by a binding energy of 284.6 eV and a FWHM value of 0.595 eV which is quite close to graphite, graphitized carbon black and even carbon fibres ($\approx 0.8\sim 0.9$ eV). This significantly low FWHM value indicates a high degree of structural homogeneity. Moreover, the CH_n species present on the surface of the tubes may also have a small contribution on this peak. The second component corresponds to hydroxyl or phenol groups (–OH) or (C–O–C) whereas the third component is associated to carbonyl (C=O) groups on the external surface of the tubes. These two peaks are shifted of 0.7 and 2.2 eV respectively from the main peak. The fourth component corresponds to carboxyl and ester groups (COOH) and (COO–R) and its peak arises at 288.6 eV (shift of 4.0 eV). The last component present in the carbon 1s envelope is attributed to $\pi\text{--}\pi^*$ shake up structure created by the interaction between the π electron of the graphene structure and the photoelectrons emitted during the acquisition. This peak arises at a binding energy of 291.2 eV (a shift of 6.6 eV from the main carbon peak) and is characterised by a FWHM value of 2.851 eV.

Table 7.2: Surface composition data (in at.%) from XPS.

MWCNT materials	Carbon (at.%)	Oxygen (at.%)	Iron (at.%)
MWCNT as produced	95.70	4.30	(≈ 0.22)
MWCNT sonicated Fenton	74.91	22.33	2.77
MWCNT shatter milled Fenton	73.87	23.46	2.67
MWCNT Birch reduced	95.18	4.82	(≈ 0.00)



a)

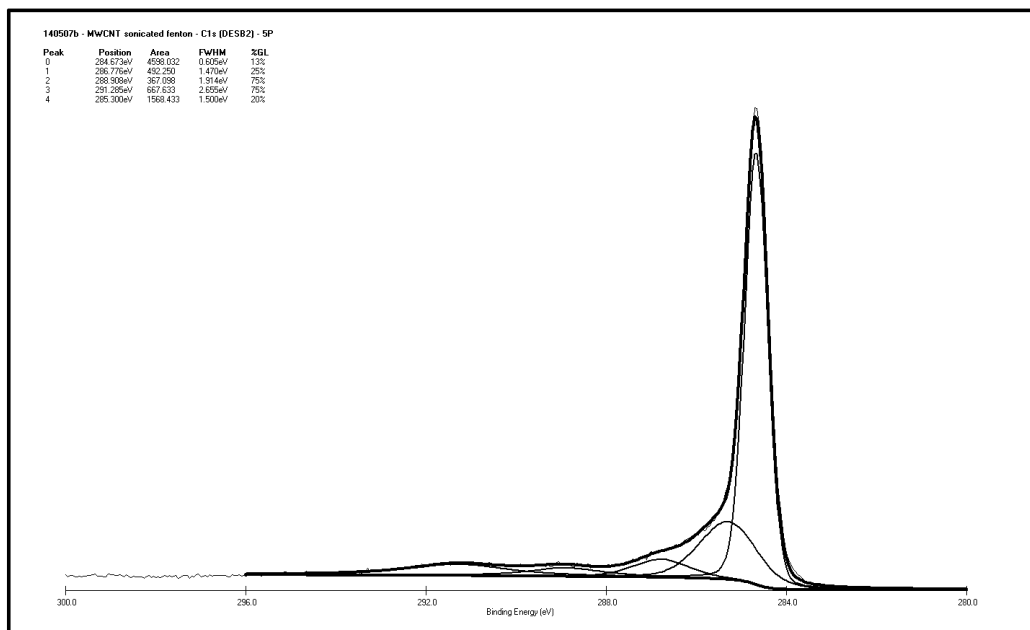


b)

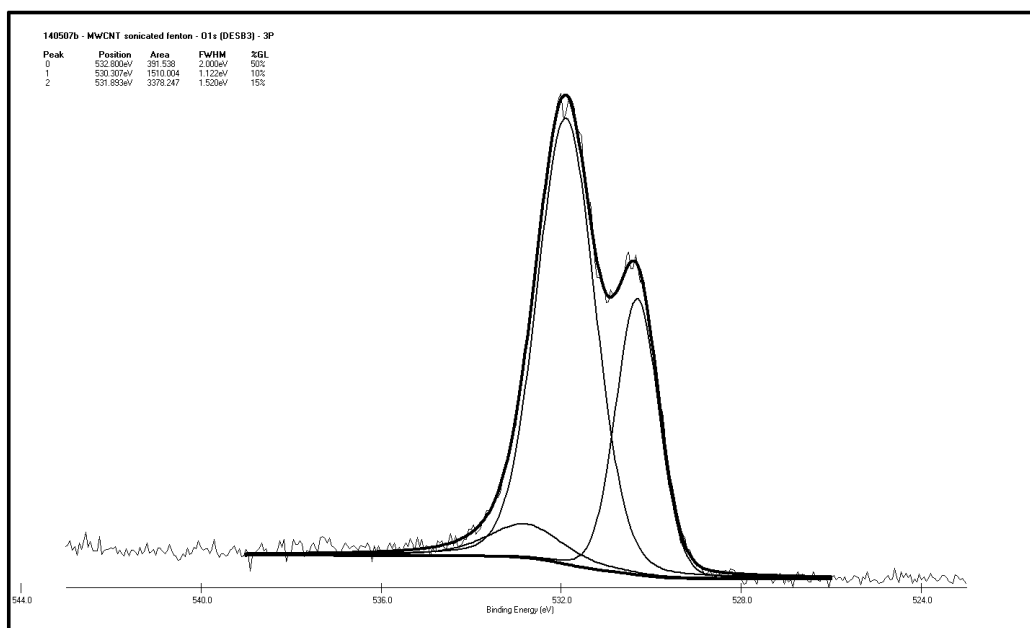
Figure 7.10: a) C1s and b) O1s peak envelopes from untreated MWCNTs.

Regarding the oxygen 1s spectrum, it can be decomposed with three envelopes. The presence of hydroxyl/ether and carbonyl groups is observed on the oxygen 1s spectrum with respective peaks at 532.63 eV and peak at 530.34 eV (Figure 7.10 b)). The third component represents the oxygen in anhydride, lactone, carboxylic acids and possibly chemisorbed oxygen and water at slightly higher binding energy. This peak arises at 533.4 eV and has the biggest area for the base material. In the case of the Birch reduced MWCNT, this peak decreases in terms of area (Figure 7.12 b)) whereas for the sonicated treated MWCNTs, it is almost inexistent.

As can be seen from Table 7.2, the Fenton reaction increases significantly the measured oxygen levels from 4 to 22~24 at.%. In addition, 2.6~2.8 at.% iron was detected from the Fe2p peak in the survey spectra and can be attributed to residual growth catalyst or more likely to residual iron(III) or iron(II) from the Fenton reaction used during the oxidation treatment. C1s and O1s narrow scan spectra from the sonicated Fenton MWCNTs are represented in Figure 7.11 a) and b) respectively. The main peak of the C1s envelope arises at a binding energy of 284.67 eV (same value than for the untreated material). The functionalisation treatment does not have any significant effect on the FWHM value (0.605 eV for sonicated Fenton and Birch reduced, 0.620eV for the shatter milled Fenton compared to 0.595 eV obtained for the base material). The three additional peaks, attributed to hydroxyl/phenol, carbonyl and carboxyl/esters groups, are still present at similar positions than those of the untreated MWCNTs with respective shifting values of 0.6 eV, 2.1 eV and 4.2 eV. Figure 7.11 b) shows the corresponding O1s envelope composed with the hydroxyl peak at 531.9 eV and the carbonyl 530.3 eV. The area ratio indicates that 79% of the surface oxygen are hydroxyl groups. Another interesting point is that after the Fenton treatment, the FWHM value of the hydroxyl peak decreased slightly from 1.690 to 1.520 eV and as said before the peak area corresponding to chemisorbed oxygen/water has been greatly reduced.

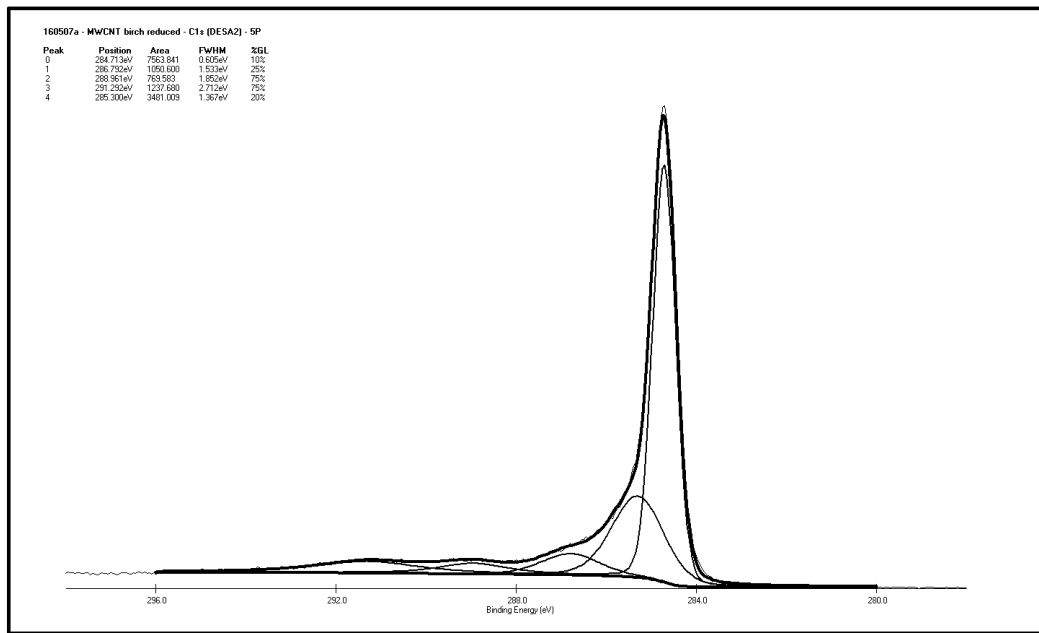


a)

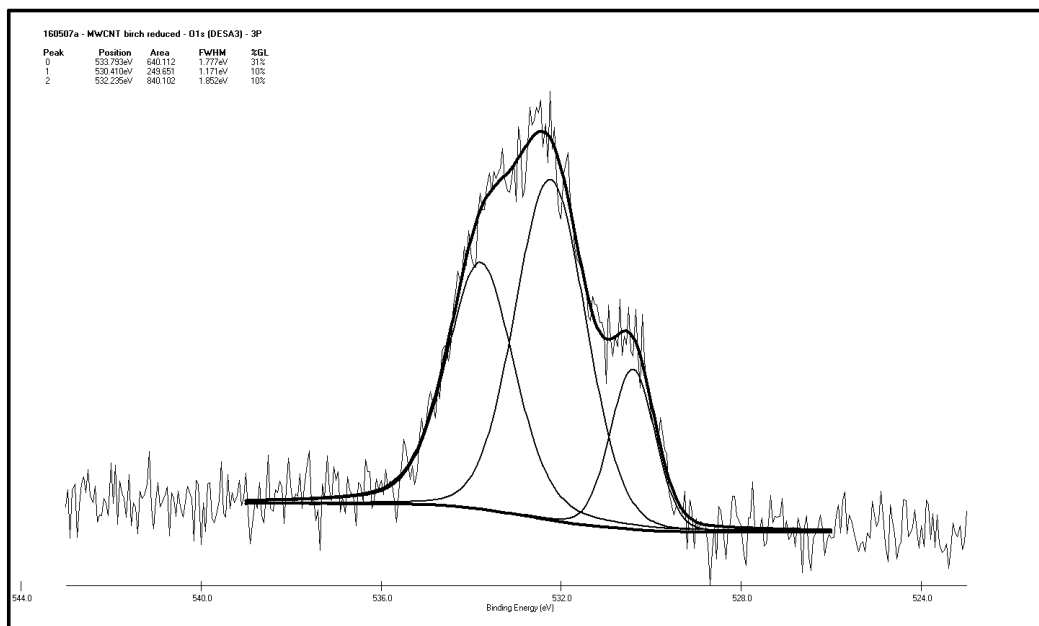


b)

Figure 7.11: a) C1s and b) O1s peak envelopes from MWCNTs treated using the Fenton reaction.



a)

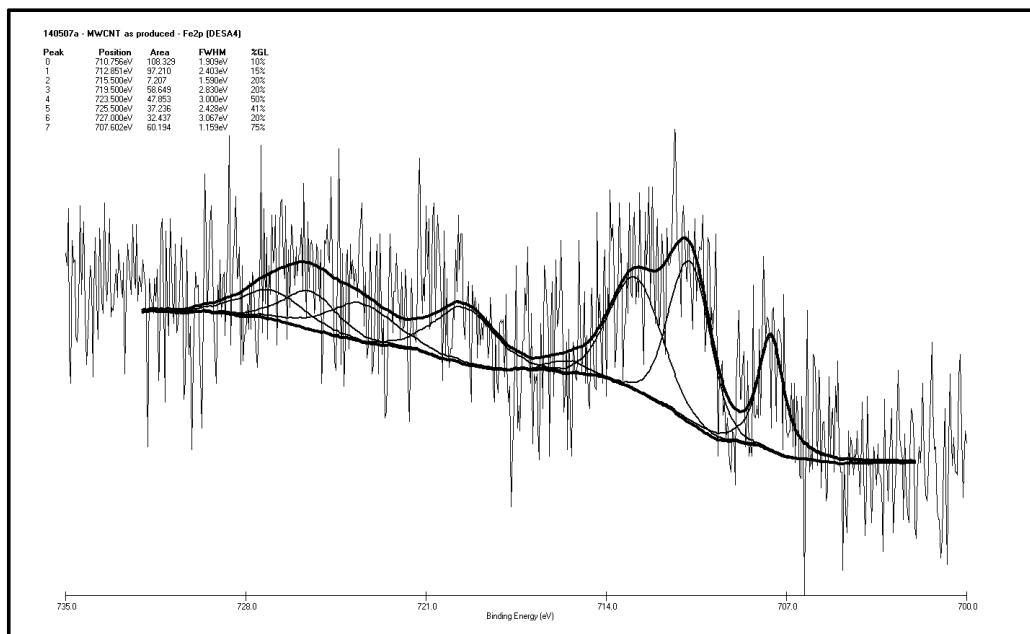


b)

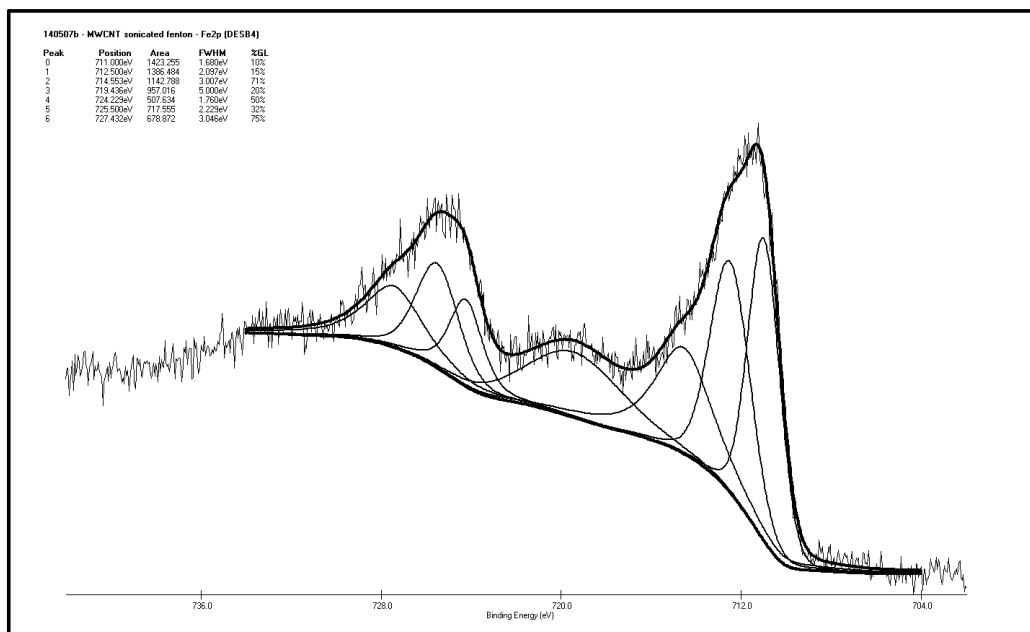
Figure 7.12: a) C1s and b) O1s peak envelopes from Birch reduced MWCNTs.

The Figure 7.12 represents the C1s and O1s narrow scan spectra from the Birch reduced MWCNTs. The oxygen level is almost identical than for the untreated material. The most significant difference with the base nanotubes is visible in the oxygen spectrum with the respective shapes of the three components. The other interesting point is the fact that the iron has been completely removed by this treatment. From these XPS data, the Birch treatment does not appear to change significantly the surface chemistry of the MWCNTs apart the 0.5 at.% increase of the oxygen concentration which will have a clearly visible influence on the water adsorption isotherm.

High resolution Fe2p spectra were also determined by XPS and were fitted following the approaches of De los Arcos et al. [24] and Wu et al. [25]. The Figure 7.13 a) was obtained for the untreated material and the spectra from the sonicated Fenton MWCNTs is shown in Figure 7.13 b). A closer look to the last one shows us that the Fe2p line is a typical mixture of Fe²⁺ (711.0 eV) and Fe³⁺ (712.5 eV) oxidation states. This is confirmed by the presence of both shake-up satellites associated with the two broad peaks at 714.6 eV and 719.4 eV respectively. The other three peaks at higher binding energies are associated to the Fe2p1/2.



a)



b)

Figure 7.13: Fe2p peak envelopes a) for the untreated MWCNTs and b) for the sonicated Fenton MWCNTs.

7.3.3 Toluene adsorption on modified MWCNTs

The toluene adsorption on the base and modified MWCNTs represented on Figure 7.14 shows that the behaviour of the Birch reduced material is quite different from the base and Fenton treated materials. The isotherm on the Birch reduced nanotubes is displaced to higher adsorption values with almost a three-fold increase. This is clearly reflecting a change in the porous structure of the nanotubes as toluene adsorption is not influenced by the oxygen groups present on the surface (or inside) of the material. The isotherm curves for the untreated and Fenton treated MWCNTs are classified as Type II but the isotherm on the Birch reduced nanotubes could be considered as a type IV as a medium hysteresis loop typical of mesoporous material is observed.

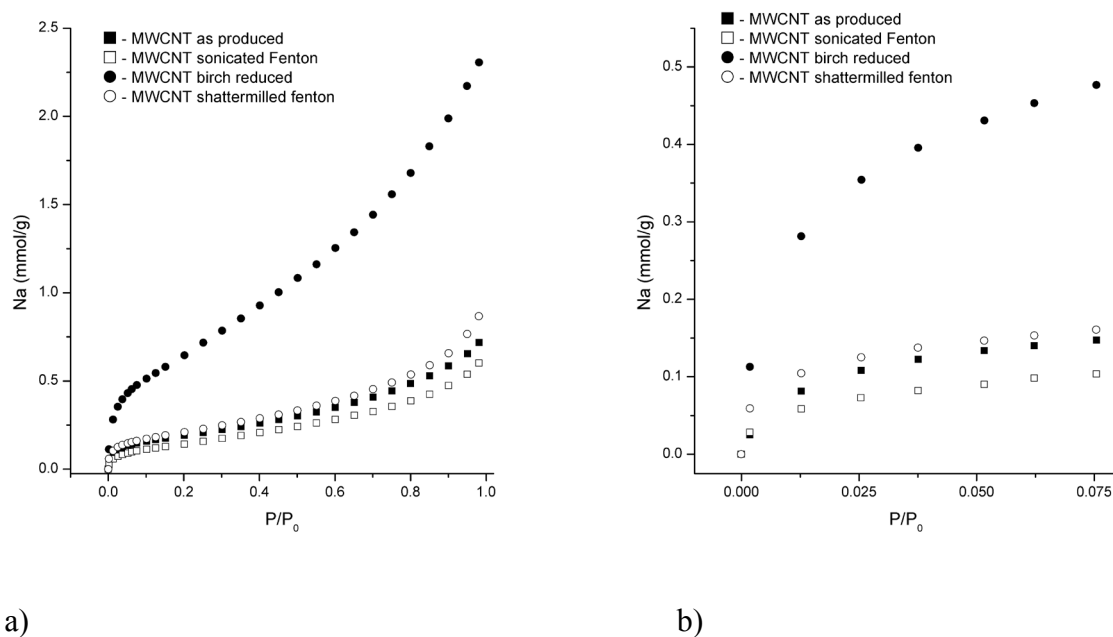


Figure 7.14: Toluene adsorption isotherms measured at 303°K for as produced and modified MWCNTs. a) View of the full isotherms and b) expansion of the very low pressure regions.

7.3.4 Water adsorption on modified MWCNTs

The water adsorption on the base and modified MWCNTs reflected clearly the change in surface polarity with increase in surface oxygen groups. The Figure 7.15 a) shows that the overall isotherms of the modified materials are displaced to higher adsorption values in relation to the surface oxygen levels measured by XPS and shown in Table 7.2. But the degree of displacement is not strictly proportional to the oxygen content. This is most noticeable on the Birch oxidised and shatter milled Fenton materials at high relative pressure. Figure 7.15 b) represents a zoom of the adsorption data at the low pressure ($p/p_0 < 0.25$). With almost identical oxygen level than the base nanotubes, the Birch material adsorbs similar, although slightly higher, water molecules than the untreated. On the contrary, as expected from its high oxygen levels, the Fenton materials show a very strong increase in water uptake presumably due to the multiplication of secondary adsorption sites with increasing p/p_0 as described by Dubinin and Serpinsky [26].

The isotherm curves for the untreated and Birch treated MWCNTs are classified as Type III (BDDT classification) as both of them follow closely the x-axis over most of the pressure range and are characteristic of relatively weak vapour-solid interactions. This type of shape is comparable to water isotherms obtained on carbon blacks with medium oxygen level as seen in the previous Chapter. On the other hand, as discussed above, the Fenton treated materials show a positive curvature in the low pressure region and can be considered as Type II in character. This reflects the increased numbers of primary sites, and polar interactions, rather than a significant increase in surface area.

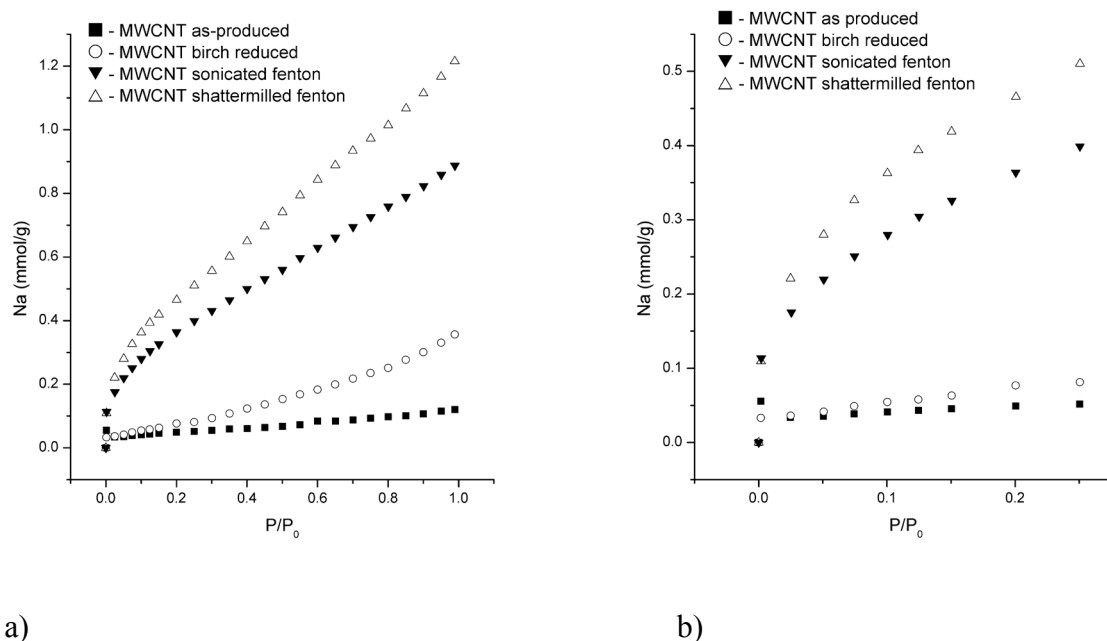


Figure 7.15. Water adsorption isotherms measured at 303°K for untreated and oxidized MWCNTs. a) view of the full isotherms and b) expansion of the low pressure regions where nucleation at primary (oxygen) sites takes place.

Mathematical analysis of water isotherms, for example has been used extensively to compare the surface chemistry of carbon materials, see for example [27][28][26]. The water adsorption data for these MWCNTs have been fitted with the following equations: original Dubinin and Serpinsky equation (Eq. 2.30), actual Dubinin and Serpinsky equation (Eq. 2.32) (represented in Figure 7.16 a)), Barton v1 equation (Eq. 2.34), Barton v2 equation (Eq. 2.35), generalized Barton v1 equation (Eq. 2.36) (represented in Figure 7.16 b)), D'Arcy & Watt equation (Eq. 2.37) (represented in Figure 7.16 c)) and generalized D'Arcy & Watt equation (Eq. 2.38). As you can see from the three plots, some equations give better fitting than the other as they depend on the type of materials. This can be explained as some of them were originally designed for microporous carbon and other for non-porous surfaces. In our case, the D'Arcy & Watt and generalized D'Arcy & Watt equations give excellent fits whether it be for base nanotubes (Type III isotherm) or for the sonicated Fenton nanotubes (Type II isotherm) whereas deviations were observed for the other equations in the low pressure region.

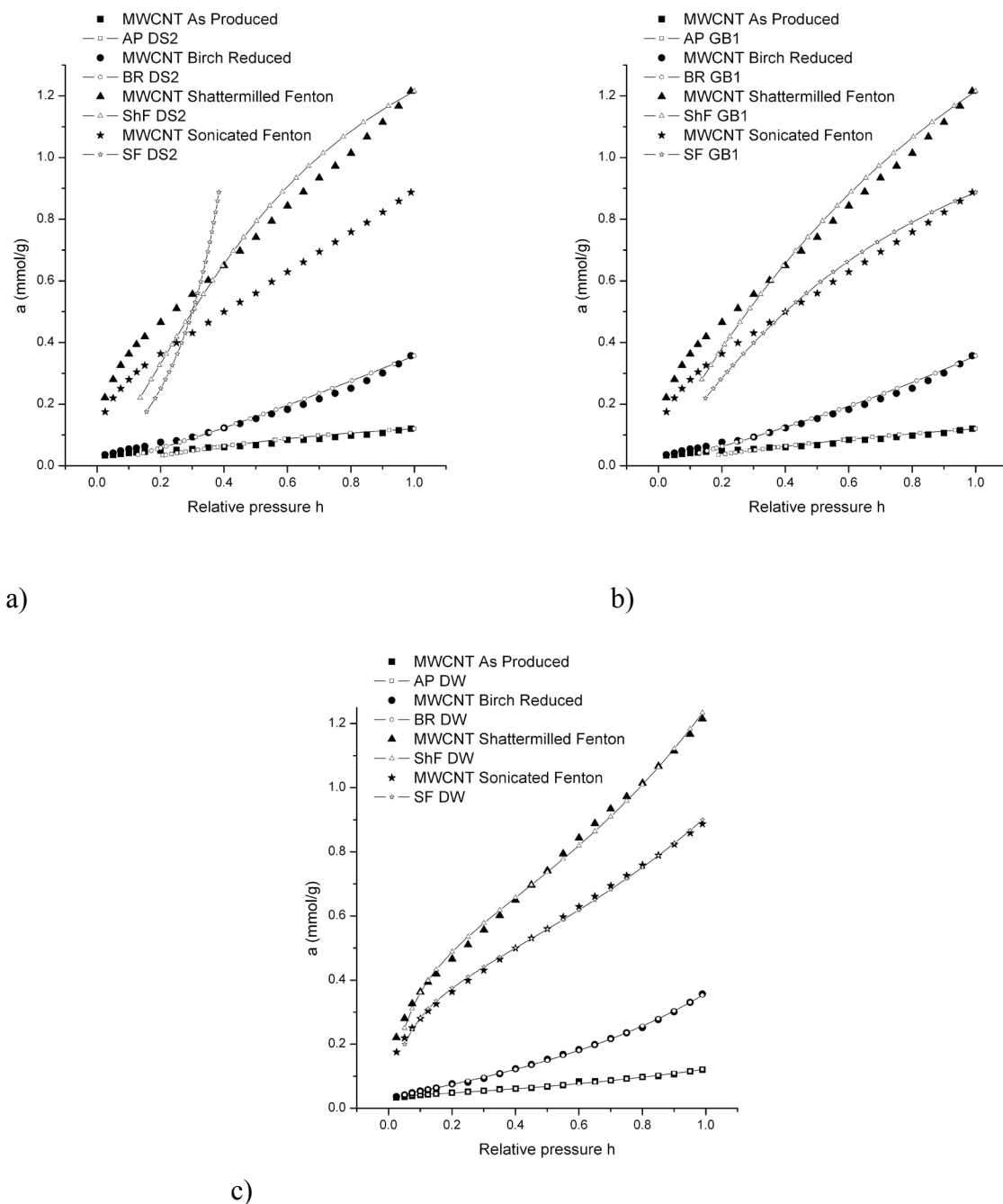


Figure 7.16: Experimental water adsorption data fitted with the following equations: a) Dubinin and Serpinsky, b) Generalized Barton and c) D'Arcy & Watt.

Preliminary measurements of enthalpies of immersion in water give values of -54 mJ/m^2 for the base nanotubes and -192 mJ/m^2 for the sonicated Fenton materials

indicating an approximate four-fold increase in polar interactions as a result of the hydroxylation treatment. Taking into account that the generally accepted energy for an ideal oxygen-free carbon surface is approximately -35 mJ/m^2 , the lower figure seems to be in agreement with values reported for moderately oxidized graphene surfaces in carbon blacks [29][30] which are, of course, much less ordered than MWCNT surfaces.

7.4 Conclusions

The Fenton functionalisation has been used on MWCNTs to increase the surface oxygen levels from 4.3 to 23.5 at.%. As the difference with the Fenton reaction, the Birch reduction, which was also studied results in surface oxygen levels of 4.8 at.% which are almost identical to the untreated MWCNTs. XPS data show that all these materials, even after functionalisation treatment, have C1s peaks with relatively narrow FWHM values synonym of highly ordered graphitic structure. Using the chemical shift data and narrow scan O1s, the predominant surface groups on the Fenton treated materials were found to be the hydroxyl ($-\text{OH}$) groups.

HRTEM photographs show that the multi-wall structure of the nanotubes is not significantly disrupted by the Fenton or Birch process. Similar number of walls for the treated and base materials was observed, with no significant evidence of the structural disruption of debris/contamination on the external surface. This appears consistent with the minimal change in the FWHM values which characterised the treated materials. The absence of physical disruption due to functionalisation suggests that the hydroxylation takes place at pre-existing graphene edge, and in-plane defect sites on the MWCNT surfaces.

Surface area and porosity data derived from nitrogen adsorption results indicate some separation of MWCNT bundles due to the functionalisation treatment and resulting in a loss of macroporosity (loss of inter-tube capillarity).

The increased surface polarity is reflected in the water adsorption isotherms which are displaced to higher adsorption values for the oxidized surfaces. Regarding interfacial bonding, the oxidised materials are expected to show an improved physicochemical wetting of the MWCNT surfaces by the resin compounds. Similar behaviours have already been reported in the literature for carbon fibres [31][32] and carbon blacks [30][33][34].

References

- ¹ H. W. Kroto, J. R. Heath, S. C. O'Brien, R. F. Curl and R. E. Smalley. C60: Buckminsterfullerene. *Nature* **318** (1985) 162-163.
 - ² T. V. Hughes and C. R. Chambers. *Manufacturing of Carbon Filaments* US Patent No. 405480-1889 (USA, 1889).
 - ³ L. V. Radushkevich and V. M. Lukyanovich. O strukture ugleroda, obrazujucesja pri termiceskom razlozenii oksii ugleroda na zeleznom kontakte. *Zurn. Fisic. Chim.* **26** (1952) 88-95.
 - ⁴ R. Andrews et al. Continuous production of aligned carbon nanotubes: a step closer to commercial realization. *Chem. Phys. Lett.* **303** (1999) 467-474.
 - ⁵ A. Oberlin, M. Endo and T. Koyama. Filamentous growth of carbon through benzene decomposition. *J. Cryst. Growth* **32** (1976) 335-349.
 - ⁶ A. Barber, R. Andrews, L. Schadler and H. D. Wagner. On the tensile strength distribution of multiwalled carbon nanotubes. *Appl. Phys. Lett.* **87** (2005) 203106/1 - 203106/3.
 - ⁷ S. Bellucci. Carbon nanotubes: physics and applications. *Physica Status Solidi (c)* **2** (2005) 34-47.
 - ⁸ M.-F. Yu, O. Lourie, M. J. Dyer, K. Moloni, T. F. Kelly and R. S. Ruoff. Strength and breaking mechanism of multiwalled carbon nanotubes under tensile load. *Science* **287** (2000) 637-640.
 - ⁹ B. G. Demczyk, Y. M. Wang, J. Cumings, M. Hetman, W. Han, A. Zettl and R. O. Ritchie. Direct mechanical measurement of the tensile strength and elastic modulus of multiwalled carbon nanotubes. *Materials Science and Engineering A* **334** (2002) 173-178.
 - ¹⁰ H. G. Chae and S. Kumar. Rigid-rod polymeric fibers. *Journal of Applied Polymer Science* **100** (2006) 791-802.
 - ¹¹ Australian Stainless Steel Development Association (ASSDA) website: <http://www.assda.asn.au/> accessed 12/02/2009.
 - ¹² R. Bradley, A. Andreu, unpublished data.
-

- ¹³ I. Mathieson and R. H. Bradley. Surface oxidation of poly ether ether ketone films using ultraviolet/ozone. *J. Mater. Chem.* **4** (1994) 1157-1157.
- ¹⁴ I. Mathieson and R. H. Bradley. Improved adhesion to polymers by UV/ozone surface oxidation. *Int. J. Adhes. Adhes.* **16** (1996) 29-31.
- ¹⁵ R. H. Bradley, I. Sutherland and E. Sheng. Relationship between carbon black surface chemistry and energy. *J. Chem. Soc., Faraday Trans.* **91** (1995) 3201-3207.
- ¹⁶ E. Sheng, I. Sutherland, R. H. Bradley and P. K. Freakley. Heat of immersion calorimetry studies of carbon blacks. *Materials Chemistry and Physics* **50** (1997) 25-30.
- ¹⁷ R. H. Bradley, R. Daley and F. Le Goff. Polar and dispersion interactions at carbon surfaces: further development of the XPS-based model. *Carbon* **40** (2002) 1173–1179.
- ¹⁸ A. Andreu, H. F. Stoeckli and R. H. Bradley. Specific and non-specific interactions on non-porous carbon black surfaces. *Carbon* **45** (2007) 1854–1864.
- ¹⁹ R. H. Bradley, A. Andreu and H. F. Stoeckli. *Correlation of water adsorption isotherms with oxygen groups on carbon black surfaces* International Conference on Carbon 2007 (Seattle, USA, 2007).
- ²⁰ E. Fitzer, K.-H. Geigl, W. Hüttner and R. Weiss. Chemical interactions between the carbon fibre surface and epoxy resins. *Carbon* **18** (1980) 389-393.
- ²¹ R. Verdejo, S. Lamoriniere, B. Cottam, A. Bismarck and M. Shaffer. Removal of oxidation debris from multi-walled carbon nanotubes. *Chem. Commun.* (2007) 513–515.
- ²² W. Z. Zhu, D. E. Miser, W. G. Chan and M. R. Hajaligol. Characterization of multiwalled carbon nanotubes prepared by carbon arc cathode deposit. *Mater. Chem. Phys.* **82** (2003) 638-647.
- ²³ H. Valdés, M. Sánchez-Polo, J. Rivera-Utrilla and C. A. Zaror. Effect of ozone treatment on surface properties of activated carbon. *Langmuir* **18** (2002) 2111–2116.
- ²⁴ T. de los Arcos et al. The influence of catalyst's oxidation degree on carbon nanotube growth as a substrate-independent parameter. *J. Phys. Chem. C* **111** (2007) 16392–16396.
- ²⁵ S. L. Wu et al. Characterization of the surface film formed from carbon dioxide corrosion on N80 steel. *Mater. Lett.* **58** (2004) 1076-1081.

- ²⁶ M. M. Dubinin and V. V. Serpinsky. Letter to the Editor. Isotherm equation for water vapor adsorption by microporous carbonaceous adsorbents. *Carbon* **19** (1981) 402-403.
- ²⁷ S. S. Barton, M. J. B. Evans and J. A. F. MacDonald. The adsorption of water vapor by porous carbon. *Carbon* **29** (1991) 1099-1105.
- ²⁸ R. L. D'Arcy and I. C. Watt. Analysis of sorption isotherms of non-homogeneous sorbents. *Trans. Faraday Soc.* **66** (1970) 1236 - 1245.
- ²⁹ R. H. Bradley, I. Sutherland and E. Sheng. Relationship between carbon black surface chemistry and energy. *J. Chem. Soc., Faraday Trans.* **91** (1995) 3201-3207.
- ³⁰ E. Sheng, I. Sutherland, R. H. Bradley and P. K. Freakley. Heat of immersion calorimetry studies of carbon blacks. *Materials Chemistry and Physics* **50** (1997) 25-30.
- ³¹ R. H. Bradley, I. L. Clackson and D. E. Sykes. XPS of oxidized wool fibre surfaces. *Surf. Interface Anal.* **22** (1994) 497-501.
- ³² R. H. Bradley, I. Mathieson and K. M. Byrne. Spectroscopic studies of modified wool fibre surfaces. *J. Mater. Chem.* **7** (1997) 2477 - 2482.
- ³³ R. H. Bradley, E. Sheng, I. Sutherland, P. K. Freakley and H. Ismail. Interfacial chemistry and mechanical effects of a multifunctional processing additive on carbon black filled rubber. *J. Mater. Chem.* **4** (1994) 1189-1193.
- ³⁴ R. H. Bradley, I. Sutherland and E. Sheng. Relationship between carbon black surface chemistry and energy. *J. Chem. Soc., Faraday Trans.* **91** (1995) 3201-3207.

8

Chapter 8 Conclusions

The major conclusions of this study are summarised as follow:

Initial characterisations were conducted on the base and oxidised carbon materials used in this work to give us a better understanding of the relationships existing between surface chemistry, carbon structure (less extent) and chemical interactions. AFM observations on graphite indicate that on the observable “*central*” region the physical structure of the graphene sheets is not disrupted by either ozone or liquid-phase oxidation. A conclusion on the possible erosion of the layer edges or structural defects is difficult to draw at this stage. SEM observations on oxidised carbon black N330 indicate that ozone and even ammonium persulfate treatments do not significantly change the surface morphology unlike HNO₃ oxidation. Regarding activated carbon materials, high magnification images indicate that only ozone treatment does not deteriorate the external structure of the activated carbon particles. Medium-temperature thermogravimetric analyses were carried out on oxidised materials and highlighted the presence of oxygen-containing functional groups on these solids along with information about their thermal decomposition temperature. Gradual heat treatments under inert atmosphere were conducted on a naturally oxidised BPL sample. The surface oxygen concentration $[O]_T$ was found to decrease linearly as the temperature increases. Toluene adsorption data also indicates that the porous carbon structure remains almost unchanged by this controlled reduction heat treatment.

The second part of this work focuses on specific and non-specific interactions of alcohols on non-porous carbon black surfaces. For this, a series of carbon black N330 with increasing surface oxygen concentration $[O]_T$ (from 1.7 at.% for the base material to 11.2 at.%) has been produced using ozone fluidized bed apparatus. The chemical composition of the resulting surfaces was measured using XPS. As data from nitrogen adsorption at 77°K indicates, this oxidation treatment has only a minimal effect on the physical structure of the carbon black. Vapour adsorption and immersion calorimetry experiments were carried out to study the interactions between these surfaces and three alcohols (i.e. methanol, ethanol and isopropanol). Strong correlations were observed between the surface oxygen level and the structure/polarity of the adsorbate molecules. The adsorption of these alcohols was found to be highly sensitive to $[O]_T$ in the low pressure domain. The increase of oxygen-containing functional groups on the surface leads to a displacement of the isotherms toward higher adsorption values, starting from a type III isotherm for the base untreated material to a type II shape for the oxidised carbon blacks. The data show a shift with methanol behaving more like water with mainly specific interactions at active sites (oxygen groups) whereas isopropanol being more similar to toluene with weaker non-specific dispersion interactions with oxygen-free carbon surface. Values obtained from immersion calorimetry experiments also reflect this transitional behaviour as the alkyl chain length of the alcohols increases. Analysis of the adsorption data using the DRK equation shows a clear relationship between the surface oxygen concentration $[O]_T$ and both E_{DRK} and $\beta_{DRK}(\text{alcohols})$. These correlations between these equation parameters and measurable physicochemical variables, such as $[O]_T$, is highly attractive for both isotherm prediction and for the refinement of adsorption models.

Presented in the third part of this work is an experimental study on the interactions of polar molecules (water) with various carbon surfaces. The same series of oxidised

carbon black N330 was used in this study. Additionally, N330 carbon black and BPL activated carbon were also oxidised with acids (nitric acid, hydrogen peroxide and ammonium persulfate) as a comparison to ozone treatment and non-porous surface. The chemical composition of all resulting surfaces was analysed using XPS. The quantification results show a significant increase of the surface oxygen level $[O]_T$ up to 11.2 at.% for N330 treated with HNO_3 and up to 17.9 at.% for BPL treated with H_2O_2 . For the ozonated carbon black series, on a first hand, the immersion calorimetry data show that the interactions shift from non-specific dispersion interactions for toluene toward specific polar interactions for water. On the second hand, the type III adsorption isotherms observed for water, are displaced to higher water adsorption uptakes as the surface oxygen level $[O]_T$ increases. Regarding the carbon blacks subjected to liquid-phase oxidation, N330 treated with H_2O_2 and Amm Per show similar isotherm shapes but slightly higher than the base N330 material. On the contrary, the adsorption isotherm of the N330 treated with HNO_3 shifted to a Type II character, associated with really high adsorption values. Activated carbon materials also exhibit type III isotherms with almost twofold increase of water adsorption uptake (a_s) for the ACs subjected to liquid-phase oxidation. In the low pressure region, significant differences in terms of adsorption capacity and kinetics of adsorption were observed. Unlike ozone treatment, the oxidation with nitric acid seems to affect both surface chemistry and physical structure of the carbon material as confirmed by adsorption data. For most of the materials, it was shown that the resulting parameter a_0 describing the surface concentration of primary polar adsorption sites, was linked to the surface oxygen level $[O]_T$ measured by XPS, which also influences both the degree of fit to the equation and the limiting experimental water adsorption value a_s . The DS2 and various Barton equations were found to fit best the AC and CB materials modified by liquid-phase oxidations and also for the N330 O_3 series with different levels of oxidation. XPS is shown to provide direct, quantitative, first principle information about carbon surfaces which correlates with their interactions with

fluid phases and consequently it has potential for increasing our detailed understanding of the specific processes which occur at such surfaces.

The final part of this work contains surface studies of functionalised multi-wall carbon nanotubes (MWCNTs). Fenton functionalisation and Birch treatment were carried out on MWCNTs to increase the surface oxygen concentration $[O]_T$ (from 4.3 at.% to 4.8 at.% for the Birch and 23.5 at.% for the Fenton material). The XPS results confirmed that the oxidised materials kept a highly graphitic structure as they exhibit C1s peak with relatively narrow FWHM values. Adsorption data for nitrogen at 77°K indicates a slight increase in area being due to separation of the tube-bundles during functionalisation. This is accompanied by a decrease in measured porosity which is consistent with an attendant loss of inter-tube capillarity. This minimal effect of the Fenton and Birch treatments on the multiwall structure was confirmed by HRTEM observations. As the oxygen level $[O]_T$ increases and even for the Birch material, the water adsorption isotherms show a clear displacement to higher adsorption values reflecting the predominance of specific interactions between water molecules and polar sites. The best isotherm fits were obtained when using the D'Arcy & Watt equations. This difference in polar surface energy is confirmed by calorimetric enthalpies of immersion in water which are -54 mJ/m^2 for the untreated and -192 mJ/m^2 for the hydroxylated materials. The treated materials therefore have significantly increased water wettability/dispersibility and a greater potential for cross-linking with matrix compounds.

Future work

I hope that the work presented in this thesis will open the way to future studies in particular in the following areas. Though some initial and very promising results have been obtained for activated carbon treated with plasma polymerisation in order to increase the hydrophobicity of the surface, it did not reach a stage to be included in this thesis. This path would need to be explored more in depth and could then be possibly translated to other carbon materials such as carbon black and more particularly carbon nanotubes.

In the present study, the XPS elemental quantification only took into account the external surface of the sample so it would be very interesting to try to characterise the “*internal*” surface chemistry of carbon materials. This could be realised using the argon etching capability of the Kratos Axis Hsi XPS to obtain a profile of the surface composition as a function of the analysis depth. It would be very useful to make a detailed study of the oxidation process of ozone (gas-phase) and acids (liquid-phase) or even the plasma deposition and their relative penetration depth inside the porous structure of these materials.

Another area of investigation would be to apply the same strategy as described afore to polar vapours other than water and methanol and also to use modelling tools such as Monte-Carlo simulation or CFD (Computational Fluid Dynamics) to compare theoretical analysis with experimental data and check the influence of surface oxygen-containing functional groups as measured by XPS for example.

A

APPENDIX A Glass ampoule fabrication

The following procedure has been designed and used in this work to make the glass ampoules necessary for immersion calorimetry experiments.

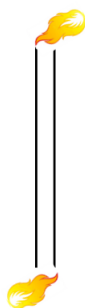
Required materials:

- Glass tube (Schott-Duran, UK): 10 mm OD x 1 mm WT x 1500 mm L
- Glass rod (Schott-Duran, UK): 3 mm OD x 1500 mm L
- Glass knife (with diamond tip)
- Blowtorch (with oxygen/acetylene gas mixture)

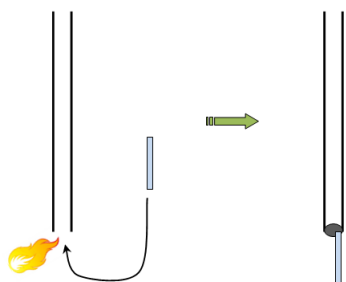


Glass tube segment of 20~25 cm length should be cut using the glass knife.

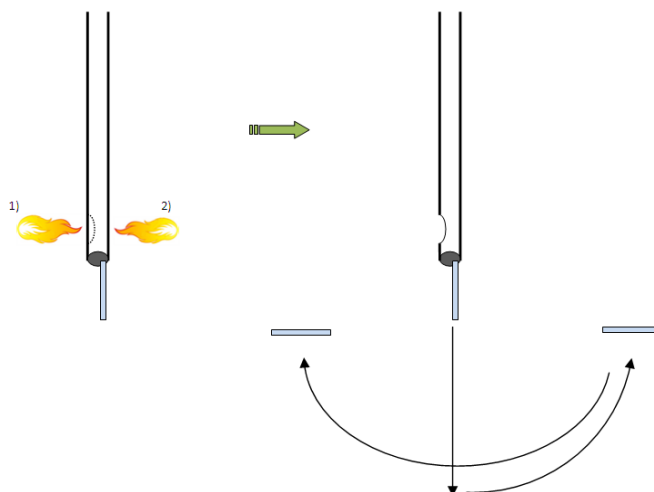
First, make a jag then moisten and snap cut the tube.



Clean the tube with the blowtorch and smooth the rough edges of the tube off.



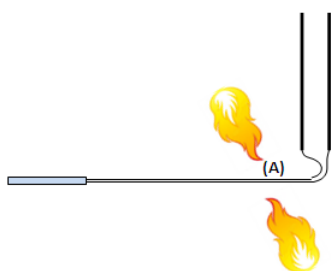
A short glass stem (of 3~4 cm length and 3 mm OD) will be used to pull down the glass in the next steps.
Melt the bottom end of the tube and stick it the glass stem.



Heat up the left part of the tube just above the stem until half of the tube has melt (the glass becomes white) (1).

Heat up very quickly on the other side of the tube during 2~3 s (2).

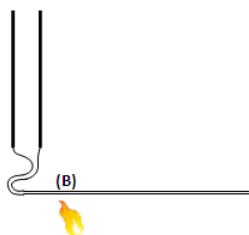
Then, pull the stem down by 20~30 cm, go up quickly in a 90° arc and finally quickly go to the other side still in a 180° arc.



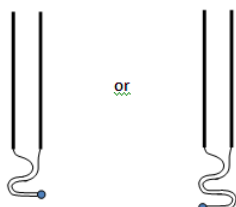
Making of the brittle end

Firstly, break the end part with the stem (in order to remove the weight)

Heat using a very small flame at the point (A) and then turn quickly on the right in a 180° arc.



Heat using a very small flame at the point (2) and then turn quickly on the left in a 180° arc.



Use a small flame to create a little ball at the extremity. Depending on the usage, two kinds of ampoules can be designed: single capillary or double capillary ampoule.



Make a relatively deep mark on the tube by melting the glass (2~3 mm deep). This will help to seal the ampoule faster after degassing.